University of Nottingham
UK | CHINA | MALAYSIA

EPSRC
Engineering and Physical Sciences Research Council

The Supramolecular Chemistry of Amphiphilic Redox-Active Organic-Inorganic Hybrid Polyoxometalates

Sharad Amin

4289544

School of Chemistry

A thesis submitted to the University of Nottingham for the degree of Doctor of Philosophy

ACKNOWLEDGEMENTS

This PhD has been an absolute roller coaster of a journey which I will always cherish and was achieved with tremendous love and support of colleagues, friends and family.

Foremost, I'd like to thank Dr Graham Newton for being an amazing supervisor. From the very start when I worked on a masters project under your supervision, you pushed me to explore science independently, and through your positive and enthusiastic attitude towards research, my mindset and outlook on science completely changed. Your encouragement to explore new research ideas is what developed me to achieve what I have today. I sincerely thank you for encouraging me to pursue a PhD.

I would like to thank Dr Victor Sans for also supervising me during his time in Nottingham and hosting me when I was on placement in Spain. Equally, I would like to thank Dr Darren Walsh for great scientific discussion, his supervision and enthusiasm for science.

I would also like to thank Dr Jamie Cameron for also being there to through every problem I've had and being a voice of reason. You have also brought about a lot of positive advice both scientifically and non-scientifically. Likewise, I'd like to thank Dr Alex Kibler for offering great scientific advice, being a great travel companion and always being up for a night out. Furthermore, I would like to thank Dr Kathi Kastner for supervising my masters project and encouraging me to pursue a PhD.

I thank Heather Damian for being a great research partner and putting up with my chaotic research schedule.

My time in Nottingham has been enjoyable with regards to research and social life. Therefore, I'd like to thank the lads of 16 park road past and present (Adam, Arjan and Toby) for some great years. I would like to also thank all my friends in Nottingham for facilitating such a memorable time.

A special thanks to Gareth Mabbett for not only providing me with the tightest of fades as my barber but also with great chat and advice as a friend over the years of my undergraduate and PhD study.

A special mention and thanks go to Pritesh Patel and his family for treating me as if were their own – you have made me feel like family which I'll never forget.

Thank you, Ka Man Shing, for being my rock through the thick and thin of my PhD journey. You have shown me nothing but love. You are amazing and I'm lucky to have you by my side.

Thank you to my entire family for believing in me, pushing me to new limits and always trusting in me. I am here today because of the way you have encouraged and motivated me. To Mum and Dad, you are both truly inspirational, through the ups and downs of my PhD journey I've always looked up to your work ethic, drive and love that you've shown me. I have achieved what I have today because of you.

Finally, I'd like to thank Bhagwan Swaminarayan, late Pramukh Swami Maharaj and Guruhari Mahant Swami Maharaj for their blessing, encouragement and guidance through life.

DECLARATION AND TECHNICAL ACKNOWLEDGEMENTS

I declare that all experimental work, analysis, writing, or figure making in this thesis was conducted by myself or with the help and input of the following mentions.

I would like to thank collaborators Dr David Robinson and Max Winslow for their excellent DFT calculations. Likewise, I would like to thank Dr Julie Watts and Dr Michael Faye for the amazing TEM data provided over the years and general enthusiasm for my research. Furthermore, I would like to thank Dr Richard Cousins for the ellipsometry and SEM analysis, James Wringley for the AFM analysis, Dr Stephen Davies for spectroelectrochemical and EPR analysis, and finally, Dr Stephen Argent and Dr Max Astle for the XRD analysis.

ABBREVIATIONS LIST

ATR-IR	Attenuated total reflectance infra-red
CT	Charge transfer
CV	Cyclic voltammetry
DFT	Density functional theory
DMA	*N,N* - Dimethylacetamide
DMF	*N,N* - dimethylformamide
DMSO	Dimethylsulfoxide
ESI-MS	Electrospray ionization mass spectrometry
Et_2O	Diethyl ether
EtOH	Ethanol
HOMO	Highest occupied molecular orbital
IVCT	Intervalence charge transfer
LMCT	Ligand to metal charge transfer
LUMO	Lowest unoccupied molecular orbital
MeCN	Acetonitrile
MeOH	Methanol
NMR	Nuclear magnetic resonance
POM	Polyoxometalate
PXRD	Powder X-ray Diffraction
TBA	Tetra-*n*-butylammonium
TBADT	Tetra-*n*-butylammonium decatungstate
TGA	Thermogravimetric analysis
UV	Ultraviolet
UV-vis	Ultraviolet visible
TMSBr	Trimethylbromosilane
D_h	Hydrodynamic diameter
R_h	Hydrodynamic radius

COLOUR SCHEME

All figures that have not been reproduced from literature adhere to the following colour scheme:

Tungsten: Light blue

Phosphorus: Pink

Vanadium: Yellow

Silicon: Orange

Molybdenum: Lime Green

Sulfur: Yellow

Carbon: Dark grey

Hydrogen: Light grey

Oxygen: Red

Nitrogen: Marine blue

PUBLICATIONS

1. **"Effects of chain length on the size, stability, and electronic structure of redox-active organic–inorganic hybrid polyoxometalate micelles"**, S. Amin, J.M. Cameron, J. A. Watts, D. A. Walsh, V. Sans and G. N. Newton*, Mol. Syst. Des. Eng., 2019, 4, 995-999*

2. **"Asymmetric Hybrid Polyoxometalates: A Platform for Multifunctional Redox-Active Nanomaterials",** E. Hampson, J. M. Cameron, S. Amin, J. Kyo, J. A. Watts, H. Oshio and G. N. Newton*, Angew. Chem. Int. Ed., 2019, 58 (50), 18281-18285.*

CONTENTS

1. Introduction **1**
1.1 Polyoxometalates 1
1.2 Structure, Bonding and Self-assembly 1
1.3 Archetypal Polyoxometalate Structures 5
1.3.1 Lindqvist Structure 6
1.3.2 Anderson Structure 7
1.3.3 Keggin Structure 8
1.3.4 Wells-Dawson Structure 10
1.3.5 Lacunary Structure 12
1.4 Electronic Structure of POMs 13
1.5 Hybridisation 15
1.6 Supramolecular Assembly Hybrid POMs 18
1.6.1 Class I Hybrid Supramolecular Assembly 19
1.6.2 Class II Hybrid Supramolecular Assembly 26
1.6.2 Hybrid-POM Amphiphiles 27
1.6.2 Surfactant-Encapsulated Hybrid-POMs 26
1.7 References 42
2. Synthesis, Characterisation and Supramolecular Assembly of Hybrid-POM Redox-active Amphiphiles **44**
2.1 Introduction 44
2.2 Aims 48
2.3 Results and Discussion 49
2.3.1 Synthesis 49
2.3.2 Structural Characterisation 52
2.3.3 Electronic Characterisation 55
2.3.4 Redox-active Micelles 56
2.4 Conclusion 63
2.5 Experimental 65
2.6 References 70
3. Hierarchical Self-Assembly of a Redox-Active Hybrid-POM Amphiphiles **71**
3.1 Introduction 71
3.2 Aims 77
3.3 Results and Discussion 78

3.3.1 Hierarchical Self-Assembly of Redox-Active Amphiphiles at Carbon Surfaces 78
3.3.1.1 Materials and Surface Preparation 78
3.3.1.2 Electrode Deposition of Redox-Active Micelles 78
3.3.1.3 Electrolyte Contribution 84
3.3.1.4 Surface Effects on the Hierarchical Self-Assembly 90
3.3.2 Temperature-Driven Hierarchical Self-Assembly 95
3.4 Conclusion 105
3.5 References 107
4. Development of Diphosphonates Hybrid POMs: Electronic Structure Modulation and Ligand Platforms 108
4.1 Introduction 108
4.2 Aims 111
4.3 Results and Discussion 112
4.3.1 Synthesis 113
4.3.2 Structural Characterisation 116
4.3.3 Electronic Characterisation 117
4.3.4 Photoreduction Investigation 119
4.3.5 Functionalisation of POMs through Disphosphonate Linkers 127
4.4 Conclusion 129
4.5 Experimental 131
4.6 References 134
5. Synthesis and Electronic Characterisation of Mixed-Addenda Organophosphonate Hybrid POMs 135
5.1 Introduction 135
5.2 Aims 139
5.3 Results and Discussion 140
5.3.1 Synthesis and Characterisation 140
5.3.2 Electronic Characterisation 144
5.3.3 Mixed-Addenda Redox-Active Assemblies 150
5.4 Conclusion 153
5.5 Experimental 155
5.6 References 156
6. Hybrid POMs as Nanocomposite Feedstock Material for Metal Oxide Microshell Synthesis 157
6.1 Introduction 157
6.2 Aims 161
6.3 Methodology 162

6.4 Results and Discussion 163
6.4.1 Preliminary Results 163
6.4.2 Optimisation of Spay-Drying 166
6.4.3 Calcination 168
6.5 Conclusion 172
6.6 References 172
7. Conclusions and Outlook **174**
8. Methods, Materials and Instrumentation **176**
9. Appendix **178**

ABSTRACT

This thesis focuses on the synthesis and supramolecular assembly of Class II hybrid-POM amphiphiles, in which these molecules will be synthesized, characterized and their supramolecular assembly studied.

Chapter 2 explores the development and supramolecular assembly of a hybrid-POM amphiphile $\{W_{17}C_{20}\}$ based on a lacunary Wells-Dawson polyphosphotungstate cluster hybridised to two hydrophobic C_n (n = 10, 12, 14, 16, 18, 20) chains through phosphonic acid linkers. This investigation focused on how ligand chain length affects the supramolecular assembly and the redox activity of the supramolecular assembly. Here, the longer chain lengths led to smaller, stable more discrete assemblies which demonstrate contrasting redox chemistry to the molecular species.

Chapter 3 studied the hierarchical self-assembly behavior of hybrid-POM amphiphile, where surface interactions and temperature stimuli were probed. Redox-active micelles based on $\{W_{17}C_{20}\}$ were found to self-assemble into monolayers and retain redox-activity at glassy carbon electrode surfaces. Furthermore, based on the hydrophobicity of various carbon surfaces, micellar structures were found to transition upon deposition to other higher order structures such as fibers. Hierarchical self-assembly transition was also found when freezing aqueous micelle solutions of $\{W_{17}C_n\}$ which led to the formation of cylindrical micelles. The degree of order was correlated to the increasing chain length of the amphiphile. Furthermore, the cylindrical micelles could be isolated and acted as soft-templates for nanostructured metal oxide material.

Chapter 4 focused on the development of new hybrid linkers and ligands based on the hybridisation of diphosphonate molecules (methylene diphosphonate (MDP), imidodiphosphonate (IDP) and pyrophosphate (PP)) with lacunary Wells-Dawson cluster $\{W_{17}\}$. We found that based on the electronic nature of the diphosphonate, the POM cluster could be photoactivated with varying degrees upon hybridisation which was tested through the photoreduction of the hybrid clusters in the presence of sacrificial electron donor DMF when irradiated with UV-Vis or visible light. This correlated to the

electron withdrawing (EW) or electron donating (ED) effects imposed by the ligand on the POM. Here, MDP hybrid {W_{17}MDP} was the most photoactivated towards oxidation of DMF under visible light irradiation and more easily reduced owing to MDPs lesser ED nature compared to the other hybrids. Furthermore, MDP type ligands could be modified to couple additional organic moieties to the POM.

Chapter 5 focused on the development of mixed-addenda hybrid organo-functionalized POMs. Here we found that the HOMO-LUMO energy levels of the POM could be further modulated and tuned with respected to organophosphate hybrids. Mo substitution (for W) into the hybrid clusters led to a positive shift in the reduction potentials with respect to it pure tungsten hybrid analogue. EPR spectroscopy also reported the localisation of the electrons on the Mo centers with respect to the first reductions. Furthermore, DFT calculations found that metal substitution lowers the HOMO-LUMO energy gap. Similarly, amphiphilic hybrid based on organophosphate mixed-metal cluster demonstrated contrasting surface confined electrochemistry to pure tungsten analogue.

Finally, chapter 6 focused on employing hybrid-POM amphiphiles as feedstock for spray-drying soft-templates for solid-state metal oxide particle fabrication. Here we found contrasting structures exhibited when processing plenary POM clusters compared to hybrid-POM amphiphiles; differences were found in the soft-template as well as in the post-calcination material. Mixed-metal hybrids were also employed to produce doped metal oxide particles. PXRD analysis showed transition from soft templates to mixed phases of WO_3.

1 INTRODUCTION

1.1 POLYOXOMETALATES

Polyoxometalates (POMS) are a group of discrete polyanionic molecular metal oxide clusters assembled from early transition metals in their highest oxidation states, most commonly vanadium,[1, 2] molybdenum,[3] and tungsten.[1] Some less common transition metals that assemble into POM structures include niobium,[4] tantalum,[5] and palladium.[6] These clusters are assembled through the condensation of pseudo-octahedral MO_x units (M = V, Nb, Mo, W, Nb, Ta or Cr). POMs possess a wide range of desirable properties, but in particular are well-known for their rich and reversible redox activity.[7] Arising from their wide-spread interest linked to their attractive properties, POMs have been applied in a broad range of applications such as medicine,[8] catalysis,[9, 10] sensing,[11] and magnetism.[12]

Along with the large library of accessible POM clusters with unique properties, POMs are particularly fascinating and attractive due to their electronic tuneability. Such flexibility in their structure, composition and modification enables POMs to be widely applicable in a broad range of fields; demonstrating a designable approach through bottom-up assembly of metal-oxo building blocks to nanoscopic materials.

1.2 STRUCTURE, BONDING AND SELF-ASSEMBLY

Although POMs exhibit an enormous library of structures, their assembly is dictated by a set of stringent rules. Firstly, despite the complexity associated with POM structures, a simple overarching description based on the assembly of individual $[MO_X]$ polyhedron units (where X = 4-7), is commonly adopted to describe POM clusters.[13, 14] These polyhedral units consist of a central metal atom (referred to as *addendum*), coordinated to O^{2-} oxo-ligands. The assembly of POMs is typically triggered by acid driven condensation of individual polyhedral $[MO_x]$ units. For an addenda atom to polycondense to into polynuclear POM clusters, they must fit certain criteria: 1) the ability to transition coordination

numbers from 4 to 6 upon acidification in solution; 2) possess high positive charge and are amongst the smaller of metal ions capable of octahedral coordination mode; 3) they are capable of forming M=O bonds *via* dπ-pπ interactions.[14, 15] As a result of these constraints, the majority of POM species compromise of addenda atoms from group V and VI transition metals such as V, Nb, Mo and W, in their highest oxidation states (d^0 or d^1). [16]

The oxo-ligands surrounding the metal addenda in the polyhedron exhibit a large degree of structural flexibility and possess the ability to form a number of bridging and terminal bonding modes, which is represented by the notion μ_n (where n = number of bridged metal atoms), which allow polycondensation with other [MO_x] addenda atoms and limit the degree of polycondensation through the formation of stable terminal M=O bonds, respectively. The bridging oxo-ligands possess the ability to link between 2 and 6 addenda atoms ($\mu_{2\text{-}6}$). The stability of POM clusters is owed to the presence of terminal M=O groups, which exhibit a strong thermodynamic *trans-effect* by weakening the opposite bridging oxo-M bond that shares the same orbital (Figure 1). The result of this *trans-effect* displaces the metal centre towards the terminal oxo-ligand and distorts the octahedral geometry.[17]

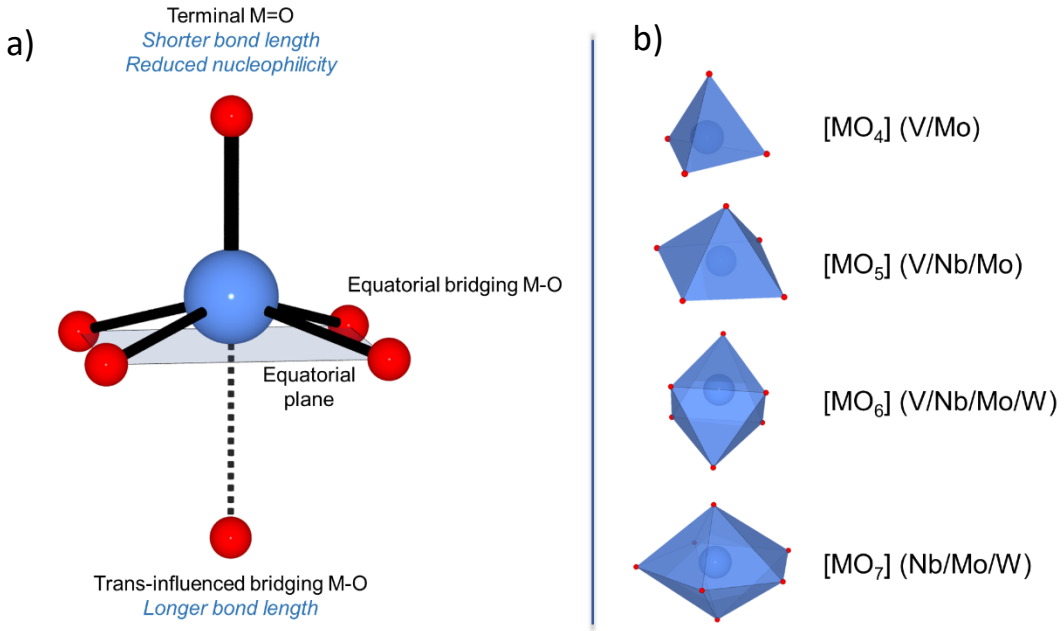

Figure 1 - a) An illustration depicting the *trans*-effect and b) a list of the possible [MO_x] polyhedral units found in POM structures and the addenda metal species capable of forming them.

This advantageously reduces the basicity of the terminal oxo-ligand and the likelihood of acid mediated protonation, which inhibits (to a large extent) its ability to further polycondensate into larger species. This is the main reason behind why POMs exist as discrete molecular clusters.

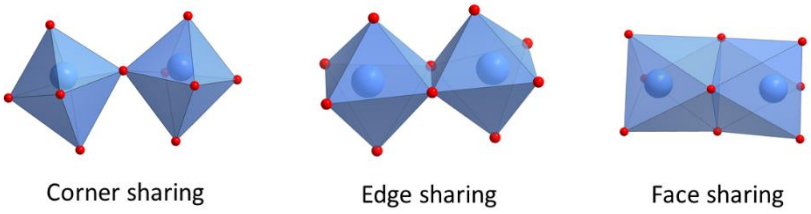

Figure 2 - Connectivity modes between [MO_x] polyhedral units upon oligomerisation which exhibit sharing of one (corner), two (edge) or three (face) oxygen atoms between two metal addenda centres.

As mentioned, POMs consist of [MO_x] polyhedral units, each of these units can form three types of condensation products (Figure 2): 1) corner sharing *via* one oxo-bridging ligands; 2) edge *via* 2 oxo-bridging ligands and 3) face sharing mode *via* 3 oxo-bridging mode (Figure 2). POMs are composed of a mixture of these three structural condensation products, however, almost all POMs are constrained by the "*Lipscombe principle*",[18] whereby each polyhedron within the cluster must contain either one or two terminal oxo-ligands (M=O), which has both structural and electronic implications on the clusters. [14] Based on this, a classification system has been established for conventional POMs, whereby the number of terminal M=O bonds on the addenda dictate the group in which the POM exists. Type I POM consist of addenda octahedra possessing one terminal M=O bond, Type II addenda octahedra possess 2 terminal M=O (*cis*-oxo) and Type III possess a combination of the addendum with either 1 or 2 terminal M=O bonds in the cluster.[14] As alluded to, the number of terminal M=O bonds can have strong implications on the electronic properties of the POMs. Type I POMs are known to observe rich and reversible redox properties. Such POMs can be mixed valence and their reduced species have been heavily investigated, formally known as "*heteropolyblues*".[19-21] Type II POMs cannot be easily reduced without decomposition. This is owed to the absence of "non-bonding" LUMO orbitals of the addenda centre octahedra in found in Type I being replaced by π anti-bonding orbital.[22]

One last crucial point must be considered with respect to individual [MO_x] polyhedral building blocks is the *trans-effect*. As mentioned, the *trans-effect* results in a distortion of the uniform M-O bonding nature of the octahedra, resulting in the shortening of the M=O and lengthening of the opposite internal M-O bond. As a consequence of lower bonding rigidity exhibited by the weakening *para* M-O bond, heteroatoms can be incorporated into the core of POMs, formally known as heteropolyoxometalates. The incorporation of these heteroatoms can have strong effects on the structure and electronic properties of POMs. The presence of heteroatoms in the structure therefore classifies POMs in two major families (Figure 3): isopolyoxometalates {$[M_xO_y]^{n-}$} when no heteroelements are present in the POM structure and heteropolyoxometalates {$[A_zM_xO_y]^{n-}$} (with $z \leq x$ and n = overall oxidation state) when there are one or more heteroatoms.[19]

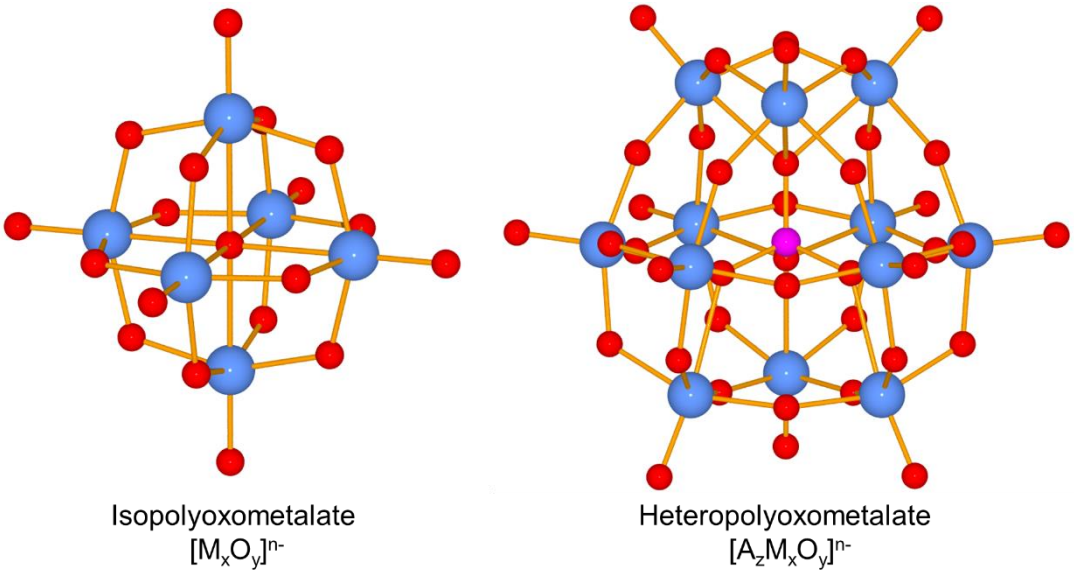

Figure 3 - Ball and stick representation of an isoplyoxometalate $[M_xO_y]^{n-}$ and a heteropolyoxometalate $[A_zM_xO_y]^{n-}$.

The synthesis of POMs occurs *via* pH controlled self-assembly of individual [MO_x] building blocks *via* acid driven condensation. Here, individual [MO_x] blocks are protonated in the presence of acid, which causes them to react and undergo polycondensation into larger structures (Figure 4). Typically, these reactions occur through pH driven condensation of oxometallate salts (e.g. Na_2MO_4 and Na_2WO_4). When synthesising heteropolyoxometalates, heteroatom reagents are added as acids or alkali metal derivatives to the reaction. The type of POM synthesised can be accessed through modifying the

conditions of the reaction, whereby experimental factors such as pH, solvent, temperature, heteroatom reagents and cations can play a large role in the assembly process of the [MO_x] fragments. The synthesis and the isolation of pure products of POMs can be relatively straight forward, however, due to the complex nature of self-assembly, isomeric and structural purity of the product can be difficult to achieve. Simple work up involves precipitating POMs out from solution with cations, or for more complex cases, purity is achieved through crystallisation efforts.

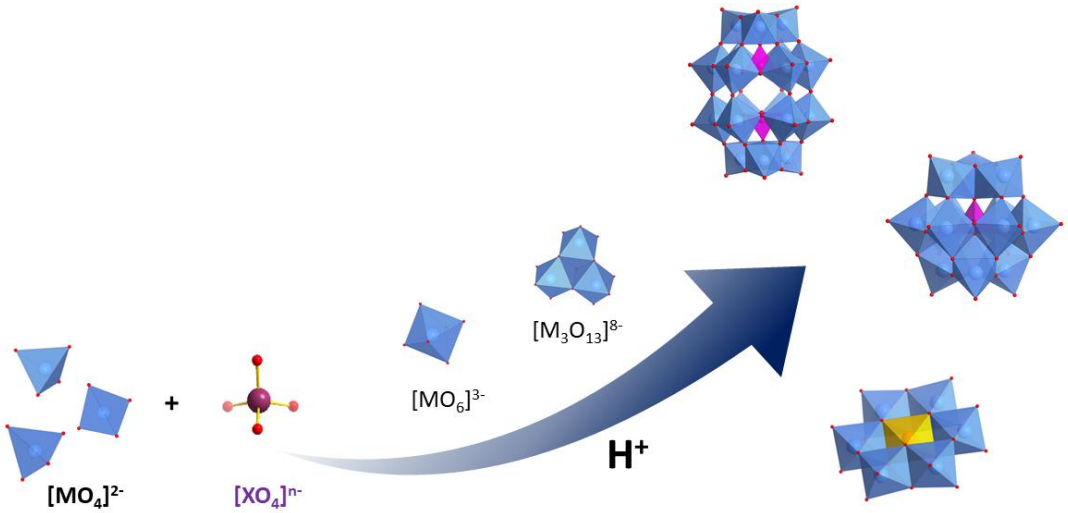

Figure 4 - A schematic illustrating the general polycondensation pathway of metal-oxo fragments to polyoxometalates (POMs).

1.3 Archetypal Polyoxometalate Structures

Although POMs exhibit an enormous range of structures, the majority of POMs can be identified as derivatives of one of the four distinct structural families: Lindqvist, Keggin, Well-Dawson, Anderson clusters. Such structures are common owing to their reproducibility and stability, and can desirably be assembled from by different types of addenda metals (i.e. V, Mo, W, Nb etc). The stability of these POMs has made them excellent candidates as starting materials for the manufacture of new POM based clusters.[23]

1.3.1 Lindqvist Structure

The hexametalate Lindqvist POM is the smallest and simplest of the archetypal POMs, and was discovered in 1950 by Lindqvist.[24] This cluster falls into the class of isopolyoxomalates and possesses a general formula of $[M_6O_{19}]^{n-}$ and can be isolated as early transition metals such as Nb,[24] Ta,[25] Mo,[26] and W.[25] This cluster is constructed of six edge-sharing $[MO_6]$ units, where the six addenda are coordinated to a μ_6-oxo ligand giving an overall O_h symmetry (Figure 5).

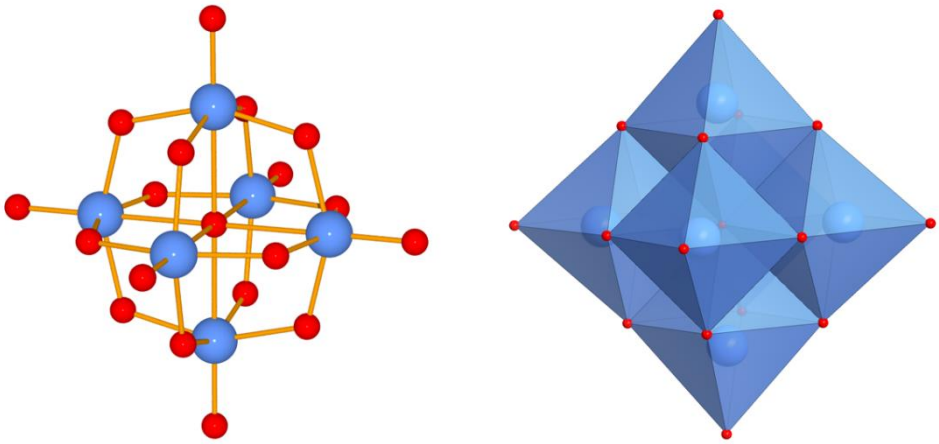

Figure 5 - Ball and stick structure (left) and polyhedral representation (right) of the Lindqvist polyoxometalate $[M_9O_{19}]^{n-}$.

1.3.2 Anderson Structure

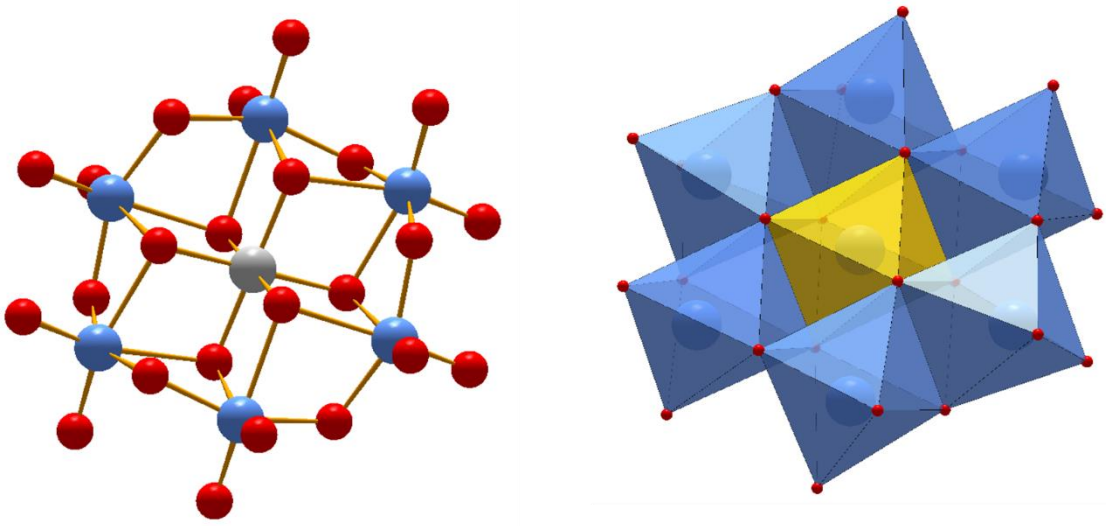

Figure 6 - Ball and stick structure (left) and polyhedral representation (right) of the Anderson polyoxometalate $[H_yXM_6O_{24}]^{n-}$.

The Anderson-Evans structure, commonly known as the Anderson cluster, was predicted by Anderson in 1937 and solved by Evans in 1948.[27, 28] The Anderson cluster is the smallest of the common heteropolyoxometalates, incorporating a single octahedral heteroatom, X, within a hexagonal planar ring of edge-sharing $[MO_6]$ octahedra to yield a heptametalate D_{3h} species of the general formula $[H_yXM_6O_{24}]^{n-}$ (y = 0 - 6) (Figure 6). Three oxo-bonding environments are present within the structure, which can be ascribed to six μ_3 oxo-ligands which connect the heteroatom to each pair of adjacent M addenda atoms, six μ_2- oxo which bridging each pair of adjacent addenda atoms to each other in the ring surrounding X, and 12 terminal M=O bonds are located in pairs on each of the six addenda atoms. The Anderson structure can be further divided into two types: the non-protonated A-type with templating central heteroatoms in high oxidation states with the general formula $[X^{n+}M_6O_{24}]^{(12-n)-}$ (X = e.g., Te, I etc.) and the protonated B-type where heteroatoms in low oxidation states are present and possess a general formula $[X^{n+}(OH)_6M_6O_{18}]^{(6-n)-}$ (X = e.g. Cr, Fe). The six protons in the B-type are found on the six μ_3 - O atoms surrounding the heteroatom. Unlike the Lindqvist cluster, the Anderson cluster can only be composed of group VI addenda metals (predominately Mo and, few cases of W) however a wide variety of transition metal and p-block elements may act as the central heteroatom,

significantly increasing the compositional diversity of Anderson type structures. The Anderson structure, unlike the vast majority of POMs, has limited redox chemistry associated with the d_0 addenda metal centres and the nature of the clusters properties is usually heavily dictated by the heteroatom. This cluster is a prime example of a type II POM.[14]

1.3.3 Keggin Structure

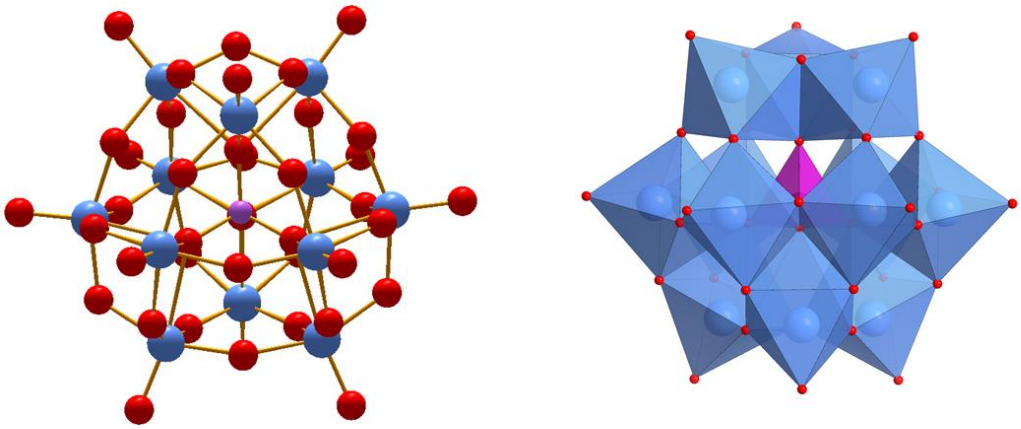

Figure 7 - Ball and stick structure (left) and polyhedral representation (right) of the Keggin polyoxometalate $[XM_{12}O_{40}]^{n-}$.

The Keggin structure was first reported in 1826 but it wasn't until 1933 that the X-ray structure was confirmed by Keggin as polytungstic acid.[29] The structure adopts a general formula of $[XM_{12}O_{40}]^{n-}$ (where X = P, Si, As, etc., M = V, Mo, W etc.). The Keggin structure is composed of four $\{M_3O_{13}\}$ triads (where M = addenda), are organised with a T_d symmetry around a central tetrahedrally coordinated heteroatom $[XO_4]$ (Figure 7). The $\{MO_6\}$ octahedra within each triad are edge sharing and the triads are connected to each other *via* corner sharing of oxygen ligands. This structure is composed of four oxygen linkage environments, 4 bridging oxygens link M addendum to central heteroatom, 24 oxo-linkages bridge each addendum by corner or edge sharing modes and 12 oxo-ligands exists as terminal single M=O bonds on each addendum. Each addendum has only one terminal M=O, therefore classed as a type I POM with high stability and accessible rich redox chemistry. For Keggin structures the most common heteroatoms (X) are p-block elements such as B, Si, Ge, P and S.[30, 31]

Keggin structures also exhibit interesting structural features, where a number of isomers can be accessed based on the degree of rotational isomerism associated with the $\{M_3O_{13}\}$ triads (Figure 7). Investigations undertaken by Baker and Figgis reported four additional isomers, each resulting from 60° rotation of the four $\{M_3O_{13}\}$ units, yielding α, β ,γ, δ and ε isomers, which exhibit T_d, C_{3v}, C_{2v}, C_{3v} and T_d symmetry, respectively.[32] With regards to α and β isomers, the four building blocks are linked *via* corner-sharing fashion, whilst for γ, δ and ε, the corner-shared linkages are replaced by one, three and six-edge sharing linkages, respectively. α and β isomers tend to be the most stable and therefore most abundant,[33, 34] and for this reason research has focused on investigating their properties. Comparatively, fewer examples exist of γ,[35] δ,[36] and ε isomers.[37]

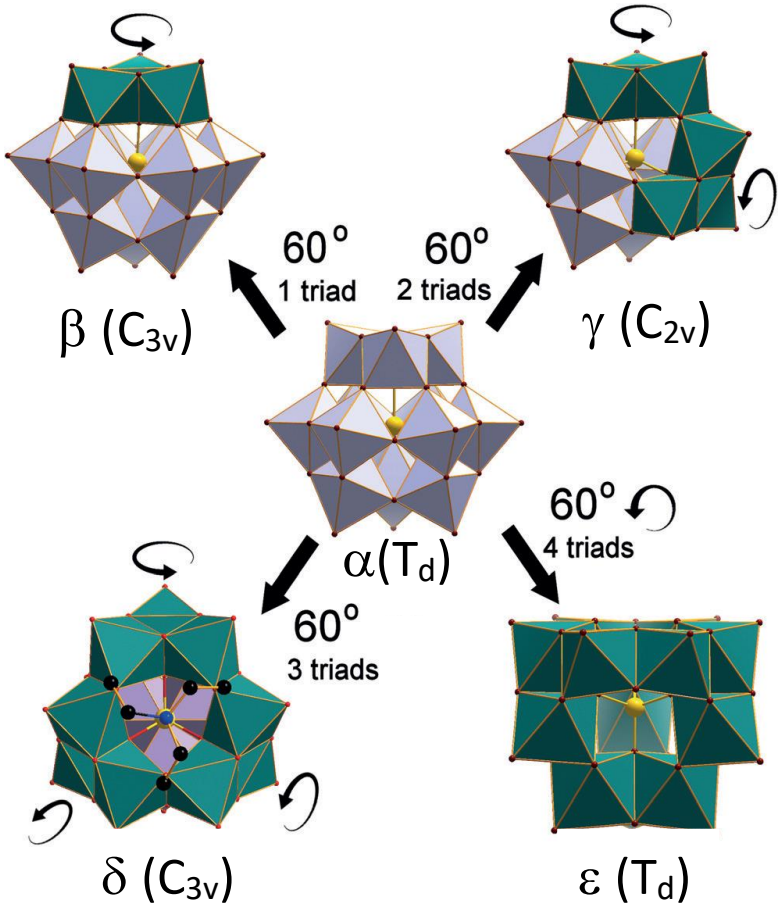

Figure 8 - Polyhedral representation of all the isomers of the Keggin structure. Reproduced from ref.36 with permission from John Wiley and Sons.

1.3.4 Wells-Dawson structure

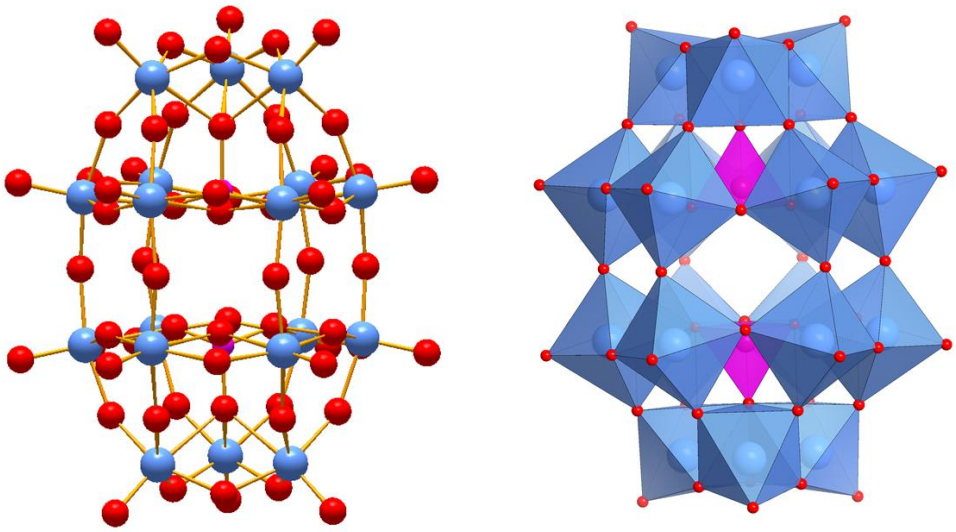

Figure 9 - Ball and stick structure (left) and polyhedral representation (right) of the Wells-Dawson polyoxometalate $[[X_2M_{18}O_{62}]^{n-}$.

The Wells-Dawson structure (commonly known as the Dawson cluster) was first discovered and reported by Dawson in 1953 where the crystal structure of potassium tungstophosphate was isolated and characterised.[38] This cluster has a general formula $[X_2M_{18}O_{62}]^{n-}$ (where X = P, Si, As, etc., M = V, Mo, W) and is a commonly encountered heteropolyoxometalate (Figure 9). This structure can be viewed as a connection of two Keggin with triad units removed, through corner-sharing modes. The overall structure consists of two cap regions, each cap consisting of M_3O_{13} triads, and a belt region consisting of 12 $[MO_x]$ units. Interestingly, the electron transfer properties are different in the "cap" and "belt" positions of the Dawson cluster, this disparity strongly influences the chemical properties of the cluster.[39] Finally, the hetero-anion, $[XO_4]_n$ links to the three addenda of a $\{M_3O_{13}\}$ cap through a μ_3-oxo coordination mode and to six of the addenda in the belt octahedra.

Similar to the Keggin structure, the different orientation of the triad caps of the Dawson cluster leads to the formation of six different isomers (α, α*, β, β*, γ and γ*). However, only the α, β, γ and γ* isomers have been synthesized and structurally characterized to date. The first type of isomerism involves a 60° rotation of the $\{M_3O_{13}\}$ cap regions to afford α-, β- and γ- forms. In the α-isomer the

terminal M=O oxo-ligands of both caps align with the corner-shared bridging oxo-ligands of the belt region. For the β isomer, one $\{M_3O_{13}\}$ unit is rotated by 60°, which results in the terminal oxo ligands now aligning with the edge-shared bridging oxo-ligands of the belt region.[40] The γ-isomer has both $\{M_3O_{13}\}$ caps rotated by 60° (Figure 10). For these isomers, the tetrahedrally coordinated heteroatom $\{XO_4\}$ of each half of the molecule eclipse one another. The second form of isomerism breaks this symmetry by rotating one half unit $\{XM_9O_{36}\}$ by 60°, causing the heteroatom polyhedra to offset and staggered with respect to alignment with each other (Figure 9). The rotation of a half unit converts α to α*, β to β* and γ to γ*. DFT (Density Functional Theory) computational studies have revealed the order of stability for Dawson isomers is α > β > γ > γ* > β* > α* which explains why the latter two isomers have not been synthetically accessed yet.[41]

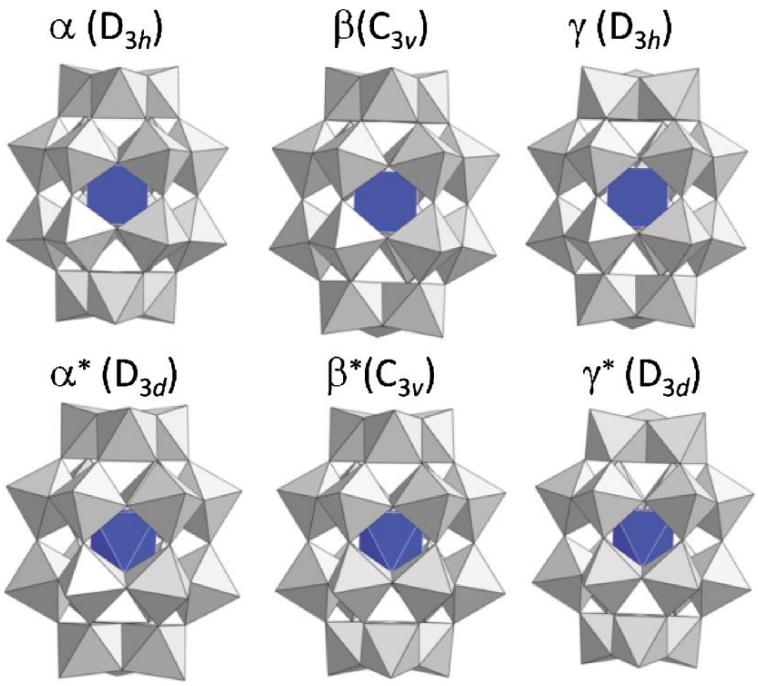

Figure 10 - The six rotational isomers of the Wells–Dawson structure. Reproduced from ref.40 with permission from the Royal Society of Chemistry.

1.3.5 Lacunary POMs

Some POM clusters, mainly Keggin and Dawson structures, can undergo pH-controlled hydrolysis of a number of addenda units, resulting in what is known as a "*lacunary*" species. In the process of removing one or more [MO_x] units expose multidentate nucleophilic oxygen vacancies in the lacuna pocket and increases the overall charge of the cluster. Lacunary species of polyoxotungstates are the only addenda species that can be isolated where as polyoxomolybdates and polyoxovanadates lacunary species have not been isolated due to their lower stability and higher reactivity.[42] Lacunary species are particularly desirable as their lacuna enables opportunities to fill the void by coordination with transition metals,[43] or organo-functionalisation with organic ligands tethered to specific p-block based oxophilic linkers.[44]

Lacunary structures based on the Keggin cluster are well-explored, and examples consist of monolacunary, dilacunary and trilacunary derivatives (n = charge of parent anion). Successive hydrolysis involves the removal of one addendum at a time, where the trilacunary exhibits a full cap removal. Similar to the plenary POM, Keggin lacunary structures also exhibits structural isomerisation.

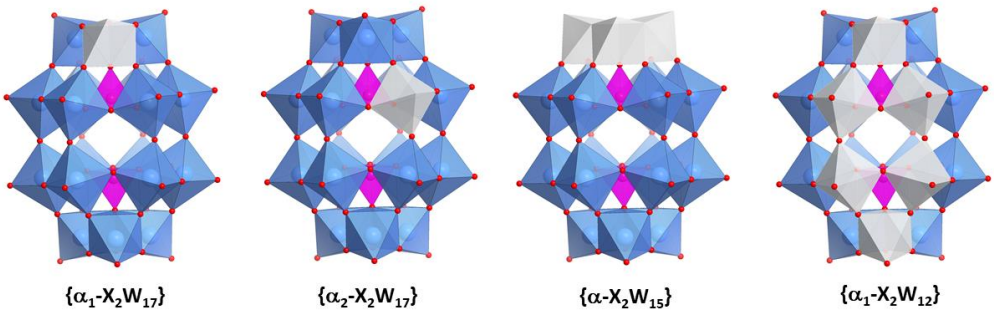

Figure 11 - Polyhedral representation of the four possible lacunary species of the Wells-Dawson cluster where missing octahedra are shaded in grey.

The removal of addenda typically destabilises the POM cluster, and isomerisation can occur to stabilise the structure. The richest class of Keggin lacunary species are the tungstosilicates, for which the various derivatives, and their isomers, are accessible *via* a complex network of competing equilibria.

Lacunary structures of based on the Wells-Dawson cluster are also common (Figure 11). Wells-Dawson based lacunary species can only be isolated by base driven hydrolysis of the plenary structure, most

likely owing to their high thermodynamic stability. Three distinct types of Dawson lacunary structures have been isolated based: 1) monolacunary $[X_2M_{17}O_{61}]^{n-4}$; 2) single cap trilacunary, $[X_2M_{15}O_{56}]^{n-6}$ and 3) hexalacunary $[X_2M_{12}O_{61}]^{n-8}$ (where n= oxidation state of the cluster). Monolacunary species are associated with either removal of addendum from the cap or removal from the belt. Formation of the trilacunary species involves the hydrolysis of three addenda, essentially removing the cap. Finally, hydrolysis to the hexalacunary species involves the hydrolysis of the face of the Dawson cluster. Furthermore, the isolated $\{W_{17}\}$ clusters are only found as α-isomers. There are no reports of positional isomerisation of monolacunary species.

1.4 Electronic Structure of POMs

As previously alluded to, in most POM clusters, the metal atoms possess an octahedral geometry with either one (*mono*-oxo) or two (*cis*-dioxo) terminal M=O, which have been classed into Type I and Type II respectively. Type III also exist where there is a mixture of the two, which some lacunary structures are an example of. The idealised local symmetry of a metal atom in a Type I cluster exhibits a local symmetry of C_{4v}, where the d-orbitals transform as a_1 (z^2), b_1 ($x^2 - y^2$), b_2 (xy), and e (xz, yz).[14] Figure 12 shows a qualitative molecular orbital diagram to depict the order of MOs (this may change with respect to the number of non-axial ligands). Here, a_1 and b_1 are anti-bonding σ orbitals, e is the π anti bonding orbital of the terminal oxo-ligands M=O, and b_2 is formally non-bonding or weakly

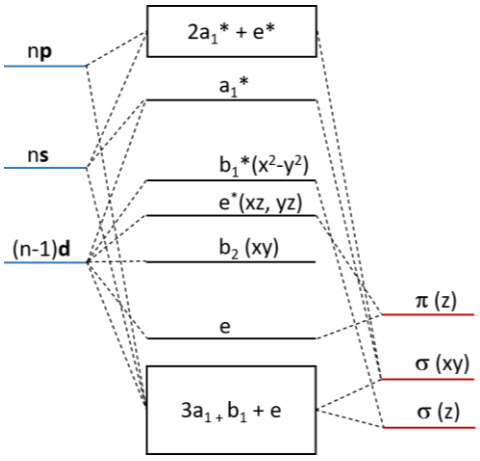

Figure 12 - Schematic molecular orbital energy diagram for MOL_5 complexes of C_{4v} symmetry. Reproduced from ref.14 with permission from Springer Nature.

antibonding. The filling of b_2 with one or two electrons should result in no significant effect on the metal-ligand bond order. Numerous examples exist of Type I $\{MOL_5\}$ complexes with d^1 or d^2 metal centres. It is therefore Type I structures that can undergo reversible reductions to yield isostructural species. Consequently, the *cis*-dioxo metal centre have no "non-bonding" *d* orbital (conversion of one equatorial ligands to a "terminal" oxo group converts the former d_{xy} orbital to a π anti-bonding orbital), hence no examples of stable d^1 complexes are known. Therefore, reduction of Type II polyoxometalate anions is irreversible, leading to rearrangement to other structures or disassembly. Due to the exotic nature of the electronic properties of Type I and Type III POMs, they will only be discussed hereon.

The relationship between POM structures and their ability to accept electrons was first described by Pope *et al*. POMs of the same addenda can accept electrons into their LUMO, this ability to do so is related to the ratio between the size and charge of POMs q/m, (q = overall negative charge and m = number of metal ions).[19] Based on this relationship, POMs that are larger and possess less overall charge are more readily reduced. Furthermore, when comparing POMs with different addenda, the LUMO energies of POMs decrease with the increase in electronegativity of the d_0 metal addenda (W < Mo < V).[45] Furthermore, the nature of the heteroatom can also have significant effect on the electronic structure of the POM. Density functional theory (DFT) calculations performed on the Keggin cluster reported that internal XO_4 units affects the POM reduction potential based on their size. It was found that X atoms of the same group exhibit slight differences. Atoms possessing lower atomic numbers are smaller in size and therefore, produces a more negative potential in the surroundings and thus a smaller capacity to accept electrons.[46]

As mentioned, upon reduction, POMs exhibit a strong blue colour transition (*heteropolyblue*) which arises due to intervalence charge transfer (IVCT) which occurs between neighbouring metal addenda atoms in the POM.[14, 20, 21] Owing to this thermally assisted electron transfer mechanism, strong absorption in the low visible-near infrared region is observed. Higher degree of electron "*hopping*" and delocalisation are observed in clusters with higher symmetry such as Kegging and Lindquist as

delocalisation occurs in regions of equivalent metal addenda. Dawson clusters exhibit two regions, the cap and belt, in which delocalisation occurs in separately. The new strong IVCT absorption bands occur upon successive reductions, rendering UV-Vis spectroscopy of the *heteropolyblue* states a useful diagnostic tool in the analysis of reduce POM states.

1.5 HYBRIDISATION

As previously discussed, POMs are well-known to exhibit an extensive broad range of structures that can be accessed through manipulating the synthetic conditions of their [MO_x] building block. POMs can be further hybridised by coupling new species to the already preassembled cluster, which can impart POMs with additional functionality and be used to tune their intramolecular properties. Hybridisation can occur through the coupling of inorganic or organic species.

Firstly, with regards to inorganic hybridisation, the formation of hybrid species involved the addition of hetero transition metals or f-block elements, either *via* one pot synthesis or through coupling with a lacunary species in which vacant pocket(s) are available for the cationic metal species to bind. The overall charge of the cationic species is accommodated by the POM's ability to both coordinate and electrostatically bond to these species. This method has been shown to be particularly useful in the modulation of POM properties.[47] Examples of mixed metal species such as tungstomolybdates POMs, which possess the stability of polyoxotungstates but introduce the lower LUMO energies and positive redox potentials associated with polyoxomolybdates.[48] Furthermore, due to the broad range of cationic species available, and their differing coordination geometries, a large plethora of structures are accessible as well as ample scope to alter the POM properties. Owing to this flexible and open-scope hybridisation of inorganic species, inorganic-hybrid POMs have demonstrated promising properties in catalysis,[49] magnetism,[12] and medicine.[8]

The organic hybridisation of POMs involves the coupling of organic moieties to inorganic clusters to generate organic-inorganic hybrid molecules. Since the development of these species, two classes

have been established, these can be defined by the type of coordination by which they associate. For instance, in Class I systems both organic and inorganic components are bound by electrostatic interactions (i.e. ionic, Van der Waals or hydrogen-bonding).[50] This class of hybrids is relatively simple to synthesis and usually involves the cationic exchange with salt of the organic component. Although this method is extremely simplistic and rapid, the stability of these compounds is hindered by the weak interactions by which they are held. These compounds are highly susceptible to further salt exchange in solution, which rendered the synergistic properties between organic and inorganic components void.

Class II systems on the other hand employ covalent linkages between organic and inorganic components. Here, the organic ligand substitutes an oxo-ligand of the POM and be directly linked to the metallic centre. The nucleophilic character of the oxygen atoms localized on the surface of the POMs can also lead to covalent interactions with electrophilic groups on the organic ligands. Unlike Class I hybridisation, the synthetic methodology associated with hybridisation of organic and inorganic components is unique to the type of metal addenda (Figure 13), where the linkages play a crucial role in the reaction to hybridise the two components. For instance, the Lindqvist cluster can react directly with primary amines through diimide catalysed nucleophilic addition-substitution, resulting in one or more substitution of terminal oxo-groups of the POM with primary amines, and the exhibited bonding motif is a formal molybdenum-nitrogen triple bond. Tripodal alcohols have also been employed to functionalise Anderson molybdates, Lindqvist hexavanadates and the vanadate cap of tungstovandate Wells-Dawson clusters. The reaction of this linker proceeds by the esterification of the protonated bridging oxo-ligands. Similarly, diolamide linkers have been employed in the linkages to vanadate cap of polyoxotungstovandate Wells-Dawson clusters.

Due to the lower stability and higher reactivity of polyoxovanadates and polyoxomolybdates, hybridisation reactions can occur between the surfaces of these clusters and organic ligands with specific functionalities. However, polyoxotungstates can only be hybridised through condensation reactions with their lacunary species. The reactive oxygen sites of lacunary POMs can react with a number of oxophilic components such as organogermanium, organotin, organosilicon, and organophosphorus compounds. As previously mentioned, these reactions usually proceed *via* condensation mechanism, however, S_N2 reactions with their chloro-derivatives are also well established.

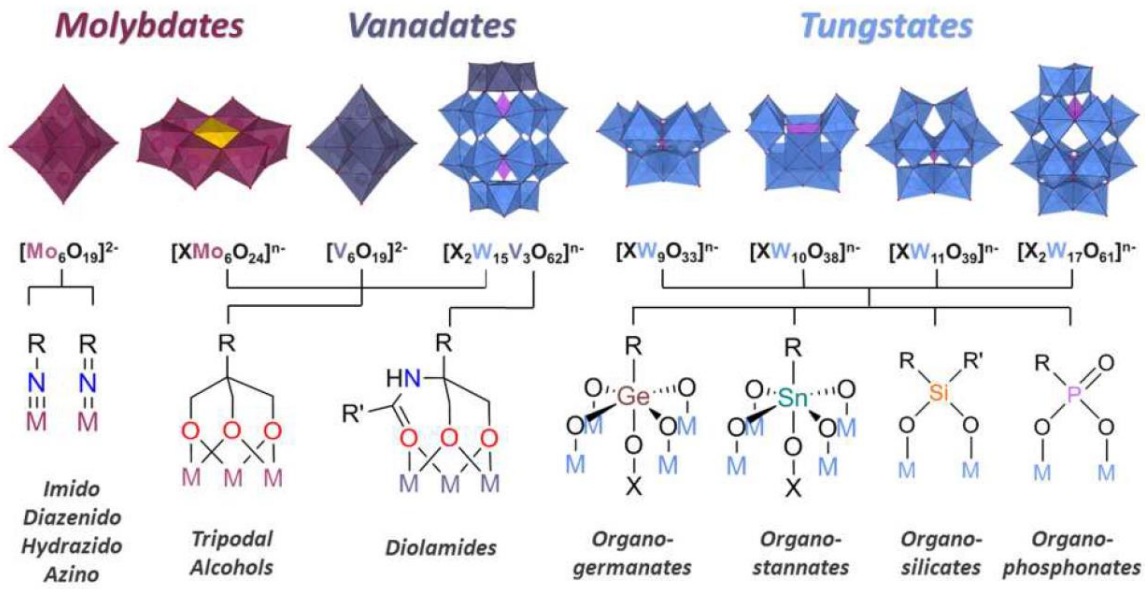

Figure 13 - A scheme depicting covalent organo-functionalisation routes of a broad range of POMs and lacunary POMs. Reproduced from ref.44 with permission from Elsevier.

Not only does the anchoring group provide a structural tool to graft organic ligands, but their electronic effects can impact the POMs HOMO-LUMO energy levels. This can be further modulated when considering the electronic effects imposed by the organic ligand itself.[44, 51-53]

As-of yet, a vast amount of research has been focused on the modification of POMs through covalent or electrostatic introduction of hetero species, solely to focus on tuning and enhancing the molecular properties. In the same regard, thousands of novel POM clusters with diverse topologies and properties have been synthesised, whilst their supramolecular assembly to develop functional soft

materials has been somewhat neglected. In the last two decades emerging research has started to focus on assembling these redox-active molecules with to develop advanced dynamic soft materials. Hereon we will describe the key modification strategies with a focus on employment of organo-functionalisation to impart POMs with supramolecular control, towards functional dynamic hybrid-organic-inorganic metal oxide superstructures.

1.6 Supramolecular assembly of Hybrid POMs

POMs in general are hydrophilic in nature, this can be attributed to their highly negative charge and oxygen enriched surface. The polyanionic nature of these clusters in their own right demonstrate solution phased supramolecular assembly in to larger "blackberry" type structures. This was first discovered by Müller *et al.* in 2000 with the discovery of spherical assemblies assembled from giant polyoxomolybdate wheels ($\{Mo_{154}\}$) in both aqueous and polar non-aqueous solutions such as methanol and acetone.[54, 55] In this example, although there is no hydrophobic effect driving force, the assembly process is driven by Van der Waals which are far more dominant than the electrostatic repulsive interactions in the system. This was later confirmed by a number of examples of POM clusters such as $\{Mo_{132}\}$, $\{Cu_{20}W_{48}\}$, $\{Mo_{154}\}$, $\{Mo_{72}V_{30}\}$, $\{Mo_{72}Cr_{30}\}$ and $\{Mo_{72}Fe_{30}\}$ exhibiting similar self-assembly behaviour.[56-58] Interestingly, it was found that through changing the charge of the POM or the solvent composition, the size of the blackberry structures could be tuned.[58, 59]

Unfortunately, the assembly process of these giant POMs into blackberry structures is extremely slow and can take between days to weeks to assemble. Organo-functionalisation of POMs offers a unique way to accelerate the self-assembly of POMs by introducing a hydrophobic component, through electrostatic or covalent coupling to the hydrophilic head of the POM, hence rendering the POM amphiphilic in nature. In this way, dominant solvophobic interactions can be exploited to encourage rapid self-assembly behaviour in a range of solvents. We will now focus on the supramolecular assembly of organo-functionalised Class I and Class II hybrid POMs and highlight their fascinating superstructures, assembly process and related functional properties.

1.6.1 Class I Hybrid Supramolecular Assembly

Class I hybrids are simplest and quickest approach to endow POMs with supramolecular properties. This can be done by stoichiometrically mixing cationic salts of hydrophobic cations to a solution of hydrophilic POMs. It is important to note that although Class I hybrids possess supramolecular and amphiphilic properties, they cannot be regarded as traditional amphiphiles. Due to the simplistic synthetic methodology, unsurprisingly, Class I hybrid POMs with amphiphilic properties were the first examples of POM supramolecular materials to be explored. Class I hybrids have been key in the quest to achieve phase transfer of POMs from the aqueous or organic phases.

The first example of supramolecular assembly of POM under non-covalent interactions was reported by Toyoki *et al.* who reported the assembly of $[V_{10}O_{28}]^{6-}$ and $[Cd_{10}(SCH_2CH_2OH)_{16}]^{4+}$ into oppositely charged multilayer cast films by the ion-exchange.[60] In a similar way, Coronado *et al.* later produced a series of magnetic POM films by employing the Langmuir-Blodgett (LB) technique, whereby POMs were dispersed in a solution with cationic surfactants assembled at the liquid-air interface.[61] Furthermore, in 2000 Chesne *et al.* first reported the concept of surfactant encapsulated POMs (SEPs) in an investigation where POM surface properties were altered by coupling a $\{Mo_{57}V_6\}$ cluster with cationic surfactants, as a result they characterised the first LB film constructed from SEPs.[62] This work paved a new avenue of POM building blocks based on SEPs. In comparison to the assembly of blackberry structures, self-assembly of clusters with amphiphilic properties involves synergy between multiple driving forces such as electrostatic interaction, hydrogen bonding and solvophobic interaction. Thus, a vast range of synthetic routes and parameters can be exploited to control the assembly of Class I hybrid POMs. Such parameters include charge density, topology, counterion effect and solvent composition.

Developing upon this foundation, in 2005, Wu *et al.* reported hybrid-POM based supramolecular assemblies constructed from DODA (dimethyl dioctadecyl ammonium) and Keggin-type $[Eu(H_2O)_2SiW_{11}O_{39}]^{8-}$ clusters.[63] The surfactant-encapsulated cluster was found to aggregate into

vesicles when dispersed in a $CHCl_3$ solution, and when cast onto solid supports assembled into micrometer honeycomb structures. Later in 2007, they discovered onion-like lamellar spherical assemblies with $DODA_4[SiW_{12}O_{40}]$ by phase transformation (Figure 14), which was isolated in both solvated and solvent-free states.[64] When solvated in $CHCl_3$, the assemblies exhibit narrow size distribution with particles observing diameters of 100-300 nm, but these structures lacked stability when isolated in the solid-state. However, upon introduction of MeOH as stabilizing agent in the solvent system, the stability of the solid-state structure improved. Consequently, this resulted in broad size distribution of the assemblies. In this work, the authors confirm that SEPs based on this system form spherical aggregates in organic solvents. XRD analysis of this assembly found that the surfactants are arranged on the exterior of the POM between the solvent-POM interface.

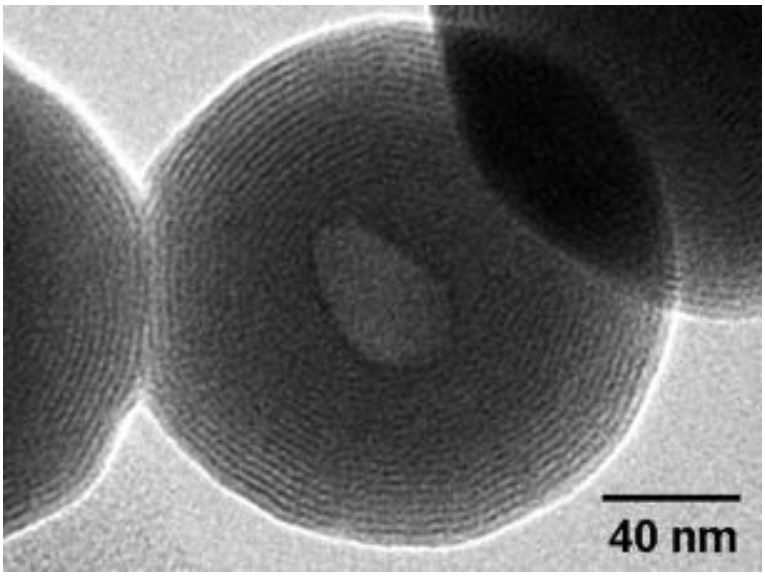

Figure 14 - TEM images of $DODA_4[SiW_{12}O_{40}]$ assemblies from a mixed solvent system ($CHCl_3$:MeOH = 4:1). Reproduced from ref.64 with permission from John Wiley and Sons.

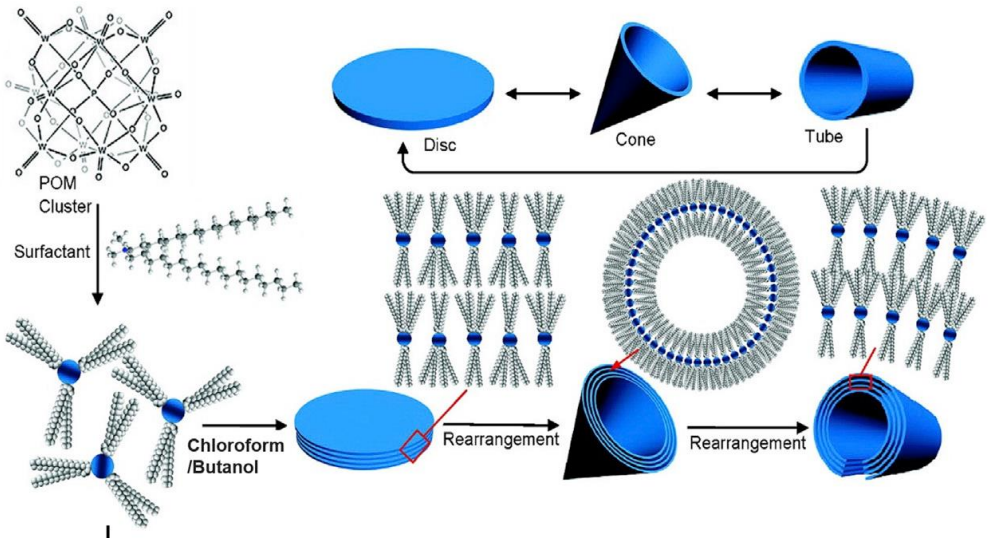

Figure 15 - A schematic illustration of SEP self-assembly: a) schematic illustration of SEP reversible self-assembling between nanodisks, nanocones, and nanotubes. Reproduced from ref.65 with permission from American Chemical Society.

Similarly, Wang *et al.* constructed monodispersed hybrid POM assemblies under solvothermal conditions and also demonstrated that these structures could be stably isolated in the solid-state.[65] In their investigation disk-like, cone-like, and tubular assemblies with high degrees of order were obtained (Figure 15). These assemblies were characterised to be constructed of a lamellar packing arrangement. In this assembly process, $DODA_3[PW_{12}O_{40}]$ and $DODA_3[PMo_{12}O_{40}]$ were employed as building blocks which displayed self-assembly into disk-like structures in a solvent ratio of $CHCl_3$:*n*-BuOH (3:1). Interestingly, the morphology of these assemblies can rapidly transition into cone-like structures by modifying the solvent ratio to 2:1 ($CHCl_3$:*n*-BuOH), which were also found to be reversible by further modulation of the solvent ratios. Tubular assemblies can also be assembled by ageing the cones in the solvent environment for a longer period of time. These structures, including disks, cones and tubes are characterised as lamellar type assemblies with a layer spacing of 2.9 nm. It was found that tubular assemblies can reversibly transition back into disks and cones by changing the ratio of $CHCl_3$/*n*-BuOH to 3:1 and 2:1, respectively. The reversible assembly behaviour demonstrates the SEPs amphiphile-like nature, where the surfactant cations rearrange around the POM surface under specific solvent conditions to achieve maximum thermodynamic stability.

As the quaternary ammonium salts pack around the POM, they play a significant role in the packing structure and dimensions of SEP assemblies. In 2013, Wang and co-workers uniquely coordinated two types of surfactants, one containing a single long chain - CTABr (cetyltrimethylammonium bromide) and the other a quadruple smaller chain surfactant - TBABr (tetrabutylammonium bromide) or TEAB (tetraethylammoniumbromide).[66] In doing so a supramolecular gel by the self-assembly of surfactant-encapsulated Wells-Dawson as $CTA_3TBA_3[P_2W_{18}O_{62}]$ in butanone and ethyl acetate was achieved. TEM analysis of this fascinating gel revealed the material was constructed by an array of interwoven nanowires (Figure 16). The cross-section analysis of the of nanowires displayed a circular layer packing arrangement with layer spacing of 3.27 nm. These nanowires also cross-linked which is thought to be the cause behind the superior viscosity and gel-like behaviour. However, the gel transitions to a solution when shaken demonstrating poor stability but was recoverable when heating the solution at 70 ^{o}C for 1 h. Besides the fascinating thermo responsive gel-like behaviour, when this material was irradiated with UV light, the gel transitioned to a dark blue colour, which can be attributed to the

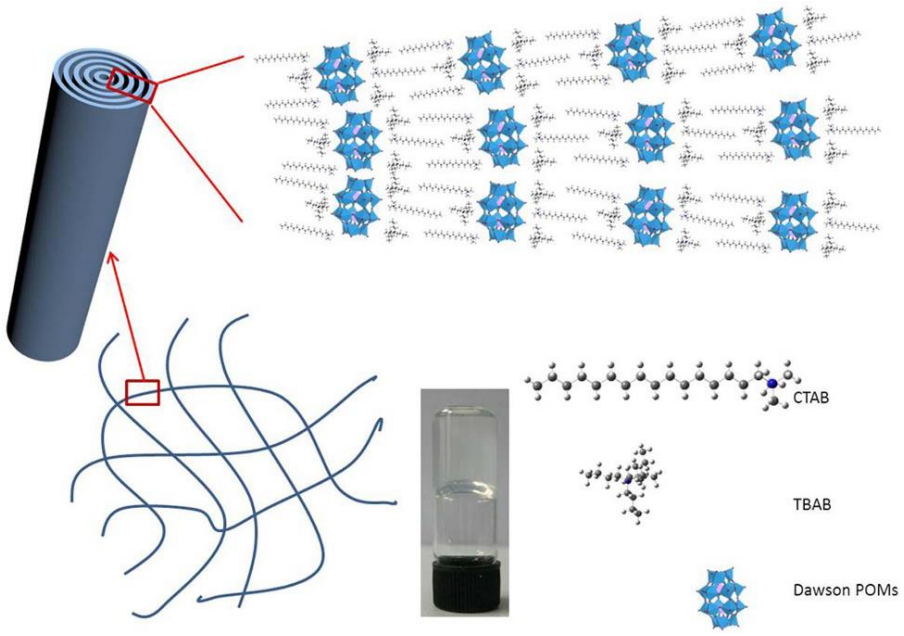

Figure 16 - A schematic illustrating the possible assembly structure of the transparent gel. Reproduced from ref.66 with permission from Springer Nature.

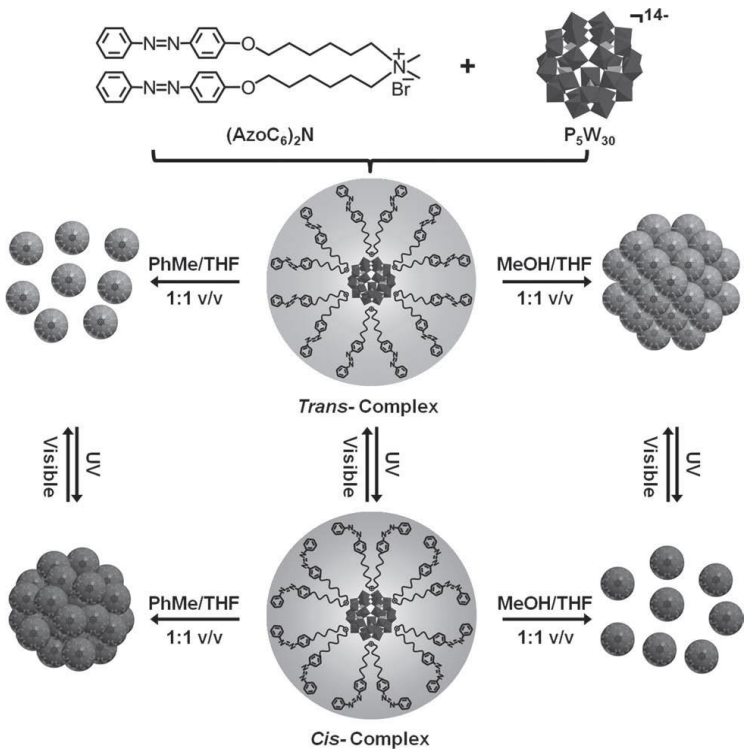

Figure 17 - Schematic illustration of SEP reversible assembly in solutions with different polarities. Reproduced from ref.67 with permission from John Wiley and Sons.

photoreduction of the POM cluster to its "*heteropolyblue*" state. The author did not indicate what the sacrificial electron donor is, however, the solvent maybe involved. Under darkness, the gel regained its transparent colour. Therefore, demonstrating the translation of the molecular photoactivity of the POM cluster in the superstructure.

Further to the development of Class I hybrid POMs towards stimuli responsive assemblies Wu *et al.* developed a surfactant encapsulated POM system by incorporating azobenzene-terminated surfactants as encapsulating agents. Their investigation demonstrated that the aggregation of the catalytically active enwrapped Preyssler anion $[NaP_5W_{30}O]^{14-}$ can be tuned by switching the conformation of the azo-bond from *trans* to *cis* (Figure 17).[67] This transition was triggered by UV/visible-light irradiation and was accompanied by a change in polarity and size in the SEP and assembly. In toluene, this led to an aggregation of the monodisperse distributed assemblies. Interestingly, Wu and co-workers reported, that as a result of this switching, the POM-catalysed oxidation of phenyl sulphide could be controlled. This is because the reaction depends on the

accessibility of the POM, therefore, the oxidation rate can be decreased by triggering the aggregation of the clusters through switching of the azo-bond configuration (Figure 17). Furthermore, Wu and co-workers went on to show that the principle of smart-photo responsive change in polarity of the cluster can also be applied for the separation of the phase-transfer catalyst.[68]

Due to the structural tuneability of POMs, a major area of research still focuses on the substitution of metals into these clusters to tune the properties of the clusters and generate functional materials.[47] For instance, metal-substituted POM clusters have been developed to build a class of mixed addenda catalysts[69]. The substitution of metals into the framework can further break the symmetry of the POM and bring about anisotropy that could be amplified into the way cationic surfactants pack around the POM. In this way Wang *et al.* developed a surfactant encapsulated palladium substituted Wells-Dawson POM (Pd-POM), $[Pd_2(P_2W_{17}O_{61})_2H]^{15-}$, which displayed interesting catalytic and supramolecular properties.[70] Firstly, the POM was encapsulated with CTAB and TBAB, the resulting SEP assembled into nanoroll assemblies with different length-to-diameter ratios with some instances of coiling (Figures 18). The interlayer spacing was analysed by SAXRD and high-resolution TEM

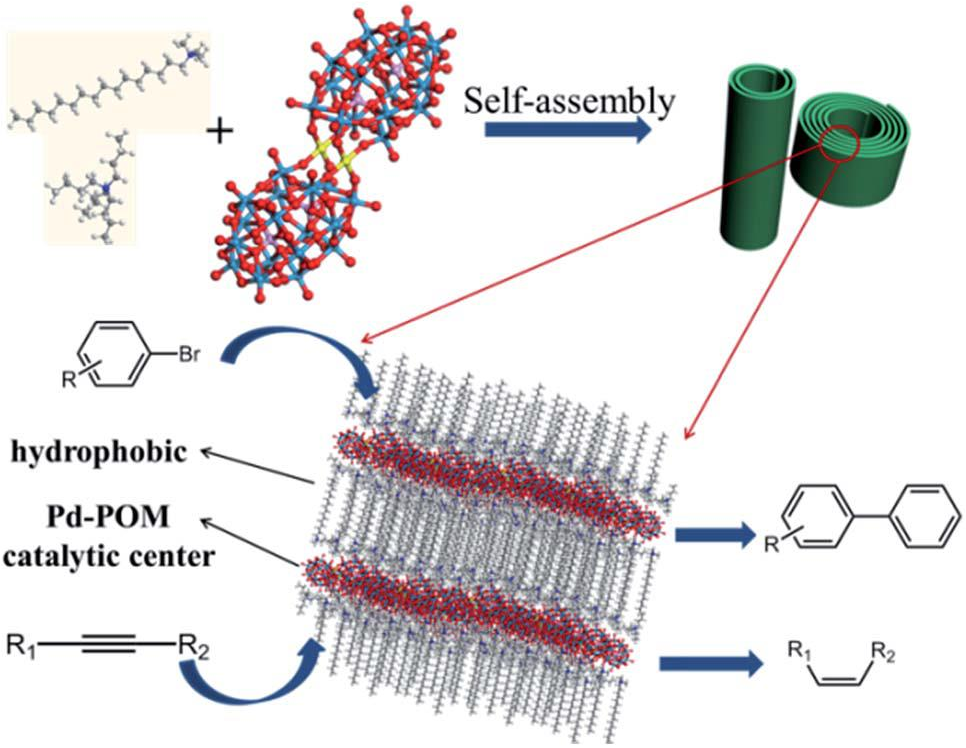

Figure 18 - Schematic illustration of the Pd-SEP nanorolls and the types of catalytic reactions. Reproduced from ref.70 with permission from the Royal Society of Chemistry.

(HRTEM) and was found to be 2.8 nm. The hollow spindles are obtained with the surfactants DTAB (dodecyltrimethylammonium bromide) and TEABr (tetraethylammonium bromide) in the aqueous phase. Interestingly, Pd-POM assemblies demonstrate excellent efficiencies toward both Suzuki-Miyaura coupling reactions and semi-hydrogenation of alkynes (Figure 18) with a turnover frequency of above 2,000 h^{-1} and stereoselectivity which is potentially owed to the design and assembly environment of the mixed addenda catalysts. Similar work by the group on single metal substitution into the monolacunary Wells-Dawson cluster demonstrated access to number of different supramolecular assemblies with the SEP by changing the substituted metal, which further exemplifies the versatility and effect of metal substitution on SEP assemblies.[71]

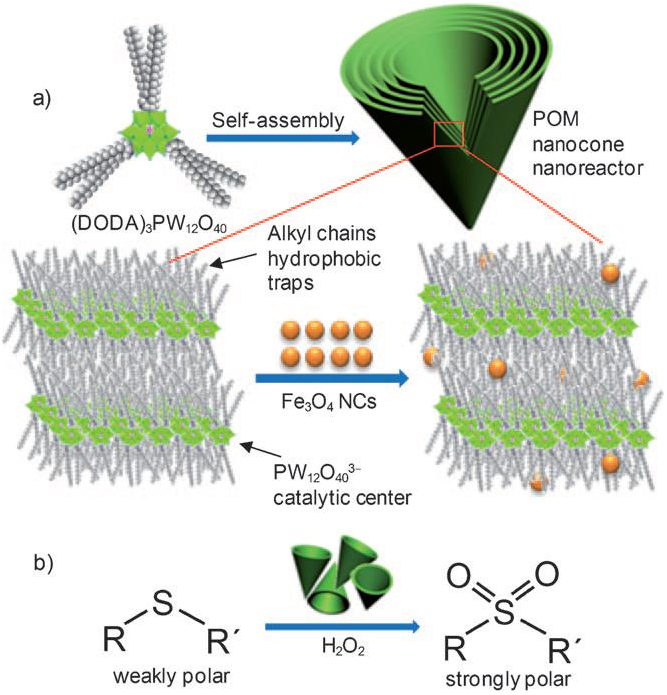

Figure 19 - a) Schematic illustration of a POM nanocone assembly and; b) oxidation of sulphides to sulfones in the presence of the cones as a catalyst. Reproduced from ref.72 with permission from John Wiley and Sons.

Further to the functional SEP assembly development, Wang et al. also developed a magnetic SEP nanocone desulphurisation catalyst.[72] In this case the system was based on hybrid-POM building block $DODA_3[PW_{12}O_{40}]$ coupled with magnetite nanocrystals (Figure 19). Here the authors proposed that the long hydrophobic chains encapsulating the catalytically active POM entrapped the weakly polar dibenzothiophene (DBT) substrate and released the polar dibenzothiophene sulphone. This

entrapment and extrusion mechanism is thought to be the reason behind the high catalytic activity of the system. Furthermore, the dense alkyl chain packing in the reported lamellar packed structure of the cones adheres with this proposal. This material also displayed activity towards the oxidation of cyclohexanol to cyclohexanone with 90 % conversation and 100 % selectivity. Many Class I hybrid-POM systems have been employed to develop supramolecular materials for catalysis,[73-76] however this system is unique owing to the introduction of the magnetite nanocrystal which imparts this system with rapid recovery of the nanocones.

SEPs have shown tremendous potential in the development of amphiphilic smart-materials with a range of functional properties that have demonstrated application in the fields of materials science and catalysis. However, as previously alluded to, Class I hybrids are held together by a range of weak interactions, mainly electrostatic. Therefore, these hybrid systems and their supramolecular assemblies are susceptible to degradation through cation exchange. Hence, the covalent hybridisation of the organic and inorganic components offers a more rewarding avenue to develop traditional amphiphilic molecules with higher stability and greater control over their supramolecular assembly processes.

1.6.2 Class II Hybrid Supramolecular Assembly

Class II organic-inorganic hybrid POMs offer an alternative route to POM based supramolecular architectures. This class of hybrid POMs possesses covalent linkages between the inorganic POM and organic component (ligand). Although the synthesis of these molecules is far more complex compared to Class I hybrids, this route offers a greater handle on the control and stability of their supramolecular assembly process and the resulting superstructures. Here we will discuss the range of unique examples of Class II hybrid POM amphiphiles, their supramolecular assemblies and functionality.

1.6.2.1 Hybrid-POM Amphiphiles

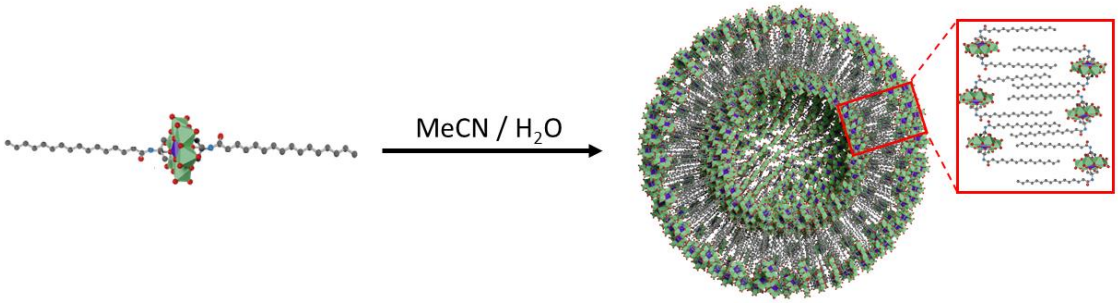

Figure 20 - Schematic representatives of the Mn-Anderson-C_{16} surfactant and their vesicle formation in MeCN/H_2O mixed solvent system. Reproduced from ref.77 with permission from American Chemical Society.

One of the first examples of a Class II hybrid-POM amphiphile was reported by Cronin *et al.* in 2008 where $TBA_3[MnMo_6O_{18}\{(OCH_2)_3\text{-}CNHCO\text{-}(CH_2)_{14}CH_3\}_2]$ (Mn-Anderson-C_{16}) was synthesised by covalently grafting two aliphatic C_{16} chains *via* an amide bond to an Anderson POM.[77] This amphiphilic molecule displayed solvent dependent supramolecular assembly (Figure 20). The author reported the assembly of vesicles from this hybrid in a mixture of MeCN/H_2O. The vesicle was formed from bending of the hydrophobic chains into a hydrophobic layer. DLS analysis of solution containing 40 % acetonitrile showed growth of large assemblies where R_h = 58 nm after several days, after 57 days the assembles reached growth equilibrium and sizes stabilised at R_h = 115 nm. similar work conducted by the group demonstrated that reverse-micelles could also be achieved by changing the solvent composition to MeCN/toluene.[78]

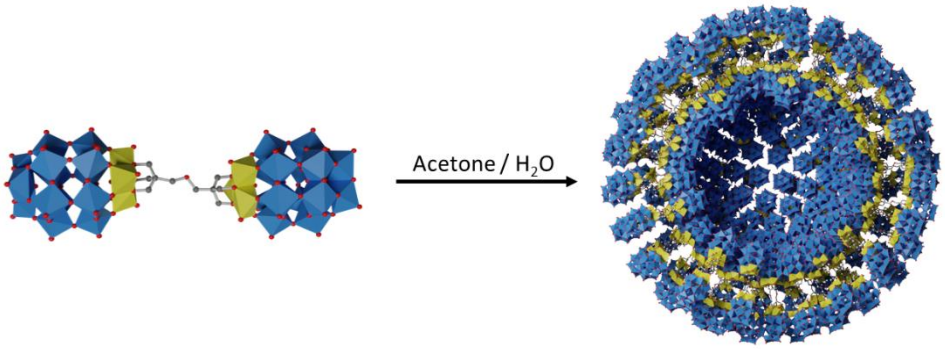

Figure 21 - Schematic illustrating the supramolecular assembly of dumb-bell type hybrid-POM in mixed solvent system (acetone/H_2O). Reproduced from ref.79 with permission from American Chemical Society.

Owing to the endless structural diversity of POMs and their wide ranging hybridisation strategies, there are a number of exotic structures that can be accessed. Subsequent work carried out by Cronin and co-workers synthesised the first amphiphilic dumbbell-type "inorganic-organic-inorganic" hybrid molecules by grafting linear bis(tris) ligands onto V_3-capped Wells-Dawson type cluster $TBA_5H_4[P_2V_3W_{15}O_{62}]$, $TBA_{10}H_2[\{P_2V_3W_{15}O_{59}(OCH_2)_3CNHCO\}_2]$ and $TBA_{10}H_2[\{P_2V_3W_{15}O_{59}(OCH_2)_3CCH_2\}_2O]$ (Figure 21).[79] These hybrids demonstrate solvent specific supramolecular assembly in acetone/H_2O solutions and were characterised using light scattering techniques and TEM. The XRD data reported shows that the TBA^+ cations intercalated between the hybrid molecules, specifically hydrogen bonded to the POM. This observation is vital in understanding the mitigation of charge repulsion between POMs by cations essentially wrapping around the POM. Interestingly, both compounds displayed amphiphilic behaviour, $TBA_{10}H_2[\{P_2V_3W_{15}O_{59}(OCH_2)_3CNHCO\}_2]$ was studied further in 0.1 $mgmL^{-1}$ in acetone/H_2O solvents containing less than 60 vol % acetone. Static light scattering (SLS) and dynamic light scattering (DLS) anlysis indicated assemblies increased in size with increasing acetone content (61 to 81 nm in solutions contain 30 to 60 vol % acetone respectively). Furthermore, a linear increase in size with increasing concentration upto 120 nm was observed, demonstrating that the assembly size was dictated by both acetone concentration and hybrid concentration. Interestingly, although the hydrophobic component of the hybrid is not large compared to the two hydrophilic POM heads, the hybrid still self-assembles into its entropically favourable superstructure. The author concludes the importance and position of the TBA^+ cations not only stabilising the electrostatic repulsion between the POMs but also positioning in the hydrophobic layer within the vesical wall, allowing the proper formation of this assembly. Simlar bola-type amphiphiles possessing two polar POM head groups connected by a hydrophobic section were later synthesised and studied.[80]

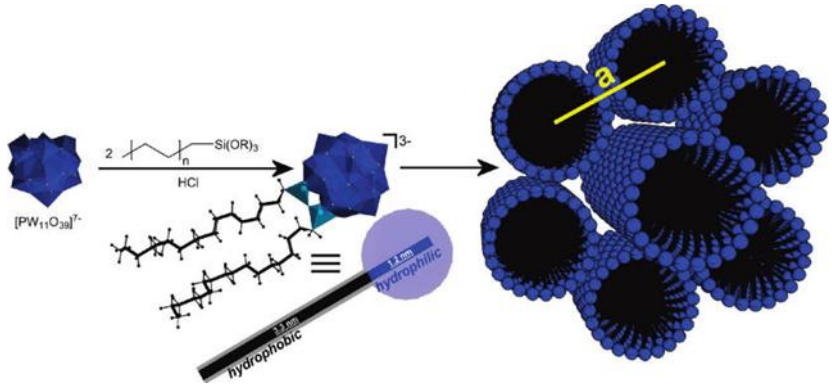

Figure 22 - A schematic illustrating lacunary POM species modified with two alkylsiloxy groups and demonstration of its lyotropic phase when in contact with water such as the shown assembly of cylinders in a hexagonal fashion. Reproduced from ref.81 with permission from American Chemical Society.

Polarz and co-workers reported the first case of utilising hybrid-POM amphiphiles as emulsifying agents and catalysts based on $[PW_{11}O_{39}(SiC_n)_2]^{3-}$, where C_n chains are covalently grafted to Keggin clusters *via* siloxane linkers (Figure 22). The author found that this class of compound formed lytropic liquid crystal state.[81] Furthermore, through polarisation microscopy it was found that by varying the chain length (C_{12} or C_{16}) or the associated cation (Na^+ or TBA^+), the liquid crystal states could be altered. These liquid crystals were characterised by polarisation microscopy, SAXS and TEM. The author reports the presence of hexagonal packed cylinders for $Na_3[PW_{11}O_{39}(SiC_{16})_2]$ which changes in structure with modifying chain length or cation. Furthermore, micelle superstructures were accessed at low concentrations (D_h = 4.3 nm) with a linear increase in size with surfactant chain length. Finally, when the cation was exchanged for H^+, these amphiphiles displayed emulsification behaviour and could catalyse the polymerisation of styrene. This example by Polarz demonstrates the effects of chain length and cation on the supramolcular assembly and their functional properties.

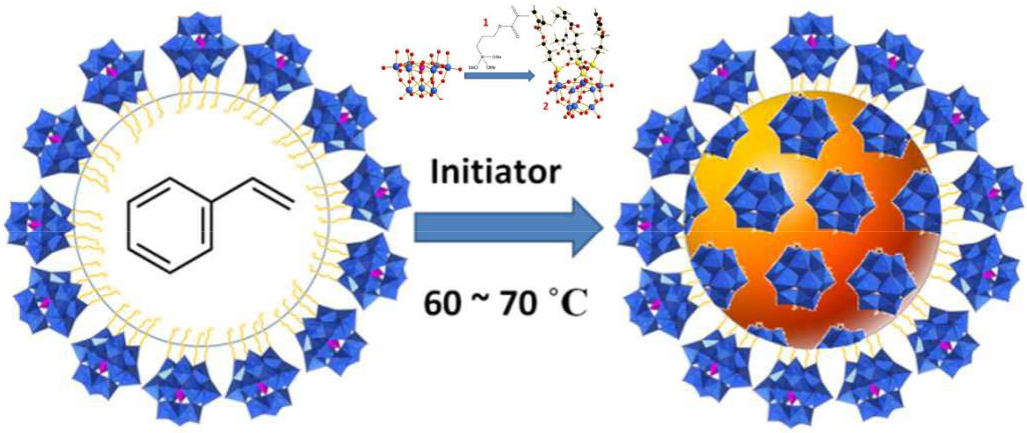

Figure 23 - A schematic representation of the emulsion polymerization process. Reproduced from ref.82 with permission from the Royal Society of Chemistry.

Later, Liu *et al.* developed upon this observed catalysis behaviour observed by Polarz. Their investigation was based on a trilacunary Keggin cluster, $Na_9[PW_9O_{34}]$, which was functionalised with methyl methacrylate (MMA) containing ligands (Figure 23).[82] Due to the copolymerisation of MMA and styrene, POM hybrids were covalently grafted to the polystyrene latex particles, forming nanocomposite hybrid particles. This allowed the hybrid molecule to stabilise the emulsion system, trigger the reaction and be chemically bound to the particles. The reported hybrid displayed supramolecular assemblies in aqueous solutions (5 nm). Conductometric measurements were used to obtain the CMC (2.0 $mgmL^{-1}$). Latex particles (80 nm) were obtained *via* emulsion polymerisation which were characterised *via* SEM, TEM and EDS. Furthermore, the hybrid POMs were confirmed to be embedded in surface of these particles. The size of the particle was also found to be tuneable by adjusting the concentration of the hybrid (lower conc. = larger particle size).

The mechanism of radical emulsion polymerisation is very different from that of the cationic miniemulsion polymerisation previously reported by Polarz *et al*. and Lui *et al.* on separate occasions.[81, 82] The former is initiated by a radical initiator and required monomer diffusion through the water phase. This investigation by Rieger *et al.* yielded polystyrene (PS) NP suspensions with and without covalent attachment to the POM.[83] A surfactant approach was based on amphiphilic organo-functionalised Wells-Dawson cluster, where the cluster was modified with a hydrophobic

dodecylamide chain through a Sn linker $[P_2W_{17}O_{61}Sn(CH_2)_2CONHC_{12}H_{25}]^{7-}$ (POM-C_{12}). The ammonium salt was employed soley to stabilise the latex NP. In this case, the POM was found to be present on the surface with the C_{12} chains buried inside the NP. The second approach takes advantage of an amphiphilic POM RAFT agent ($[P_2W_{17}O_{61}Sn(CH_2)_2CONHR]^{7-}$, POM-TTC$C_{12}$, ammonium salt) which incorporated a trithiocarbonate (TTC) group, that is commonly employed as a reactive component in radical polymerization through RAFT mechanism. The POM-TTC-C_{12} is therefore expected to participate in the polymerization mechanism as a reversible chain transfer agent, thus leading to covalent linking of the POM to the PS (polystyrene). The group conducted a control by carrying out an emulsion polymerisation in the absence of a stabilising agent (e.g. surfactant, POM-amphiphile etc.) which lead to the formation of extra-large particles that precipitated. It was found that > 0.1 mol % of POM-C_{12} was needed to reach quantitative formation of stable PS NP (polystyrene nanoparticle) without coagulation and the size of the particles decreased with increasing NPs. With regards to POM-TTCC_{12}, the organic side chains should not only stabilise the emulsions but also allow initiation of styrene polymerisation after chain transfer. This hybrid's CMC was found to be below the concentration for polymerisation, therefore the author has speculated a micellar nucleation mechanism.[84] The particles exhibted stability for up to 4 months and a slightly broader size range compared to POM-C_{12}. Post centrifugation, a majority of the POM was anchored to the surface for POM-TTC-C_{12} PS NP compared to POM-C_{12}, confirming the presence of strong covalent bonds anchoring the POMs. The photoreduction properties were also reported to be transferring to the composite material. Thus, emphasising the oppertunities to not only use hybrid POM amphiphiles to catalyse polymerisation of styrene, but to also incoporate them into to nanocomposite materials with molecular properties.

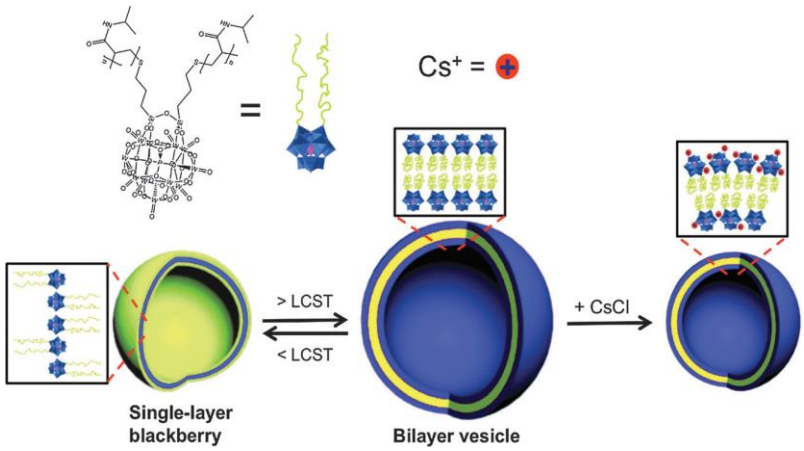

Figure 24 - A schematic representation of the reversible supramolecular assembly controlled by temperature and salt concentration. Reproduced from ref.85 with permission from the Royal Society of Chemistry.

Poly(N-isopropylacrylamide)(PNIPAM) is a thermoresponsive polymer that is known to exhibit a low critical solution temperature (LCST) phase transition from a hydrophilic coiled conformation to a hydrophobic collapsed globular assembly in water (32 ^{o}C) (Figure 24). Therefore, this polymer is a good model for probing biomacromolecules under various conditions and can be used to facilitate supramolecular self-assembly processes. An interesting study conducted by Liu *et al*. reported the synthesis of a PNIPAM Keggin hybrid coordinated to K^+ cations.[85] This molecule consists of two PNIPAM liagnds covalently grafted to a Keggin cluster *via* siloxane linkers. In aqueous solutions, there was no observation of assemblies at r.t., however, upon increasing the temperature to 39 ^{o}C, hollow spherical assemblies were observed, which further increased in size with increasing temperature. This thermoresponsive assembly is a result of the PNIPAM chains switching from the hydrophilic to the hydrophobic state, leading to bilayer vesicle structures. TBA^+ hybrids displayed assemblies (40 nm) in KCl solutions, which are speculated to be blackberry formations (at r.t.) induced by TBA^+ cations. Furthermore, the author reports an increase in size with increasing temperature, resulting in the reversible formation of bilayer vesicles. These assemblies proved to be salt-responsive as the size decreased with salt addition to the pre-heated solution. This observation was concluded to be a result of cations with smaller hydration spheres coordinating and creating a bigger surface area for the POM head, leading to higher curvature and smaller assemblies. This investigation by Liu demonstrated the

effectiveness of hybridising functional ligands to fabricate moelcules with "*smart*"-responsive behaviours.

Understanding how conditons in the environment of supramolecular assemblies affect the superstructres is important in the control and development of functional soft materials. Cronin and co-workers studied the effects of counter ions and pH on the supramolecular assembly of a hybrid POM composing of 15-carbon alkyl chain and tris(hydroxymethyl)amidomethane moiety that was covalently grafted to $[P_2V_3W_{15}O_{62}]^{6-}$ obtaining POM-hybrid molecule $TBA_5H[P_2V_3W_{15}O_{59}(OCH_2)_3CNHCOC_{15}H_{31}]$.[86] The author reports the the supramolecular assembly of this molecule into vesicles shows a liner trend between increasing concentration and size of the assembly, reporting an increase from 50 to 115 nm when the concentration was increased from 0.02 to 0.5 $mgmL^{-1}$. Furthermore, vesicle size measured by DLS and TEM showed a linear relationship between the inverse of the dielectric contact of the solvent, which has been associated with a charge-regulated process by many studies. This phenomenon can be explained by the dissociation of counter ions, as TBA^+ cations diffuse faster than the hybrid in polar solvents, resulting in an increase in hydrophilicity of the POM head, whereas the diffusion speed is similar in non-polar solvents. The counter ions dissociation is controlled by factors such static charge interaction, solvent polarity and the solvation of ions. This molecule possesses a 6 - charge which means it can form vesicles in less polar solvents compared to molecules with lower charge. Furthermore, the author reports that with the increasing concentration of $ZnCl_2$, the vesicle sizes decreased. This is a result of the $ZnCl_2$ being highly solvated and preferring to coordinate to terminal oxo-groups on the POM. Therefore, entrapping itself between the POMs which leads to higher curvature and inherently, smaller assemblies (also lower shielding of charge). Whereas, NaI addition seems to replace and promote a faster diffusion rate for TBA^+, also shielding the charge more efficiently around the POM, leading the entrapment, but lower curvature and large vesicular size. The author finally investigates the effect of pH on the vesicle size which is reported to decrease in size from pH 1.5 (81 nm), pH 5 (64 nm) and pH 9-12 (34 nm). This result is attributed to the loss of protons from the POM head, therefore increasing the overall charge of the

POM, leading to stronger effective charge and larger curvature. Fundamental studies like such have addded to the wealth of knowledge concerning the behaviour of hydrid-POM amphiphiles under different environmental stimuli.

Another fundamental study conducted by Polarz *et al*. investigated how the charge of the POM head can affect the assemblies in aqueous solutions, without changing the shape of the overall surfactant.[87] This study focused on the same POM hybrid structures but with different heteroatom backbones which give rise to different overall redox states across the molecules, $X_3[PW_{11}O_{40}(SiC_{16}H_{33})_2]$, $X_4[SiW_{11}O_{40}(SiC_{16}H_{33})_2]$ and $X_5[BW_{11}O_{40}(SiC_{16}H_{33})_2]$, where X = Na or H. $Na_3[PW_{11}O_{40}(SiC_{16}H_{33})_2]$ formed (lyotropic liquid crystals) LLCs at high concentrations, and were observed to be in a cylindrical hexagonal packing morphology, *P6/mm*. Comparatively, compound $Na_4[SiW_{11}O_{40}(SiC_{16}H_{33})_2]$ with a 4- charge displayed a lamellar type packing in the LLC phase, where the alkyl chains are interdigitated. $Na_5[BW_{11}O_{40}(SiC_{16}H_{33})_2]$ which possessed a 5- charge higher did not show any organised assemblies under the same conditions. At lower concentrations, $H_3[PW_{11}O_{40}(SiC_{16}H_{33})_2]$, displayed spherical micellar aggregates with D_h = 4.8 nm which corresponds to an assembly where the chains are orientated into the centre and partially interdigitated. $H_4[SiW_{11}O_{40}(SiC_{16}H_{33})_2]$ also assembled into nanoagreggates with D_h = 32 nm (DLS) which were found to be 25 nm in length and 5-7 nm in width. The observed assemblies were a dumbbell morphology. Based on this investigation, it is clear that the charge of the POM plays a fundamental part in the supramolecular assembly driving force and the assembled structure.

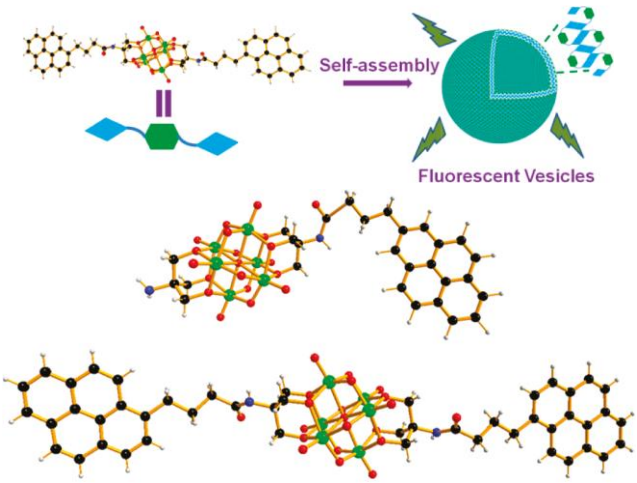

Figure 25 - A schematic illustrating the hybrid POMs, their supramolecular assembly and fluorescence properties. Reproduced from ref.88 with permission from American Chemical Society.

Developing new organo-functionlisation strategies can be a useful too to graft ligands with deseriable properties to POM clusters. In this way, Hill and co-workers demonstrated smart self-assembly of two photoactive hybrid POM amphiphiles. Two inorganic-organic hybrid molecules with one or two covalently linked pyrene fluorescent groups, $TBA_2[V_6O_{13}\{(OCH_2)_3C(NH(CO)(CH_2)_3C_{16}H_9)\}]$ and $TBA_2[V_6O_{13}\{(OCH_2)_3\text{-}C(NH(CO)(CH_2)_3C_{16}H_9)\}_2]$, respectively, were synthesized from Lindqvist type POMs (Figure 25).[88] The author first demonstrates the supramolecular assembly of such molecules in a solvent mixture of H_2O:DMSO, leading to vesicular assemblies (50 nm), and further reporting the presence of excimer peaks in the assembly domain. The presence of the excimer peaks is attributed to the close packing of the hybrid molecules, specifically the pyrene ligands. This fluorescence profile was not observed in the molecular state and in the supramolecular state in the presence of large bulky cations (e.g. TBA^+), but only when the cation was exchanged for H^+. Furthermore, the author demonstrates that the intensity of the excimer peak is pH dependent. This smart assembly has not only shown the ability to control assembly size through pH, but also trigger fluorescence *via* supramolecular assembly in conjunction with cation exchange. This investigation is a great example in

the development of hybrid molecules towards smart assemblies and how functional ligands can be employed to probe the packing structure of such assemblies.

An interesting result was reported by Yongge *et al.* based on a simplified hexavanadate–organic hybrid amphiphile molecule, $TBA_2[V_6O_{13}\text{-}\{(OCH_2)_3CCH_2OOC(CH_2)_{16}CH_3\}_2]$, where the supramolecular assembly resulted in unexpected photoluminescence properties.[89] This hybrid was synthesised by grafting two C_{18} chains onto both sides of a hexavandate cluster. This molecule was also crystallised. Although POMs like such are known to be luminescence quenchers as a result of their ability to store electrons, this hybrid displayed blue luminescence in both water and acetone solutions. this result was achieved by the cation swap from TBA^+ to H^+ or Na^+, both emitted strong blue luminescence with peaks at 392 nm, 409 nm and 429 nm when excited with light of wavelengths 300-420 nm. The results are attributed to the ligand to metal charge transfer (LMCT) absorption wavelength, and the origins of emission was loosely associated with an emissive state derived from such a transition. The reason behind the exchange of cations triggering this luminescence may be a result of POM head groups increasing in interaction with decreasing size of stabilizing cations. Interestingly, the excitation at 410 nm of the aggregates of this hybrid in aqueous solutions was observed using fluorescence microscopy, and intensity of the observed dots did not decay over 30 mins which demonstrated higher stability compared to other organic fluorophores that undergo photo-bleaching when exposed to UV light. Furthermore, the author reports the ability of water to promote dissociation of the TBA+ ions from the POM head, therefore increasing the net charge of the POM, and rendering the molecule to become amphiphilic in nature. Vesicles were observed with the proportions of water/acetone was above 20 %, further increasing in size with increasing water content. Increasing the water content above 35 %, the solution turned turbid as a result of microscrystal formation. The dissociation of TBA^+ and vesicle formation was stated to be correlated as the zeta potential became more negative with increasing water content, leading to vesicle formation and then onto larger vesicles at higher water concentrations. Due to the unusual relationship between water and the TBA^+ cations, the hybrid amphiphilic molecule's hydrophilicity can be controlled. This example demonstates a unique and rare

case of luminesence associated with POMs and their assembly packing. These examples suggest that by forcing POMs into supramolecuar assemblies, their molecular properties can change. In a later investigation, these molecules in their supramolecular states showed emulsification catalytic behaviour.[90]

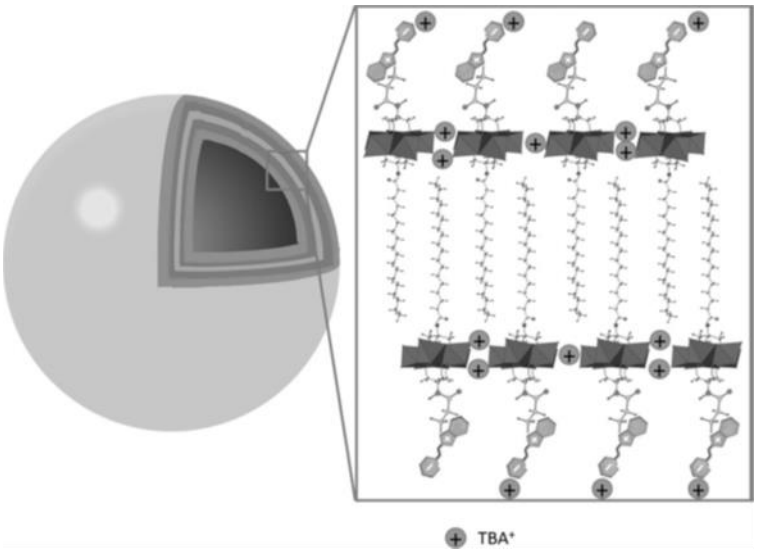

Figure 26 - A model of the self-assembled structure of hybrid SP-POM-C_{16} in polar solvents. Reproduced from ref.91 with permission from John Wiley and Sons.

Spiropyrans (SP) are particularly investigated for their interesting optical properties and their synthetic availability. The colourless molecules possess a C-O bond which can be cleaved with UV irradiation, resulting in the formation of a zwitterionic merocyanine (MC) isomer. MC strongly absorbs in the visible regions and is hydrophilic. Lui *et al*. reported the synthesis of an asymmetric hybrid, covalently grafting a photo-switchable spiropyran fragment, a hydrophilic Anderson POM body and a long hydrophobic chain ($TBA_3[MnMo_6O_{18}\{(OCH_2)_3CNHC_{21}H_{19}N_2O_4\}\{(OCH_2)_3CNH_2\}]$).[91] This hybrid showed good solubility in MeCN, but was insoluble in water and toluene. Self-assembly was triggered when the hybrid solution was irradiated under UV light (λ = 365 nm) after 10 h in MeCN solutions containing 0.1 $mgmL^{-1}$ of hybrid-POM and 2 and 2.5 v/v % H_2O, and stabilised after 30 h. Furthermore, these hybrids showed very little photodegradation after 24 h of UV irradiation. The assembly size dramatically increased with increasing water content from R_h = 13 nm for 2 v/v % H_2O to R_h = 110 nm for 2.5 v/v % H_2O. This change in structure of the SP → MC comes with a change in absorption, which suggests the assembly process can be tracked. In 84 v/v % toluene/acetonitrile, the intensity stabilizes

after three days, leading to spherical assemblies thought to be reverse vesicles due to solvent polarity, where R_h = 112 nm (Figure 26). This assembly process is reported to be reversible. Sizes of the assemblies were found to be inversely proportional to the dielectric constant of the mixed solvent.Irrespective of size, these assemblies exhibited high stability and reversibility.

Work by Wang *et al*. has also focused on developing bulky hydrophobic polyhedral oligomeric silsesquioxane (POSS) hybrid-POM amphiphiles, which have displayed a range of intricate and fascinating hierarchical structures (i.e. 2D honeycomb lattices, lamellar sheets, layered spherical assemblies etc.).[92, 93]

1.6.2.2 Surfactant-Encapsulated Hybrid POMs

Surfactant-encapsulated hybrid POMs combine the effects of class II hybrids which may possess lower levels of amphiphilic behaviours, with the additional cationic surfactant coordination of class I hybrids to boost the overall amphiphilicity.

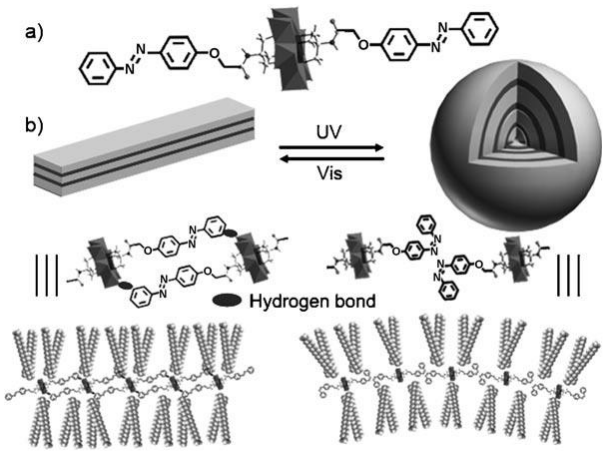

Figure 27 - An illustration of a) structure of SEOP and b) reversible morphology change of SEOP-2 between fibrous and spherical structures upon stimulation by light. Reproduced from ref.94 with permission from John Wiley and Sons.

Wu and co-workers were the first to report a photo-induced supramolecular morphology transition by grafting photo-isomerisable azo-benzene moiety to an Anderson POM, which allowed the molecule to not only self-assemble into superstructures, but also make a photon-induced smart morphological transition between spherical and fibrous assemblies (Figure 27).[94] The author reported that by

swapping the counter cation TBA^+ for $DODA^+$, a more compact superstructure was achieved, resulting in more favourable assemblies. The initial state was majority *trans* with the conversion of majority to *cis* after irradiation with UV (365 nm) light. This transition was tracked *via* UV-vis and ^1H NMR. The high isomerisation reversibility suggested that there was less packing interaction between the azo groups which is particularly desirable when carrying out morphological transitions in the supramolecular state. The hybrid material was dissolved in CH_2Cl_2/MeOH (4:1 v/v) solution and then irradiated (365 nm) for 120 min. During irradiation samples were analysed under SEM, which displayed a clear transition over time from fibrous assemblies to spherical micellar structures. Thermally induced *cis* to *trans* isomerisation in the dark was reported and displayed a transition from *cis*-spherical aggregates to trans willow-leaf like aggregates. This investigation showcases the benefits of combining stimuli responsive ligands that invoke structural isomerisation with POMs and cationic surfactants to fabricate smart responsive materials.

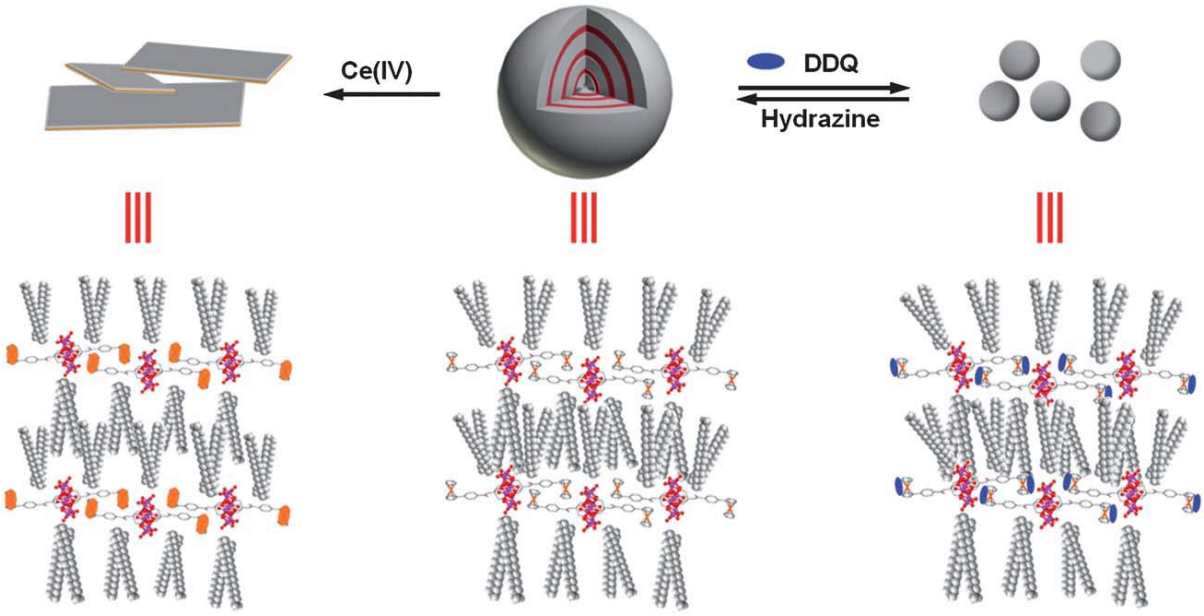

Figure 28 - A schematic illustration of reversible supramolecular assembly and morphologic changes of SEOP-2 self-assemblies upon redox stimulation by Ce(IV), DDQ and hydrazine. Reproduced with permission from the Royal Society of Chemistry.

Further studies conducted by this group developed a ferrocene symmetrically modified Anderson POM with organic ammonium cations, denoted as surfactant enwrapped organically modified POMs (SEOPs). Hybrid molecule SEOP-1 possessed TBA^+ cations whereas SEOP-2 coordinated to surfactant-

like dioctadecyldimethylammonium ($DODA^+$) cations.[95] Here, Wu and co-workers demonstrate that by coupling two redox-active components, ferrocene and POM, assembly modulation can be probed (Figure 28). The electrochemical analysis of this hybrid displayed redox process for the ferrocene moieties ($E_{1/2}$ = 0.55 V) which has shifted 50 mV with respect to the ferrocene molecule, and the POM (Mn_{ox} = 1.0 V and Mo_{ox} = 0.28, - 0.62 V *vs*. Ag/AgCl), implying that a redox active and stable hybrid was synthesised. Furthermore, scan rate dependent analysis confirmed these processes are diffusion controlled. According to DLS analysis, both SEOP-1 and SEOP-2 hybrid molecules displayed assemblies in organic solvents, monodisperse sample range with D_h = 220 nm in MeCN and polydisperse sample range with D_h = 342 nm in CH_2Cl_2 respectively. Although SEOP-1 displayed monodisperse assemblies in solution, once drop-cast, the integrity of the assemblies was compromised, likely due to the short alkyl chains of TBA^+ not providing enough structural stabilisation. In contrast, SEOP-2 composed with larger cations show larger stable and spherical aggregates. TEM analysis of these hybrids displayed layered packing (3.7 nm spacing), which was attributed to an inverse bilayer morphology with $DODA^+$ located either side of the POMs. To probe structural rearrangement *via* change in redox state of the hybrid, inorganic Ce^{IV} and organic DDQ were employed oxidants and hydrazine as a reductant. Upon oxidation with Ce^{IV}, SEOP-2 displayed a broad absorption band near 700 nm and a change in morphology from spherical superstructures in the neutral state to irregular flake-like assemblies. Interestingly, XRD data for both morphologies exhibit layered structures and seemed to increase in spacing from 3.7 nm in the neutral state to 4.6 nm in the oxidised state. The author speculates that this is a result of the Ce^{IV} irreversibly binding to the POM, leading to the DODA cations being bound between POMs, leading to closer packing and the alkyl chains becoming less interdigitated, therefore increasing the layer distance. The uptake of Ce^{IV} meant this process of oxidation was not reversible. Conversely, because both DDQ and hydrazine are non-ionic in both oxidised and reduced state, they are easily up taken and released from aggregates, allowing them to be better candidate as redox probes. Cycling between the two probes displayed the reversible appearance of an absorption band at 590 nm, which is assigned to the CT band of DDQ-ferrocene pair. Coupled with this process, smaller

spherical assemblies were observed in the oxidised state with smaller layer spacing of 3.32 nm which is reported to be reversible with cycling of redox states. Overall, the investigation concludes the main driving force to assemble these layered structures are owed to the hydrophobic interaction of the surfactant DODA cations.

In summary, we have discussed a broad range of investigations regarding Class I and II hybrid-POMs and reviewed their supramolecular assembly, functional properties, and contribution to the field. We will now focus on Class II hybrids for the following chapters.

1.7 REFERENCES

1. H. So and M. T. Pope, *Inorg. Chem.,* **1972**, 11, 1441-1443.
2. J. Forster, B. Rösner, R. H. Fink, L. C. Nye, I. Ivanovic-Burmazovic, K. Kastner, J. Tucher and C. Streb, *Chem.*, **2013**, 4, 418-424.
3. A. Banerjee, F. S. Raad, N. Vankova, B. S. Bassil, T. Heine and U. Kortz, *Inorg. Chem.*, **2011**, 50, 11667-11675.
4. B.-X. Liu, Z.-W. Cai, T. Yang, X.-X. Li, G.-Y. Yang and S.-T. Zheng, *Inorg. Chem.*, **2017**, 78, 56-60.
5. L. B. Fullmer, C. E. Malmberg, D. B. Fast, L. A. Wills, P. H.-Y. Cheong, M. R. Dolgos and M. Nyman, *Dalton T.*, **2017**, 46, 8486-8493.
6. N. V. Izarova, M. T. Pope and U. Kortz, *Angew. Chem. Int.*, **2012**, 51, 9492-9510.
7. X. López, J. A. Fernández and J. M. Poblet, *Dalton T.*, **2006**, 1162-1167.
8. J. T. Rhule, C. L. Hill, D. A. Judd and R. F. Schinazi, *Chem. Rev.*, **1998**, 98, 327-358.
9. D. Sloboda-Rozner, K. Neimann and R. Neumann, J. Mol. Catal. Chem., **2007**, 262, 109-113.
10. N. Mizuno and K. Yamaguchi, *Chem. Rec.*, **2006**, 6, 12-22.
11. M. Ammam, *J. Mater. Chem. A*, **2013**, 1, 6291-6312.
12. J. M. Clemente-Juan, E. Coronado and A. Gaita-Ariño, *Chem. Soc. Rev.*, **2012**, 41, 7464-7478.
13. C. L. Hill and C. M. Prosser-McCartha, *Coord. Chem. Rev.*, **1995**, 143, 407-455.
14. M. T. Pope, in *Polyoxometalate Molecular Science*, eds. J. J. Borrás-Almenar, E. Coronado, A. Müller and M. Pope, Springer Netherlands, Dordrecht, **2003**, 3-31.
15. L. C. W. Baker and D. C. Glick, *Chem. Rev.*, **1998**, 98, 3-50.
16. J. R. Winkler and H. B. Gray, in *Molecular Electronic Structures of Transition Metal Complexes I*, eds. D. M. P. Mingos, P. Day and J. P. Dahl, Springer Berlin Heidelberg, Berlin, Heidelberg, **2012**, 17-28.
17. F. Basolo and R. G. Pearson, *Mechanisms of Inorganic Reactions: A Study of Metal Complexes in Solution*, Wiley, **1958.**
18. W. N. Lipscomb, *Inorg. Chem.*, **1965**, 4, 132-134.
19. M. T. Pope, *Heteropoly and Isopoly Oxometalates*, WILEY-VCH Verlag GmbH, **1983**.
20. M. T. Pope and E. Papaconstantinou, *Inorg. Chem.*, **1967**, 6, 1147-1152.
21. G. M. Varga, E. Papaconstantinou and M. T. Pope, *Inorg. Chem.*, **1970**, 9, 662-667.
22. J. E. Molinari, L. Nakka, T. Kim and I. E. Wachs, *ACS Catal.*, **2011**, 1, 1536-1548.
23. D. L. Long, R. Tsunashima and L. Cronin, *Angew. Chem. Int.*, **2010**, 49, 1736-1758.
24. I. Lindqvist, *Arkiv Kemi*, **1950**, 2, 349-355.
25. P. I. Molina, D. J. Sures, P. Miró, L. N. Zakharov and M. Nyman, *Dalton T.*, **2015**, 44, 15813-15822.
26. Tijmen M. A. Bakker, S. Mathew and J. N. H. Reek, *SUSTAIN ENERG FUELS*, **2019**, 3, 96-100.
27. J. S. Anderson, *Nature*, **1937**, 140, 850-850.
28. H. T. Evans, *J. Am. Chem. Soc.*, **1948**, 70, 1291-1292.
29. J. F. Keggin and W. L. Bragg, *Proc. Math. Phys.*, **1934**, 144, 75-100.
30. M. Abbessi, R. Contant, R. Thouvenot and G. Herve, *Inorg. Chem.*, **1991**, 30, 1695-1702.
31. C. Rocchiccioli-Deltcheff, M. Fournier, R. Franck and R. Thouvenot, *Inorg. Chem.*, **1983**, 22, 207-216.
32. L. C. W. Baker and J. S. Figgis, *J. Am. Chem. Soc.*, **1970**, 92, 3794-3797.
33. K. Akiko and S. Yukiyoshi, *Bull. Chem. Soc. Jpn.*, **1975**, 48, 885-888.
34. F. Robert, A. Tézé, G. Hervé and Y. Jeannin, *Acta Crystallogr., Sect. B*, **1980**, 36, 11-15.
35. A. Tézé, E. Cadot, V. Béreau and G. Hervé, *Inorg. Chem.*, **2001**, 40, 2000-2004.
36. H. Sartzi, H. N. Miras, L. Vila-Nadal, D. L. Long and L. Cronin, *Angew, Chem. Int. Ed.*, **2015**, 54, 15488-15492.
37. D. Sloboda-Rozner, K. Neimann and R. Neumann, *J. Mol. Catal. A Chem.*, 2007, **262**, 109-113.
38. B. Dawson, *Acta Crystallogr.*, **1953**, 6, 113-126.
39. L. Vilà-Nadal, S. Romo, X. López and J. Poblet, L. Vilà-Nadal, S. Romo, X. López and J. M. Poblet, *Structure and Electronic features of Wells-Dawson Polyoxometalates,* Dordrecht, **2012**, 171-183
40. L. Vilà-Nadal, S. G. Mitchell, D.-L. Long, A. Rodríguez-Fortea, X. López, J. M. Poblet and L. Cronin, *Dalton T.*, **2012**, 41, 2264-2271.
41. F.-Q. Zhang, W. Guan, L.-K. Yan, Y.-T. Zhang, M.-T. Xu, E. Hayfron-Benjamin and Z.-M. Su, *Inorg. Chem.*, **2011**, 50, 4967-4977.
42. A. Hashikawa, M. Fujimoto, Y. Hayashi and H. Miyasaka, *Chem. Commun.*, **2011**, 47, 12361-12363.
43. A. Patel and R. Sadasivan, *Prog. Mater. Sci*, **2021**, 118, 100759.
44. A. J. Kibler and G. N. Newton, *Polyhedron*, **2018**, 154, 1-20.
45. X. López, C. Bo and J. M. Poblet, *J. Am. Chem. Soc.*, **2002**, 124, 12574-12582.
46. I.-M. Mbomekallé, X. López, J. M. Poblet, F. Sécheresse, B. Keita and L. Nadjo, *Inorg. Chem.*, **2010**, 49, 7001-7006.
47. E. N. Glass, J. Fielden, Z. Huang, X. Xiang, D. G. Musaev, T. Lian and C. L. Hill, *Inorg. Chem.*, **2016**, 55, 4308-4319.
48. L. Parent, P. A. Aparicio, P. de Oliveira, A.-L. Teillout, J. M. Poblet, X. López and I. M. Mbomekallé, *Inorg. Chem.*, **2014**, 53, 5941-5949.
49. N. Mizuno and M. Misono, *Chem. Rev.*, **1998**, 98, 199-218.
50. M. Stuckart and K. Y. Monakhov, *Chem. Sci.*, **2019**, 10, 4364-4376.

51. S. Fujimoto, J. M. Cameron, R.-J. Wei, K. Kastner, D. Robinson, V. Sans, G. N. Newton and H. Oshio, *Inorg. Chem.*, **2017**, 56, 12169-12177.
52. J. M. Cameron, S. Fujimoto, R. J. Wei, G. N. Newton and H. Oshio, *Dalton T.*, **2018**, 47, 10590-10594.
53. J. M. Cameron, S. Fujimoto, K. Kastner, R. J. Wei, D. Robinson, V. Sans, G. N. Newton and H. H. Oshio, *Chem. Eur. J.*, **2017**, 23, 47-50.
54. A. Müller and C. Serain, *Acc. Chem. Res*, **2000**, 33, 2-10.
55. A. Müller, E. Diemann, C. Kuhlmann, W. Eimer, C. Serain, T. Tak, A. Knöchel and P. K. Pranzas, *Chem.Comm.*, **2001**, 1928-1929.
56. M. L. Kistler, A. Bhatt, G. Liu, D. Casa and T. Liu, *J. Am. Chem. Soc*, **2007**, 129, 6453-6460.
57. G. Liu, T. Liu, S. S. Mal and U. Kortz, *J. Am. Chem. Soc.*, **2006**, 128, 10103-10110.
58. M. L. Kistler, T. Liu, P. Gouzerh, A. M. Todea and A. Müller, *Dalton T.*, **2009** , 5094-5100.
59. M. L. Kistler, K. G. Patel and T. Liu, *Langmuir*, **2009**, 25, 7328-7334.
60. I. Ichinose, T. Asai, S. Yoshimura, N. Kimizuka and T. Kunitake, *Chem. Lett.*, **1994**, 23, 1837-1840.
61. M. Clemente-León, H. Soyer, E. Coronado, C. Mingotaud, C. J. Gómez-García and P. Delhaès, *Angew, Chem. Int. Ed.*, **1998**, 37, 2842-2845.
62. D. G. Kurth, P. Lehmann, D. Volkmer, H. Cölfen, M. J. Koop, A. Müller and A. Du Chesne, *Chem. Eur. J.*, **2000**, 6, 385-393.
63. W. Bu, H. Li, H. Sun, S. Yin and L. Wu, *J. Am. Chem. Soc.*, **2005**, 127, 8016-8017.
64. H. Li, H. Sun, W. Qi, M. Xu and L. Wu, *Angew. Chem. Int. Ed*, **2007**, 46, 1300-1303.
65. A. Nisar, J. Zhuang and X. Wang, *Chem. Mater.*, **2009**, 21, 3745-3751.
66. P. He, B. Xu, H. Liu, S. He, F. Saleem and X. Wang, *Sci. Rep.*, **2013**, 3, 1833.
67. Y. Yang, L. Yue, H. Li, E. Maher, Y. Li, Y. Wang, L. Wu and V. W.-W. Yam, *Small*, **2012**, 8, 3105-3110.
68. Y. Yang, B. Zhang, Y. Wang, L. Yue, W. Li and L. Wu, *J. Am. Chem. Soc.*, **2013**, 135, 14500-14503.
69. M. Sadakane and E. Steckhan, *Chem. Rev.*, **1998**, 98, 219-238.
70. P. He, B. Xu, X. Xu, L. Song and X. Wang, *Chem. Sci.*, **2016**, 7, 1011-1015.
71. Q. Liu, P. He, H. Yu, L. Gu, B. Ni, D. Wang and X. Wang, *Sci. Adv.*, **2019**, 5, 1081.
72. A. Nisar, Y. Lu, J. Zhuang and X. Wang, *Angew. Chem. Int. Ed.*, **2011**, 50, 3187-3192.
73. K. Inumaru, T. Ishihara, Y. Kamiya, T. Okuhara and S. Yamanaka, *Angew. Chem. Int. Ed,* **2007**, 46, 7625-7628.
74. A. Nisar, J. Zhuang and X. Wang, *Adv. Mater.*, **2011**, 23, 1130-1135.
75. Y. Wang, H. Li, W. Qi, Y. Yang, Y. Yan, B. Li and L. Wu, *J. Mater. Chem.*, **2012**, 22, 9181-9188.
76. H. Lü, J. Gao, Z. Jiang, Y. Yang, B. Song and C. Li, *ChemComm.*, **2007**, 2, 150-152.
77. J. Zhang, Y. F. Song, L. Cronin and T. Liu, *J. Am. Chem. Soc.*, **2008**, 130, 14408-14409.
78. J. Zhang, Y.-F. Song, L. Cronin and T. Liu, *Chem. Eur. J.*, **2010**, 16, 11320-11324.
79. M. F. Misdrahi, 2011.
80. F. Xiao, M. F. Misdrahi, J. Zhang, P. Yin, J. Hao, C. Lv, Z. Xiao, T. Liu and Y. Wei, *Chemistry*, **2011**, 17, 12006-12009.
81. S. Landsmann, C. Lizandara-Pueyo and S. Polarz, *J. Am. Chem. Soc.*, **2010**, 132, 5315-5321.
82. X. Chen, H. Li, P. Yin and T. Liu, *ChemComm.*, **2015**, 51, 6104-6107.
83. J. Lesage de La Haye, J.-M. Guigner, E. Marceau, L. Ruhlmann, B. Hasenknopf, E. Lacote and J. Rieger, *Chem. Eur. J.*, **2015**, 21, 2948-2953.
84. S. C. Thickett and R. G. Gilbert, *Polymer*, **2007**, 48, 6965-6991.
85. J. Zhou, P. Yin, X. Chen, L. Hu and T. Liu, *Chem.Comm.*, **2015**, 51, 15982-15985.
86. P. Yin, C. P. Pradeep, B. Zhang, F.-Y. Li, C. Lydon, M. H. Rosnes, D. Li, E. Bitterlich, L. Xu, L. Cronin and T. Liu, *Chem. Eur. J.*, **2012**, 18, 8157-8162.
87. A. Klaiber, C. Lanz, S. Landsmann, J. Gehring, M. Drechsler and S. Polarz, *Langmuir*, **2016**, 32, 10920-10927.
88. D. Li, J. Song, P. Yin, S. Simotwo, A. J. Bassler, Y. Aung, J. E. Roberts, K. I. Hardcastle, C. L. Hill and T. Liu, *J. Am. Chem. Soc.*, **2011**, 133, 14010-14016.
89. P. Yin, P. Wu, Z. Xiao, D. Li, E. Bitterlich, J. Zhang, P. Cheng, D. V. Vezenov, T. Liu and Y. Wei, *Angew. Chem. Int. Ed.*, **2011**, 50, 2521-2525.
90. P. Yin, J. Wang, Z. Xiao, P. Wu, Y. Wei and T. Liu, *Chem. Eur. J.*, **2012**, 18, 9174-9178.
91. Y. Chu, A. Saad, P. Yin, J. Wu, O. Oms, A. Dolbecq, P. Mialane and T. Liu, *Chem. Eur. J.*, **2016**, 22, 11756-11762.
92. M.-B. Hu, Z.-Y. Hou, W.-Q. Hao, Y. Xiao, W. Yu, C. Ma, L.-J. Ren, P. Zheng and W. Wang, *Langmuir*, **2013**, 29, 5714-5722.
93. X.-S. Hou, G.-L. Zhu, L.-J. Ren, Z.-H. Huang, R.-B. Zhang, G. Ungar, L.-T. Yan and W. Wang, *J. Am. Chem. Soc.*, **2018**, 140, 1805-1811.
94. Y. Yan, H. Wang, B. Li, G. Hou, Z. Yin, L. Wu and V. W. W. Yam, *Angew. Chem. Int. Ed.*, **2010**, 49, 9233-9236.
95. Y. Yan, B. Li, Q. He, Z. He, H. Ai, H. Wang, Z. Yin and L. Wu, *Soft Matter*, **2012**, 8, 1593-1600.

2 SYNTHESIS, CHARACTERISATION, AND SUPRAMOLECULAR ASSEMBLY OF HYBRID-POM REDOX-ACTIVE AMPHIPHILES

2.1 INTRODUCTION

Research into multi-functional hybrid-POM species has led to the recent development of a new class of hybrid organic-inorganic redox-active amphiphiles, allowing a range of unique hybrid supramolecular assemblies to be prepared.[1-3] These species display a range of interesting properties resulting from the incorporation of a functional POM head-group and have been proposed as charge carriers for novel energy storage applications.[4] In particular, the easy and wide-ranging tuneability of the hydrophobic organic component allows access to a variety of different assemblies and lyotropic phases where, for example, modification of chain length, structure or functionality has been used to control the supramolecular and electronic properties of the hybrid molecules.[5-8] Although the molecular properties are well explored, very little is known about the translation of molecular properties to the supramolecular domain, and the structure-property relationship between the amphiphile and its supramolecular assembly's redox properties. To develop the next generation of functional nanoscopic soft materials, it is crucial to understand the translatability of the molecular properties to their supramolecular architectures.

The first investigation comparing the redox behaviour of a hybrid-POM molecule $H_6[P_2W_{17}O_{57}(H_{27}C_{17}O_4PS)_2].3C_4H_9NO$ and its supramolecular assembly was conducted by Newton and co-workers (Figure 29) .[9] Here, the hybrid molecule of interest consisted of a hydrophilic Wells-Dawson POM and two hydrophobic C_{11} carbon chains with terminal thiol groups. This type of amphiphile, which consist of two hydrophilic terminal components linked by a hydrophobic segment

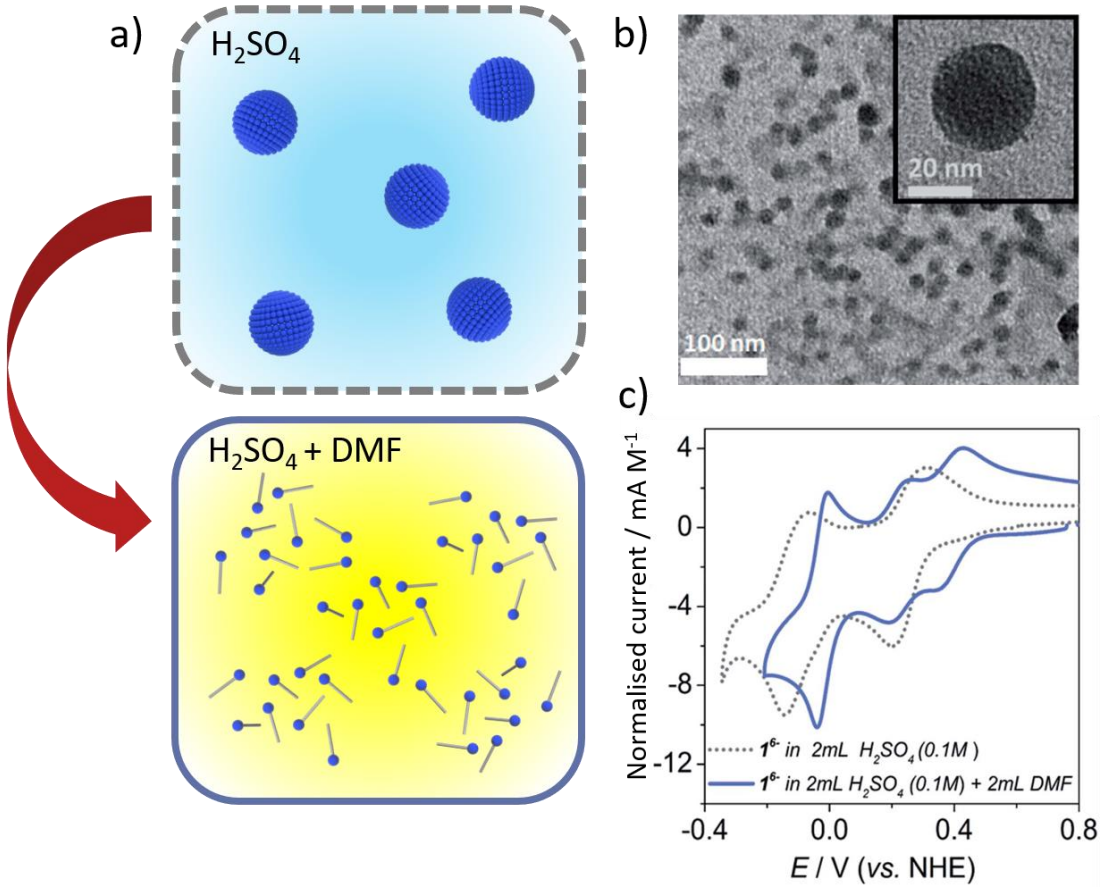

Figure 29 - a) A schematic illustrating the presence of assemblies in aqueous solutions followed by the disassembly into individual molecules with the addition of DMF; b) TEM images of micelles assembled from hybrid-POM in water after rapid heating to 70-80 °C; c) cyclic voltammogram of 1.4 mM hybrid-POM in 0.1 M H_2SO_4 showing two broad redox processes associated with the supramolecular aggregates (grey) and three associated with the molecular state post addition of DMF (blue). Reproduced from ref.9 with permission from the Royal Society of Chemistry.

is classed as a *bolaform* amphiphile (or *bolaform* surfactant) and are known to form larger vesicle structures.[10, 11] In this investigation, the author reports that this molecule displayed excellent molecular solubility in DMF, however, required rapid heating to solubilise the amphiphile in aqueous solutions where DLS analysis revealed the presence of micelles (D_h = 9 nm). The electrochemical behaviour of the hybrid was initially studied in DMF (0.1 M [TBA][PF_6] supporting electrolyte) which displayed 3 redox processes, where a + 400 mV shift in the first redox process compared to the parent anion $K_6[P_2W_{18}O_{62}]$(**{W_{18}}**) was observed. This redox potential shift is attributed to the electron-withdrawing nature of the phosphonate linker, which in effect lowers the LUMO energy level.[12, 13] The electrochemical profile of the assembly was probed by dissolution of the hybrid in 0.1 M H_2SO_4 with

the aid of rapid heating, resulting in the formation of assemblies (D_h = 9 nm) observed through DLS analysis. This solution was then electrochemically probed, displaying two redox processes centred at $E_{1/2}$ = - 0.11 V and $E_{1/2}$ = 0.26 V (*vs.* NHE), each ascribed to two electron processes which were characterised by bulk electrolysis and spectroelectrochemical analysis. Developing upon this observation, DMF was added to the solution to disassemble the vesicles. CV of the resulting solution showed two redox processes at $E_{1/2}$ = 0.39 V and $E_{1/2}$ = 0.23 V (*vs*. NHE) replaced the one broad redox process previously situated at $E_{1/2}$ = 0.26 V. The coalescing of the first two redox process (which are typical of the molecular electrochemical profile), to one process in a supramolecular assembly is speculated to be a result of intermolecular cooperation or coulombic repulsion between the POM headgroups. Furthermore, DLS analysis was conducted on the reduced and reoxidised assemblies which resulted in no significant size change, indicating that these redox-active assemblies are electrochemically stable. This investigation presents the first example of micelle redox-activity assembled from hybrid-POM molecules, demonstrating greater understanding of the property transfer from molecular to supramolecular domains.

Although the POM component of hybrid-POM surfactants can store charge, the large amphiphilic component is redox-inactive. Understanding this, Polarz and co-workers set out to construct a fully conjugated POM-hybrid surfactant, capable of storing charge on its hydrophobic moiety, which would then render the resulting supramolecular micelles better candidates for potential energy storage applications.[4] This was achieved by grafting redox-active organic molecule, anthraquinone (AQ), to a Keggin POM $[PW_{11}O_{39}]^{7-}$ *via* a π-conjugated chain and siloxane linkers, affording AQπPOM, with the aim to allow electron transfer through the ligand to the quinone. At 0.01 gL^{-1} concentration, micelles were observed with D_h = 8.7 nm in aqueous solutions. The electrochemical behaviour of the AQπPOM micelles display reduction of the POM and core AQ (Figure 30). This supramolecular electron storage characteristic is a fascinating concept with wide scope opportunities to create nanoscale micellar battery materials.

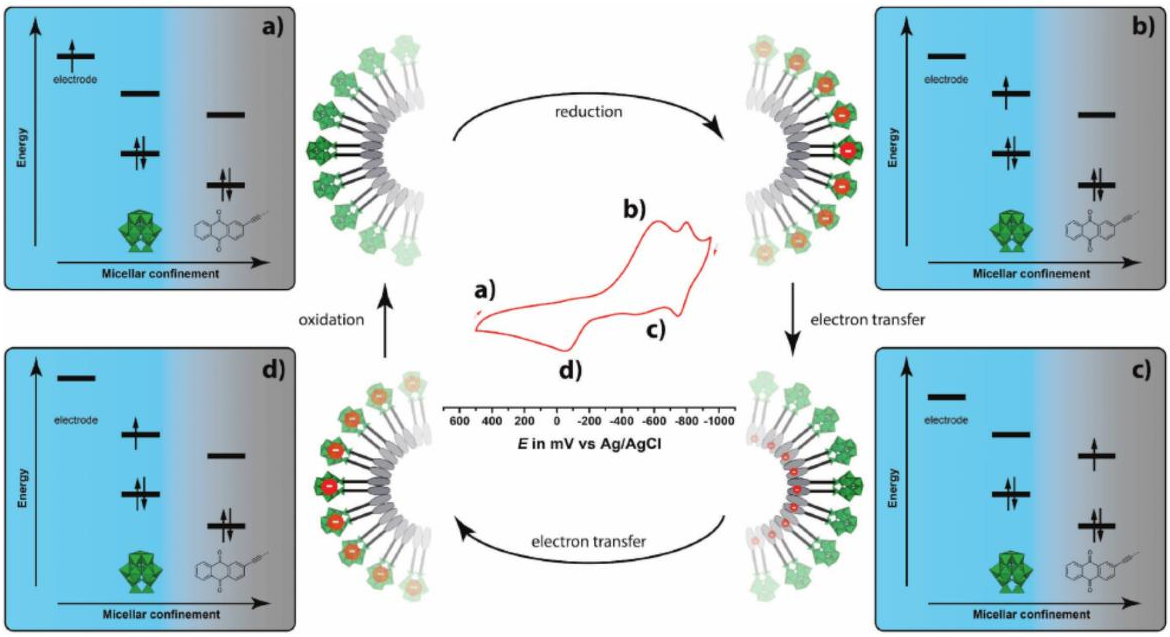

Figure 30 - Redox mechanism for AQπPOM: a) AQπPOM micelles in aqueous solution; b) Reduction of the accessible POM cluster; c) Transfer of the electron to the anthraquinone unit *via* the conjugated linker; d) Reoxidation originates from anthraquinone residue. Reproduced from ref.4 with permission from the John Wiley and Sons.

It is understood that the size of the hydrophobic component plays a significant role in the assembly dynamics of amphiphiles. The likes of Polarz *et al.* and Cronin *et al.* have previously reported investigations on the effects of chain length on the supramolecular assemblies of hybrid-POM amphiphiles.[1, 14] Although we have a greater understanding on the effects of amphiphile structure on the supramolecular assembly morphology, little is known regarding the effects of the amphiphile hydrophobic chain length on the electronic properties of the hybrid-POM assemblies.

2.2 AIMS

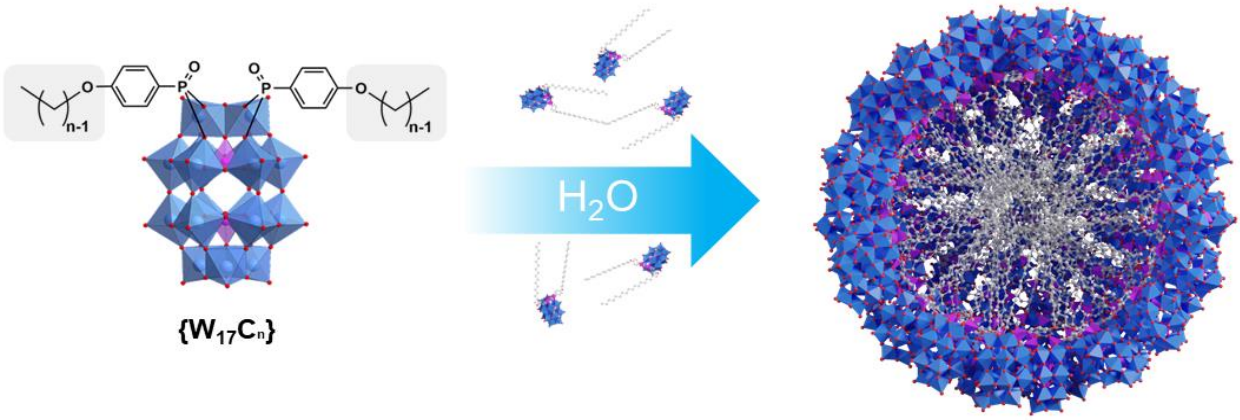

Figure 31 - A schematic illustration of solvent dependent supramolecular assembly of **{$W_{17}C_n$}** into a micelle, where hydrophobic carbon chains are located on the inside of the micelle and POM on the outer shell. C_n represents the number of carbon atoms in the aliphatic segment of the molecule (n = 10, 12, 14, 16, 18 and 20). Molecule colour code: blue polyhedra = {WO_6}, purple polyhedra = {PO_4} or {PO_3C}, red spheres = O; Micelle colour code: blue ball = POM, grey stick = carbon chain.

Many examples of hybrid-POM amphiphiles exist in the literature, however, only a handful possess the ability to self-assemble in purely aqueous systems and few investigations probe the electronic properties of the supramolecular assembly.[15, 16] In this chapter, our aim was to develop the synthesis of a novel hybrid-POM amphiphile and gain a better understanding of the contrasting properties exhibited between the molecular hybrid-POM and the supramolecular nanostructures it forms in solution. This was investigated by probing the properties of the micelles formed when the hybrid-POM was dissolved in aqueous solution (Figure 31), which were assembled from a library of structurally modified POM molecules with varying chain lengths.

2.3 RESULTS AND DISCUSSION

2.3.1 Synthesis

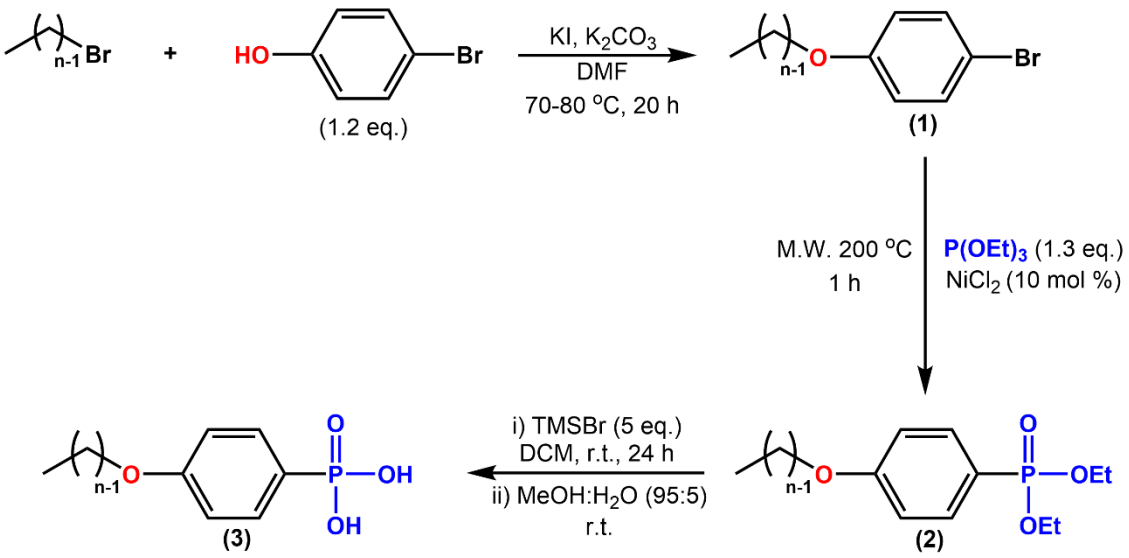

Figure 32 - Synthetic scheme for the fabrication of the adopted hydrophobic ligand moiety.

The synthesis methodology of our chosen surfactant moiety was adopted and modified from a previously reported *bolaform* hybrid surfactant example by Kastner *et al.,* where the structure possessed a terminal thiol at the end of a 11-carbon chain (C_{11}).[9] Similarly, 4-bromophenol was employed to join both hydrophobic alkyl chain and phosphonic acid linker group for hybridising to the POM (Figure 32). Step 1 involved the alkylation of phenol *via* the -OH group, K_2CO_3 was employed as a base which deprotonated the phenol.[17] The alkyl-bromide simultaneously underwent a Finklestein reaction in the presence of KI where the bromide was exchanged for an iodide, generating a better leaving group,[18] which was subsequently attacked by the phenolate nucleophile *via* an S_N2 mechanism to produce the desired bromo-alkoxybenzene **1**. Once we had synthesised the hydrophobic component, a phosphonic acid group was employed as the linker moiety to generate a phosphonic acid surfactant molecule.

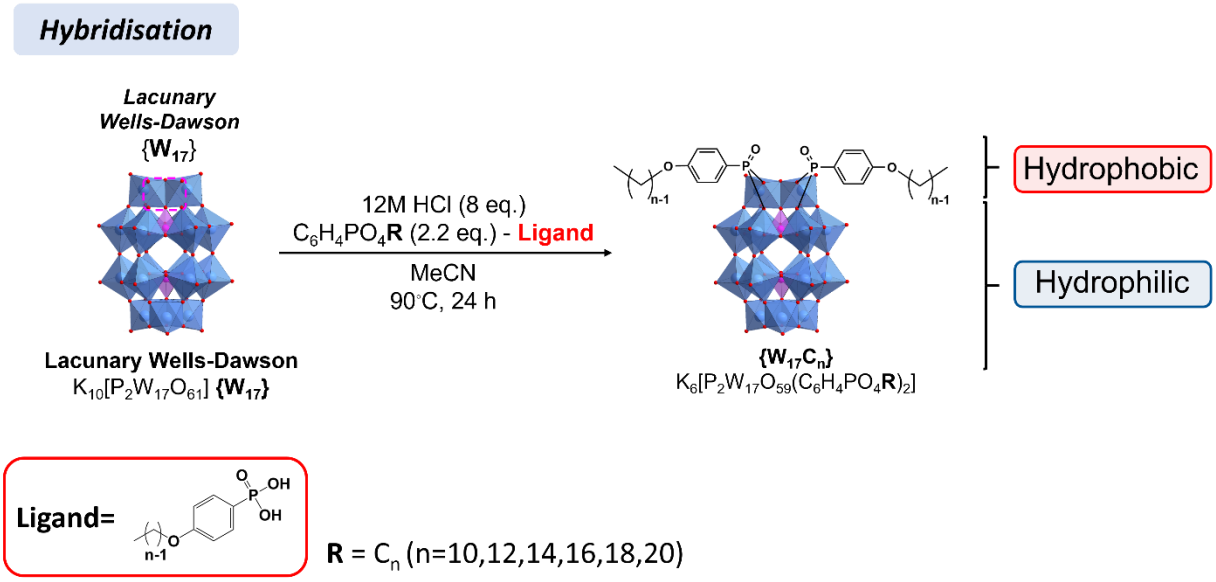

Figure 33 - Hybridisation scheme illustrating the synthesis of the desire hybrid-POM surfactant.

Phosphonate ester **2** (Figure 32) was prepared by **1** undergoing a Michaelis-Arbuzov reaction with triethylphosphite in the presence of a catalytic amount of $NiCl_2$ (10 mol%) at 200 °C in a microwave reactor.[19] **2** was then converted to the desired phosphonic acid ligand **3** by reacting with trimethylbromosilane (TMSBr) overnight, followed stirring in a mixture of MeOH:H_2O to hydrolysed the TMS groups (Figure 32).

As previously mentioned in (Chapter 1.3.5), POMs can be converted to lacunary structures through pH-controlled hydrolysis, which exposes reactive binding sites primed for hybridisation.[20] Our model system incorporated a Wells-Dawson cluster where the lacunary molecule $K_{10}[P_2W_{17}O_{61}]$(**{W_{17}}**) was achieved through controlled hydrolysis from parent anion $K_6[P_2W_{18}O_{62}]$(**{W_{18}}**).[21] Finally, the hydrophobic aliphatic phosphonic acid chain and the polar hydrophilic POM cluster were hybridised through a condensation reaction in the presence of a small equivalent of acid, generating hybrid POM surfactant $K_6[P_2W_{17}O_{61}(PO_2C_6H_4(C_nH_{2n+1})_2]$(**{$W_{17}C_n$}**) (Figure 33). The conditions for this reaction were initially adopted from a previous report based on a similar system by Newton *et al.*(Figure 29).[9] Here, the hybridisation reaction was conducted in the presence of a large excess of HCl in DMA at 75 °C for 3 days, resulting in a yield of 34 %. The product was not readily soluble in aqueous solution and was

only solubilised with the aid of rapid heating, where assemblies were reported by DLS. This observation is unusual as the product is expected to be an acid salt of the hybrid with 6 H^+ and 4 DMA molecules coordinated,[9] which should exhibit high solubility in aqueous solutions. It is possible that the cations are wrongly assumed and could in fact be the dimethylammonium cations resulting from acid catalysed amide hydrolysis of DMA.[18] The presence of these cations could be the reason behind the poor solubility without additional heat. To optimise the reaction conditions, the DMA solvent was exchanged for MeCN which eliminated the possibility of adventitious cations forming in the reaction mixture. Furthermore, organic phosphonates are capable of acid-catalysed hydrolysis which may have contributed to the low yield (34 %).[22] Therefore, the quantity of acid was significantly reduced to 8 equivalents and the reaction time was reduced from 3 days to 1 day to reduce the chance of degradation during the reaction. To mitigate the lower reaction time, the temperature was raised from 75 ^oC to 90 ^oC to increase the reaction rate. By optimising the conditions, the reaction yield increased from 34 % to 70-80 % across the range of the synthesised surfactants. Additionally, all hybrid surfactants were isolated as potassium salts and displayed high solubility in aqueous solutions.

2.3.2 Structural Characterisation

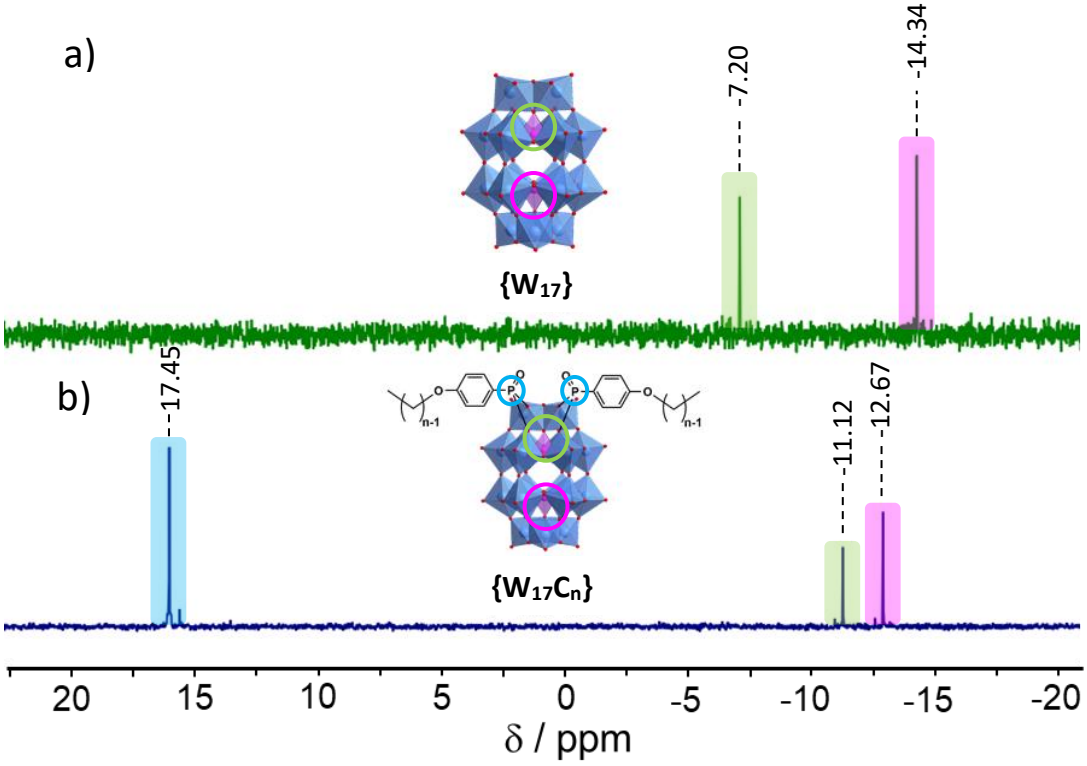

Figure 34 -^{31}P NMR overlay stack of a) $\{W_{17}\}$ in D_2O (green), and hybrid-POM amphiphile b) $\{W_{17}C_{20}\}$ (blue) in d_3-MeCN, highlighting the shifts associated with P environments of the POM.

All hybrids were synthesised and characterised however, for the duration of this and the following chapter, we will be focussing on **$\{W_{17}C_{20}\}$**. ^{31}P NMR proved to be a useful tool in characterising the components of the hybrids due to the presence of unique phosphorus environments, which are either in the POM core as inorganic phosphates or on the phosphonic acid linker present on the linker. Due to the electronic nature of the POM, we can track the success of the hybridisation with ^{31}P NMR. Here, we will be discussing the characterisation of **$\{W_{17}C_{20}\}$** which is representative of the library of synthesised hybrids, data regarding the other hybrid-POMs can be found in the experimental section at the end of the chapter. Figure 34a & b displays the ^{31}P NMR spectrum of **$\{W_{17}\}$** and **$\{W_{17}C_{20}\}$** respectively. Interestingly, we observe a shift in the internal P environments of the POM upon hybridisation with phosphonic acid ligands. The top phosphate (Figure 34b - green) exhibits a downfield shift compared to the bottom phosphate (Figure 34b - pink) due to the absence of a

tungsten fragment electron density, whereas the bottom phosphate feels greater shielding due to a larger number of [WO_6] fragments present in its surrounding environment.[23] Following hybridisation, the upper phosphate (pink) is surrounded by electron density introduced by the phosphonic acid ligands, causing the original peak to shift upfield from -7.20 ppm to -11.12 ppm. The bottom phosphate (Figure 34b - green) exhibits an opposite downfield shift from -14.37 ppm to -12.67 ppm due to an overall electron-withdrawing effect imposed by the phosphonic acid ligand, leading to electron density shifting towards the upper region of the POM.

Mass-spectrometry was also employed to confirm the nature of the products. Figure 35 displays the mass spectra which highlights the two main species, **{$W_{17}C_{20}$}**$^{2-}$ detected between 2504.28 and 2553.22 m/z, and **{$W_{17}C_{20}$}**$^{3-}$ detected between 1681.81 and 1689.14 m/z. The peak max of the centroid at m/z = 2542.23 corresponds to the doubly charged {$H_2K_2[P_2W_{17}O_{61}(PO_2C_{26}H_{45})_2]$}. Table 1 notes the m/z peaks with their corresponding molecular formula, where various cationic pairings have been detected and assigned.

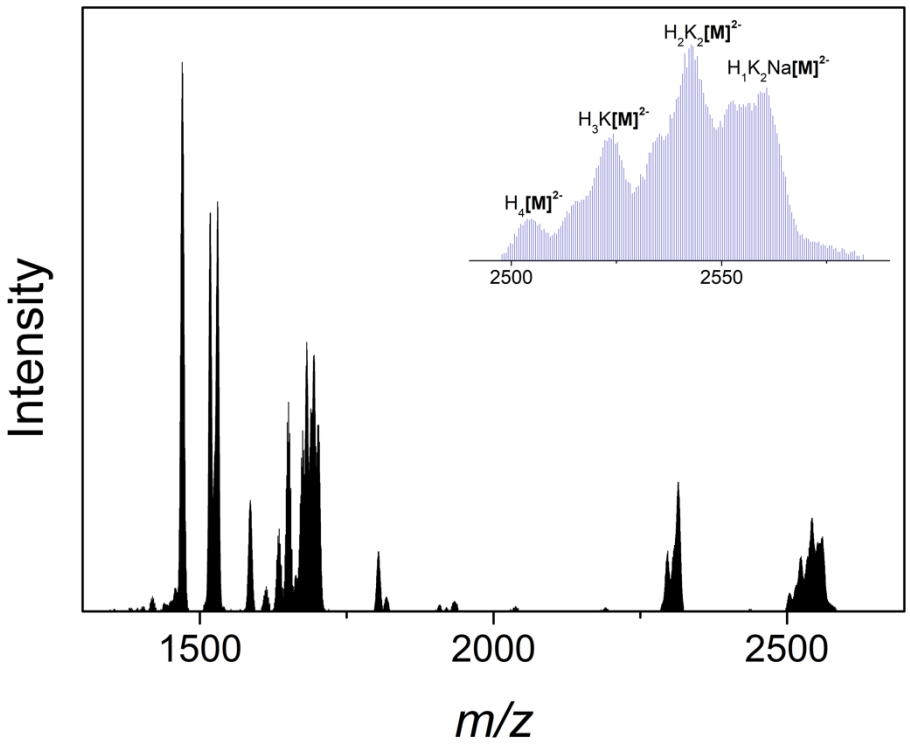

Figure 35 - ESI-MS spectra of {$W_{17}C_{20}$}.

Assignment	z	m/z (calc.)	m/z (obs.)
$\{H_4[P_2W_{17}O_{61}(PO_2C_{26}H_{45})_2]\}$	2-	2504.20	2504.28
$\{H_3Na[P_2W_{17}O_{61}(PO_2C_{26}H_{45})_2]\}$	2-	2515.19	2515.26
$\{H_3K[P_2W_{17}O_{61}(PO_2C_{26}H_{45})_2]\}$	2-	2523.17	2523.25
$\{H_2KNa[P_2W_{17}O_{61}(PO_2C_{26}H_{45})_2]\}$	2-	2534.17	2534.24
$\{H_2K_2[P_2W_{17}O_{61}(PO_2C_{26}H_{45})_2]\}$	2-	2542.15	2542.23
$\{HK_2Na[P_2W_{17}O_{61}(PO_2C_{26}H_{45})_2]\}$	2-	2553.14	2553.22
$\{H_2K[P_2W_{17}O_{61}(PO_2C_{26}H_{45})_2]\}$	3-	1681.78	1681.81
$\{[P_2W_{17}O_{61}(PO_2C_{26}H_{45})_2]\}$	3-	1689.11	1689.14

Table 1 - ESI-MS peak assignments corresponding to different cationic pairing of $\{W_{17}C_{20}\}$.

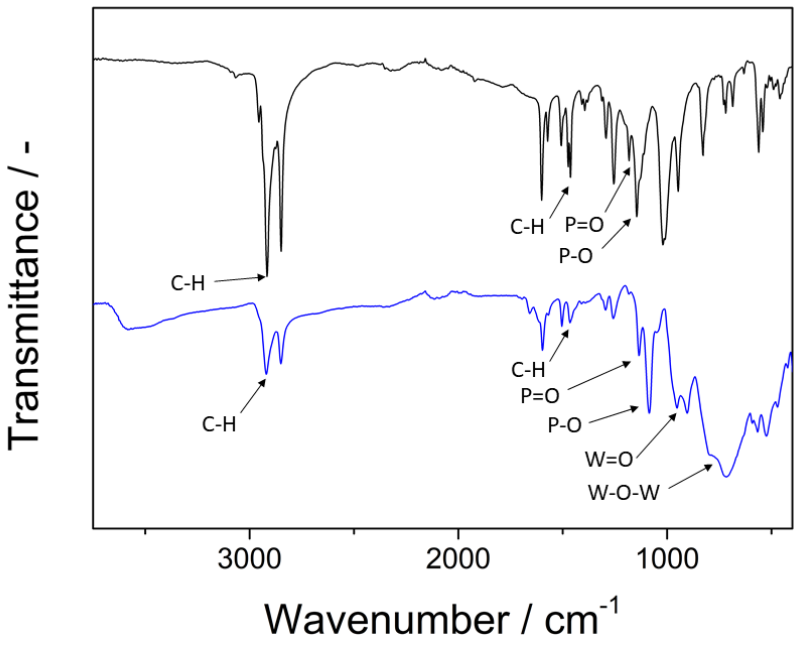

Figure 36 - An FT-IR ATR-spectrum of C_{20} ligand (black) overlayed with $\{W_{17}C_{20}\}$ (blue).

To further characterise the new hybrid molecules, infrared spectroscopy was employed (Figure 36). Firstly, the peaks observed at 2849 cm^{-1} and 2916 cm^{-1} were assigned to the C-H symmetric and antisymmetric stretching modes respectively, which have contribution from C-H bond both present on the ligands aromatic ring and the C_{20} aliphatic chain. The peak identified at 1465 cm^{-1} is also of bending mode of C-H bonds. Further into the fingerprint region, POM and linker specific bands can be found. The P-O and P=O stetch associated with the linker and POM phosphate is observed at 1048 cm^{-}

[1] and 1134 cm^{-1} respectively. The W-O-W bending mode of the bridging oxygens can be found as a broad band between 600-870 cm^{-1} and the W=O stretching modes are assigned to the bands at 905 cm^{-1} and 952 cm^{-1}.

2.3.3 Electronic Characterisation

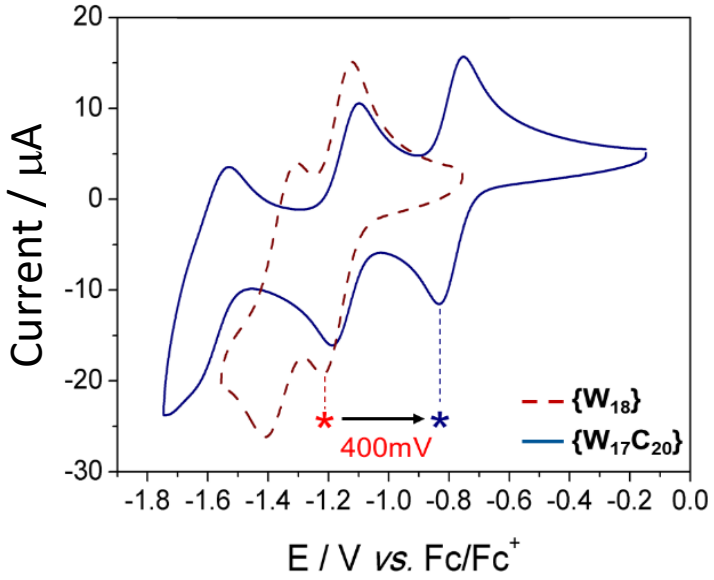

Figure 37 - CV of 1.4 mM $\{W_{17}C_{20}\}$ (blue) and $\{W_{18}\}$ (red) in DMF with 0.1 M [TBA][PF_6] as the supporting electrolyte.

Given the multi redox-active properties of the POM head group, we were interested to probe the electrochemical behaviour of the molecular **$\{W_{17}C_n\}$** amphiphilic hybrids and how this might be affected by their assembly into larger supramolecular structures. As a representative species, cyclic voltammetry (CV) of **$\{W_{17}C_{20}\}$** was first analysed in DMF (thus preserving its molecular character) at a concentration of 1.4 mM using 0.1 M tetrabutylammonium hexafluorophosphate ([TBA][PF_6]) as the supporting electrolyte (Figure 37). In each case, three well-defined pseudo-reversible redox waves were observed ($E_{1/2}$ = - 0.793 V, - 1.431 V and - 1.616 V) in the potential range - 0.5 to - 1.8 V *vs*. Fc/Fc^+, in close agreement to our previous studies on related systems. A positive shift of 375 mV is also observed in the first reduction potential of **$\{W_{17}C_{20}\}$** when compared to the parent polyoxoanion, $K_6[P_2W_{18}O_{62}]$ **$\{W_{18}\}$**($E_{1/2}$ = - 1.168 V and - 1.36 V); a known consequence of the electron-withdrawing

effect induced by inclusion of the phosphonate groups on the metal oxide core.[24] UV-vis spectroscopy was also employed to probe the absorption properties for the hybrid-POMs. POMs as a whole exhibit strong and broad UV absorption bands which are associated with ligand to metal charge transfer (LMCT) O→W,[25, 26] and we assume that any ligand mediated electronic effects post hybridisation should be visible in the absorption profile, however, this is not the case when comparing **{$W_{17}C_{20}$}** to its parent anion **{W_{18}}** (see appendix Figure S1), no major differences are observed in the absorption profile. This observation is speculated by Fujimoto *et al.* to be due to complex optical behaviour as observed from its broad LMCT UV-bands.[12, 27]

2.4 REDOX-ACTIVE MICELLES

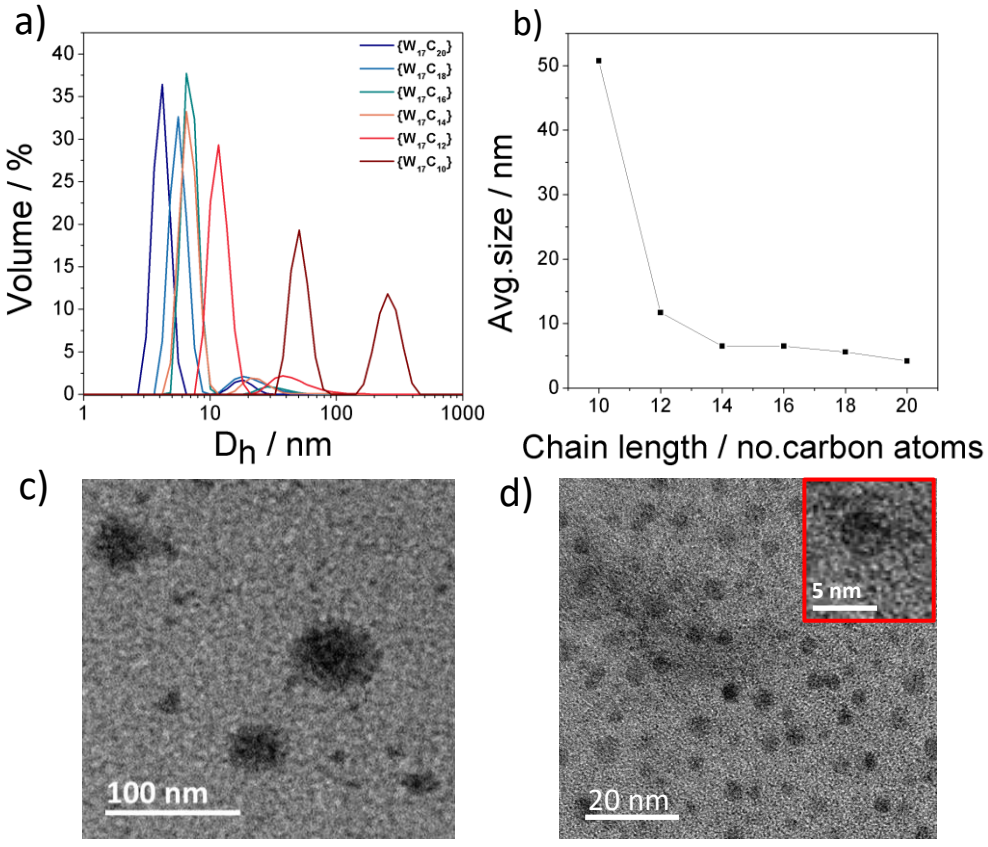

Figure 38 - a) Particle size analysis measured by DLS of 1.4 mM micelle solutions; b) average size *vs.* chain length plot extrapolated from a) TEM images formed by 1 mM solution of c) **{$W_{17}C_{18}$}** and d) **{$W_{17}C_{18}$}**; Colour code for **{$W_{17}C_n$}**: n = 10 (brown), 12 (red), 14 (orange), 16 (green), 18 (blue), 20 (marine blue).

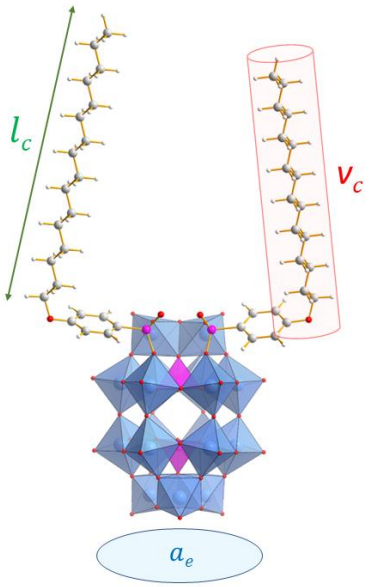

$$N_s = \frac{v_c}{a_e l_c}$$

l_c= 1.54 + 1.265n Å (1)

v_c = 27.4 + 26.9n Å^3 (2)

Figure 39 - A diagram illustrating the calculation of the packing parameter *P* using the Tanford equations to calculate length (l_c) and volume (v_c) of the hydrophobic chain.

As expected from their amphiphilic structures, all **{$W_{17}C_n$}** hybrid surfactants were found to display rapid supramolecular assembly into nanoscopic micellar species when dissolved in H_2O (e.g. 1.4 mM at r.t.), as confirmed *via* dynamic light scattering (DLS) (Figure 38A) and transmission electron microscopy (TEM) (Figure 38 c & d). Note that no evidence for supramolecular assembly was observed by DLS when the hybrid surfactants were prepared in DMF solutions, which fully solubilise the POM hybrids. DLS measurements of each **{$W_{17}C_n$}** species was used to probe the formation of these nano-sized assemblies, where the hydrodynamic diameter (D_h) was found to decrease on moving from **{$W_{17}C_{10}$}** to **{$W_{17}C_{20}$}** (Figure 38B). Furthermore, assemblies formed by **{$W_{17}C_{10}$}** were found to be polydisperse, with two distinct signals corresponding to structures in the range of 20-50 and 150-500 nm. This indicates relatively poor solution stability in assemblies formed by **{$W_{17}C_{10}$}**, which is further corroborated by TEM analysis in the solid state (Figure 38C).

As the surfactant chain length is increased, there is a clear decrease in both the polydispersity and the size of the micelles, where the D ranges from 8-12 nm in **{$W_{17}C_{12}$}** to 3-7 nm in **{$W_{17}C_{20}$}**. Note, that some larger aggregates in the region of 10-100 nm (where shorter chain lengths tend towards larger species) were also observed for **{$W_{17}C_{12\text{-}20}$}** when measurements were performed on solutions with

concentrations above 1 mM (i.e. 1.4 mM in the case of Figure 38a). In more dilute solutions, a single peak corresponding to the discrete micelle (ranging from 4-12 nm) is typically observed, which suggests that these unknown larger species may be the result of the agglomeration of individual micelles. Additional TEM analysis on drop-cast from aqueous solution on graphene-oxide (GO) shows well-formed spherical particles of the correct size in each case (Figure 38c and d), where larger species (i.e. > 10 nm) are not observed. These results suggest that a chain length of C_{10} is the approximate threshold for stability in these hybrid micellar structures and that longer chain lengths tend to lead to tighter, more stable packing structures. This can be ascribed to the greater impact of the hydrophobic effect in these species,[28, 29] though the unusually high angle (ca. 180°) between the two hydrophobic 'arms' imposed by the structure should be noted as this may negatively affect the stability of the shorter chain species.

The shape of a surfactant can be described by its theoretical packing parameter (P = v/al, where, a is the equilibrium area per molecule, *v* is the hydrophobic tail volume and l is the hydrophobic tail length) which correlates to a predicted assembly morphology in aqueous solutions (Figure 39).[30-33] The estimation suggests that when P < 0.33 the surfactant tends to assemble into spherical micelles, when 0.33 ≤ P < 0.5 the surfactants assemble into cylindrical micelles and when P ≥ 0.5 bilayer aggregates are favoured. We applied this parameter to understand whether our system behaves as a traditional surfactant would. Here we calculated the surfactant tail length (l_c) and tail volume (v_c) using equations 1 and 2 (Figure 39), which gave us 26.84 Å and 1130.83 $Å^3$ respectively. The equilibrium area (a_e) of the hydrophilic headgroup was calculated by measuring the cross-sectional spherical area based on the Van der Waals radius of the POM which gave us 139.77 Å, this value is in close proximity to reported a_e for double-chained Wells-Dawson siloxane amphiphile (124.3 Å) by Errington *et al*.[34] Finally, equating all the parameters, we obtained a packing parameter of P = 0.30 which indicates that **{$W_{17}C_{20}$}** should assemble into spherical micelles, this estimation corroborates well with the experimental data where spherical micelles (D_h = 6 nm) were observed in an aqueous solution. However, it must be noted that this value is extremely close to the P value expected for the

aggregation into cylindrical micelles, therefore, small changes in the surfactant environment may lead to a transition from spherical micelles to cylindrical micelles. Furthermore, the cations can play a large role in the assembly structure and charge neutralisation which will be discuss further in the next chapter.[35]

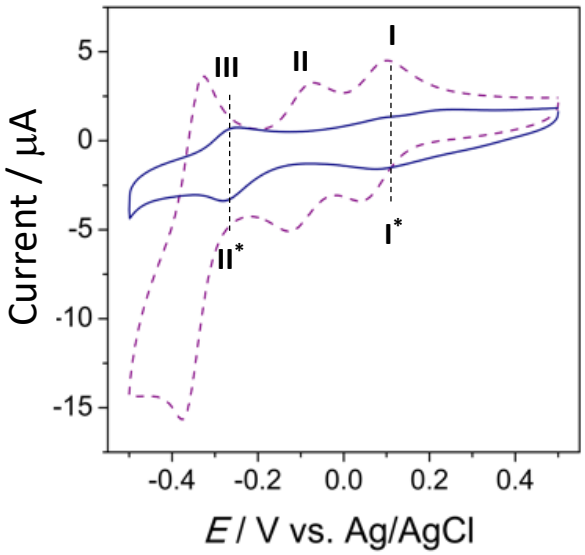

Figure 40 - CV of **{$W_{17}C_{20}$}** in 0.1 M H_2SO_4 (i.e., micellar form; blue line), and upon addition of 2 mL DMF (i.e. molecular form, purple dashed line) *vs*. Ag/AgCl.

Building on this observation, CV experiments were performed on each **{$W_{17}C_n$}** species to elucidate differences in the electrochemical properties of the micellar assemblies in response to the structural modification of the molecular surfactant. Figure 40 shows the voltammogram of **{$W_{17}C_{20}$}** when measured in 0.1 M H_2SO_4 with the corresponding redox potentials listed in Table 2. Two distinct redox processes are observed for the micellar species: an ill-defined process at more positive potential (**I***, $E_{1/2}$ = 0.089 V *vs.* Ag/AgCl) and a well-defined, highly reversible wave at more negative potential (**II***, $E_{1/2}$ = -0.265 V), which are both ascribed to $2e^-$ redox processes. Though process **I*** is not sufficiently well-resolved to analyse in detail, the ΔE_p value for **II*** of 29 mV is highly characteristic of a reversible

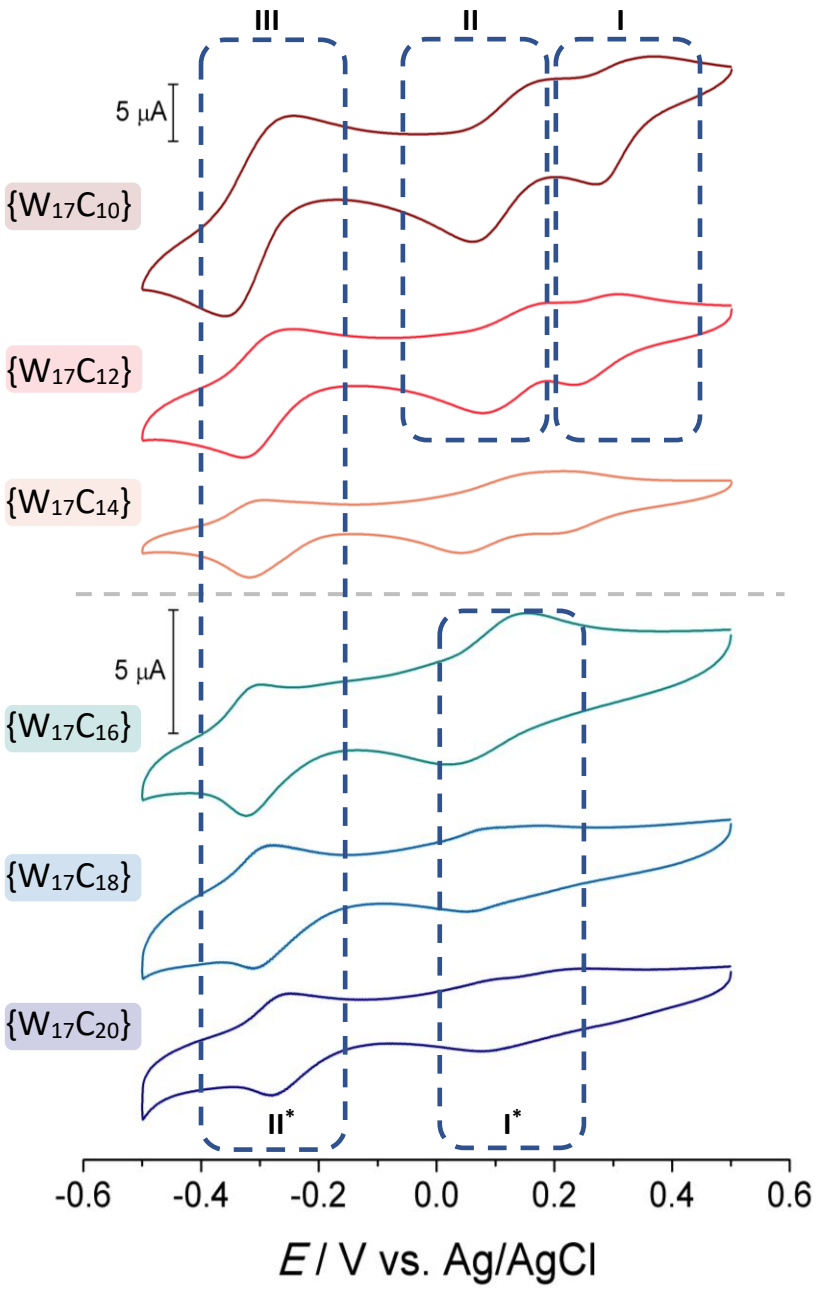

Figure 41 - CVs of supramolecular assemblies based on 1.4 mM $\{W_{17}C_{10\text{-}20}\}$ in (0.1 M) H_2SO_4 at 100 mVs^{-1}.

$2e^-$ process (*i.e.* 59 mV/n, where n = no. of electrons). We also demonstrate the reversibility of this effect by the addition of 2 mL DMF to an equivalent volume of the aqueous **$\{W_{17}C_{20}\}$** CV solution (Figure 39 & Table 2), leading to the rapid *in-situ* disassembly of the micellar structures (as confirmed by DLS). This alters the redox behaviour of the system, and three distinct processes can now be observed ($E_{1/2}$ = 0.070 V (**I**), - 0.027 V (**II**) and - 0.353 V (**III**)) corresponding closely to the

	$E_{1/2}$ / V *vs*. Ag/AgCl					
	0.1 M H_2SO_4			0.1M H_2SO_4 + 2 mL DMF		
	I/I*	**II/II***	**III**	**I**	**II**	**III**
{$W_{17}C_{10}$}	0.319	0.112	-0.301	0.057	-0.137	-0.382
{$W_{17}C_{12}$}	0.270	0.124	-0.294	0.056	-0.135	-0.376
{$W_{17}C_{14}$}	(-)†	0.129	-0.304	0.053	-0.139	-0.387
{$W_{17}C_{16}$}	0.0863	-0.311	-	0.021	-0.159	-0.402
{$W_{17}C_{18}$}	0.0697 (0.116)‡	-0.294	-	0.023	-0.141	-0.379
{$W_{17}C_{20}$}	0.0889 (0.157)§	-0.265	-	0.070	-0.0266	-0.353
† $E_{1/2}$ value for the first reduction process was difficult to assign as a reliable corresponding oxidation process was not observed. **‡** & **§** Are $E_{1/2}$ values that are calculated from resolved irreversible oxidations observed in the CVs at more positive potentials.						

Table 2 - CV $E_{1/2}$ values of micelles in 0.1 M H_2SO_4 and micelles in 0.1 M H_2SO_4 + DMF.

electrochemical behaviour of the molecular hybrid species in neat DMF. This can be attributed to the deconvolution of process **I*** into two new 1e$^-$ waves (**I** and **II**), whilst **III** corresponds closely to the micellar redox process **II*** (note that the addition of less polar solvent to the aqueous solution is expected to lead to a negative shift in potential). The coalescing of the first two redox processes when the hybrid surfactant is assembled into micelles agrees with our previous studies and is loosely attributed to increased coulombic repulsion or intramolecular cooperation between the neighbouring POM head groups.

On further comparison of the electrochemical behaviour of the **{$W_{17}C_n$}** nanostructures, several clear trends can be observed (Figure 41). Hybrid assemblies with chain lengths of ≥ 16 carbon atoms typically conform to redox behaviours strongly associated with micellar species, showing two distinct redox processes (**I*** and **II***), as in the case of **{$W_{17}C_{20}$}** described in detail above. As the chain length decreases from 20 to 16, $E_{1/2}$ of couple **II*** shifts negatively, from - 0.265 V for **{$W_{17}C_{20}$}** to - 0.311 V for

{$W_{17}C_{16}$}, while process I* becomes increasingly well-defined. At a chain length of 14, molecular electrochemistry emerges, and three reduction and two oxidation processes are observed. Below this threshold, several phenomena are observed: (i) splitting of process **I*** into redox waves **I** and **II** becomes increasingly apparent, (ii) process **I** shifts increasingly positive (compared to **I***), due to decreasing coulombic repulsion between POMs, and (iii) peak currents increase with decreasing chain length, consistent with the existence of a greater concentration of smaller, freely diffusing, molecular species within the solution. This electrochemistry is similar to that observed in mixed H_2O/DMF, suggesting that the **{$W_{17}C_{10}$}** and **{$W_{17}C_{12}$}** systems retain significant molecular character in aqueous acid. We note that DLS analysis of all aqueous voltammetry solutions shows signals corresponding to 6-10 nm micelles (see appendix Figure S2). That the electrochemistry of the shorter chain species is predominantly molecular suggests that both free POMs and micelles exist in these solutions. Finally, we notice a reduction in the Faradaic current of the redox profile when increasing chain length/ decreasing micelle size and closing peak-to-peak separation for the redox process II, which indicates potential surface confined electrochemistry or slower diffusion of micelles to the electrode. This will be further explored in the following chapter.

2.5 CONCLUSION

The development of organo-functionalised hybrid POM species has brought about opportunities to tune the physio-chemical properties of the metal oxide clusters, leading to synergistic effects brought through the coupling of inorganic and organic components. Not only can the electronic properties of the clusters be tuned, the structural modification through covalent grafting of amphiphilic ligands has presented us with new supramolecular soft materials. Such materials have proved to be unique in their composition and behave as traditional amphiphiles but possess far greater photo/electrochemical properties. Although many examples exist of POMs self-assembling into superstructures,[36] few investigations have sought to understand the translation of molecular properties (e.g. discrete building blocks) into the superstructure. Specifically, the rich redox properties of the clusters lead to fundamental questions surrounding the electrochemical behaviour of the electron-rich POMs when packed in close proximity to a number of neighbouring POM headgroups.

In this chapter, we set out to understand the effects on the supramolecular assembly morphology and it's redox-activity through structural modification of double-chained redox-active hybrid POM **{$W_{17}C_n$}**. Here, we synthesised a library of hybrid-POMs with varying chain length, through the condensation reaction between 2 phosphonic acid derived aliphatic ligands and a monolacunary Wells-Dawson cluster **{W_{17}}**. These molecules were structurally characterised by MS, NMR, IR, and UV-Vis spectroscopy. The electrochemical characterisation of the molecular and their micellar assemblies was conducted through cyclic voltammetry.

In our quest to understand the fundamental relationship between the structural properties of the molecule and supramolecular assembly, we found that by increasing the chain length, the size of the assemblies decreased. C_{10} demonstrated larger and polydisperse aggregates, which can be attributed to its smaller hydrophobic contribution, whereas $C_{14\text{-}20}$ resulted in smaller tightly packed micelles. Furthermore, their stability was found to depend on the length of the hydrophobic 'tails' of the surfactants, with longer alkyl chains leading to more stable supramolecular redox species. Following

this observation, we analysed the redox behaviour of the assemblies in aqueous conditions. Here, we found that longer chain length surfactants **{$W_{17}C_{16\text{-}20}$}** with smaller assemblies, exhibited contrasting redox profiles between their redox-active supramolecular assembly (2 redox processes) and molecular state (3 redox processes). This was not observed as clearly for amphiphiles with smaller chain lengths, **{$W_{17}C_{10\text{-}14}$}**. Furthermore, we also observed some evidence of surface confined electrochemical behaviour for longer chained surfactant **{$W_{17}C_{20}$}** which will be explored further in the next chapter.

In summary, we explored the structure-property relationship between a redox-active amphiphile and its supramolecular assembly. We have reported evidence of how the surfactant not only effects the superstructure but also the electronic properties. This tuneable approach to molecular and supramolecular material fabrication provides a benchmark for the design of redox-active soft nanomaterials and will underpin future studies into the design of these systems as novel electrocatalysts, nanocapsules, and charge carriers in the next generation of energy storage technologies.

2.6 EXPERIMENTAL

All reagents were obtained from commercial sources and were used without further purification. The precursors $K_6[P_2W_{18}O_{62}]$ and $K_{10}[P_2W_{17}O_{61}]$ were prepared by reported methods.[1]

Step 1 – Alkylation

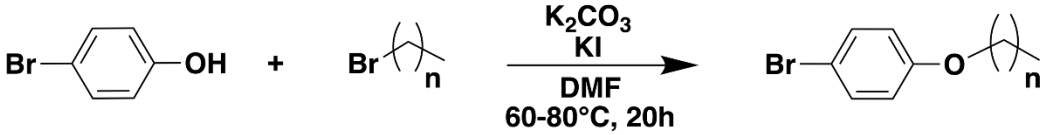

***n*= 9 (*A*), 11 (*B*), 13 (*C*), 15 (*D*), 17 (*E*) and 19 (*F*)**

The general method for the preparation of each alkylated bromophenol intermediate is as follows: The corresponding bromoalkane compound (8.54 mmol) and 4-bromophenol (10.5 mmol) were dissolved in DMF (40 mL). To this solution, KI (1.51 mmol) and K_2CO_3 (32.6 mmol) were added, the reaction mixture was then heated to T °C (see below) for 20 h. The reaction was then cooled to r.t. and the solvent was then removed *in vacuo*. The resulting solid product was dissolved in diethyl ether (100 mL) and washed with a combination of 2 M NaOH (2 x 100 mL) and brine (100 mL). The organic fraction was dried over $MgSO_4$ and the solvent was removed *in vacuo* to form an orange oil. The crude product was then recrystallized with minimal amount of hot EtOH.

Compound (1A)- 1-bromo-4-(decyloxy)benzene - $C_{16}H_{25}BrO$

Colourless oil; T= 60°C; Yield= 2.41 g (89 %); ^{1}H NMR (400 MHz, $CDCl_3$): δ= 7.38 – 7.33 (m, 2H, C**H**), 6.80 – 6.74 (m, 2H, C**H**), 3.91 (t, J = 6.6 Hz, 2H, C$\mathbf{H_2}$), 1.81 – 1.71 (m, 2H, C$\mathbf{H_2}$), 1.49 – 1.39 (m, 2H, C$\mathbf{H_2}$), 1.38 –1.19 (m, 12H, C$\mathbf{H_2}$), 0.89 (t, J = 6.9 Hz, 3H, C$\mathbf{H_3}$).

Compound (1B)- 1-bromo-4-(dodecyloxy)benzene - $C_{18}H_{29}BrO$

White solid; T=70°C; Yield: 2.46 g (69 %); ^{1}H NMR (500 MHz, $CDCl_3$) δ= 7.46 – 7.30 (m, 2H, C**H**), 6.88 – 6.63 (m, 2H, C**H**), 3.93 (t, *J* = 6.6 Hz, 2H, C$\mathbf{H_2}$), 1.79 (dt, *J* = 14.7, 6.7 Hz, 2H, C$\mathbf{H_2}$), 1.49 – 1.42 (m, 2H, C$\mathbf{H_2}$), 1.38 – 1.24 (m, 16H, C$\mathbf{H_2}$), 0.91 (t, *J* = 6.9 Hz, 3H, C$\mathbf{H_3}$).

Compound (1C)- 1-bromo-4-(tetradecyloxy)benzene - $C_{20}H_{33}BrO$

White solid; Yield:2.86 g (95 %);T=75°C;^{1}H NMR (500 MHz, $CDCl_3$) δ= 7.38 (d, *J* = 8.7 Hz, 2H, C**H**), 6.80 (d, *J* = 8.7 Hz, 2H, C**H**), 3.94 (t, *J* = 6.6 Hz, 2H, C$\mathbf{H_2}$), 1.79 (p, *J* = 6.8 Hz, 2H, C$\mathbf{H_2}$), 1.46 (q, *J* = 7.7 Hz, 2H, C$\mathbf{H_2}$), 1.39 – 1.21 (m, 20H, C$\mathbf{H_2}$), 0.92 (t, *J* = 6.8 Hz, 3H, C$\mathbf{H_3}$).

Compound (1D)- 1-bromo-4-(hexadecyloxy)benzene - $C_{22}H_{37}BrO$

White solid; Yield: 2.69 g (80 %); T=75°C; ^{1}H NMR (400 MHz, $CDCl_3$) δ= 7.45 – 7.32 (m, 2H, C**H**), 6.85 – 6.70 (m, 2H, C**H**), 3.93 (t, J = 6.6 Hz, 2H, C$\mathbf{H_2}$), 1.78 (dq, J = 8.2, 6.6 Hz, 2H, C$\mathbf{H_2}$), 1.52 – 1.42 (m, 2H, C$\mathbf{H_2}$), 1.28 (s, 26H, C$\mathbf{H_2}$), 0.96 – 0.82 (m, 3H, C$\mathbf{H_3}$).

Compound (1E)- 1-bromo-4-(octadecyloxy)benzene - $C_{24}H_{41}BrO$

White solid; Yield: 3.07g (85 %); T=80°C ^{1}H NMR (400 MHz, $CDCl_3$) δ= 7.43 – 7.32 (m, 2H, C**H**), 6.85 – 6.74 (m, 2H, C**H**), 3.93 (t, *J* = 6.6 Hz, 2H, C$\mathbf{H_2}$), 1.78 (dq, *J* = 8.1, 6.6 Hz, 2H, C$\mathbf{H_2}$), 1.46 (dq, *J* = 11.7, 6.8 Hz, 2H, C$\mathbf{H_2}$), 1.28 (s, 28H, C$\mathbf{H_2}$), 0.97 – 0.85 (m, 3H, C$\mathbf{H_3}$).

Compound (1F)- 1-bromo-4-(icosyloxy)benzene - $C_{26}H_{45}BrO$

White solid; Yield: 3.05 g (78 %); T=80°C; ^{1}H NMR (500 MHz, $CDCl_3$) δ= 7.44 – 7.33 (m, 2H, C**H**), 6.83 – 6.77 (m, 2H, C**H**), 3.93 (t, *J* = 6.6 Hz, 2H, C**H$_2$**), 1.79 (dt, *J* = 14.8, 6.7 Hz, 2H, C**H$_2$**), 1.52 – 1.41 (m, 2H, C**H$_2$**), 1.28 (s, 32H, C**H$_2$**), 0.91 (t, *J* = 6.9 Hz, 3H, C**H$_3$**).

Step 2 – Phosphorylation

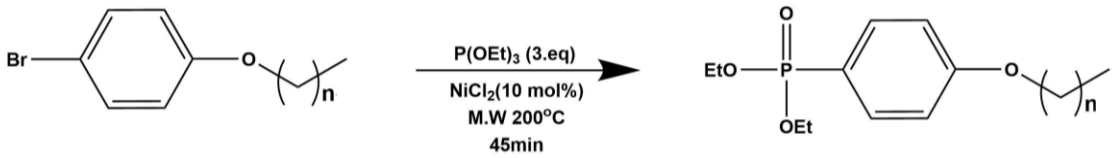

***n**= 9 (**A**), 11 (**B**), 13 (**C**), 15 (**D**), 17 (**E**) and 19 (**F**)*

To a microwave vessel, triethylphosphite (1.8 mL, 10.5 mmol) and anhydrous $NiCl_2$ (0.045 g, 0.35 mmol) was added, stirred and purged with argon for 10 mins. Dried **1(A-F)** (3.5 mmol) was added to the black mixture, heated (to dissolve) and purged with argon for a further 10 mins. The vessel was then heated in the M.W at 200 °C for 45 mins. The reaction mixture was then cooled to r.t. and dissolved in diethyl ether (100 mL). The solution was then filtered and centrifuged for 15 mins (8000 rpm). The black precipitate was filtered off and the solvent was evaporated *in vacuo* to give a yellow oil. The crude product was then dissolved in hot MeCN (60 mL) and filtered. Ethyl acetate (50 mL) was then added to the filtrate and the solvent was evaporated under vacuum.

Compound (2A) - diethyl-(4-(decyloxy)phenyl)phosphonate - $C_{20}H_{35}O_4P$

Clear/Yellow oil; Yield 0.67 g (57%); ^{1}H NMR (400 MHz, $CDCl_3$) δ 7.84 – 7.66 (m, 2H, C**H**), 7.00 – 6.89 (m, 2H, C**H**), 4.20 – 3.96 (m, 6H, C**H$_3$**), 1.81 (p, *J* = 6.7 Hz, 2H, C**H$_2$**), 1.47 (p, *J* = 7.1 Hz, 2H, C**H$_2$**), 1.39 – 1.18 (m, 18H, C**H$_2$**/C**H$_3$**), 0.95 – 0.71 (m, 3H, C**H$_3$**); ^{31}P NMR (162 MHz, $CDCl_3$) δ 19.89. ESI-MS (MeCN) *m/z* (calculated, found): $[L+H]^+$ (371.23, 371.23).

Compound (2B) - diethyl (4-(dodecyloxy)phenyl)phosphonate - $C_{22}H_{39}O_4P$

Clear/Yellow oil; Yield**:** 0.95g (68%); ^{1}H NMR (500 MHz, Chloroform-*d*) δ 7.83 – 7.64 (m, 2H, C**H**), 7.06 – 6.87 (m, 2H, C**H**), 4.24 – 3.93 (m, 6H, C**H$_2$**), 1.82 (q, *J* = 7.7, 7.2 Hz, 4H, C**H$_2$**), 1.53 – 1.22 (m, 22H, C**H$_2$**/C**H$_3$**), 0.90 (t, *J* = 6.9 Hz, 3H, C**H$_3$**). ^{31}P NMR (202 MHz, Chloroform-*d*) δ 19.90.; ESI-MS (MeCN) *m/z* (calculated, found): $[L\text{-}OEt]^-$(369.22,369.22)

Compound (2C) - diethyl (4-(tetradecyloxy)phenyl)phosphonate - $C_{24}H_{43}O_4P$

Yellow oil; Yield:0.97g (65%); ^{1}H NMR (500 MHz, Chloroform-*d*) δ 7.80 – 7.67 (m, 2H, C**H**), 7.02 – 6.92 (m, 2H, C**H**), 4.20 – 3.96 (m, 6H, C**H$_2$**), 1.86 – 1.76 (m, 2H, C**H$_2$**), 1.52 – 1.22 (m, 30H, C**H$_2$**/C**H$_3$**), 0.89 (t, *J* = 6.9 Hz, 3H, C**H$_3$**); ^{31}P NMR (202 MHz, Chloroform-d) δ 19.89; ESI-MS (MeCN) *m/z* (calculated, found): $[L+H]^+$ (427.3,427.3)

Compound (2D) - diethyl (4-(hexadecyloxy)phenyl)phosphonate- $C_{26}H_{47}O_4P$

Yellow waxy solid; Yield:1.02g (64%);^{1}H NMR (500 MHz, Chloroform-*d*) δ 7.74 (dd, *J* = 12.7, 8.4 Hz, 2H, C**H**), 6.96 (dd, *J* = 8.7, 3.4 Hz, 2H, C**H**), 4.18 – 4.00 (m, 4H, C**H$_2$**), 4.00 (t, *J* = 6.6 Hz, 2H, C**H$_2$**), 1.80 (p, *J* = 6.8 Hz, 2H, C**H$_2$**), 1.51 – 1.41 (m, 2H, C**H$_2$**), 1.32 (t, *J* = 7.0 Hz, 6H, C**H$_2$**), 1.27 (s, 24H, C**H$_2$**/C**H$_3$**) , 0.89 (t, *J* = 6.8 Hz, 3H, C**H$_3$**).^{31}P NMR (202 MHz, Chloroform-*d*) δ 19.90; ESI-MS (MeCN) *m/z* (calculated, found): $[L+H]^+$ (455.33, 455.32).

Compound (2E) - diethyl (4-(octadecyloxy)phenyl)phosphonate - $C_{28}H_{51}O_4P$

Off-white waxy solid; Yield:1.03g (61%); ^{1}H NMR (500 MHz, Chloroform-*d*) δ 7.82 – 7.63 (m, 2H, C**H**), 7.04 – 6.89 (m, 2H, C**H**), 4.29 – 3.92 (m, 6H, C**H$_2$**), 1.81 (dt, *J* = 14.0, 6.6 Hz, 2H, C**H$_2$**), 1.53 – 1.42 (m, 2H, C**H$_2$**), 1.40 – 1.17 (m, 34H, C**H$_2$**/C**H$_3$**), 0.90 (t, *J* = 6.9 Hz, 3H, C**H$_3$**). ^{31}P NMR (202 MHz, $CDCl_3$) δ 19.7. ESI-MS (MeCN) *m/z* (calculated, found):[L+ H^+](483.36, 483.36).

Compound (2F) - diethyl (4-(icosyloxy)phenyl)phosphonate - $C_{30}H_{55}O_4P$

Off-white waxy solid; Yield:1.2g (67%); ^{1}H NMR (500 MHz, Chloroform-*d*) δ 7.82 – 7.69 (m, 2H, C**H**), 7.00 – 6.92 (m, 2H, C**H**), 4.19 – 3.97 (m, 6H, C**H$_2$**), 1.95 – 1.74 (m, 4H, C**H$_2$**), 1.55 – 1.19 (m, 39H, C**H$_2$**/C**H$_3$**), 0.90 (t, *J* = 6.9 Hz, 3H, C**H$_3$**). ^{31}P NMR (202 MHz, $CDCl_3$) δ 19.90; ESI-MS (MeCN) *m/z* (calculated, found):[L+H^+](511.39, 511.38).

<u>Step 3 – Phosphonate hydrolysis</u>

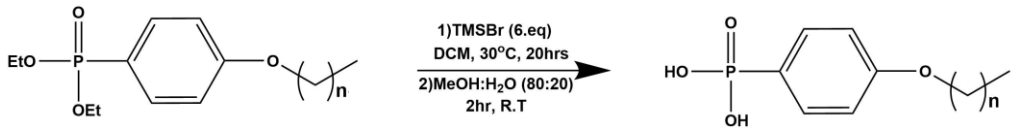

***n*= 9 (*A*), 11 (*B*), 13 (*C*), 15 (*D*), 17 (*E*) and 19 (*F*)**

Dried **2A-F** was added to a 100 mL schlenck flask. The vessel was evacuated and filled with argon. To the vessel dry CH_2Cl_2 (6 mL) was added followed by bromotrimethylsilane (TMSBr) to form a yellow/green solution. The solution was then stirred for 20 h at 30°C. Upon completion, the vessel was cooled to r.t. The solvent and excess TMSBr was removed *in vacuo* to yield a yellow oil. To the flask, 30 mL of MeOH:H_2O (80:20) was added and stirred for 2 h to form a white suspension. The mixture was then centrifuged (5 mins, 7000 rpm) and the solvent was decanted off. The resulting solid was dried under vacuum to yield a crude off-white solid.

For compound **3A,** the solid was then recrystallized from minimal amount of hot MeCN 30mL and filtered.

For compounds **3B-F** The crude product was then washed with Et_2O (2 x 25 mL). The solid was then stirred in hot MeCN (50 mL) and filtered.

NOTE that the –O**H** peaks were not present in *d*$_4$-MeOH and is expected due to the exchange of deuterium with the protons on the phosphonate.

Compound (3A) (4-(decyloxy)phenyl)phosphonic acid - Chemical Formula: $C_{16}H_{27}O_4P$

2A: 1g, 2.7 mmol; TMSBr: 1.95 ml, 14.78 mmol; White powder; Yield: 0.82 g, 96%; ^{1}H NMR (400 MHz, $(CD_3)_2CO$) δ 7.81 – 7.62 (m, 2H, C**H**), 7.01 (dd, *J* = 8.7, 3.1 Hz, 2H, C**H**), 4.07 (t, *J* = 6.5 Hz, 2H, C**H$_2$**), 1.81 (dq, *J* = 8.2, 6.6 Hz, 2H, C**H$_2$**), 1.54 – 1.42 (m, 2H, C**H$_2$**), 1.39 – 1.24 (m, 14H, C**H$_2$**), 0.97 – 0.76 (m, 3H, C**H$_3$**); ^{31}P NMR (162 MHz, DMSO-*d*$_6$) δ 13.43; IR(ATR) cm^{-1} = 447, 542, 686, 826, 942, 1012, 1140, 1255, 1294, 1474, 1504, 1599, 2852, 2918; Elemental Analysis: (calculated, found) [(C, 61.13; H, 8.66; N, 0 %), (C, 59.61; H, 8.79; N, 0.05 %)]; ESI-MS (MeCN) *m/z* (calculated, found): [L - H]$^-$ (313.16, 313.16).

Compound (3B) (4-(dodecyloxy)phenyl)phosphonic acid - Chemical Formula: $C_{18}H_{31}O_4P$

2B: 0.95g, 2.33 mmol; TMSBr: 1.84ml, 13.98; White powder; Yield: 0.72g, 90%; ^{1}H NMR (400 MHz, Methanol-*d*$_4$) δ 7.83 – 7.65 (m, 2H, C**H**), 7.01 (dd, *J* = 8.7, 3.0 Hz, 2H, C**H**), 4.04 (t, *J* = 6.4 Hz, 2H, C**H$_2$**), 1.85 – 1.74 (m, 2H, C**H$_2$**), 1.32 (s, 18H, C**H$_2$**), 0.97 – 0.87 (m, 3H, C**H$_3$**); ^{31}P NMR (162 MHz, Methanol-*d*$_4$) δ 17.14; IR(ATR) cm^{-1} = 451, 540, 686, 826, 943. 1014, 1142, 1250, 1474, 1504, 1599, 2850, 2918;

Elemental Analysis: (calculated, found) [(C, 63.14; H, 9.13; N, 0 %), (C, 62.76; H, 9.39; N, 0.07 %)]; ESI-MS (MeCN) *m/z* (calculated, found): $[L\text{-}H]^-$ (341.17,341.18).

Compound (3C) - (4-(tetradecyloxy)phenyl)phosphonic acid - Chemical Formula: $C_{20}H_{35}O_4P$

2C: 0.92g, 2.16 mmol; TMSBr: 1.7ml, 12.96; White powder; Yield: 0.74g, 92%; ^{1}H NMR (400 MHz, Methanol-d_4) δ 7.80 – 7.65 (m, 2H, C**H**), 7.08 – 6.94 (m, 2H, C**H**), 4.04 (t, *J* = 6.4 Hz, 2H, C$\mathbf{H_2}$), 1.88 – 1.75 (m, 2H, C$\mathbf{H_2}$), 1.31 (d, *J* = 2.2 Hz, 22H, C$\mathbf{H_2}$), 1.00 – 0.81 (m, 3H, C$\mathbf{H_3}$); ^{31}P NMR (162 MHz, Methanol-d_4) δ 17.18; IR(ATR) cm^{-1} = 451, 542, 686, 826, 946, 1022, 1144, 1253, 1292, 1476, 1504, 1599, 2850, 2916; Elemental Analysis: (calculated, found) [(C, 64.84; H, 9.52; N, 0 %), (C,64.91; H,9.81; N,0.06 %)]; ESI-MS (MeCN) *m/z* (calculated, found): $[L\text{-}H]^-$ (369.22,369.22).

Compound (3D) - (4-(hexadecyloxy)phenyl)phosphonic acid - Chemical Formula: $C_{22}H_{39}O_4P$

2D: 1.66 g, 3.49 mmol; TMSBr: 3 ml, 22.59 mmol; White powder; Yield: 1.17 g, 84%; ^{1}H NMR (400 MHz, Methanol-d_4) δ 7.81 – 7.65 (m, 2H, C**H**), 7.01 (dd, *J* = 8.7, 3.1 Hz, 2H, C**H**), 4.04 (t, *J* = 6.5 Hz, 2H, C$\mathbf{H_2}$), 1.81 (p, *J* = 6.6 Hz, 2H, C$\mathbf{H_2}$), 1.31 (d, *J* = 2.6 Hz, 26H, C$\mathbf{H_2}$), 0.96 – 0.88 (m, 3H, C$\mathbf{H_3}$);^{31}P NMR (162 MHz, Methanol-d_4) δ 17.23; IR(ATR) cm^{-1} = 455, 544, 688, 826, 944, 1020, 1144, 1253, 1474, 1253, 1506, 1599, 2850, 2916; Elemental Analysis: (calculated, found) [(C, 66.31; H, 9.86; N, 0 %), (C,66.37; H,10.12; N,0.08 %)]; ESI-MS (MeCN) *m/z* (calculated, found): $[L\text{-}H]^-$ (397.25, 397.25).

Compound (3E) (4-(octadecyloxy)phenyl)phosphonic acid - Chemical Formula: $C_{24}H_{43}O_4P$

2E: 1.04 g, 2.07 mmol; TMSBr: 1.95 ml, 14.78 mmol; White powder; Yield: 0.84 g, 96 %; ^{1}H NMR (500 MHz, Methanol-d_4) δ 7.80 – 7.68 (m, 2H, C**H**), 7.01 (dq, *J* = 9.3, 2.7 Hz, 2H, C**H**), 4.04 (t, *J* = 6.5 Hz, 2H, C$\mathbf{H_2}$), 1.89 – 1.74 (m, 2H, C$\mathbf{H_2}$), 1.31 (d, *J* = 4.8 Hz, 30H, C$\mathbf{H_2}$), 0.92 (t, *J* = 6.9 Hz, 3H, C$\mathbf{H_3}$);^{31}P NMR (202 MHz, Methanol-d_4) δ 17.27; IR(ATR) cm^{-1} = 449, 542, 686, 826, 946, 1020, 1142, 1255, 1463, 1506, 1599, 2850, 2918; Elemental Analysis: (calculated, found) [(C, 67.58; H, 10.16; N, 0 %), (C,67.51; H,10.49; N,0.08 %)]; ESI-MS (MeCN) *m/z* (calculated, found): $[L\text{-}H]^-$ (425.29,425.29).

Compound (3F) (4-(icosyloxy)phenyl)phosphonic acid - Chemical Formula: $C_{26}H_{47}O_4P$

2F: 0.99 g, 1.95 mmol; TMSBr: 1 ml, 7.35 mmol; White powder; Yield: 0.85 g, 96 %; ^{1}H NMR (400 MHz, Methanol-d_4) δ 7.78 – 7.66 (m, 2H, C**H**), 7.01 (dd, *J* = 8.7, 3.1 Hz, 2H, C**H**), 4.04 (t, *J* = 6.4 Hz, 2H, C$\mathbf{H_2}$), 1.81 (p, *J* = 6.6 Hz, 2H, C$\mathbf{H_2}$), 1.31 (d, *J* = 3.7 Hz, 34H, C$\mathbf{H_2}$), 0.96 – 0.86 (m, 3H, C$\mathbf{H_3}$);^{31}P NMR (162 MHz, Methanol-d_4) δ 17.27; IR(ATR) cm^{-1} = 457, 544, 684, 719, 828, 946, 1020, 1146, 1252, 1294, 1463, 1506, 1601, 2848, 2916; Elemental Analysis: (calculated, found) [(C, 68.69; H, 10.42; N, 0 %), (C,68.74; H,10.81; N,0.09 %)]; ESI-MS (MeCN) *m/z* (calculated, found): $[L\text{-}H]^-$(453.63, 453.34).

<u>Step 4 – Hybridisation</u>

3A-F (0.33 mmol) and $K_{10}W_{17}O_{61}$ (0.5 g, 0.11 mmol) were suspended in MeCN (50 mL) and 12 M HCl (0.14 mL). The reaction mixture was stirred at 90 °C for 24 h to form a yellow solution. Upon completion, the reaction was cooled to r.t. and filtered. The solvent was then evaporated *in vacuo,* resulting in an orange solid. The solid was then redissolved in cold acetone and left overnight in the fridge. The cold solution was then centrifuged at 8000 rpm for 15 mins. The yellow solution was then filtered, and the solvent removed *in vacuo* to form a dark red powder. The solid was then sonicated in Et_2O (2 x 100 mL) and decanted. The remaining solvent was removed *in vacuo*.

Compound (4A) - {$W_{17}C_{10}$} - $K_6[P_2W_{17}O_{61}(PO_2C_6H_4(C_{10}H_{21})_2]$

Red powder; Yield: 0.4g (74%); ^{1}H NMR (500 MHz, DMSO-d_6) δ 8.04 – 7.85 (m, 4H, C**H**), 6.98 (td, *J* = 8.8, 3.1 Hz, 4H, C**H**), 4.03 (t, *J* = 6.4 Hz, 4H, C$\mathbf{H_2}$), 1.74 (t, *J* = 7.3 Hz, 4H, C$\mathbf{H_2}$), 1.43 – 1.20 (m, 28H, C$\mathbf{H_2}$), 0.87 (t, *J* = 6.7 Hz, 6H, C$\mathbf{H_3}$).^{31}P NMR (202 MHz, DMSO-d_6) δ 15.94, -11.37, -13.00; IR(ATR) cm^{-1} = 525, 719, 803, 903, 954, 1084, 1136, 1251, 1504, 1597, 2850, 2920; Elemental analysis for {$W_{17}C_{10}$} in wt% (calculated): C 8.07(7.75), H 1.24 (1.02), N 0.11(0.00).

Compound (4B) - {$W_{17}C_{12}$} - $K_6[P_2W_{17}O_{61}(PO_2C_6H_4(C_{12}H_{25})_2]$

Red powder; Yield: 0.38g (70%); ^{1}H NMR (500 MHz, DMSO-d_6) δ 8.00 – 7.83 (m, 4H, **CH**), 6.98 (td, *J* = 8.9, 4.5 Hz, 4H, **CH**), 4.02 (dt, *J* = 16.8, 6.5 Hz, 4H, **CH$_2$**), 1.78 – 1.71 (m, 4H, **CH$_2$**), 1.47 – 1.20 (m, 36H, **CH$_2$**), 0.90 – 0.83 (m, 6H, **CH$_3$**).^{31}P NMR (202 MHz, DMSO-d_6) δ 15.93 (t, *J* = 13.4 Hz), -11.37, -13.00; IR(ATR) cm^{-1} = 525, 570, 717, 799, 905, 954, 1086, 1138, 1261, 1504, 1597, 1696, 2848, 2922; Elemental analysis for {$W_{17}C_{12}$} in wt% (calculated): C 8.91(8.62), H 1.24 (1.17), N 0.00(0.00).

Compound (4C) - {$W_{17}C_{14}$} - $K_6[P_2W_{17}O_{61}(PO_2C_6H_4(C_{14}H_{29})_2]$

Red powder; Yield: 0.39g (71%); ^{1}H NMR (400 MHz, DMSO-d_6) δ 8.03 – 7.84 (m, 4H, C**H**), 6.98 (dt, *J* = 10.0, 5.0 Hz, 4H, C**H**), 4.05 – 4.01 (m, 4H, C**H$_2$**), 1.73 (d, *J* = 7.5 Hz, 4H, C**H$_2$**), 1.47 – 1.22 (m, 44H, C**H$_2$**), 0.86 (t, *J* = 6.7 Hz, 6H, C**H$_3$**).^{31}P NMR (162 MHz, DMSO-d_6) δ 15.94, -11.37, -13.00; IR(ATR) cm^{-1} = 530, 570, 719, 793, 901, 955, 1086, 1136, 1261, 1506, 1599, 2854, 2916; Elemental analysis for {$W_{17}C_{14}$} in wt% (calculated): C 10.13 (9.47), H 1.44 (1.31), N 0.00(0.00).

Compound (4D) - {$W_{17}C_{16}$} - $K_6[P_2W_{17}O_{61}(PO_2C_6H_4(C_{16}H_{33})_2]$

Red powder; Yield: 0.43g (77%); ^{1}H NMR (400 MHz, DMSO-d_6) δ 7.89 (dd, *J* = 13.5, 8.5 Hz, 4H, C**H**), 6.99 (dd, *J* = 9.1, 3.1 Hz, 4H, C**H**), 4.03 (t, *J* = 6.5 Hz, 4H, C**H$_2$**), 1.73 (d, *J* = 7.4 Hz, 4H, C**H$_2$**), 1.26 (d, *J* = 6.4 Hz, 52H C**H$_2$**), 0.89 – 0.84 (m, 6H, C**H$_3$**).^{31}P NMR (162 MHz, DMSO-d_6) δ 15.93, -11.37, -13.00; IR(ATR) cm^{-1} = 528, 567, 731, 905, 954, 1086, 1138, 1255, 1597, 2852, 2918; Elemental analysis for {$W_{17}C_{16}$} in wt% (calculated): C 11.35 (10.30), H 1.63 (1.45), N 0.25(0.00).

Compound (4E) - {$W_{17}C_{18}$} - $K_6[P_2W_{17}O_{61}(PO_2C_6H_4(C_{18}H_{37})_2]$

Red powder; Yield: 0.43g (76%); ^{1}H NMR (400 MHz, DMSO-d_6) δ 7.93 (ddd, *J* = 33.5, 13.5, 8.4 Hz, 4H, C**H**), 6.98 (dt, *J* = 10.2, 5.1 Hz, 4H, C**H**), 4.01 (dt, *J* = 13.2, 6.5 Hz, 4H, C**H$_2$**), 1.76 – 1.64 (m, 4H C**H$_2$**), 1.25 (s, 60H, C**H$_2$**), 0.90 – 0.82 (m, 6H, C**H$_3$**). ^{31}P NMR (162 MHz, DMSO-d_6) δ 15.93, -11.37, -13.00; IR(ATR) cm^{-1} = 528, 567, 721, 798, 909, 956, 1088, 1138, 1260, 1595, 2852, 2922; Elemental analysis for {$W_{17}C_{18}$} in wt% (calculated): C 11.22 (11.11), H 1.61 (1.59).

Compound (4F) - {$W_{17}C_{20}$} - $K_6[P_2W_{17}O_{61}(PO_2C_6H_4(C_{20}H_{41})_2]$

Red powder; Yield: 0.42g (73%); ^{1}H NMR (400 MHz, DMSO-d_6) δ 7.99 – 7.84 (m, 4H, C**H**), 6.98 (td, *J* = 9.2, 3.2 Hz, 4H, C**H**), 4.01 (dt, *J* = 13.4, 6.4 Hz, 4H, C**H$_2$**), 1.78 – 1.68 (m, 4H, C**H$_2$**), 1.24 (s, 68H, C**H$_2$**), 0.90 – 0.82 (m, 6H, C**H$_3$**).^{31}P NMR (162 MHz, DMSO-d_6) δ 15.95 (d, *J* = 3.5 Hz), -11.36, -12.99; IR(ATR) cm^{-1} = 525, 562, 708, 795, 907, 956, 1088, 1136, 1255, 1597, 2852, 2920; Elemental analysis for {$W_{17}C_{20}$} in wt% (calculated): C 11.97 (11.91), H 1.75 (1.73).

2.7 REFERENCES

1. S. Landsmann, C. Lizandara-Pueyo and S. Polarz, *J. Am. Chem. Soc.*, **2010**, 132, 5315-5321.
2. M. F. Misdrahi, M. Wang, C. P. Pradeep, F.-Y. Li, C. Lydon, L. Xu, L. Cronin and T. Liu, *Langmuir*, **2011**, 27, 9193-9202.
3. P. Yin, C. P. Pradeep, B. Zhang, F.-Y. Li, C. Lydon, M. H. Rosnes, D. Li, E. Bitterlich, L. Xu, L. Cronin and T. Liu, *Eur. J. Chem*, **2012**, 18, 8157-8162
4. A. Klaiber, T. Kollek, S. Cardinal, N. Hug, M. Drechsler and S. Polarz, *Adv. Mater. Interfaces*, **2018**, 5, 1701430.
5. A. Klaiber and S. Polarz, *ACS Nano*, **2016**, 10, 10041-10048.
6. S. Polarz, B. Smarsly and M. Antonietti, *ChemPhysChem*, **2001**, 2, 457-461.
7. S. J. Xue, A. Chai, Z. J. Cai, Y. G. Wei, C. S. Xiang, W. D. Bian and J. Shen, *Dalton Trans.*, **2008**, 4770-4775.
8. C. P. Pradeep, M. F. Misdrahi, F. Y. Li, J. Zhang, L. Xu, D. L. Long, T. Liu and L. Cronin, *Angew. Chem. Int.*, **2009**, 48, 8309-8313.
9. K. Kastner, A. J. Kibler, E. Karjalainen, J. A. Fernandes, V. Sans and G. N. Newton, *J. Mater. Chem. A*, **2017**, 5, 11577-11581.
10. S. Landsmann, M. Luka and S. Polarz, *Nat. Commun.*, **2012**, 3, 1299.
11. R. Zana, in *Specialist Surfactants*, ed. I. D. Robb, Springer Netherlands, Dordrecht, **1997**, 81-103.
12. J. M. Cameron, S. Fujimoto, K. Kastner, R. J. Wei, D. Robinson, V. Sans, G. N. Newton and H. H. Oshio, *Chem. Eur. J.*, **2017**, 23, 47-50.
13. S. Fujimoto, J. M. Cameron, R.-J. Wei, K. Kastner, D. Robinson, V. Sans, G. N. Newton and H. Oshio, *Inorg. Chem.*, **2017**, 56, 12169-12177.
14. W. Chen, D. Ma, J. Yan, T. Boyd, L. Cronin, D.-L. Long and Y.-F. Song, *ChemPlusChem*, **2013**, 78, 1226-1229.
15. Y. Chu, A. Saad, P. Yin, J. Wu, O. Oms, A. Dolbecq, P. Mialane and T. Liu, *Chem. Eur. J.,* **2016**, 22, 11756-11762.
16. P. Yin, P. Wu, Z. Xiao, D. Li, E. Bitterlich, J. Zhang, P. Cheng, D. V. Vezenov, T. Liu and Y. Wei, *Angew. Chem. Int.*, **2011**, 50, 2521-2525.
17. J. Clayden, N. Greeves and S. Warren, *Organic Chemistry*, OUP Oxford, **2012**.
18. M. B. Smith and J. March, *March's Advanced Organic Chemistry: Reactions, Mechanisms, and Structure*, Wiley, **2007**.
19. T. M. Balthazor and R. C. Grabiak, *J. Org. Chem.* , **1980**, 45, 5425-5426.
20. A. Dolbecq, E. Dumas, C. R. Mayer and P. Mialane, *Chem. Rev.*, **2010**, 110, 6009-6048.
21. C. R. Graham and R. G. Finke, *Inorg. Chem.*, **2008**, 47, 3679-3686.
22. G. S. Kim, K. S. Hagen and C. L. Hill, *Inorg. Chem.*, **1992**, 31, 5316-5324.
23. M. Pascual-Borràs, X. López and J. M. Poblet, *Phys. Chem. Chem.*, **2015**, 17, 8723-8731.
24. J. M. Cameron, S. Fujimoto, R. J. Wei, G. N. Newton and H. Oshio, *Dalton Trans*, **2018**, 47, 10590-10594.
25. M. T. Pope, in *Polyoxometalate Molecular Science*, eds. J. J. Borrás-Almenar, E. Coronado, A. Müller and M. Pope, Springer Netherlands, Dordrecht, **2003**, 3-31.
26. M. T. Pope and E. Papaconstantinou, *Inorg. Chem.*, **1967**, 6, 1147-1152.
27. J. M. Cameron, S. Fujimoto, R.-J. Wei, G. N. Newton and H. Oshio, *Dalton T.*, **2018**, 47, 10590-10594.
28. Y. Wu, R. Shi, Y. L. Wu, J. M. Holcroft, Z. Liu, M. Frasconi, M. R. Wasielewski, H. Li and J. F. Stoddart, *J. Am. Chem. Soc.*, **2015**, 137, 4111-4118.
29. L. Maibaum, A. R. Dinner and D. Chandler, *J. Phys. Chem.*, **2004**, 108, 6778-6781.
30. R. M. Fitch, *J. Polym. Sci., Polym. Lett. Ed.*, **1984**, 22, 508-509.
31. R. Nagarajan, *Langmuir*, **2002**, 18, 31-38.
32. J. F. Rusling and Z. Zhang, in *Handbook of Surfaces and Interfaces of Materials*, ed. H. S. Nalwa, Academic Press, Burlington, **2001**, 33-71.
33. J. N. Israelachvili, D. J. Mitchell and B. W. Ninham, *J. Chem. Soc., Faraday Trans.*, **1976**, 72, 1525-1568.
34. A. Di, J. Schmitt, M. A. da Silva, K. M. Z. Hossain, N. Mahmoudi, R. J. Errington and K. J. Edler, *Nanoscale*, **2020**, 12, 22245-22257.
35. V. Lutz-Bueno, S. Isabettini, F. Walker, S. Kuster, M. Liebi and P. Fischer, *Phys. Chem. Chem.*, **2017**, 19, 21869-21877.
36. D. Li, P. Yin and T. Liu, *Dalton T.*, **2012**, 41, 2853-2861.

3 HIERARCHICAL SELF-ASSEMBLY OF A REDOX-ACTIVE HYBRID-POM AMPHIPHILES

3.1 INTRODUCTION

Hierarchical self-assembled structures are extremely prevalent in nature and feature in the smart construction of biological systems from single molecules such as amino acids and phospholipids, into larger superstructures (e.g. micelles, vesicles, β-sheets and α-helicies),[1] and further into complex functional hierarchical systems (e.g cylindrical micelles, lamellar sheets and tertiary fibres etc.) through specific non-covalent interactions (e.g H-bonding, π-π stacking, Van der Waals, ionic, coordination, hydrophobic effect etc.).[2-4] Artificial self-assembled nanostructures can also be prepared in a similar way through specific non-covalent interactions and kinetic/thermodynamically driven assembly processes associated with amphiphilic molecules.[5, 6] The design of soft nanomaterials through hierarchical assembly of functional amphiphilic molecules is a key goal in the field of nanotechnology,[7] where the translation of molecular properties to the higher-ordered structures allows us to generate advanced materials for a range of applications including medicine,[8] sensing,[9] and catalysis.[10] However, to generate stable higher-order structures remains a difficult task due to the sensitive nature associated with non-covalent interactions. Owing to the dynamic nature of these interactions, the self-assembly of amphiphiles can be controlled through external stimuli including concentration, solvent, temperature, pH, ionic strength of the solution and light.[11-14] By exploiting these conditions, it is possible to control the assembly of amphiphilic molecules to carefully design nanoarchitectures with emerging properties.

Bottom-up approach to functional nanomaterial fabrication requires careful design and synthesis of amphiphilic molecules with enhanced properties (e.g redox-activity, photo-activity, conductivity etc). Likewise, POMs have drawn significant amounts of interest in the field of supramolecular chemistry,

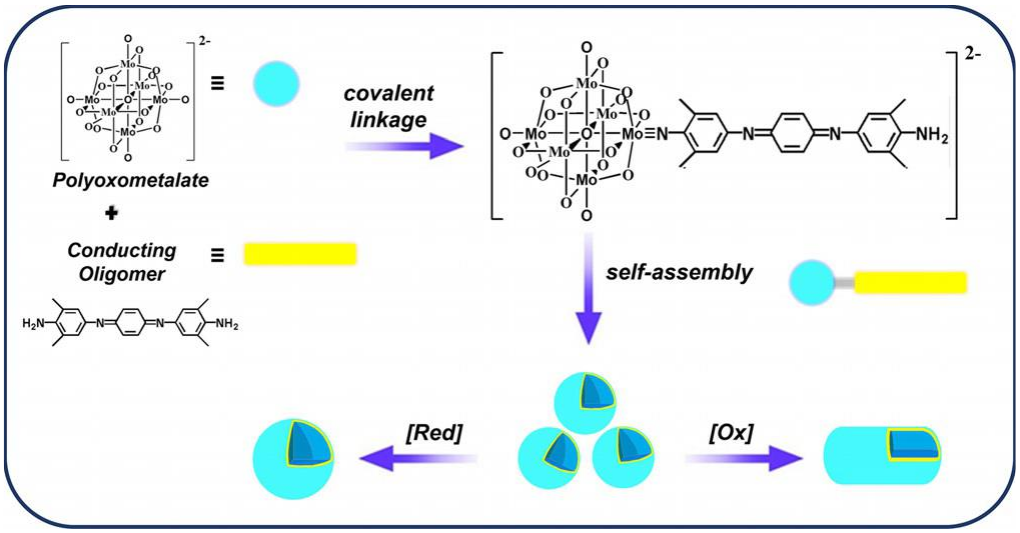

Figure 42 - Graphical representation of the synthesis of POM-TANI@EB and the morphological transitions from a spherical vesicle to a larger vesical or a short cylindrical vesicle by redox stimulation. Reproduced from ref.15 with permission from the John Wiley and Sons.

due to their well-known inherent photo/redox-activity, and ability to undergo organo-functionalisation with a vast range of ligands with established linkers. Over the last two decades, many examples of hybrid-POM amphiphiles have been reported, such as Class I hybrids based on surfactant encapsulated POMs or POM block co-polymer composite materials, Class II hybrid amphiphiles and lastly, a fusion between the two classes, surfactant encapsulated hybrid POMs. Across the regimes, their supramolecular assembly is well explored, however, investigations into the hierarchical self-assembly is relatively rare. Only a handful for examples associated with stimuli triggered "*smart*" hierarchical assembly exists.

An interesting example of redox-triggered hierarchical self-assembly was reported by Wei *et al.* In this case Wei and co-workers fabricated a hybrid-POM amphiphile by covalently grafting a conductive tri(aniline)(TANI) to a Lindqvist hexamolybdate POM.[15] TANI possesses three oxidation states, including leucoemeraldine base (LEB) state, emeraldine base (EB) state, and pernigraniline base (PNB) state, which possess different structural arrangements based on *trans-syn*, *trans-anti*, and *cis-anti* isomers, therefore imparting the overall hybrid POM with redox-responsive structural transition opportunity. To stimulate the isomerisation of POM-TANI to each of the redox states,

tetrabutylammonium peroxydisulfate [$(Bu_4N)_2S_2O_8$] was employed as the oxidant and 1,2-diphenyldiazane [$(PhNH)_2$] was selected as the reductant. The formation of POM-TANI@PNB and POM-TANI@LEB was triggered by addition of 1 eq. of oxidant or reductant respectively to POM-TANI@EB, this transition was confirmed by unique spectral bands tracked through UV-Vis spectroscopy. An acetone/toluene mixture (1.5:1) was employed as the solvent medium to enable self-assembly. Through DLS analysis, assemblies were present with R_h = 97.8 nm. When quantitative amounts of oxidant or reductant were added, the sizes of the assembly increased to R_h = 153.8 nm and R_h = 126.8 nm respectively. The results indicated that not only does the supramolecular assembly retain the molecular redox responsiveness, the redox-driven molecular transition is amplified to the superstructure, causing a transition to a new morphology. SEM was then employed to confirm the product of the oxidation was a shorter cylindrical micelle and the transition associated with the reduction was the increase in size to a larger vesicle. Wei *et al*. have demonstrated that by connecting functional ligands with amphiphilic nature to hydrophilic POMs, the molecular properties can be exploited to trigger higher-order transitions in their superstructure morphology and showcasing

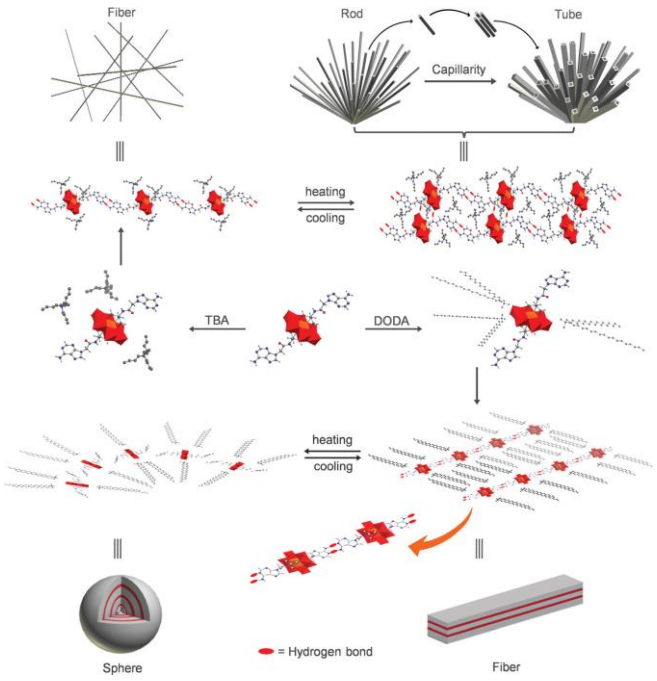

Figure 43 - Schematic illustration of thermal-induced dynamic self-hierarchical assembly process of SEOP-1 and SEOP-2. Reproduced from ref.16 with permission from the John Wiley and Sons.

potential opportunities behind grafting redox-active ligands to POMs, to assemble the next generation of redox-responsive nanomaterials.

Similarly, Wu *et al*. fabricated a temperature-responsive surfactant encapsulated hybrid-POM based on grafting two adeninyl groups onto a $MnMo_6$ cluster *via* a "tris" linker, which were encapsulated by two different surfactants: TBA^+ and $DODA^+$. Once again, Wu *et al*. set out to exploit the hydrogen bonding nature of adeninyl ligands where such interactions can be utilised constructively to form H-bonding networks and induce supramolecular assembly,[16] conversely such electrostatic interactions are weak and heavily affected by temperature. SEM was used to study the assembly process for TBA-POM and DODA-POM. TBA-POM samples prepared at 5 ^oC exhibited cross-linked fibrous structures which were microns in length and 100-200 nm in diameter. When the temperature was increased to 15 ^oC, the fibres became shorter and rigid rods - forming a flower like morphology, with individual rods exhibiting 200-300 nm diameters. Upon further heating to 45 ^oC, the rods formed tubes where the thickness of the tube walls matched the diameter of the rods, indicating that the tubes formed *via* agglomeration of the rods. Wu and co-workers demonstrated that these morphologies could indeed be recovered through cooling and furthermore, upon calcination, Mo nanostructures where obtained. Interestingly, with regards to the DODA-POM, similar fibrous structures were obtained at low temperatures, however, upon heating to 35 ^oC, the fibres aggregated which was further influenced by a temperature increase to 45 ^oC where the fibrous network transitioned to "*willow-leaf*" like assemblies. Finally, heating to 55 ^oC lead to a transition to spherical assemblies which could reversible be cooled back to fibrous morphologies. It was found that the hybrids exhibited axial hydrogen bonding between the adeninyl groups of adjacent hybrids, causing the organisation of molecules into polymer-like chain. Additional hydrogen bonding was found between adjacent chains. The presences of numerous hydrogen bonds led to the formation of fibre structures where TBA^+ did not affect the linear structure of the assemblies. However, the dominant additional van der Waals interactions exhibited by $DODA^+$ disrupted the hydrogen bonding, and at higher temperature, the linear structure was disfigured to a spherical morphology. This thermally induced hierarchical self-assembly process

was attributed to the synergistic effects of the hydrogen bonding, temperature, and disruptive nature of the associated surfactants. This investigation demonstrates the effectiveness of introducing non-innocent ligands which can contribute to supramolecular interactions and be exploited to form stimuli responsive smart assemblies.

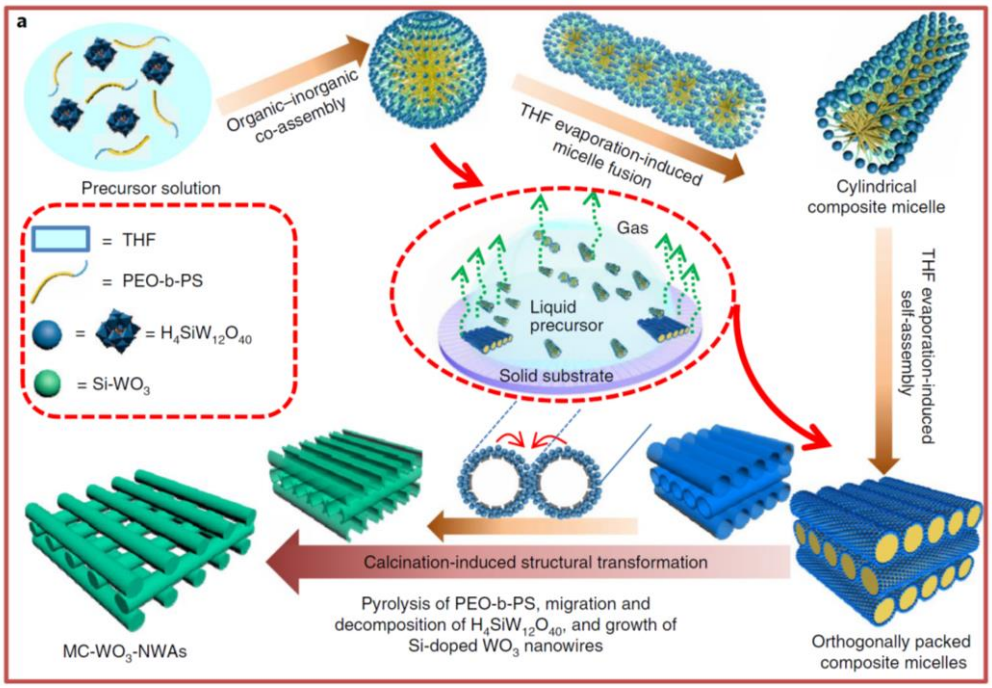

Figure 44 - Schematic illustration of the soft-assembly and fabrication process of the MC-WO_3-NWAs. Reproduced from ref.17 with permission from Springer Nature.

Regarding the design of nanostructured materials, Deng *et al.* recently reported a unique example where hierarchical self-assembly process was exploited to fabricate WO_3 nanowire assemblies. This fascinating report is a prime example of bottom-up approach to nanomaterial fabrication through POM based soft-matter. In this case Deng *et al.* successfully constructed 3D multilayer cross-hatched metal-oxide semiconducting nanowire arrays through the co-assembly of diblock copolymer (poly(ethylene oxide)-block-polystyrene (PEO-b-PS) and $H_4[SiW_{12}O_{40}]\cdot 15H_2O$.[17] In this example the hierarchical assembly was triggered by an increase in concentration induced by solvent evaporation. This was carried out firstly through the mixing of separate THF solutions containing dissolved (PEO-b-PS) and $H_4[SiW_{12}O_{40}]$, where an electrostatic interaction between (PEO-b-PS) and $H_4[SiW_{12}O_{40}]$ was formed *via* the protonation of PEO segment of (PEO-b-PS) by H^+ from $H_4[SiW_{12}O_{40}]$, causing an

electrostatic pairing with (PEO-b-PS) and $[SiW_{12}O_{40}]^{4-}$. This led to the formation of a colloidal solution, owing to the unfavourable negative repulsion now exhibited between the polymer chains. Thus, spherical micelles with a PS core and PEO/POM shell were assembled with narrow size distributions (D_h = 28.5 nm) confirmed by DLS. Interestingly, a hierarchical transition to cylindrical micelles was observed upon evaporation of the solvent, these structures exhibited similar diameter of 25 nm but were microns in length. The cylindrical micelles were also found to stack in a cross-hatch arrangement. DFT calculations indicated the arrangement was a result of cylindrical micelles stacking to minimise contact surface area, hence minimising unfavourable repulsion. Films of these higher-ordered structures were fabricated and then calcined. Upon calcination, another transition associated with the conversion of cylindrical micelles to nanowires was observed, generating a cross-hatched crystalline Si-doped ε-WO_3 matrix which exhibited promising gas sensing properties. Furthermore, this process was repeated with $H_4[SiMo_{12}O_{40}]$, $H_3[PW_{12}O_{40}]$ and $H_3[PMo_{12}O_{40}]$, to fabricate Si-doped MoO_3, P-doped WO_3 and P-doped MoO_3 nanowire arrays, respectively. This multi-faceted approach is a versatile example of the potential hybrid-POM soft-assemblies possess with regards to exploiting hierarchical bottom-up approaches towards controlled fabrication of nanostructured materials.

To develop intricate, stable and active nanostuctures at the solid-liquid interface from soft materials requires specific design and fabrication of active-amphiphiles, understanding of their assembly properties and their fundamental interactions with various surfaces. As-of-yet, the interaction between organic-inorganic hybrid POM soft materials with various carbon surfaces has been unexplored. In this chapter we will discuss two hierarchical self-assemblies based on surface effects and temperature induced transitions from micelles in aqueous solutions towards, higher-order materials. We will elaborate on our findings and probe the mechanism behind the observed assembly, and how these examples contribute to the field of hybrid-POM hierarchical assemblies.

3.2 AIMS

Amphiphilic molecules are known to be sensitive to environmental stimuli, which can cause transitions in their supramolecular assemblies to hierarchical structures. Based on the surface-confined electrochemistry of the **{$W_{17}C_{20}$}** micelles and its packing parameter value sitting at the threshold of micelles and cylindrical micelles, this molecule possessed clear potential to self-assemble into higher ordered structures. This became clear when **{$W_{17}C_{20}$}** was exposed to different environmental stimuli, specifically, its interaction with surfaces based previous results in Chapter 1 and witnessed transitions associated with temperature. The aim of this chapter is to characterise the higher-order structures of **{$W_{17}C_{20}$}** and understand the responsible mechanism or stimuli associated with the observed hierarchical self-assembly.

.

3.3 RESULTS AND DISCUSSION

3.3.1 Hierarchical Self-Assembly of Redox-Active Amphiphiles at Carbon Surfaces

In this section, we will discuss the hierarchical self-assembly of **{$W_{17}C_{20}$}** with regards to 0D micelles to 2D/3D surface structures. The surface confined electrochemistry observed in chapter 1 will be explored further to understand and characterise the electrode surface, assembly structure and retention of molecular properties in the hierarchical superstructure. Here, electrolyte contribution will also be explored. Once the deposition at the electrode surface was understood, we investigated the interaction of the solution micelles with two carbon surfaces; highly ordered pyrolytic graphene (HOPG) and graphene oxide (GO)), each possessing contrasting degrees of hydrophilicity. This allowed us to probe the effects on the solution phase supramolecular structures and elucidate the surface nature of the glassy carbon (GC) by comparing the observed assemblies to that observed at the GC electrode surface.

3.3.1.1 Materials and Surface Preparation

Hybrid-POM amphiphile **{$W_{17}C_{20}$}** was prepared by the condensation of (4-(icosyloxy)phenyl)phosphonic acid ($C_{26}H_{47}O_4P$) and lacunary Wells-Dawson POM **{W_{17}}** to yield hybrid-POM surfactant $K_6[P_2W_{17}O_{61}(POC_6H_4O(C_{20}H_{41}))_2]$ **{$W_{17}C_{20}$}**, following methods mentioned in Chapter 1.

To prepare our modified glassy carbon electrode, **{$W_{17}C_{20}$}** was dispersed into 0.1 M H_2SO_4 to form a 1.4 mM solution of redox-active micelles, the glassy carbon (GC) electrode was dipped in the solution for 1 min, removed and rinsed with deionised water. Deposition at hydrophilic graphene oxide (GO) and hydrophobic highly ordered pyrolytic graphite (HOPG) were prepared by drop-casting a 1.4 mM aqueous solution of **{$W_{17}C_{20}$}** in water onto the material and blotting to remove excess solution.

3.3.1.2 *Electrode Deposition of Redox-Active micelles*

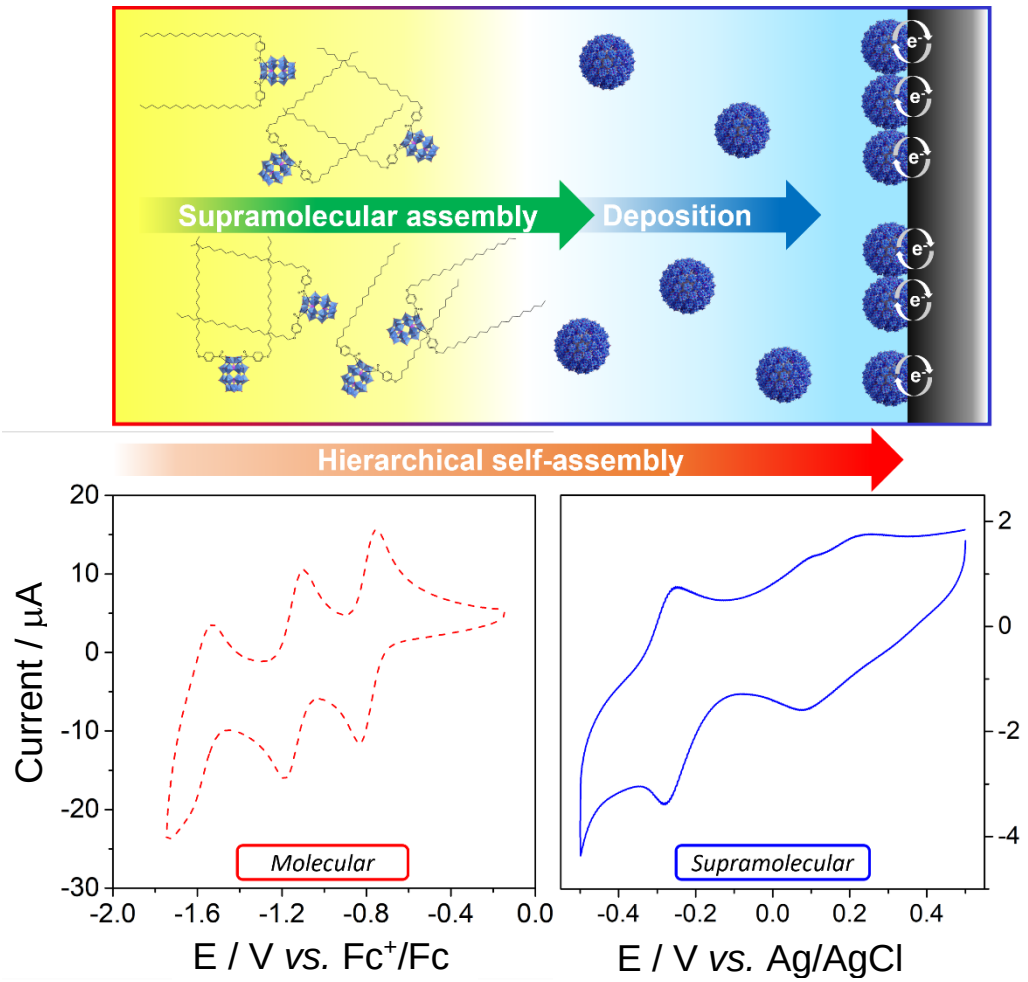

Figure 45 - A schematic illustrating the hierarchical supramolecular assembly of redox-active $\{W_{17}C_{20}\}$ in aqueous solutions onto glassy carbon, and CV plots of (red) 1.4 mM $\{W_{17}C_{20}\}$ in DMF with 0.1 M [TBA][PF_6]; (blue) 1.4 mM $\{W_{17}C_{20}\}$ in 0.1 M H_2SO_4.

Previously, we reported a difference in redox behaviour when comparing **$\{W_{17}C_{20}\}$** in the molecular form *vs*. the micellar superstructure. Firstly, we established the assemblies were observed in aqueous solutions, which could then be disassembled by the addition of DMF. We then employed this solvation behaviour to analyse redox-activity of these redox active micelles, where cyclic voltammetry was conducted in 0.1 M H_2SO_4, followed by analysis post-addition of DMF (50:50 mixed solution of 0.1 M H_2SO_4:DMF) to disassemble the micelles and study the electrochemistry of the molecules. Two pseudo-reversible redox processes are observed in the micellar form: an ill-defined process at (I*, $E_{1/2}$ = 0.089 V) and a well-defined, highly reversible wave at more negative potential (II*, $E_{1/2}$ = −0.265 V), which are both ascribed to $2e^-$ redox processes. This transitioned to 3 pseudo-reversible redox

processes with the addition of DMF to disassemble the micelles to individual molecules ($E_{1/2}$ = 0.070 V (I), − 0.027 V (II) and − 0.353 V (III)), which corresponds closely to the electrochemical behaviour of the molecular hybrid species in neat DMF (Figure 45).

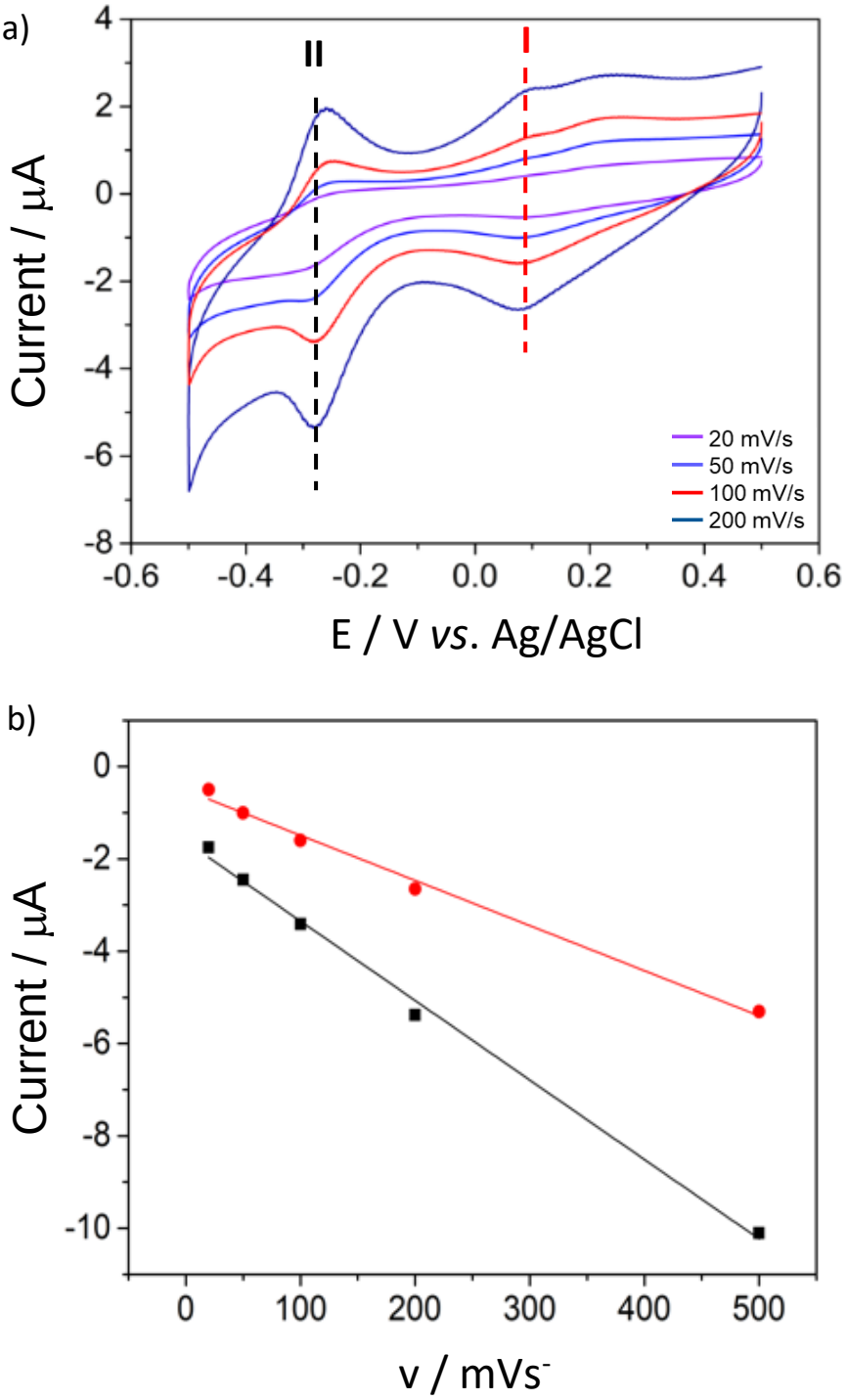

Figure 46 - a) CV plot of $\{W_{17}C_{20}\}$ at various scan rates (v) in 0.1 M H_2SO_4; b) a plot of the peak current (I_p) *vs.* v extrapolated from CVs in a) for redox process I (red) and II (black).

Investigating the redox chemistry of **{$W_{17}C_{20}$}** micelles further, a decrease in faradaic current of the redox processes was observed when comparing the CVs of **{$W_{17}C_{20}$}** (smaller monodisperse micelles) to **{$W_{17}C_{10}$}** (larger polydisperse assemblies), which indicated potential blocking of the electrode surface. Extrapolating the peak current (I_p) at various scan rates (v) (Figure 46a), a plot of I_p *vs*. v was constructed (Figure 46b). The plot displays a linear trend, suggesting the observed electrochemistry is surface confined. Note, that this observation only occurred in aqueous solutions and therefore, under these conditions we set out to understand whether the electrode was decorated with electro-active micelles by analysing the material stability and surface morphology, which if indeed is what we expect can perhaps lead to new and exciting electrode materials for applications in electrocatalysis and sensing.[18, 19]

The deposition process of this redox-active self-assembling monolayer (SAM) was confirmed by dipping the electrode in a 1.4 mM solution of **{$W_{17}C_{20}$}** for 1 min, removing and rinsing thoroughly with deionised water. The electrode was then placed in a 0.1 M H_2SO_4 electrolyte solution and tested by running CV for 100 cycles (Figure 47), which displayed no significant change in the redox process after the first cycle. The change in faradaic current after the first cycle maybe a result of micelles loosely bound to the surface or other micelles diffusing off the electrode into solution, leading to a stabilised micelle@GC surface. This preparation confirmed that the micelles are not electrodeposited, but adsorb due to the intermolecular interaction between the GC surface functionality (i.e. carboxyl groups etc.) with the W=O exterior of the micelles.[20-22]The absence of a significant change post cycling indicates that we have produced a stable layer of redox active material at the electrode surface. Furthermore, a dip test in an aqueous solution containing **{$W_{17}C_{20}$}** and no electrolyte led to no surface deposition of redox active **{$W_{17}C_{20}$}** at the GC electrode. This suggests either H_2SO_4 promotes surface oxidation which produces functional groups that facilitate electrostatic bonding between **{$W_{17}C_{20}$}** and GC surface or the protons act as bridging agents to facilitate deposition.

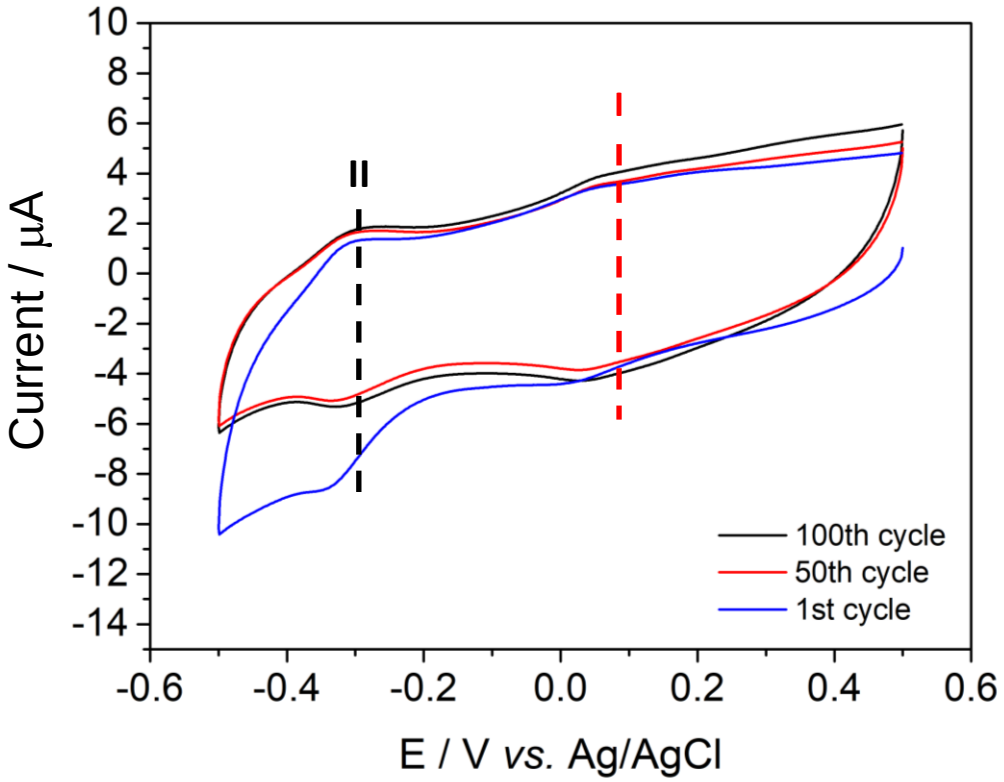

Figure 47 - A CV of $\{W_{17}C_{20}\}$ SAM on GC electrode displaying cycle 1(blue), 50 (red) and 100 (black) in 0.1 M H_2SO_4 supporting electrolyte.

Once the deposition mechanism and stability of the material was understood, we set out to estimate the number of redox-active micelles at the electrode surface. If we assume the approximate surface area of the electrode (d = 3 mm) is 7.07 x 10^{-6} m^2 and the micelle (D_h = 6 nm, 80 POM clusters per micelle) average cross-sectional area is 2.83 x 10^{-17} m^2, then the approximate number of micelles in a full monolayer would be 2.5 x 10^{11} micelles (5.9 x 10^{-11} mol of POM). From reduction process II (100^{th} cycle), which we know to be a $2e^-$ process, the charge passed (Q = 9.3 x 10^{-7} C) was acquired by integrating the area under the curve and was used to calculate the number of moles of POMs (8 x 10^{-12}) involved in the reduction process using the equation $Q = nFM$, (where n = no. of electrons transferred per molecule, F = faraday constant (96500 C mol^{-1}) and M = no. of moles of species reacting). This calculation concluded that in a theoretical full monolayer of micelles on a flat GC surface, 13 % of the POMs in a micelle were involved in the redox process. Although, this value suggests that the full monolayer is not active, this could be attributed to slow electron transfer kinetics around the micelle or regions of the electrode not covered by micelles.

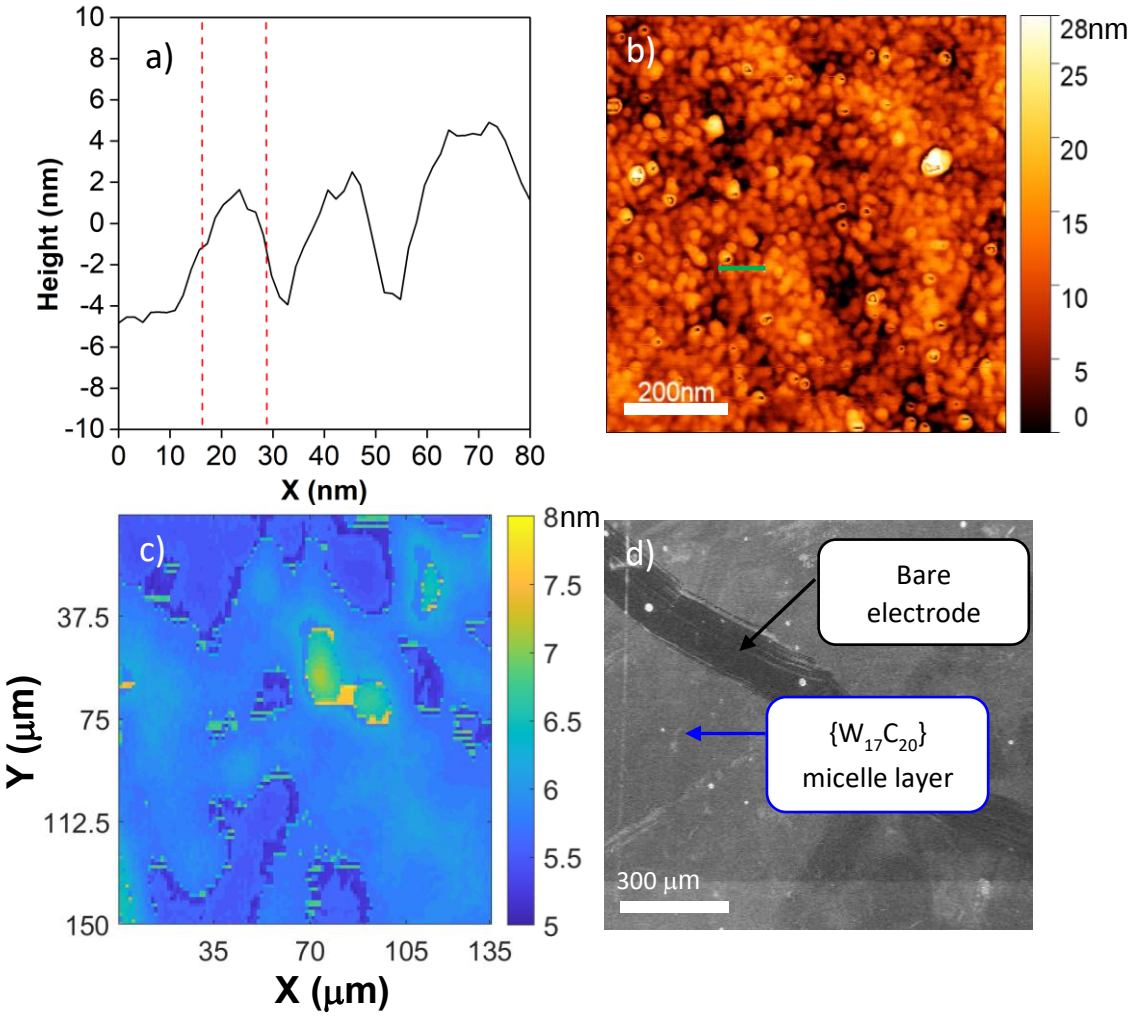

Figure 48 - a) $\{W_{17}C_{20}\}$@GC electrode height trace plot of section highlighted (green) in b) displaying peak full width half maxima of 12.1 nm; b) AFM plot of $\{W_{17}C_{20}\}$@GC electrode; c) Ellipsometry map of the prepared GC square electrode post CV, displaying regions of deposition from 5-8nm thickness; d) SEM image displaying areas of deposition (light grey) and an area of bare electrode that has been wiped (dark grey).

Having confirmed the stability and deposition mechanism at the electrode-solution interface, surface characterisation was key to identify the supramolecular morphology of the deposited material. The surface structure of the electrode was analysed using imaging ellipsometry. Figure 48c displays the ellipsometry surface mapping of the prepared GC electrode. Here we observed a layer of metal oxide with a thickness of 6-8 nm, which corroborates well with the hydrodynamic diameter of a **$\{W_{17}C_{20}\}$** micelle observed through DLS analysis (Figure 38a). However, although we observe large areas of monolayer micelles assembling at the surface, we also observe areas of bare GC as highlighted in Figure 48d, where the SEM displayed two contrasting areas thought to be bare (dark region) and

deposited (light region) surfaces. Atomic force microscopy (AFM) was employed to analyse the modified electrode on a nanoscale, Figure 48b confirms the presence of spherical structures at the surfaces with diameters between 5-30 nm. The height analysis of the electrode (Figure 48a) displays spherical assemblies with height of 6 nm and width of 12.1 nm. The additional width of the assemblies could be a result of agglomeration or "*squashing*" upon deposition. The phase image (see appendix Figure S3) displayed clear structures with sizes between 5-15 nm. It is now clear that we can prepare a stable redox-active monolayer of micelles at the surface of GC electrodes which are held through electrostatic interactions between the POM and carbon surface functionalitly (e.g. carboxylic acids) introduced by acid catalysed surface oxidation or proton bridged hydrogen bonding between GC functional groups and micelle surface.[23] Similar efforts have been made by Newton *et al.* and Cuentas-Gallos *et al.* to non-covalently graft POMs to carbon surfaces through acid catalysed active surface oxidation.[24, 25] To the best of our knowledge, our result represents the first example of redox-active hybrid-POM monolayers (ML) or SAM consisting of electrostatically bound hybrid-POM micelles. Although we have now characterised the assembly morphology at the surface to be a pseudomonolayer, we do not fully understand the dominant interactions between the micelles and the surface. We therefore progressed to explore how the electrolyte effects the surface aggregation and how the hydrophillic/phobic nature of the surface effects the heirarchical assembly.

3.3.1.3 Electrolyte Contributions

Not only can the electrolyte play a big role in the redox profile of POMs, the associated cations can also have an effect on the curvature of their assemblies and coordination with the electrode surface. To explore the effects of electrolyte and whether H^+ played a significant role in bridging the contact between the micelles and the GC surface, KCl was employed as the supporting electrolyte. This allowed us to mitigate any cation exchange effects and to probe the effects on the surface structure morphology. To solubilise **{$W_{17}C_{20}$}**, rapid heating in 0.1 M aqueous (aq) KCl was required due to low molecular solubility, DLS measurements reported polydisperse assemblies where D_h = 10-100 nm (Figure 50). The electrochemistry observed in 0.1 M KCl (aq) (Figure 50) displayed contrasting redox

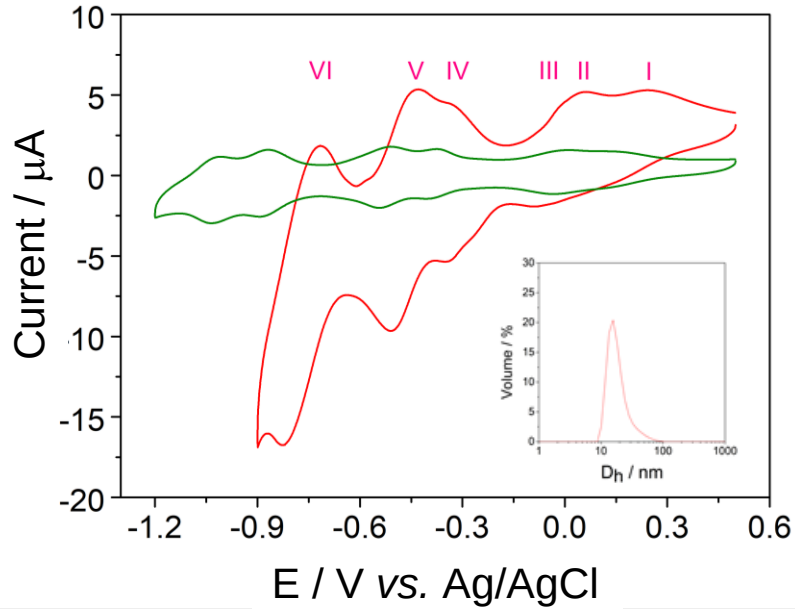

Figure 50 - CV overlay of 1.4 mM $\{W_{17}C_{20}\}$ in 0.1 M KCl (aq) (red) and resulting deposition at GC electrode from 1.4 mM $\{W_{17}C_{20}\}$ KCl solution in 0.1 M KCl (aq) (green). DLS analysis plot of 1.4 mM $\{W_{17}C_{20}\}$ in 0.1 M KCl (aq) is displayed in the inset.

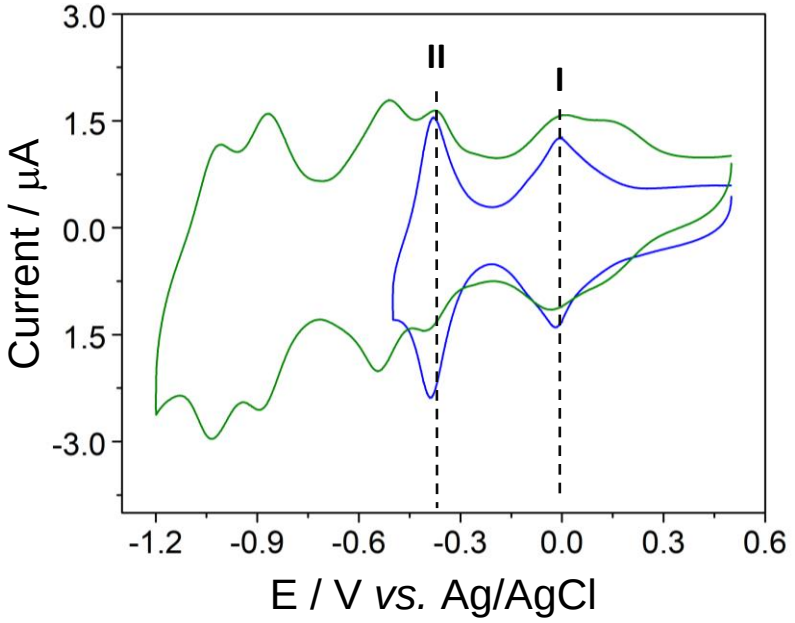

Figure 49 - CV of $\{W_{17}C_{20}\}$ deposited material at GC electrode formed from 0.1 M KCl (aq) taken in 0.1 M H_2SO_4 (blue) and 0.1 M KCl (aq) (green).

profile to the results observed in 0.1 M H_2SO_4. Here, we can see 6 redox processes situated at $E_{1/2}$ = 0.154 V(I), - 0.071 V(II), - 0.363 V(III), - 0.512 V(IV), - 0.659 V(V) and - 0.801 V(VI). Only redox process I and III displayed ΔE_p = 67-69 mV, therefore exhibiting partial solution phase reversible behaviour.

However, after running a dip test, by removing, rinsing, and placing the electrode in 0.1 M KCl (aq), we observed surface confined redox processes, which indicated once again, surface deposition of an aggregate species on the electrode surface (KCl-**{$W_{17}C_{20}$}**ML). The CV of KCl-**{$W_{17}C_{20}$}**ML (Figure 49 & 50 - green CV) displays 6 redox processes situated at - 1.030 V, - 0.880 V, - 0.525 V, - 0.385 V, - 0.014 V and 0.163 V, each exhibiting ΔE_p = 20-30 mV. KCl-**{$W_{17}C_{20}$}**ML displayed stability up to 100 cycles with no observable change in its CV profile. KCl-**{$W_{17}C_{20}$}**ML was then dipped into 0.1 M H_2SO_4 and we observe a change in the coalescence of the first four redox processes to two processes. This can be ascribed to cation effects, specifically proton coupled redox process.

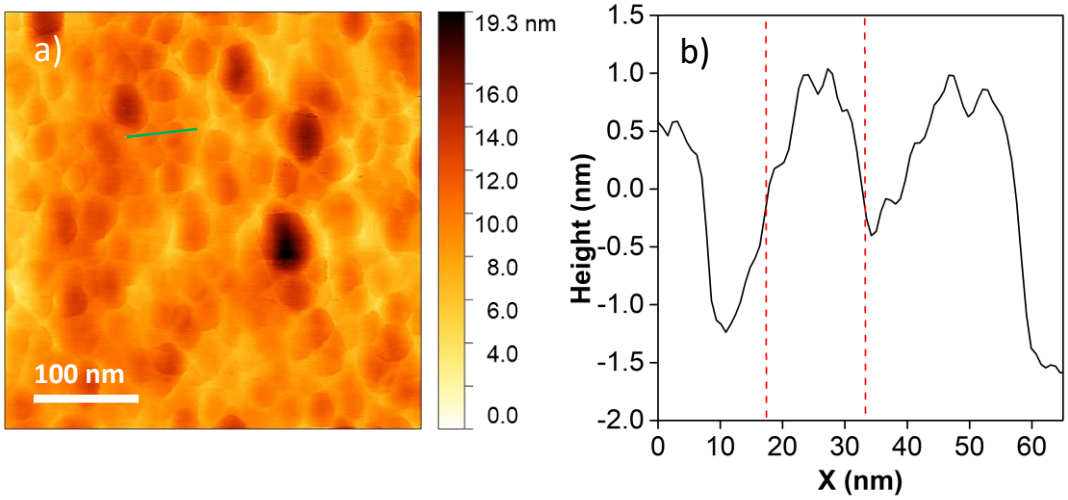

Figure 51 - AFM analysis: a) KCl-{$W_{17}C_{20}$}ML@GC electrode height trace plot of section highlighted (green) in b) displaying peak full width half maxima of 15.9 nm; b) AFM plot of KCl-{$W_{17}C_{20}$}ML@GC electrode.

To confirm the morphology of KCl-**{$W_{17}C_{20}$}**ML, AFM analysis was conducted on the electrode. Figure 52a confirms the presence of spherical structures at the surfaces with diameters between 12-45 nm. The height analysis of the electrode (Figure 51b) displays spherical assemblies with height of approx. 2.5 nm and width of 15.9 nm. Overall, we observe lower dispersity in the size of micelles and greater faradaic current with MLs prepared in 0.1 M H_2SO_4, which indicates that the degree of deposition of redox-active micelles at the surface and supramolecular/hierarchical assembly process is largely influenced by the nature of surrounding ions, specifically the absence of acid will result in less surface oxidation sites to which the POMs can tether to, or protons may facilitate better coordination through hydrogen bonding between micelle surface and GC surface functional groups. Therefore, we observe

that the cations can have varying effects on the dispersity, electrochemistry, and magnitude of deposition of hybrid-POM redox-active assemblies.

Interestingly, upon returning to the CV solution (1.4 mM **{$W_{17}C_{20}$}** in 0.1M KCl (aq)), the solution had now formed a hydrogel (**{$W_{17}C_{20}$}-Gel**) (Figure 52) which indicated the potential presence of higher order supramolecular structure. This unique occurrence led us to probe the properties of the material. Firstly, we found that **{$W_{17}C_{20}$}-Gel** separated from the water content within 2 hours which indicated that the electrostatic hydrogen bonding structure between the water phases and potential assemblies was weak (Figure 52). Next, we set out to understand the morphology of the **{$W_{17}C_{20}$}-Gel**. This was achieved through optical and electron microscopy (Figure 53). Under the optical microscope, we observed a number of thin films. Interestingly, when exposed to polarised light, the material reflects the light in a unilateral order, indicating the material is isotropic in nature, which suggests the material may possess a degree of long-range order and crystallinity.

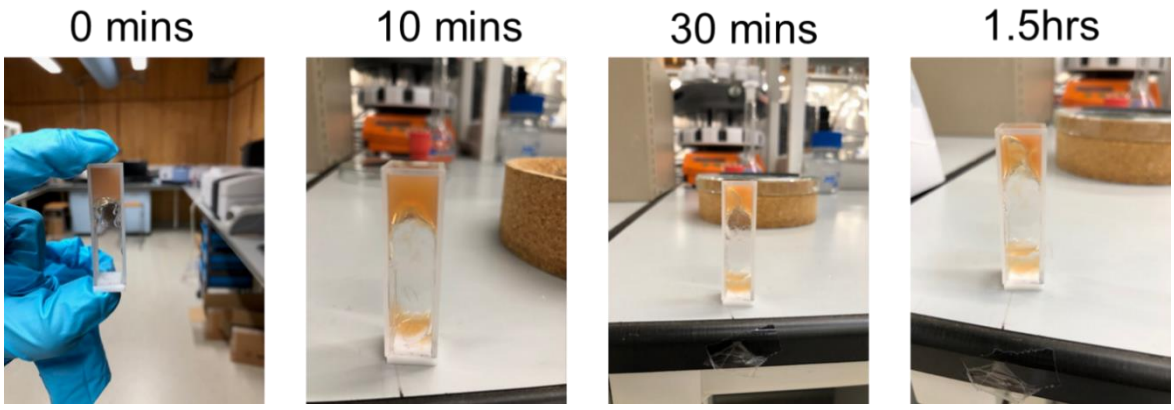

Figure 52 - Images of the gel formed from 1.4 mM {$W_{17}C_{20}$} CV solution in 0.1 M KCl (aq) overnight. The images were taken at separate time intervals after {$W_{17}C_{20}$}-Gel was turned upside-down.

To confirm this observation, the material was analysed *via* TEM. As predicted, **{$W_{17}C_{20}$}-Gel** consisted of thin films which were assembled from lamellar or cylindrical micelle structures packed together in 2D sheets. Figure 54 shows clearly ordered structures, where the darker lines correspond to the positions of the POMs in the structure and the lighter region corresponding to the internal cavity where the hydrophobic chains are present. The darker regions are associated with regions of higher electron density atoms, in this case the presence of tungsten atoms deflecting the electrons, leading to lower electron counts at the detector. The spacing between the structures measured to be 5-6 nm which fits well with the solution phase DLS diameter measurements of **{$W_{17}C_{20}$}** micelles (Figure 38a). Distinguishing between whether this material is lamellar or 2D sheets of cylindrical micelles is extremely difficult, however, there is reason to believe the structures we observe are hierarchical

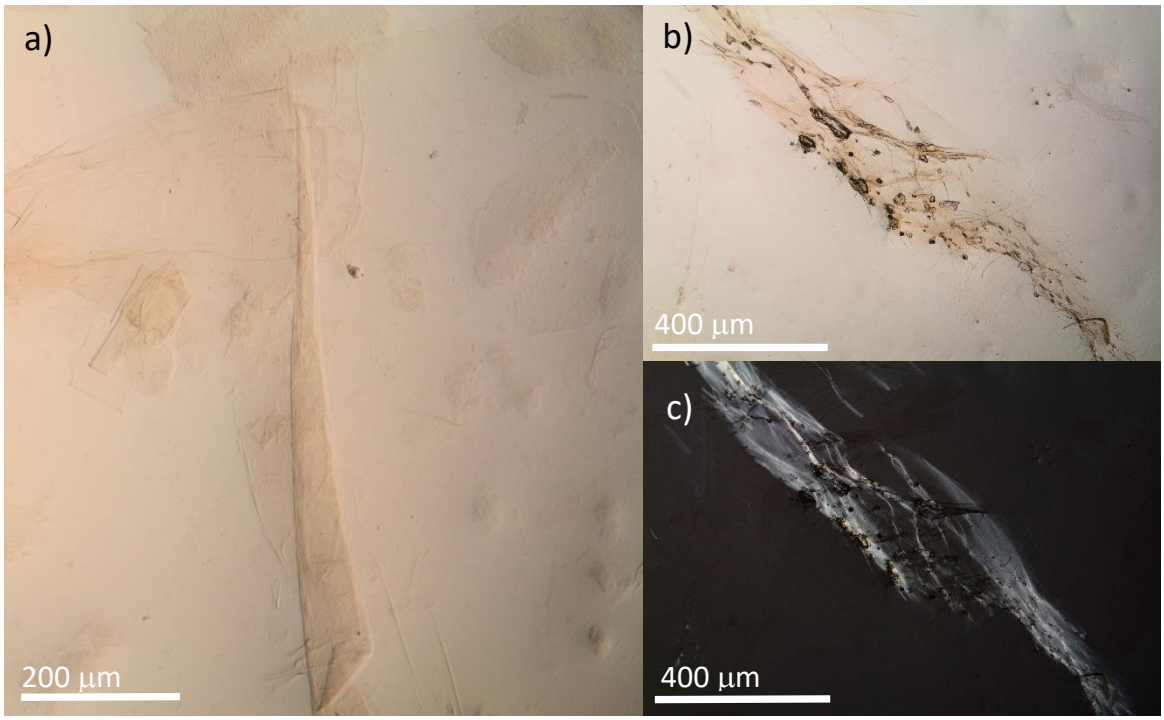

Figure 53 - Optical images captured from the deposition of the gel material produced from {$W_{17}C_{20}$} in 0.1 M KCl (aq), where a) and b) are imaged under normal settings an c) with polarized light.

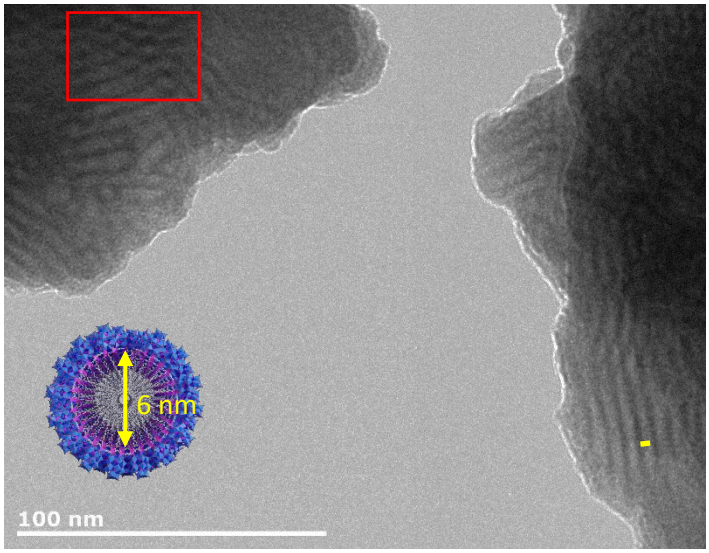

Figure 54 - TEM image of the gel material produced from the solubilisation of 1.4 mM $\{W_{17}C_{20}\}$ in 0.1 M KCl (aq) where the yellow bar is the measured distance between POMs and the red box highlighted displays regions of cross-hatching. Inset displays a front view of cylindrical micelle with POM-to-POM distance estimated to be 6 nm for $\{W_{17}C_{20}\}$.

assembly of micelles to 2D sheets of cylindrical micelles. In Figure 54, we observe cross-hatching arrangement (top left) where we believe that the 2D sheets consisting of polyanionic cylindrical micelle sheets stack aligning the tubes perpendicular to each other to minimise repulsion; this would not be observed for lamellar structures as they tend to be planar bilayer sheets.[17] In this case we observe an interesting product of 2 types of hierarchical structures, (i) surface deposition of micelles or 2D surface micelle monolayers, and (ii) 2D sheets of cylindrical micelles produced by a kinetic trap associated with cation driven gelation. This serendipitous result is a fascinating example of hierarchical assembly of redox-active metal-oxide supramolecular assemblies into higher-order structures, whilst retaining their molecular properties.

3.3.1.4 *Surface Effects on the Hierarchical Self-Assembly*

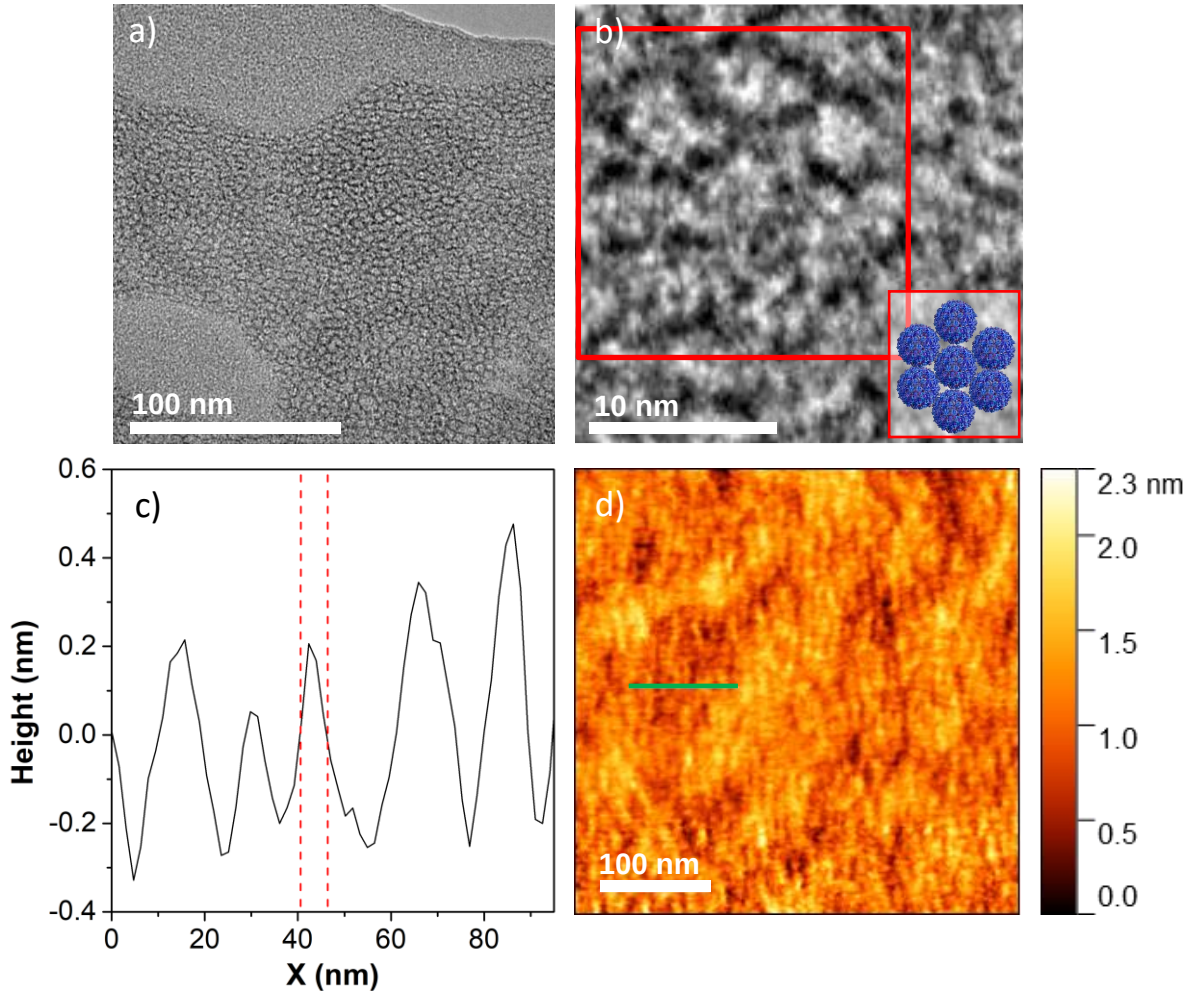

Figure 55 - a) TEM image of micelle hexagonal packing nanopattern assembled by drop casting 1.4 mM $\{W_{17}C_{20}\}$ on to GO TEM grid; b) zoomed in section of the hexagonal packing on GO; c) height trace plot of green line segment 1 in d) with fitted half width full maxima displaying a width of 5.5 nm; d) Atomic force microscopic surface analysis of micelle packing on GO TEM grid.

Leading on from our redox-active micelle ML result, we were interested in how these assemblies are affected when in contact with different types of carbon surfaces. To gain a better understanding of the dominant interactions involved in the micelle surface-assembly, we prepared (by drop casting) two different surfaces with 1.4 mM **$\{W_{17}C_{20}\}$** in H_2O; hydrophobic HOPG (Figure 56) and hydrophilic GO (Figure 55). The intereaction between **$\{W_{17}C_{20}\}$** and GO leads to a fascinating micelle packing arrangement, with assemblies retaining a diameter of 6-9 nm, matching the hydrodynamic diameter of the micelles in solution (as observed by light scattering measurements). This packing is unexpected as these micelles are electron dense and highly charged, which normally would lead to repulsion.

However, this observation is most likely a result of cation intercalation between the charged micelles and macroions, which has been discussed in depth by the likes of Liu *et al*.[26, 27] AFM analysis (Figure 55d) displays the surface analysis of the TEM grid, which further backs up the surface morphology on of this micelle packing arrangement. From this data we can obtain a roughness plot of the surface (Figure 55c), which displays structures with a diameter of 5.5 nm. Measurements in the y direction (height), do not corroborate with the solution-phase dimensions of the micelles due to their close packing (where the AFM tip is only measuring the shallow 'groove' or ca. 0.5 nm between neighbouring micelles). Unlike the HOPG surface, graphene oxide is more hydrophilic due to surface oxidation,[28] which makes the interaction between the hydrophilic oxo-exterior of the micelle interaction and the functionality (e.g. epoxides, alcohols, and carboxylic acids etc.) at the GO surface dominant, hence, retaining the integrity of the micelle's structure.

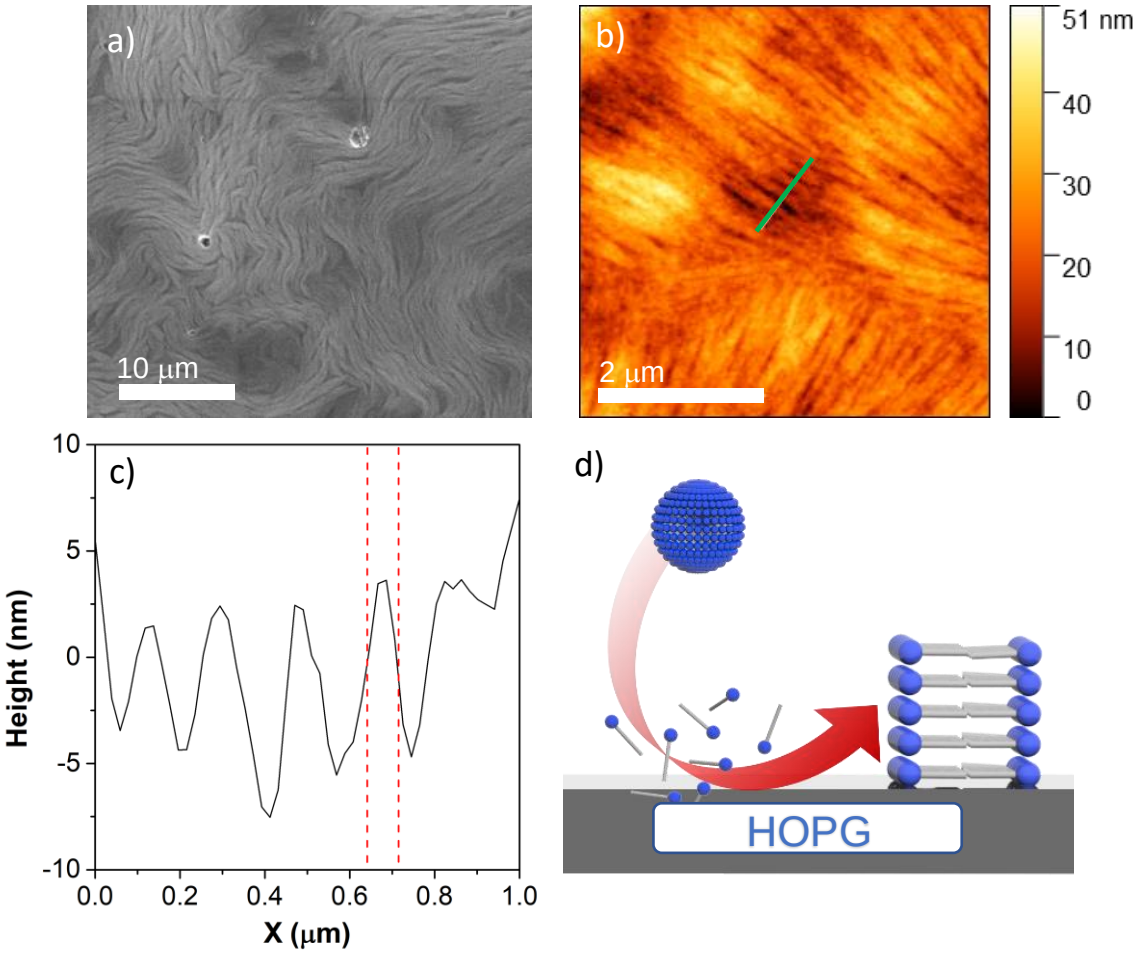

Figure 56 - a) SEM image of $\{W_{17}C_{20}\}$ drop casted onto hydrophobic HOPG; b) AFM plot of $\{W_{17}C_{20}\}$@HOPG; c) $\{W_{17}C_{20}\}$@HOPG height trace plot of section highlighted (green) in b) displaying lamellar structures approximately 8 nm in height and the half with full maxima of width of 70 nm; d) an schematic illustrating the destabilisation of micelles at the surface of hydrophobic HOPG to form fibres.

Conversely, we found that by employing HOPG to model the assembly of micelles, we could gain an insight into the effects of hydrophobic surface interactions on micellar assemblies in aqueous solutions. Figure 56a displays a SEM image of the prepared surface, which shows large lamellar structures, which demonstrates a transition from a micellar structure in solution to a lamellar structure at the surface of HOPG. The AFM height trace data shows the assemblies are 0.1-0.4 μm in width and 20-30 nm in height, which may be constructed from 20-30 layers of POMs arranged with chains running parallel to the surface of the HOPG and facing each other in a lamellar structure (Figure 56d). This is in agreement with observations by Bai *et al.* and Volkmer *et al.*, where nanofiber/tubular assemblies on the surface of HOPG were obtained by depositing cationic surfactants

hexadecyltrimethylammonium bromide and an amphiphilic hexapyridinium cation with six alkyl chains.[29, 30] The arrangement of the surfactant molecules by Bai and co-workers was reported to be horizontal and head-to-head, where the interaction between the carbon chains and graphite surface in the wetting stage dominate, causing the alkyl chains to align parallel to the graphite surface (Figure 56d). The proposed mechanism fits with our systems as the POM head being polar, hydrophilic and anionic will have a less favourable interaction with the hydrophobic graphite surface compared to the hydrophobic chains, causing the micelle in aqueous solutions to reassemble to allow the long and hydrophobic carbon chains to assemble at the surface.[29, 31] This transition is most likely largely to be a result of reduced surface oxidation, leading to reduced anchoring points for the micelle surface, leading to disassembly where the dominant Van der Waals interactions with the HOPG surface and carbon tails are favoured. We observed similar growth of solution phase fibres when a solution of **{$W_{17}C_{20}$}** was exposed to non-polar hydrophobic hexane antisolvent. This further elucidates the preferential fibre growth when **{$W_{17}C_{20}$}** is exposed to hydrophobic environments.

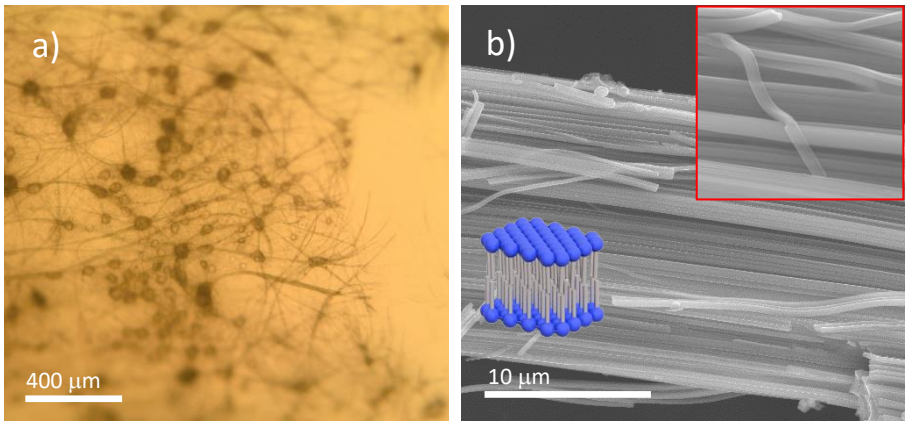

Figure 57 - Displays optical image a) and SEM image of fibres in b), produced from layer crystallisation with acetone and the solvent and hexane as the anti-solvent.

Based on the surface characterisation of **{$W_{17}C_{20}$}** at contrasting carbon-based surfaces, the carbon electrode assembly bears similar resemblance to the results observed at GO. Therefore, the 2D micelle monolayer we observe is dictated by favourable hydrophilic interactions most likely brought about by functional groups caused by surface oxidation at the carbon surface and the POM micelle outer-shell.

We also report opportunities to access hierarchical fibrous and surface micellar growth to higher-order metal-oxide structure, due to specific surface-induced interactions of preformed supramolecular assemblies of **{$W_{17}C_{20}$}** and carbon-based surfaces in aqueous solutions. Overall, we have demonstrated that different hierarchical assemblies can be accessed, and retain overall redox-activity and stability, as a function of the carbon surface type; allowing such materials to be applied in the fabrication of nanostructured surface and electrode materials.

3.3.2 Temperature-Driven Hierarchical Self-Assembly

Based on our previous findings in Chapter 1, **{$W_{17}C_{20}$}** was found to self-assemble into 6 nm 0D redox-active micelles. We then found that these micelles can self-assemble into 2D monolayers when exposed to hydrophilic surfaces and 3D fibrous networks when exposed to hydrophobic surfaces or in contact with non-polar organic solvents. In this section, we will discuss a fascinating temperature triggered transition from 0D to 3D hierarchical structure that has been discovered with **{$W_{17}C_{20}$}**.

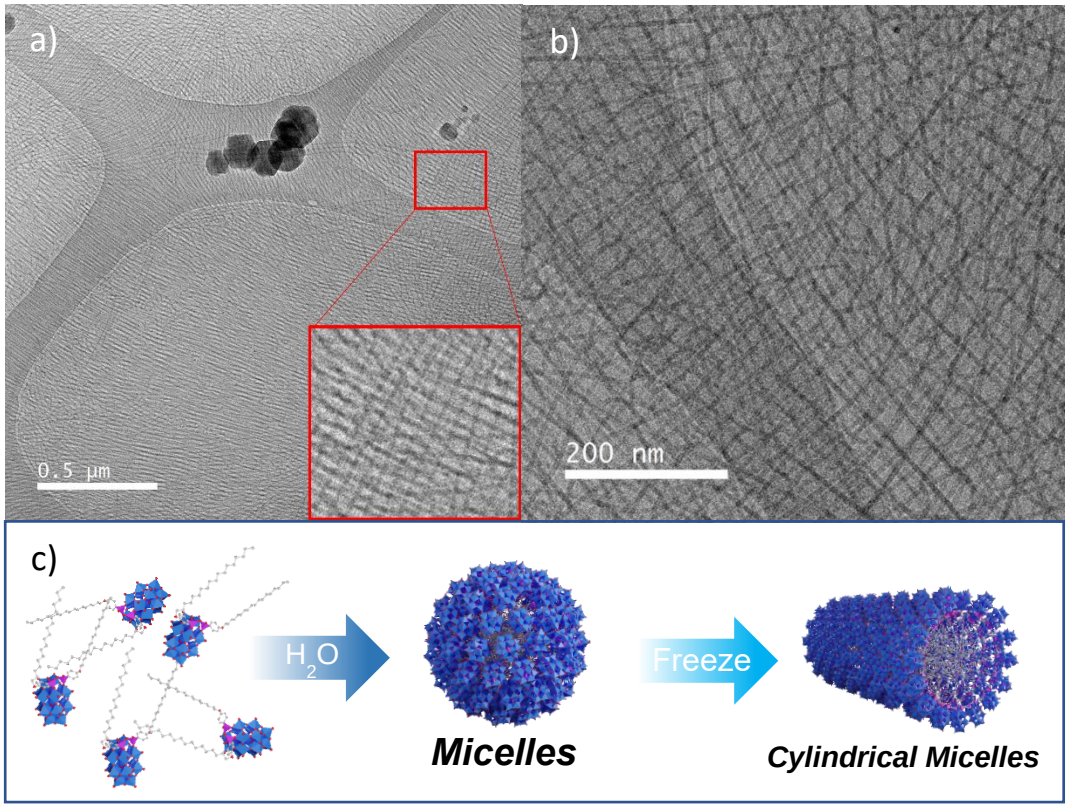

Figure 58 - Cryo-TEM of cylindrical micelles assembled from {$W_{17}C_{20}$} under cryogenic conditions: a) displays a large network of POM cylindrical micelles where a region of cross-hatched arrangement is highlighted; b) closer image of cylindrical micelle network and c) a schematic illustration the hierarchical self-assembly.

When a 1.4 mM **{$W_{17}C_{20}$}** aqueous solution was analysed using cryo-TEM, we initially expected to see the presence of dispersed micelles in solution. Surprisingly, we witnessed the presence of large arrays of cylindrical micelles with diameters of 7 nm and microns in length (Figure 58). It is well known that the nature of supramolecular assemblies is dynamic and can transition to energetically and

structurally favourable morphologies in response to external stimuli (e.g. temperature, salt concentration, co-surfactants, concentration etc.).

The cylindrical micelles exhibit a unique 1D growth pattern. Figure 58 displays a fascinating growth pattern where cylindrical micelles have grown in the ices pocket suspended in a lacey carbon support void. We notice growth of these tubes avoid the hydrophobic lacey carbon surface (which is also negatively charged due to the glow-discharge process for grid preparation) and when the growth approaches the wall, tubes grow at a 90^{o} angle triggered by anionic electrostatic repulsion. Similarly, the growth tends to also avoid collision with neighbouring tubes which is also speculated to be a result of electrostatic repulsion between the polyanionic structures. Moreover, we do observe growth of tubes crossing each other at 90^{o} angles, resulting in a cross-hatching pattern previously reported by Deng *et al.* as a result of an energetically favourable conformation to reduce the electrostatic repulsion contact area between anionic tubes.[17] Finally, we observe occurrences where the tube growth is trapped and forms a bridge to continue growing in another void. Although there is a huge amount of

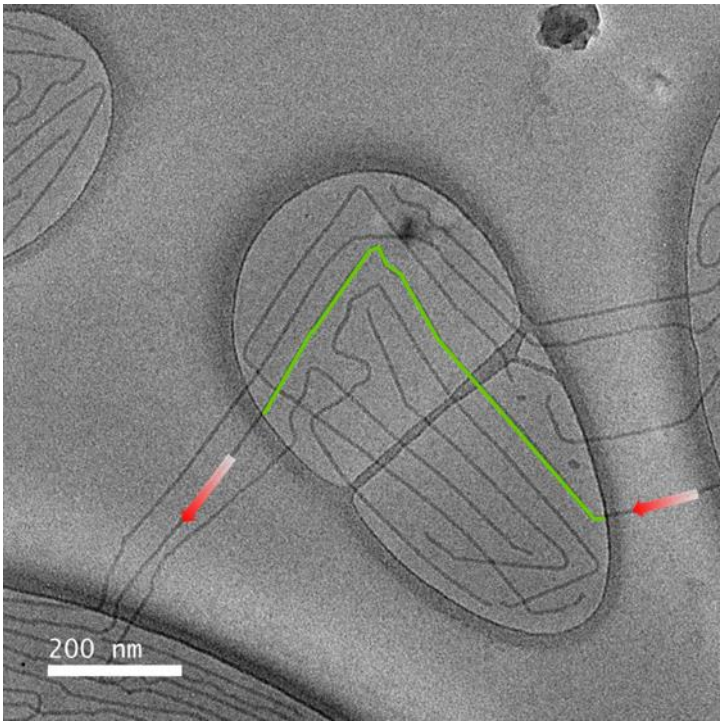

Figure 59 - Cryo-TEM of cylindrical micelles assembled from {$W_{17}C_{20}$} under cryogenic conditions which demonstrates a growth pattern dictated by electrostatic repulsion.

understanding behind the growth mechanism that needs to be investigated, overall, we can deduce that the extended growth of these structures is confined by electrostatic repulsion.

To confirm the effect of concentration, cryo-TEM analysis was also conducted on 0.5 mM, 1.4 mM and 3 mM solutions, no distinct difference in the assembly morphologies was observed – only cylindrical micelles were present. Furthermore, we examined whether the preparation of the cryo-grid was the cause of assembly transition. This was carried out by altering the blotting time of the grid which also resulted in no observable difference in the assembly morphology. Therefore, we hypothesise that this fascinating hierarchical assembly represents a growth event trigger by a rapid drop in temperature. Specifically, cation dissociation and localised concentration can be largely affected by freezing of an analyte solution.

As mentioned previously, the packing parameter for **{$W_{17}C_{20}$}** was calculated to be 0.30 which is extremely close to the N_s value of a surfactant structure predicted to assemble into cylindrical micelles. To observe a transition to the cylindrical micelles, the denominator of the equation has to increase in value which would result in $N_s > 0.33$. The two parameters present in the denominator are surfactant chain length (l_c) and effective equilibrium area of the surfactant head (a_e). We know that the l_c is fixed, therefore an increase in a_e can result in an increase in N_s which corresponds to the assembly of cylindrical micelles. One hypothesis for this transition could be associated to a change in positioning or behaviour of counter cations (K^+) when frozen. At room temperature, cations possess adequate energy to dissociate from the POM variably in solution and form a net charge around the micelle, however, when the temperature drops and the surrounding solution is frozen, cations are forced to pack tightly around the micelle, POM and between neighbouring POMs in a more ordered fashion. Therefore, leading to a somewhat larger effective area and altering the curvature of the assembly, transitioning to cylindrical micelles.

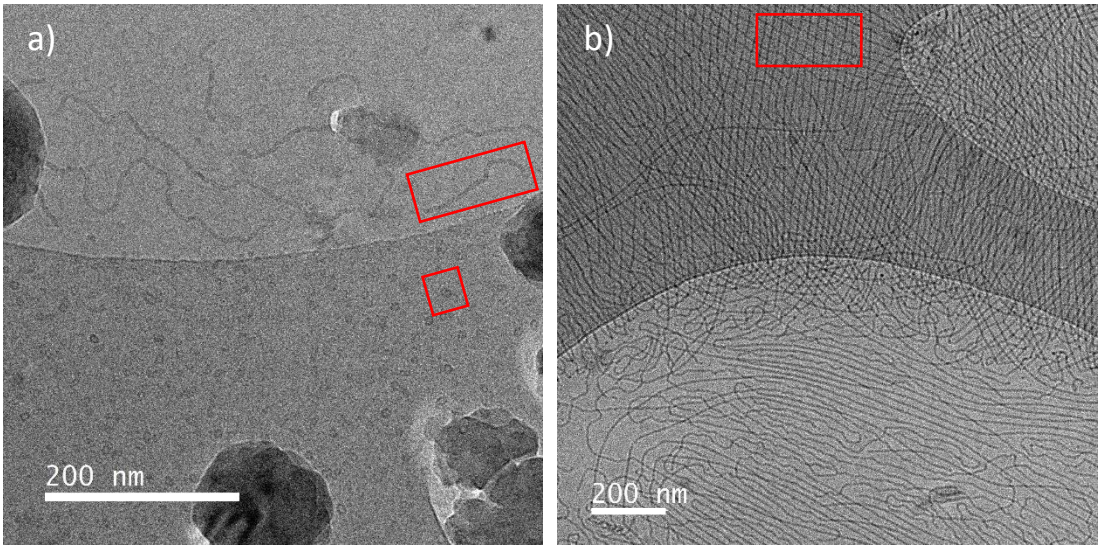

Figure 60 - Cryo-TEM of cylindrical micelles assembled from a) $\{W_{17}C_{12}\}$ highlighting assemblies and b) $\{W_{17}C_{16}\}$ which highlights cross-hatching arrangement under cryogenic conditions.

Our second hypothesis is based on the work of Perez *et al.*, where they discovered freezing induced self-assembly of amphiphilic block-copolymer consisting of ethylene oxide and propylene oxide blocks.[32] Here, Perez employed SAXS to analyse the behaviour of amphiphiles upon freezing. They discover that gradual freezing of the amphiphile solution can provide pathway to access various different assembly structures, witnessing transition from micelles to a hexagonally packed phase of micelles, and finally to hexagonally packed cylindrical micelles. This transition was due to ice crystals growing in solution with decreasing temperature, leading to pockets of increasing amphiphile concentration, which inherently forced amphiphiles to critical concentrations adequate to induce new morphological transitions. This observation reported by Perez *et al*. could indeed be the causation behind the transition we observe. Interestingly, we observe noticeable differences in the assembly structures observed for C_{12} and C_{16} prepared under the same cryogenic conditions. Figure 60 displays cryo-TEM analysis of 1.4 mM **$\{W_{17}C_{12}\}$** (Figure 60a) and **$\{W_{17}C_{16}\}$** (Figure 60b) in H_2O. We can clearly see that both surfactants form cylindrical micelles but the order within the structure is perturbed by the decrease in chain length. Unlike **$\{W_{17}C_{20}\}$**, **$\{W_{17}C_{12}\}$** and **$\{W_{17}C_{16}\}$** display noticeable degrees of disorder in the cylindrical micelle growth. Across the prepared **$\{W_{17}C_{12}\}$** sample, "*worm-like*" cylindrical micelles were observed, the quantity of these structures was significantly lower than what

we observe for longer chain lengths. These structures were also significantly shorter in length but possessed similar diameters (approx. 8 nm). Furthermore, these tubular structures were found to only grow in the pockets of frozen ice, and only micelles (d = 7-20 nm) were observed on the charged lacey carbon support. We suspect that the unfavourable repulsive interaction overcame the weaker solvophobic interactions prevented growth and caused disassembly of cylindrical micelles to a more energetically stable structure. By increasing the chain length to C_{16}, we observe a noticeable development in the growth behaviour, where **{$W_{17}C_{16}$}** exhibits an intermediate growth behaviour between **{$W_{17}C_{12}$}** and **{$W_{17}C_{20}$}**. In Figure 60b, we observe long-range growth similar to **{$W_{17}C_{20}$}** and 90° angle growth when intersecting neighbouring cylindrical micelles. However, presence of "*worm-like*" structures where the cylindrical micelles possess far more variability in the curvature like **{$W_{17}C_{12}$}** indicated a higher degree of disorder compared to **{$W_{17}C_{20}$}**. Interestingly, for **{$W_{17}C_{16}$}**, the presence of disordered cylindrical micelles is only located in the frozen H_2O pocket and becomes straighter, and highly ordered when in contact with the carbon surface. It is clear the carbon surface interacts with the cylindrical micelles to reduce curvature of the tubes, causing the tubes to form longer and straighter arrays, therefore reducing the contact area between the tubes and carbon surface. Note, that the magnitude of repulsion is lower compared to **{$W_{17}C_{20}$},** as we see **{$W_{17}C_{16}$}** cylindrical micelles grow closer to neighbouring tubes in the solvent pocket and appear to not divert growth away from the carbon support at the interface to the same magnitude. Therefore, the chain length of the hybrid surfactant does indeed play a significant role in the assembly process, and the behavioural differences are amplified through the interaction with charged carbon supports. Moreover, although the packing parameter does not predict the cylindrical micelles in this case due to factors such as temperature, concentration and cation effects not being accounted for, it does give us values which correlate well with surfactant chain length, which suggest that longer chain lengths are more likely to form cylindrical micelles. The calculated packing parameter (N_s) trend is somewhat present in the cryo-TEM investigation based on the structural order exhibited across the chain length range.

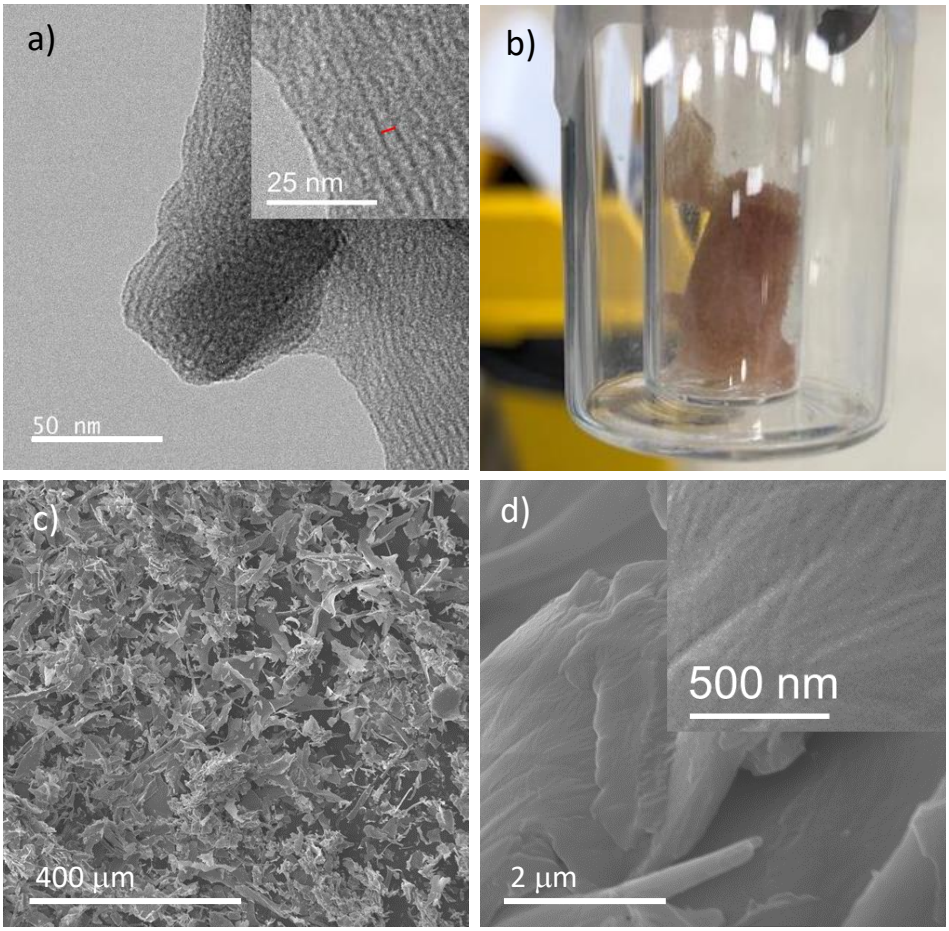

Figure 61 - a) TEM image of freeze-dried cylindrical micelles of $\{W_{17}C_{20}\}$, where the inset displays parallel alignment and pretzel-like intertwining; b) optical image of materials acquired from freeze-dried 1.4 mM aqueous solution of $\{W_{17}C_{20}\}$; c) and d) displays SEM images of freeze-dried material in b).

Once we had discovered this new transition to cylindrical micelles, we set out to isolate cylindrical micelles. Knowing the growth is triggered by freezing, we freeze-dried the cryo-prepared grid and analysed the grid under room tempterature TEM (Figure 61a). TEM analysis revealled material which possessed an ordered packing structure which closely resembled lamellar type assembly. However, due to the curvature and irregularities, it was clear that freeze-drying had removed the solvent but caused the cylindrical micelles to aggregate. Upon freeze-drying the micelle solution, a sponge-like material was produced, SEM analysis showed this material was contructed from thin flakes of material (Figure 61b & c). TEM analysis on the thin films confirmed that the sponge material is contrctued from 2D sheets of cylindical micelles packed together into a porus network (Figure 62a & b). Furthemore, we oberved sheets of material aligning perpendicular to each other, which was also observed by Deng

et al.[17] As mentioned this unique packing arrangement is due to the energetically favourable stacking of the cylindical micelles in order to reduce unfavourable repulsive contact area between polyanionic tubes (Figure 62b). This process respresents transition from 0D micelles to 3D higher-ordered metal-oxide materials.

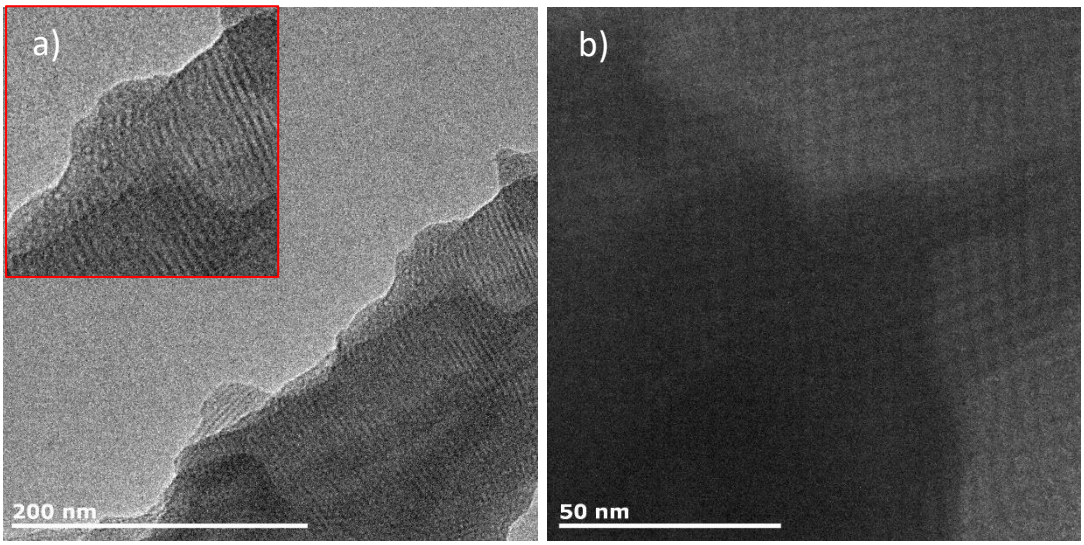

Figure 62 - TEM image displaying curled sheets of $\{W_{17}C_{20}\}$ cylindrical micelles a) and the cross-hatching stacking arrangement of cylindrical micelles b).

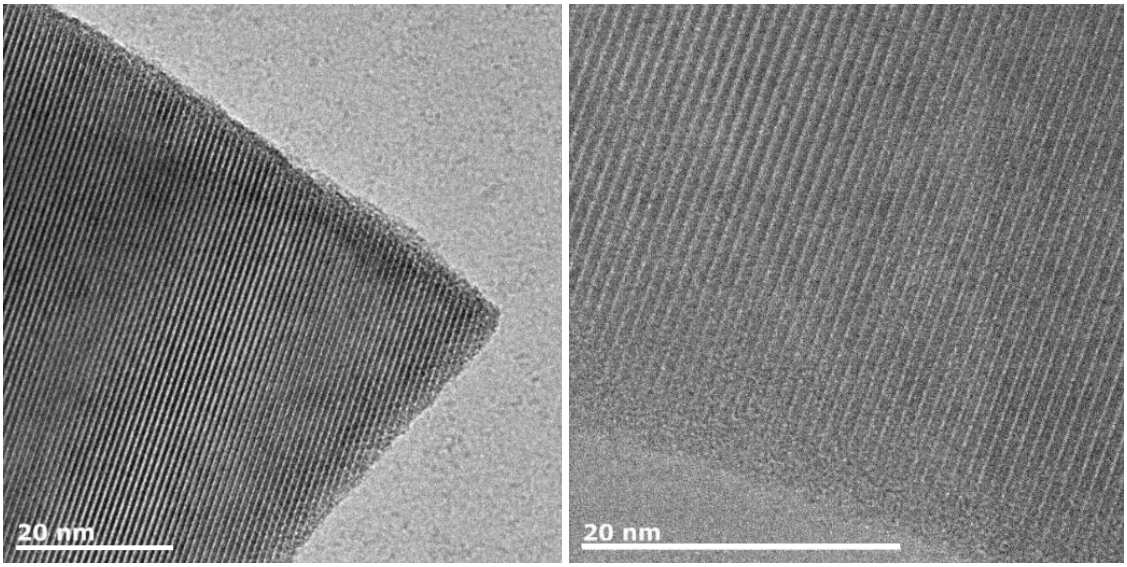

Figure 63 - WO_3 material produced from the calcination of $\{W_{17}C_{20}\}$ freeze-dried material at 700 °C for 1 h.

Once, we had characterised the cylindrical micelle network (**$\{W_{17}C_{20}\}$-CMN**), we endeavoured to convert this soft material to solid-state WO_3 whilst retaining the nanostructure. When the "sponge material was calcined at 700 °C, a grey flakey powder was obtained (**$\{W_{17}C_{20}\}$-CMN@700**). Under the

TEM (Figure 63), thin wafers of cystalline material were observed which possessed d-spacing of approx. 0.95 nm. This does not corroberate with literature values of WO_3,[33] however, this distance is slightly smaller than the width of a POM. Based on the TEM, there is crystallinity and long-range order, neverthless, this highly ordered material cannot be WO_3. Similar to the calcination product obseved by Wei *et al.*, the cylindrical micelles seem to have transitioned to into nanowire sheets consisting of rows of POMs or mixed phases of WO_3,[17] where the amphiphilic carbon has been pyrolysed, leaving a highly ordered framwork structure. Based on the IR spectrum (Figure 64b) we can see that the there is a clear tranistion in the W-O-W bending modes at 850-550 cm^{-1} upon calcination at different temperatures. This suggests that there is a phase transition still occuring at 800 °C. Interestingly, the

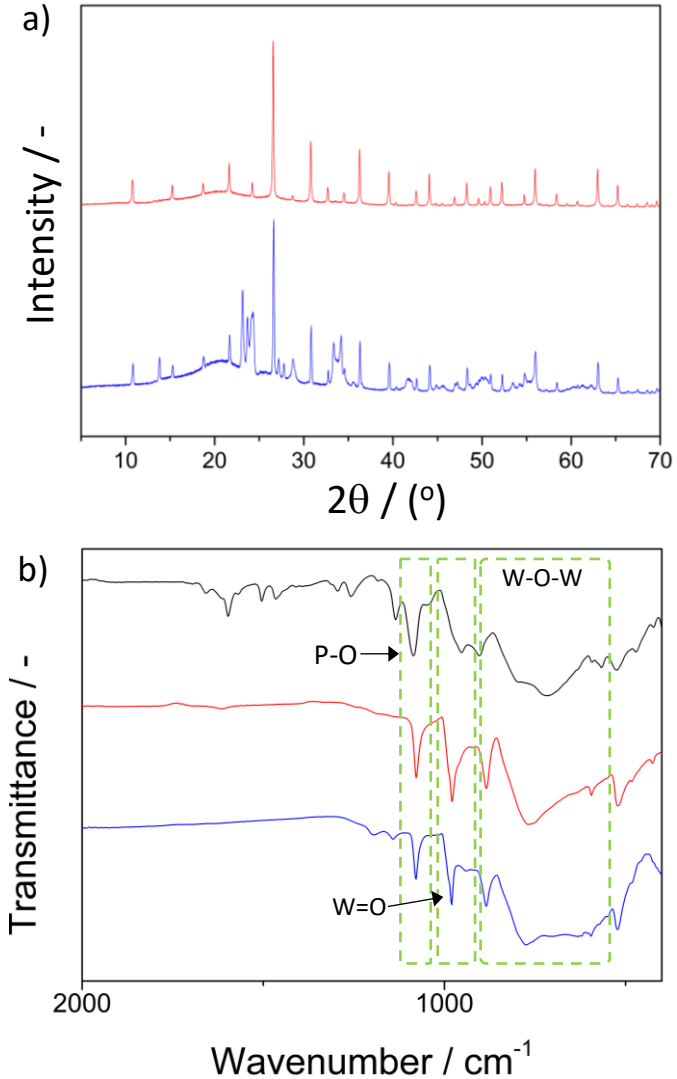

Figure 64 - Displays the PXRD spectra a) of {$W_{17}C_{20}$}-CMN@700 (red) and {$W_{17}C_{20}$}-CMN@800 (blue); and FT-IR spectrum b) of {$W_{17}C_{20}$}NT (black) and {$W_{17}C_{20}$}-CMN@700 red) and {$W_{17}C_{20}$}-CMN@800 (blue) with key peaks highlighted.

P-O stretch at 1075 cm^{-1} remains post calcination at which suggests the product maybe dopped with phosphorus. Furthermore, the calcined material at 700 °C observes a high degree of crystallinity based on PXRD analysis (Figure 64a). However, the resprentitive peaks do not resemble the index peaks of WO_3. Futhermore, based on the PXRD of the 800 °C calcined material, three new major diffraction peaks at 2θ angles 23.1°, 23.6°, and 24.3° represent the (002), (020), and (200) planes, respectively, for monoclinic-WO_3.[35] However, peaks in the material calcined at 700 °C are also present, this infers the presense of mixed WO_3 phases. Therefore, a longer time is needed to reach pure phases of the WO_3 product.

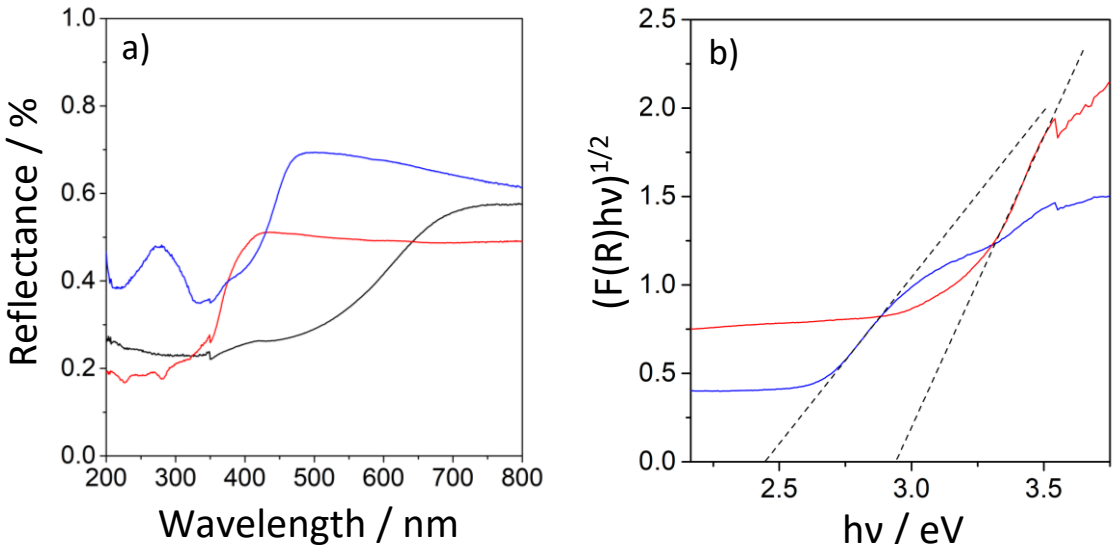

Figure 65 - Displays the diffuse reflectance (R %) spectra a) of {$W_{17}C_{20}$}-CMN (black), {$W_{17}C_{20}$}-CMN@700 (red) and {$W_{17}C_{20}$}-CMN@800 (blue); and b) K-M function *vs*. photon energy to determine optical bandgap of {$W_{17}C_{20}$}-CMN@700 (red) and {$W_{17}C_{20}$}-CMN@800 (blue).

For **{$W_{17}C_{20}$}-CMN@700** and **{$W_{17}C_{20}$}-CMN@800** and the **{$W_{17}C_{20}$}-CMN** analogue, diffuse reflectance spectroscopy was conducted to analyse its optical absorption (Figure 65). **{$W_{17}C_{20}$}-CMN** optical absorption onset was far into the visible region owing to its red colour (Figure 65a). However, both calcined materials absorption onset was blue shifted towards the UV region. Due to the fact that **{$W_{17}C_{20}$}** sponge material is a soft-assembly with molecular based HOMO-LUMO energy levels, the band-gap energy was not extrapolated. For both calcined materials, the Kubelka-Munk function was applied as $(Fhv)^{1/2}$ *vs*. hv, where $F = \frac{(1-R)^2}{2R}$ is the Kubelka–Munk absorption coefficient (R is the

reflectance) and hv is the photon energy.[34] The onset of light absorption was extrapolated to determine the indirect band-gap energy (E_g). **{$W_{17}C_{20}$}-CMN@700** and **{$W_{17}C_{20}$}-CMN@800** displayed band-gap energies of 2.44 eV and 2.94 eV respectively. These values fall well with in the values obtained in the literature.[35, 36] However, further analysis of the PXRD and longer calcination temperatures are needed to fully characterise the WO_3 phases.

We have demonstrated and investigated a hierarchical self-assembly associated with the transition from 0D micelles to a 3D solid state network of cylindrical micelles, trigger by freezing. To the best of our knowledge this is the first example of freezing induces hierarchical self-assembly associated with hybrid-POM amphiphiles. Furthermore, we have demonstrated the opportunities around isolating these high-ordered structures in the fabrication of nanostructured metal-oxide materials.

3.4 CONCLUSION

This project demonstrated unique hierarchical self-assembly events with regards to redox-active hybrid POM amphiphiles. Specifically, both cases represent the rare hierarchal structures exhibited with in Class II hybrid-POM species.

We have reported the spontaneous self-assembly of redox-active amphiphiles at various carbon surfaces, which resulted in contrasting surface assemblies based on the hydrophilicity of the surface. This dynamic assembly process led to the formation of a redox-active SAM at GC electrode surface, which displayed stable redox-activity, and was characterised electrochemically and structurally through cyclic voltammetry and a range of surface techniques such as, AFM, ellipsometry and SEM. We observed that when **{$W_{17}C_{20}$}** was introduced to a hydrophobic surface, a deconstructive interaction led to the hierarchical transition of micelles to fibrous structures. Whereas, when **{$W_{17}C_{20}$}** micelles were exposed to hydrophilic surfaces, 2D SAM were formed, retaining the micelle structural integrity and therefore, indicating that the dominant interaction at the electrode was hydrophilic in nature.

Freezing-induced hierarchical self-assembly from micelles to cylindrical micelles was also observed. These assemblies demonstrated long-range order and displayed growth patterns dictated by the electrostatic repulsion between neighbouring tubes and the charged carbon surfaces. Furthermore, the effect of chain length demonstrated that shorter chain length led to larger degree of disorder, based on the formation of shorter "worm-like" micelles, and less stable cylindrical micelles upon contact with the electrostatic repulsion of the carbon surface, where we only observed micelles for **{$W_{17}C_{12}$}**. Based on the complexity of the hierarchical assembly system, it is particularly difficult to deduce the mechanism associated with the transition, however, it is clear that chain length has a clear effect on the construction of stable cylindrical micelles with long range order. Furthermore, as these assemblies are only observed when frozen, temperature is likely to play a significant role in the hierarchical transition. Moreover, we demonstrated that these structures could be isolated by freeze-

drying, which led to the fabrication of a 3D sponge material constructed of 2D sheets of parallel stacked cylindrical micelles. Therefore, we have demonstrated hierarchical self-assembly from 0D micelles to a 3D network constructed from 2D cylindrical sheets, which were characterized by TEM and SEM. This work represents the first example of freezing induced hierarchical-self-assembly of Class II hybrid POMs.

Finally, the 3D sponge material was calcined to nanostructured WO_3. Here, we demonstrated that upon calcination, the structure of the 2D sheets was retained when annealed at 700°C to from thin sheets of WO_3. Furthermore, upon calcination at 800 °C, a new phase of WO_3 was accessed with respect to the lower temperature calcination product. Each material was characterized by IR, SEM, TEM, diffuse reflectance spectroscopy and PXRD. We found that the WO_3 phase access at 800°C possessed a smaller bandgap than the product produced at 700 °C.

Overall, the showcased hierarchical self-assembly demonstrated by **{$W_{17}C_{20}$}** gives rise to opportunities to stimulate the growth of higher-ordered structures, which have exhibited the ability to act as redox-active self-assembling electrode materials, with potential application in electrocatalysis and sensing. Moreover, this example of stimulated growth has also highlighted the opportunities to isolate networks of nanostructured metal oxide superstructures which can be annealed to produce metal oxide nanomaterials, with potential photo/electrocatalytic properties.

3.5 REFERENCES

1. N. Mizuno, J. Varkey, N. C. Kegulian, B. G. Hegde, N. Cheng, R. Langen and A. C. Steven, *J. Biol. Chem.*, **2012**, 287, 29301-29311.
2. P. Bajpai, in *Biermann's Handbook of Pulp and Paper (Third Edition)*, ed. P. Bajpai, Elsevier, **2018**, 381-400.
3. W. T. Godbey, in *An Introduction to Biotechnology*, ed. W. T. Godbey, Woodhead Publishing, **2014**, 9-33.
4. J. Feher, in *Quantitative Human Physiology (Second Edition)*, ed. J. Feher, Academic Press, Boston, **2017**, 130-141.
5. L. A. Rodríguez-Guadarrama, S. K. Talsania, K. K. Mohanty and R. Rajagopalan, *Langmuir*, **1999**, 15, 437-446.
6. J. N. Israelachvili, D. J. Mitchell and B. W. Ninham, *J. Chem. Soc., Faraday Trans.*, 1976, 72, 1525-1568.
7. Y. Lu, J. Lin, L. Wang, L. Zhang and C. Cai, *Chem. Rev.*, **2020**, 120, 4111-4140.
8. X. Ma and Y. Zhao, *Chem. Rev.*, **2015**, 115, 7794-7839.
9. S. Mondal, T. K. Ghosh, B. Chowdhury and P. Ghosh, *Inorg. Chem.*, **2019**, 58, 15993-16003.
10. V. Khentov, V. V. Semchenko and H. H. H. Hussein, in *Direct Synthesis of Metal Complexes*, ed. B. Kharisov, Elsevier, **2018**, 279-313.
11. M. Lee, S.-J. Lee and L.-H. Jiang, *J. Am. Chem. Soc.*, **2004**, 126, 12724-12725.
12. A. C. Mendes, E. T. Baran, R. L. Reis and H. S. Azevedo, *WIRES NANOMED NANOBI*, **2013**, 5, 582-612.
13. T. Kakuta, T.-a. Yamagishi and T. Ogoshi, *Acc. Chem. Res*, **2018**, 51, 1656-1666.
14. J. Luo, B. Zhang, C. Yvon, M. Hutin, S. Gerislioglu, C. Wesdemiotis, L. Cronin and T. Liu, *Eur. J. Inorg. Chem.*, **2019**, 380-386.
15. S. She, Z. Huang, P. Yin, A. Bayaguud, H. Jia, Y. Huang, Y. Wei and Y. Wei, *Chem. Eur. J.*, **2017**, 23, 14860-14865.
16. Z. He, Y. Yan, B. Li, H. Ai, H. Wang, H. Li and L. Wu, *Dalton T.*, **2012**, 41, 10043-10051.
17. Y. Ren, Y. Zou, Y. Liu, X. Zhou, J. Ma, D. Zhao, G. Wei, Y. Ai, S. Xi and Y. Deng, *Nat. Mater*, **2020**, 19, 203-211.
18. D. Mandler and S. Kraus-Ophir, *J Solid State Electrochem.*, **2011**, 15, 1535.
19. C. Freire, D. M. Fernandes, M. Nunes and M. Araújo, in *Advanced Electrode Materials*, **2016**, 147-212.
20. R. DeClements, G. M. Swain, T. Dallas, M. W. Holtz, R. D. Herrick and J. L. Stickney, *Langmuir*, **1996**, 12, 6578-6586.
21. B. Khadro, I. Baroudi, A.-M. Goncalves, B. Berini, B. Pegot, F. Nouar, T. N. Ha Le, F. Ribot, C. Gervais, F. Carn, E. Cadot, C. Mousty, C. Simonnet-Jégat and N. Steunou, *J. Mater. Chem. A*, **2014**, 2, 9208-9220.
22. A. S. Cherevan, S. P. Nandan, I. Roger, R. Liu, C. Streb and D. Eder, *Adv. Sci. Lett.*, **2020**, 7, 1903511.
23. Y. Yi, G. Weinberg, M. Prenzel, M. Greiner, S. Heumann, S. Becker and R. Schlögl, *Catal.*, **2017**, 295, 32-40.
24. N. S. Mughal, D. A. Walsh and G. N. Newton, *ACS Appl. Energy Mater.*, **2020**, 3, 12308-12315.
25. A. K. Cuentas-Gallegos, S. López-Cortina, T. Brousse, D. Pacheco-Catalán, E. Fuentes-Quezada, H. Mosqueda and G. Orozco-Gamboa, *J. Solid State Electrochem.*, **2016**, 20, 67-79.
26. Z. Liu, T. Liu and M. Tsige, *Sci. Rep*, **2016**, 6, 26595.
27. Z. Liu, T. Liu and M. Tsige, *Sci. Rep*, **2018**, 8, 13076.
28. I. Khosravi, Z. Shahryari, S. M. Jazaeri Moghadas, H. T. Sarraf and M. Yeganeh, in *Corrosion Protection at the Nanoscale*, eds. S. Rajendran, T. A. N. H. Nguyen, S. Kakooei, M. Yeganeh and Y. Li, Elsevier, **2020**, 127-140.
29. S.-L. Xu, C. Wang, Q.-D. Zeng, P. Wu, Z.-G. Wang, H.-K. Yan and C.-L. Bai, *Langmuir*, **2002**, 18, 657-660.
30. H. Gong, B. Bredenkötter, C. Meier, C. Hoffmann- Richter, U. Ziener, D. G. Kurth and D. Volkmer, *ChemPhysChem*, **2007**, 8, 2354-2362.
31. H. Kawasaki, M. Uota, T. Yoshimura, D. Fujikawa, G. Sakai, R. Arakawa and T. Kijima, *Langmuir*, **2007**, 23, 11540-11545.
32. P. A. Albouy, S. Deville, A. Fulkar, K. Hakouk, M. Impéror-Clerc, M. Klotz, Q. Liu, M. Marcellini and J. Perez, *Soft Matter.*, **2017**, 13, 1759-1763.
33. D. Nagy, D. Nagy, I. M. Szilágyi and X. Fan, *Rsc Adv.*, **2016**, 6, 33743-33754.
34. P. Makuła, M. Pacia and W. Macyk, J. Phys. Chem. Lett, **2018**, 9, 6814-6817.
35. W. L. Kwong, N. Savvides and C. C. Sorrell, *Electrochim. Acta.*, **2012**, 75, 371-380.
36. P. P. González-Borrero, F. Sato, A. N. Medina, M. L. Baesso, A. C. Bento, G. Baldissera, C. Persson, G. A. Niklasson, C. G. Granqvist and A. Ferreira da Silva, *Appl. Phys. Lett.*, **2010**, 96, 061909.

4 DEVELOPMENT OF DIPHOSPHONATES HYBRID POMS: ELECTRONIC STRUCTURE MODULATION AND LIGAND PLATFORMS

4.1 INTRODUCTION

Class II hybrid POMs are a more recently developed field of POM research which we can benefit from synergistic effects of the organic moieties and POM clusters through covalent hybridisation. As we have previously discussed, based on this type of construction, POMs have been grafted to hydrophobic ligands to produce redox-active amphiphiles and assemblies.[1-3] Not only has this demonstrated the ability to impart the POM with functionality based on coupling of functional ligands, but has also been shown to modulate the electronic properties of POMs based on their electronic effects.[4, 5, 6] For instance, Odobel *et al*. initially reported an investigation into the electrochemical difference between siloxane linkers and phosphonate linkers when hybridised to the POM.[7, 8] Here, the phosphonate hybrid induced a positive shift of the first and the second redox potential, whereas the siloxane group had the opposite effect, compared to the parent POM **{W_{18}}**. This was attributed to the electron withdrawing and inductive electron donating nature of the phosphonate and siloxane group respectively. This was further developed by Oshio *et al*. where the phosphonate's electron -withdrawing nature was probed by coupling electron-rich and electron-poor aromatic groups to the POM *via* the phosphonate linker, resulting in predictable tuning of the redox potentials. This demonstrated that the electronic structure could be further tuned through design of the organic scaffold in addition to the grafting group.[4, 7]

Monophosphonate linkers are now well established as linkers for Keggin and Wells-Dawson clusters. However, diphosphonate (DP) molecules are relatively unexplored as linkers or ligands for lacunary POM species despite being heavily employed for their medicinal properties in relation to anti-tumour and calcification inhibition properties.[9-11] These species possess the same number of -OH ligands bound to the phosphorus with respect to the phosphonates, which enables them to act as linkers or

ligands in a similar way. Generally, diphosphonate molecules are commercially available and synthetically attainable by a variety of different routes.[11, 12]

To date, a range of examples exist of DP hybrid-POMs. Key examples by Dolbeque *et al*. have worked on the development of DP molecules with the general formula $H_2O_3PC(OH)(R)PO_3H_2$, some of which have shown anti-tumour properties.[13] It was found that once these ligands are deprotonated, they can form complex structures with V, Mo and W, with the formation of polynuclear complexes (1-12). Dolbeque and co-workers set out to combine the anti-tumour properties of both ligand and metal fragments to develop POMs with enhanced anti-tumour properties. Initial investigations found that the DP alendronate (Ale) complexed to Mo, yielding $Mo_{12}Ale_4$, exhibited IC_{50} values of ~10 µM against human breast cancer cells (MCF-7) in vitro. This represents a fourfold activity compared to alendronate alone, indicating some synergistic effects.[13]

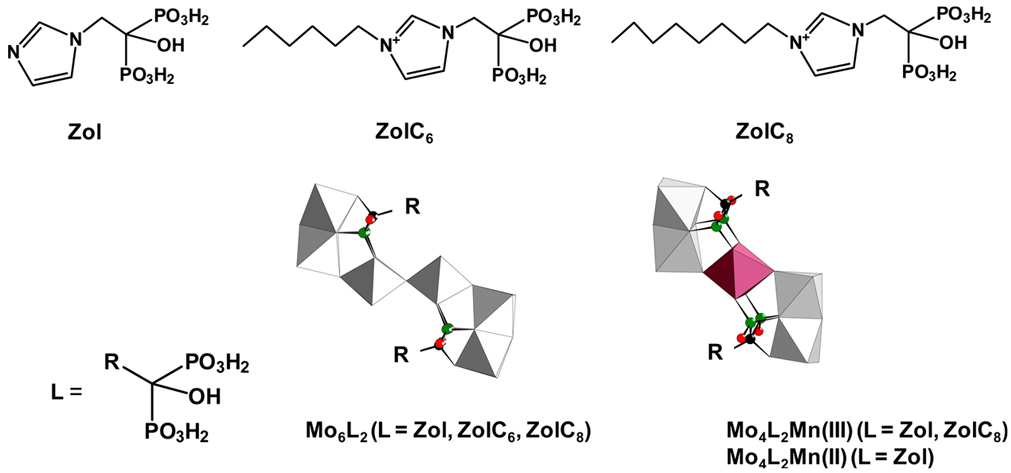

Figure 66 - Schematic structures of biologically active diphosphonate hybrid-POMs. Gray polyhedra= MoO_6, purple polyhedron = MnO_6, green spheres = P, black spheres= C, red spheres = O. Reproduced from ref.13 with permission from American Chemical Society

Later, the group then conducted similar synthesis with zoledronate (Zol), affording a hexanuclear complex $[(Mo^{VI}_3O_8)_2O(Zol)_2]^{6-}$. By also incorporating a Mn centre, Mn(III)-containing POM $[(Mo^{VI}_2O_6)_2(Zol)_2Mn]^{5-}$ was synthesised (Figure 66). This POM displayed activity against breast cancer cells. Interestingly, the type of DP played a role in the cell growth inhibition, demonstrating that the

structure of these ligands could be manipulated to enhance the activity of POM DP hybrids towards enhanced anti-cancer properties. [10, 13, 14]

Furthermore, DP ligands have been hybridised with [MO_x] fragments to synthesise a large range of intricate multinuclear organo-metallic structures.[15] The first example of a polytungstate diphosphate hybrid was the polyanion $[(P_2O_7)_4W^{VI}_{12}O_{36}]^{16-}$ (W^{VI}_{12}**POP**$_4$)(POP=pyrophosphate), this structure possessed a unique dodecameric structure of an unusual open "*saddle-shaped*" **{W_{12}}** architecture, capped by four POP groups (P-O-P angle = 123.71°). A similar compound was synthesised by incorporating isoelectronic methylene diphosphonate ligand (PCP). Both compounds **{$W^{VI}_{12}POP_4$}** and **{$W^{VI}_{12}PCP_4$}** displayed anti-DNA polymerase activity and inhibition activity towards HIV-1 reverse transcriptase, with IC_{50} values ranging from 2-10 μM.[16]

It is clear that hybrid-POM complexes incorporating DP ligands have potent synergistic effects with applications in medicine. However, it is still unclear how the change in DP structure effects the electronic properties of the overall POM. To the best of our knowledge, no examples exist of these ligands being employed to modulate the electronic properties of redox rich Wells-Dawson POMs and simultaneously be modified to act as linkers.

4.2 AIM

The aim of this chapter is to investigate how commercially available DP moles can be employed as ligands to hybridised to lacunary Wells-Dawson clusters and whether they can be used to modulate the properties of the POM cluster. Three new Wells-Dawson hybrid clusters will be synthesised based on the hybridisation of 3 different diphosphonate ligands: i) methylenediphosphonate (MDP), ii) imidodiphosphonate (IDP) and iii) pyrophosphate (PP). These cluster will be structurally characterised, and the electronic effects exhibited on the POM will be evaluated. Furthermore, their photooxidative properties will be tested. Finally, we aim to demonstrate that based on modifications on the MDP linker motif, DP molecules can be used as linkers to couple other organic moieties to the POM cluster.

4.3 Results and Discussion

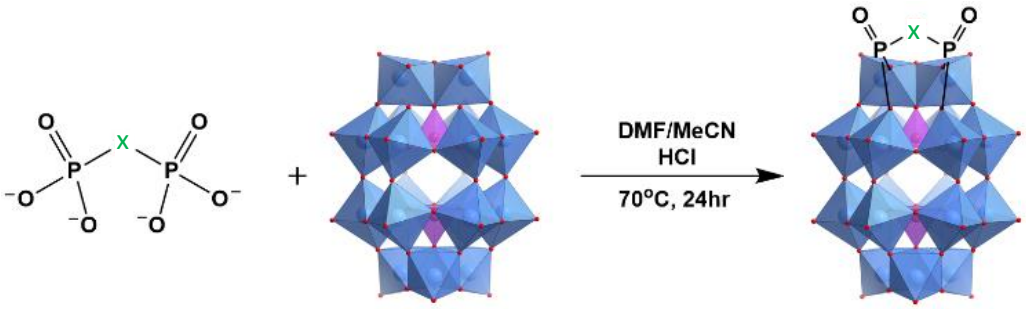

Figure 67 - Schematic illustrating the hybridisation reaction between $\{W_{17}\}$ and DP to form $\{W_{17}DP\}$ hybrid molecules where X= CH_2, NH and O. Molecule colour code: blue polyhedra = $\{WO_6\}$, purple polyhedra = $\{PO_4\}$, red spheres = O.

4.3.1 Synthesis

The synthesis of these compounds was optimised from a previously known method for producing K^+ salts of the hybrids. Firstly, all three hybrids were synthesised in the presence of DMF and a catalytic amount of HCl (Figure 67). Owing to the hydrolytic instability of the acidic PP and IDP ligands, the ligands are only commercially available as tetra-sodium salts. Combining the hydrolytic instability and basic nature of these salts, several attempts were made to mitigate ligand hydrolysis in solution and basic degradation of the POM. We found that the most effective way to synthesise pure IDP and PP hybrids was to acidify the POM and ligand separately for 5 mins in solution at 40 °C, followed by mixing both solutions (or suspensions) together and heating at 70 °C. This ensured that both the surrounding solution and the molecules were sufficiently protonated and both yielded as light green powders (15 % and 20% respectively). Note that only a catalytic amount of acid was used to also mitigate acid catalysed hydrolysis of the ligand. Due to the robust nature of the MDP ligand, an already established 1 pot method was adopted to yield the pure hybrid cluster as a light-yellow powder (61 %). Details regarding the work up for these molecules can be found in the experimental section. These hybrid-POM molecules will now be named as **$\{W_{17}MDP\}$**, **$\{W_{17}IDP\}$** and **$\{W_{17}PP\}$**.

4.3.2 Structural Characterisation

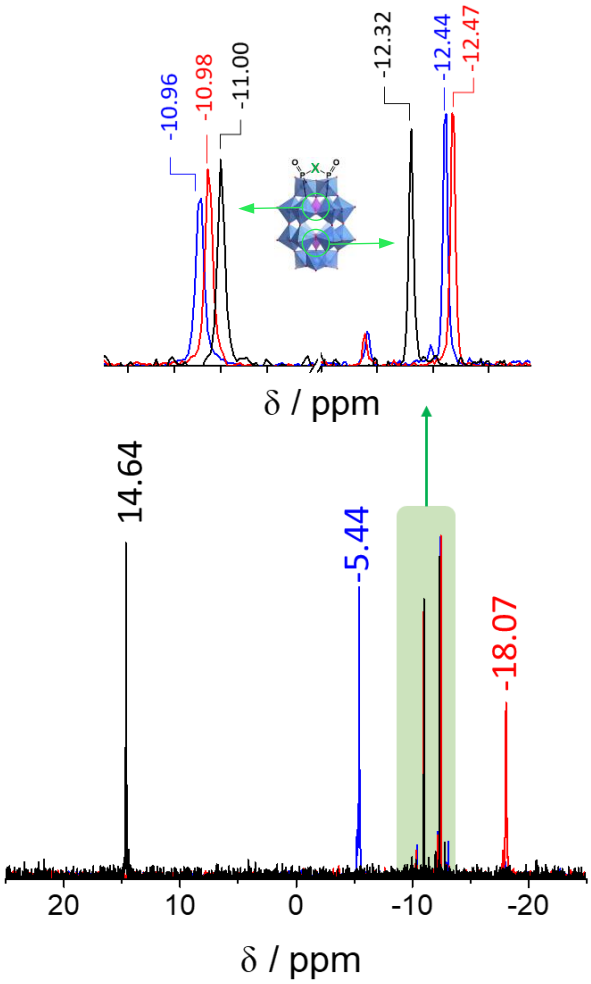

Figure 68 - ^{31}P NMR of {W_{17}DP} hybrids MDP (black), IDP (blue) and red (oxygen) in d_3-MeCN.Top spectra is a zoomed in region highlighted in green on the bottom spectra.

Due to the lack of non-exchangeable protons on the ligands, the main tool employed to confirm hybridisation was ^{31}P NMR (Figure 68). We observe three peaks for each hybrid which corresponds to one peak for the phosphorus on the symmetrical ligand and two peaks for internal phosphates of the POM. Due to the electronic contribution of phosphonate-based ligands, the phosphorus environments of the POM shift from values associated with the monolacunary Wells-Dawson **{W_{17}}.** If we first look at the relative signals of the ligands, the peak associated with the MDP in **{W_{17}MDP}** is significantly shifted downfield at 14.64 ppm with respect to ligand environments of **{W_{17}IDP}** and **{W_{17}PP}**. Shifts associated with the ligands of **{W_{17}IDP}** and **{W_{17}PP}** can be found upfield at -5.44 ppm and -18.07 ppm respectively. The trend we observe regarding the relative position of the phosphorus peaks of the ligands are directly correlated to the electronic contribution of the central heteroatom of the

ligand. For example, noting that the POM exhibits an overall electron-withdrawing nature on the ligand, each ligand exhibits a downfield shift. Although the methylene group has a slight overall inductive electron donating effect, we observed a downfield shift. When comparing **{W_{17}IDP}** and **{W_{17}PP}**, we see the ligands peaks are significantly more shielded compared to **{W_{17}MDP}**. This trend is a result of significant electron-donating contribution associated with the inductive effects where the lone pairs located on the central N and O facilitate extensive orbital mixing. The presence of two lone pairs on the PP oxygen results in a significantly higher degree of shielding of the phosphorus compared to the MDP and IDP. When analysing the peak associated with the internal POM phosphates of the hybrids, we observe a similar trend associated with the degree of electron induction contributed by the ligand, where the bottom phosphate (P2) tends to be most shielded for **{W_{17}PP}** and least for the **{W_{17}MDP}**. However, for the upper phosphate (P1) located closer to the lacuna, the trend stands for **{W_{17}IDP}** and **{W_{17}PP}**, and not for the **{W_{17}MDP}**, where P1 for the **{W_{17}MDP}** and is the most upfield and shielded.

The nature of these molecules was also characterised by ESI-MS. See Tables 1-3 for the corresponding assigned peaks. The most intense peak in the sigmoid for **{W_{17}MDP}** corresponds to observed m/z = 2186.98 for 2- charged species which is assigned to $H_3(C_2H_8N)$**{W_{17}MDP}**$^{2-}(H_2O)$, where 3 protons and a dimethylammonium cation (DMA^+) are coordinated to the cluster. Similarly, intense peak in the sigmoid for **{W_{17}IDP}** and **{W_{17}PP}** corresponds to observed m/z = 2170.96 and 2160.93 for 2- charged species which is assigned to HNa_3**{W_{17}IDP}**$^{2-}$ and $H_3(C_2H_8N)$**{W_{17}PP}**$^{2-}$ respectively.

{W_{17}MDP}			
Assignment	**z**	***m/z (calc.)***	***m/z (obs.)***
{$Na_3(C_2NH_8)[W_{17}P_2O_{61}(P_2CH_2O_2)]$}	2-	2192.86	2192.98
{$Na_2(C_2NH_8)_2[W_{17}P_2O_{61}(P_2CH_2O_2)]$}	2-	2204.40	2204.48
{$HNa(C_2NH_8)_2[W_{17}P_2O_{61}(P_2CH_2O_2)]$}	2-	2193.41	2193.47
{$H_2K(C_2H_8N)[W_{17}P_2O_{61}(P_2CH_2O_2)]$}	2-	2178.86	2178.97
{$H_3(C_2H_8N)[W_{17}P_2O_{61}(P_2CH_2O_2)H_2O$}	2-	2168.89	2168.97
{$H_3(C_2H_8N)[W_{17}P_2O_{61}(P_2CH_2O_2)](H_2O)_2$}	2-	2177.90	2177.99
{$H_3(C_2H_8N)[W_{17}P_2O_{61}(P_2CH_2O_2)](H_2O)_3$}	2-	2186.90	2186.98
{$(C_2H_8N)H_3[W_{17}P_2O_{61}(P_2CH_2O_2)](H_2O)_4$}	2-	2195.91	2195.98
{$(C_2H_8N)Na_2H_4[W_{17}P_2O_{61}]$}	3-	1419.60	1419.64
{$Na_3H_3(C_2H_8N)[W_{17}P_2O_{61}]$}	3-	1426.93	1426.98

Table 3 - Mass spectrum peaks corresponding to {W_{17}MDP}$^{n-}$.

{W_{17}IDP}			
Assignment	**z**	***m/z (calc.)***	***m/z (obs.)***
{$H_4[W_{17}P_2O_{61}(P_2O_2NH)]$}	2-	2137.86	2137.96
{$H_3Na[W_{17}P_2O_{61}(P_2O_2NH)]$}	2-	2148.85	2148.85
[{$H_2Na_2\{W_{17}P_2O_{61}(P_2O_2NH)]$}	2-	2159.84	2159.95
{$HNa_3[W_{17}P_2O_{61}(P_2O_2NH)]$}	2-	2170.83	2170.96
{$H_3[W_{17}P_2O_{61}(P_2O_2NH)]$}	3-	1424.90	1424.95
{$H_3Na_4[W_{17}P_2O_{61}]$}	3-	1419.24	1419.28

Table 4 - Mass spectrum peaks corresponding to {W_{17}IDP}$^{n-}$.

{W_{17}PP}			
Assignment	**z**	***m/z (calc.)***	***m/z (obs.)***
{$H_4[W_{17}P_2O_{61}(P_2O_3)]$}	2-	2138.35	2138.46
{$H_3Na[W_{17}P_2O_{61}(P_2O_3)]$}	2-	2149.34	2149.45
{$H_3K[W_{17}P_2O_{61}(P_2O_3)]$}	2-	2157.33	2157.46
{$H_3(C_2H_8N)[W_{17}P_2O_{61}(P_2O_3)]$}	2-	2160.88	2160.93
{$H_3(C_2H_8N)]\{W_{17}P_2O_{61}(P_2O_3)](H_2O)$}	2-	2169.88	2169.92
{$H_4[W_{17}P_2O_{61}(P_2O_3)(H_2O)]$}	2-	2147.35	2147.44
{$H_7[W_{17}P_2O_{61}](H_2O)$}	3-	1395.93	1395.93

Table 5 - Mass spectrum peaks corresponding to {W_{17}PP}$^{n-}$

4.3.3 Electronic Characterisation

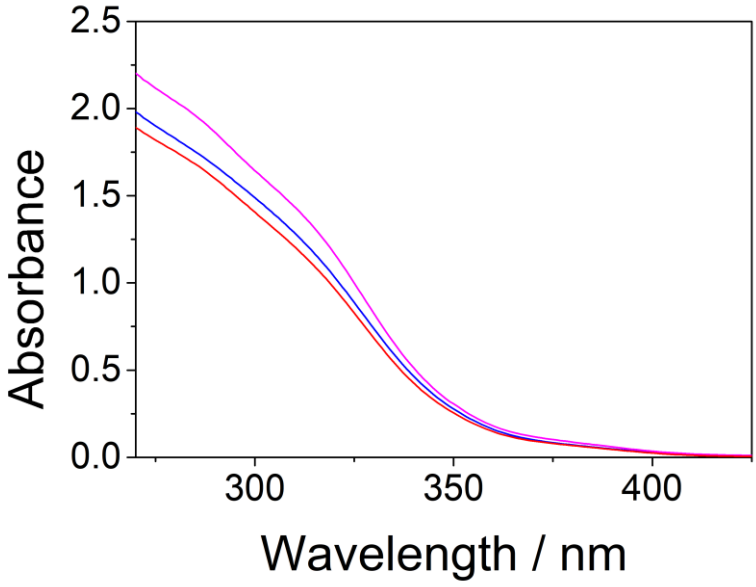

Figure 69 - UV-Vis spectrum of 5 x 10^{-5} mM {W_{17}MDP} (pink), {W_{17}IDP} (blue) and {W_{17}PP} (red).

POMs exhibit rich photochemical properties which can be triggered through the excitation of the O→M charge transfer (LMCT) band.[17] The result of this is the formation of a short-lived charge separated state where an electron is excited from a spin-paired, doubly occupied bonding orbital (HOMO) to an empty antibonding orbital (LUMO), this results in the formation of radical centred at the oxo-ligand, rendering it a potent oxo-radical that can take part in a range of oxidation and hydrogen abstraction reactions.[18,19] Commonly, this photo-activation is limited to the UV region of the spectrum. Modification of POMs through organo-functionalisation has proven to also be an effective method to modulate the HOMO-LUMO levels of the molecule and push this excitation towards visible wavelengths. UV-Vis spectroscopy can be employed to investigate alterations in the optical properties of POMs post-hybridisation, including the presence of charge transfer bands, the contribution of the organic component to the LUMO and, most importantly, the absorption edge at which POM-based LMCT can occur. However, due to the complexity in the optical properties of these polynuclear clusters, the observed LMCT bands are particularly broad, which causes difficulties in identifying noticeable changes in the absorption properties, regardless of the ligand mediated effects. When

comparing the three hybrid-POMs, we observe minor differences as we suspected, however, an increase trend in the molar extinction coefficient **{W_{17}MDP}** > **{W_{17}IDP}** > **{W_{17}PP}** up to the solvent window was observed. **{W_{17}MDP}** also appeared to be slightly red-shifted in relation to the other two hybrids and demonstrated a more intense LMCT absorption band.

To further elucidate the correlation between the ligand's electronic properties and the hybrid molecule's electronic structure, we employed cyclic voltammetry (CV) as a tool to acquire the relative reduction potentials. CV was performed on all hybrid-POMs in anhydrous DMF with 0.1 M [TBA][PF_6] as the supporting electrolyte under an argon atmosphere (Figure 70). A three-electrode setup was employed with a glassy carbon (d = 3 mm) working electrode, Pt wire was the counter electrode, Ag

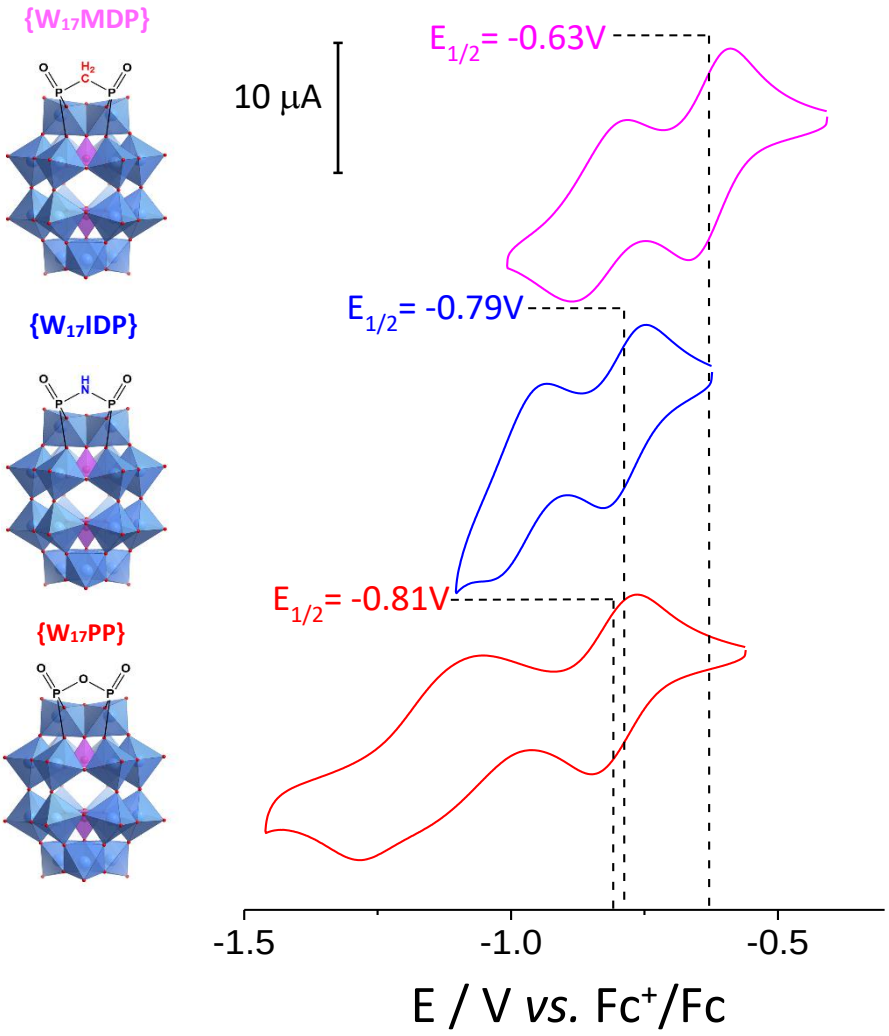

Figure 70 - CV of {W_{17}DP} *vs.* Fc^+/Fc redox couple. The $E_{1/2}$ potentials are highlighted for the first redox process.

wire as a pseudo-reference and Ferrocene/Ferrocenium (Fc^+/Fc) redox couple as the external reference.

As mentioned, the electronic nature of the coupled ligands can have profound effects on the HOMO-LUMO energies of the hybrid-POM molecule. The chosen ligands all differ when comparing the electronegativity and the number of lone pairs associated with the central heteroatom, resulting in varying electronic induction effects imposed on the POM. The electronic characteristics therefore are expected to affect the redox properties of the POM in contrasting ways. Comparing the first redox process for all three compounds (Figure 70), we can see that all three compounds exhibit two quasi-reversible processes, all of which are shifted positive with respect to their parent anion **{W_{18}}** ($E_{1/2}$ = - 1.168 V *vs.* Fc^+/Fc). This observation is ascribed to the electron-withdrawing nature of the phosphonates, leading to reduced electron density on the W centres, which in turn lowers the LUMO energy.[5, 7, 20] **{W_{17}MDP}** displayed the most positive redox process ($E_{1/2}$ = - 0.63 V), followed by **{W_{17}IDP}** ($E_{1/2}$= -0.79 V) and **{W_{17}PP}** ($E_{1/2}$ = - 0.81 V). This trend can be attributed to the induction effects presented by central heteroatom of the DP ligand. The **{W_{17}PP}** possess two lone pairs of electrons on the central O atom of the ligand which can further contribute electron-density onto the POM through the phosphonates, this addition orbital mixing and electron density contribution will, therefore, reduce the ability of the POM cluster to accept electrons, leading to a more negative reduction potential. The lone pair trend also explains the positive shift (+ 20 mV) of the first redox process of **{W_{17}IDP}** with respect to **{W_{17}PP}**, where only one lone pair of electrons are located on the nitrogen. As a result, **{W_{17}MDP}** electron-donation onto the POM is minimal which leads to a positive shift of + 160 mV and + 180 mV of the redox process with respect to compounds **{W_{17}IDP}** and **{W_{17}PP}** is observed. The observed trend in the electrochemical behaviour fits well with the ^{31}P NMR trend where **{W_{17}PP}** hybrid exhibits an upfield shift due to induction electron-donating behaviour and **{W_{17}MDP}** observing weaker inductive behaviour. Based on the relative reduction potentials, **{W_{17}MDP}** is the most readily reduced, indicating that it should have the lowest LUMO energy. Conversely, **{W_{17}PP}** should have the highest.

4.3.4 Photoreduction Investigation

As previously alluded to, In 2018 Newton *et al*. discovered that based on the electronic effects imposed by the ligand on the POM, the frontier LUMO orbitals of the POM could be engineered to photoactivate the POM for photocatalysis.[4] Here they correlated the magnitude of electron withdrawing effects of the phosphonate ligand to the photocatalytic degradation of indigo blue dye. The cluster with the most electron withdrawing group (-COOH) displayed the highest photoactivation and catalysis towards oxidative dye degradation. Similarly, we embarked on understanding how the trend observed in the electronic characterisation reflected in the molecule's photoactivity *vs*. parent anion **{W_{18}}.**

In this experiment, we irradiated the hybrid-POM in the presences of DMF which is employed to act as the sacrificial electron doner and solvent. Upon irradiation, LMCT will be triggered, giving rise to a localised d_1 electron on the metal centre and a short-lived charge separated state, where an oxo-radical is formed. This radical is then quenched through oxidation of DMF. This results in a trapped d_1 electron forming a reduced POM, where the trapped electron will undergo IVCT, resulting in the delocalised electron blue colour of the POM – *"heteropolyblue*" state. The reaction was monitored using UV-Vis spectroscopy where we expect to observe an increase in the ICVT band corresponding to the increasing concentrations of the n electron reduced species and growth of new bands based on multiple electron reduced species of the POM, each observing a unique IVCT band.[21, 22] We explored the photoactivity using 500 W mercury-xenon lamp (operating at 200 W) which emits strong UV and visible light. To determine the photoactivity of these clusters with visible light, additional experiments were run with a 395 nm cut-off filter.

Each experiment was conducted under an inert atmosphere to mitigate any reoxidation of the reduced species by atmospheric oxygen. A reoxidation experiment was also conducted by measuring the regression of the IVCT band every 2 mins for approx. 1.5 hours with the solution exposed to atmospheric oxygen to monitor the rate of reoxidation.

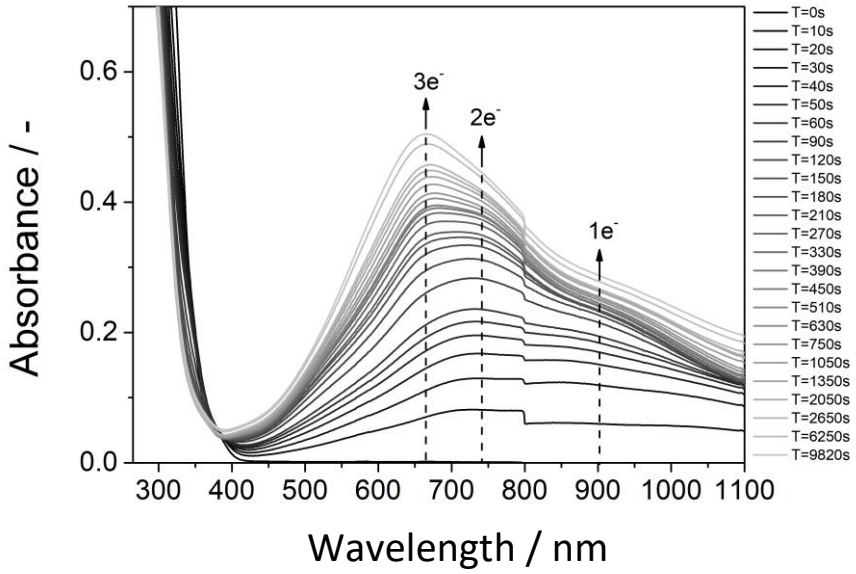

Figure 71 - Photoreduction of $\{W_{18}\}$ using UV-vis light which displays growth of the IVCT bands representing single to triple reduced states.

To start the investigation, we conducted the experiment with parent analogue **$\{W_{18}\}$**, by irradiating with UV-Vis light in DMF (Figure 71). Here we observe instant reduction to the second electron species within 10 seconds with the corresponding IVCT bands located for the $1e^-$ and $2e^-$ at 902 nm and 732 nm respectively. These reduced states become saturated upon 90 s and 330 s irradiation. The 3rd electron reduction also gradually appears at 664 nm and appears to dominate the spectral absorbance with its growth from 60s onwards and saturates at 9820 s. When employing the cut-off filter at 395 nm, saturation of the expected 1st electron reduction was negligible after 5 hours of irradiation. This is likely due to the lack of energy provided through visible light to photoexcite an electron from the HOMO to the LUMO due to a large energy gap. Therefore, **$\{W_{18}\}$** is not photoactive under-visible light irradiation.

Now that we have analysed the reduced states of the parent anion, we can now compare the results of the hybrids to this benchmark. Figure 72a displays the UV-Vis spectrum of **{W_{17}MDP}** when irradiated with UV-Vis light. Here we observe the rapid initial growth of the $1e^-$ and $2e^-$ IVCT bands at

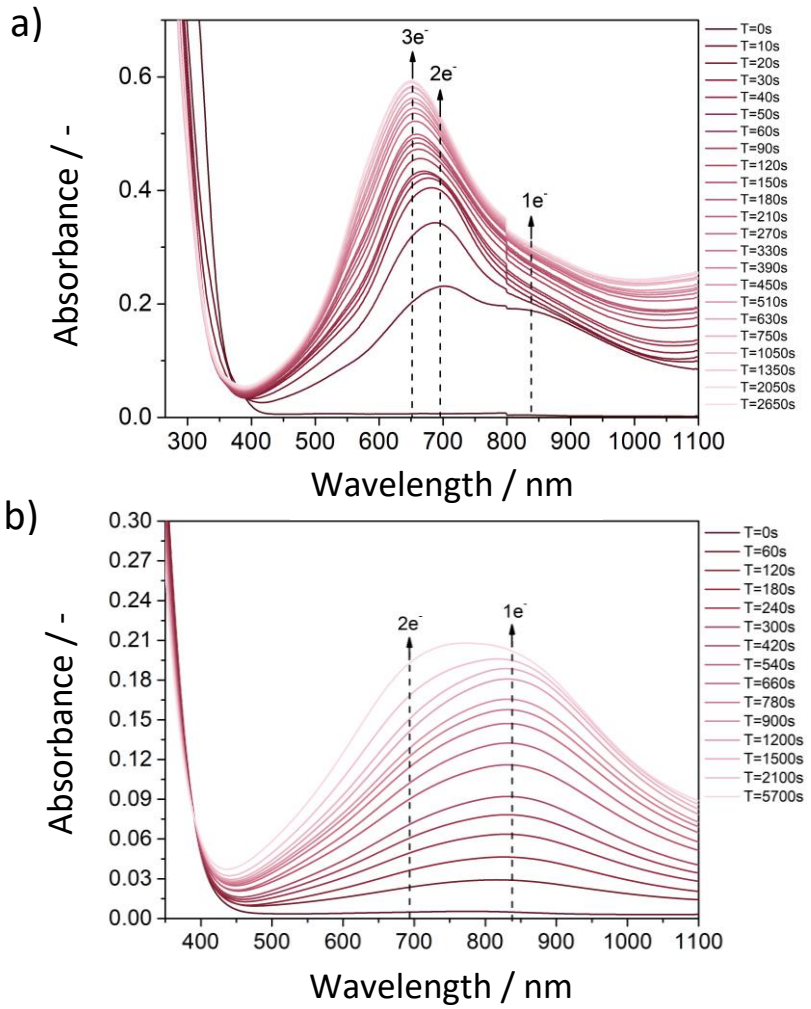

Figure 72 - Photoreduction of {W_{17}MDP} using a) UV-vis and b) visible light which displays growth of the IVCT bands representing single to triple reduced states.

691 nm and 873 nm respectively after the first 10 s of irradiation. The IVCT band corresponding to the 3rd electron reduced POM species grows after 60 s at 652 nm. Similarly, the same experiment was repeated but with a 395 nm cut-off filter. Figure 72b displays the photoreduction profile where we can observe the growth of the IVCT bands. Here we observe lower photoactivity based on the relative absorbance intensity of the IVCT bands in the same time frame compared to the experiment conducted with UV-Vis. Unlike the parent analogue, **{W_{17}MDP}** does exhibit significant visible light

photoactivity. Here, we can see the saturation of the IVCT band corresponding the $1e^-$ reduced species at 837 nm after 2100 s. Interestingly, we also observe the growth of the $2e^-$ reduced species band at 691 nm after 2100 s. Comparing the observed activity to the **{W_{18}}**, we can see a significantly greater photoactivity in the visible regime. This can be attributed to the overall electron withdrawing effects of the phosphorus located on the ligand. As mentioned, this photoactivation corroborates well with results observed by Newton *et al*.[4]

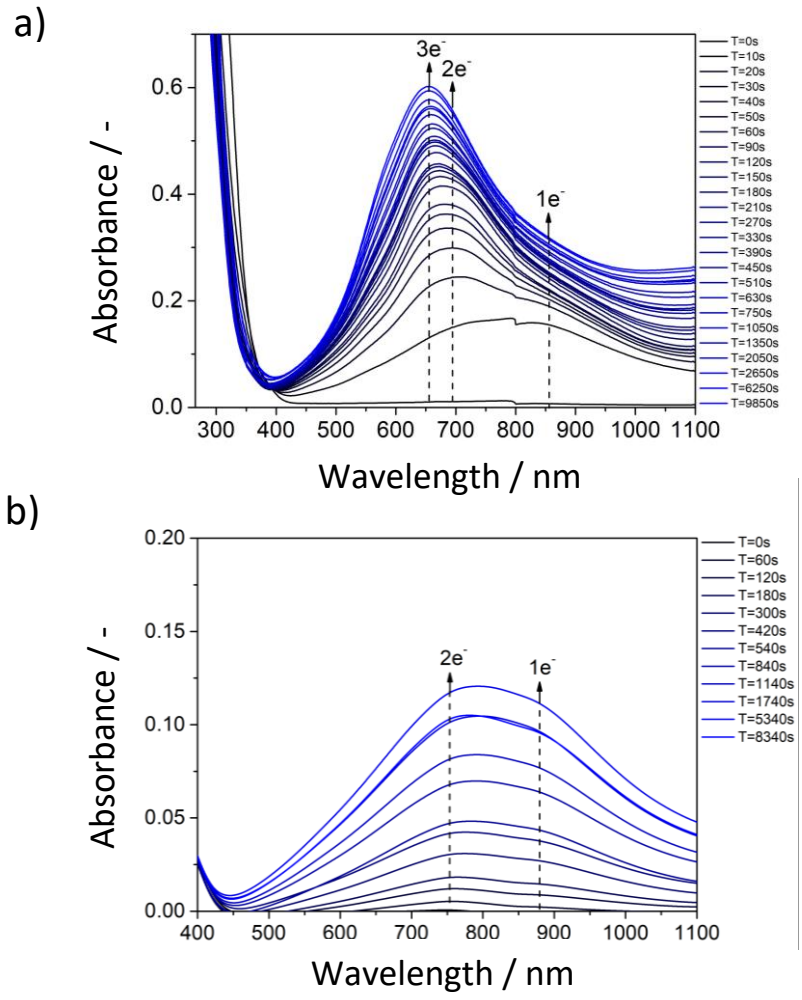

Figure 73 - Photoreduction of {W_{17}IDP} using a) UV-vis and b) visible light which displays growth of the IVCT bands representing single to triple reduced states.

Next, we analysed **{W_{17}IDP}** in the same manner (Figure 73a and b). Under the full UV-Vis spectral irradiation, the IVCT band corresponding to the $1e^-$ and $2e^-$ reduced species emerges at 855 nm and 693 nm respectively within 10 s. The $1e^-$ and $2e^-$ reduced species saturate in 30 s and 90 s respectively. The 3e- species is observed to dominate the growth in absorbance after 90 s and is located at 655 nm. Moving to the visible-light photoirradiation study, we see the growth of the $1e^-$ and $2e^-$ species at a similar pace at 880 nm and 753 nm, saturating at 8340 s. Interestingly, we observe the growth of the $2e^-$ species at a higher wavelength compared to the UV-Vis photo experiment. This maybe a result of isolating the more energetically favourable tautomer of the ligand with UV irradiation, therefore, leading to a different absorption profile for the doubly reduced species.[23] This could also be a result of hybrid degradation to another photoactive species.

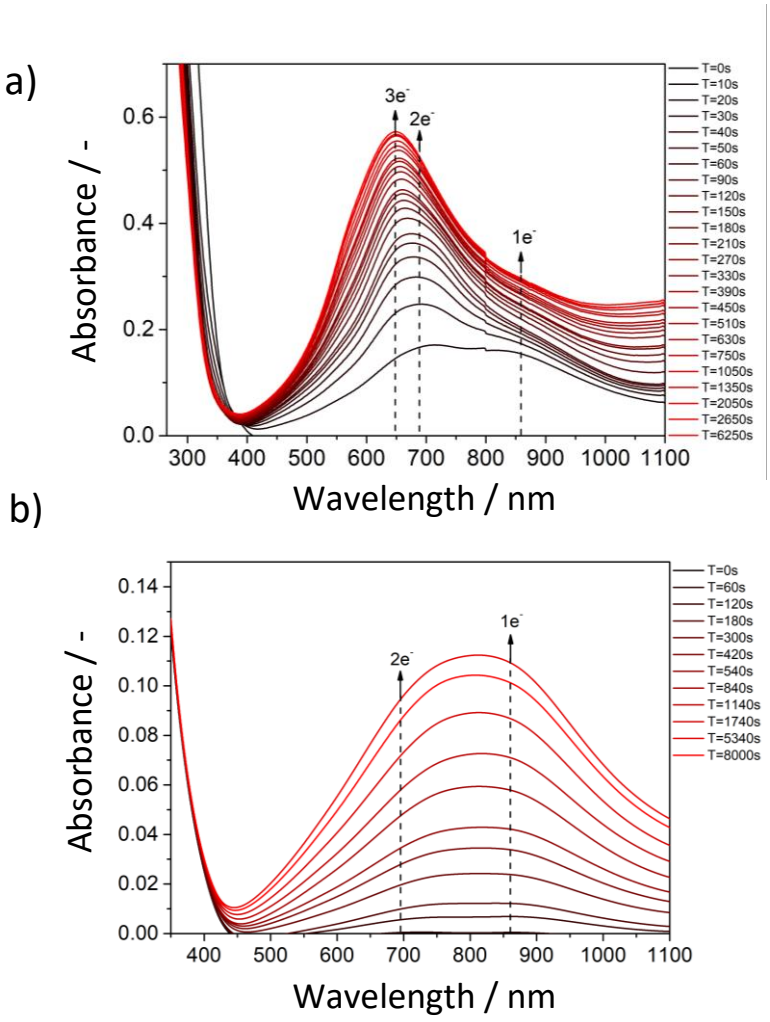

Figure 74 - Photoreduction of {W_{17}PP} using a) UV-vis and b) visible light which displays growth of the IVCT bands representing single to triple reduced states.

Finally, with the same approach we analysed the final hybrid **{W_{17}PP}** (Figure 74a and b). Under the full UV-Vis spectral irradiation, the IVCT band corresponding to the $1e^-$ and $2e^-$ reduced species grew in at 861 nm and 695 nm respectively within 10 s. The $1e^-$ and $2e^-$ reduced species saturate in 30 s and 90 s respectively. The $3e^-$ species is observed to dominate the growth in absorbance post 60 s and is located at 649 nm. Moving to the visible-light photoirradiation study, we see the growth of the 1e- and $2e^-$ at 880 nm and 753 nm. The growth of the $2e^-$ species is less defined compared to the previous two hybrids, which is expected based on its more negative reduction potential (indicating higher LUMO). Therefore, we can expect the rate of reduction to be slower for this compound.

To compare the direct photoactivity of the hybrid POM series, a plot of the absorption percentage (converted from its max saturation) was plotted against time for 1-$3e^-$ reduced species (Figure 75a & b and 76). Where the rate for the $2e^-$ and $3e^-$ species was extrapolated from the UV-Vis irradiation experiment and the $1e^-$ species from the visible light irradiation. Figure 9a & b shows the plots representing the relative growth of the IVCT bands under the UV-Vis irradiation experiments. Here we can see a trend in the photoexcitation of the hybrid: **{W_{17}MDP}** > **{W_{17}IDP}** > **{W_{17}PP}** > **{W_{18}}**. This trend correlates well with the reduction potentials acquired from CV, where the **{W_{17}MDP}** is reduced at lower potential followed by **{W_{17}IDP}** and **{W_{17}PP}** closely. Therefore, the rate of reduction for **{W_{17}MDP}** is expected to be faster than that of the other two hybrids and inevitably better photoactivity against the parent analogue **{W_{18}}**.

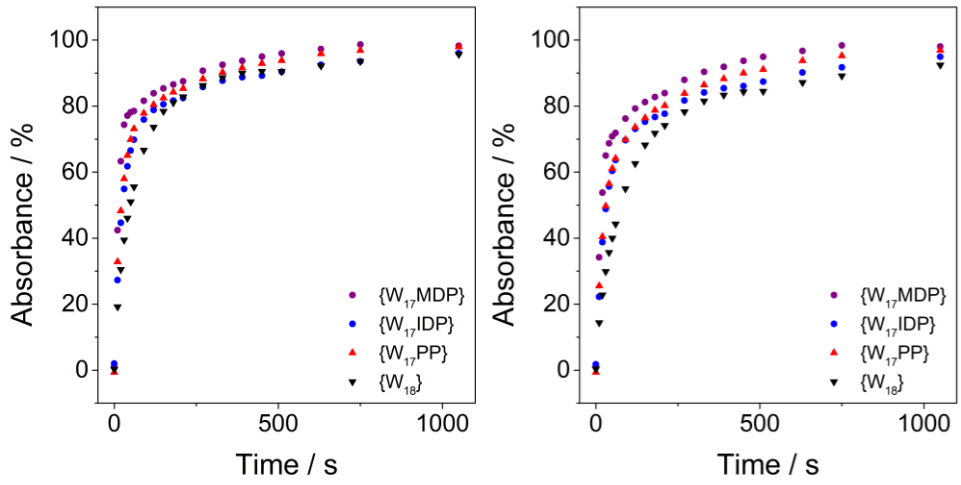

Figure 76 - Plots of absorbance *vs*. time for the rate of IVCT band evolution for a) $3e^-$ (UV-Vis) and b) $2e^-$ (UV-Vis)

Based on the visible-light photoreduction experiment (Figure 76), the trend based on the nature of the ligand holds well, with the exception of the slightly greater rate of reduction observed for **{W_{17}IDP}** against **{W_{17}PP}**. Due to their similar reduction potentials, they are expected to perform relatively similar. What we do observe here is that the relative rates of reduction correlated well with the magnitude of electron-donating behaviour and reduction potentials (i.e. **{W_{17}MDP}** has the least electron-donating character, lowest reduction potential and fastest reduction rate). Under the visible-light regime, we observe a similar trend. However, **{W_{17}IDP}** observes a slightly faster reduction rate

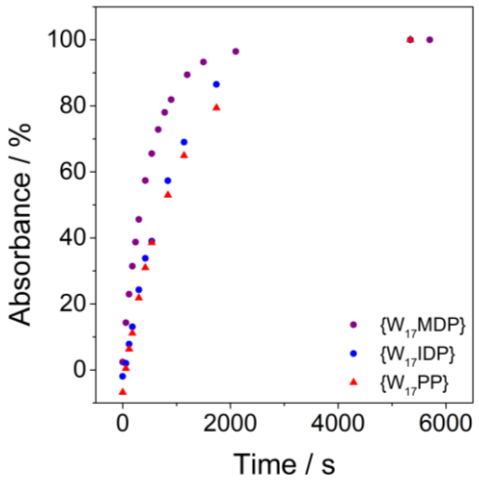

Figure 75 - Plots of absorbance *vs.* time for the rate of IVCT band evolution for $1e^-$ reduced species.

than **{W_{17}PP}** in the visible regime. This may be a result of **{W_{17}PP}** possessing a higher LUMO energy level, therefore the quantum efficiency will be lower compared to the UV-Vis regime.

To ascertain whether these species could perform as aerobic photocatalysts, rapid regeneration is crucial. For this reason, once the POM reduced states were saturated, the reduced solutions were left to re-oxidise in the presence of atmospheric oxygen. Figure 77 displays the plots of the decay in the IVCT bands vs time. Here we see an inverse trend in the reoxidation of the POM, where the more readily reduced **{W_{17}MDP}** possesses the slowest reoxidation rate. We can see the trend for the reoxidation fits the inverse trend for the $3e^-$ and $1e^-$ experiments conducted under UV-Vis and Visible light irradiation, respectively.

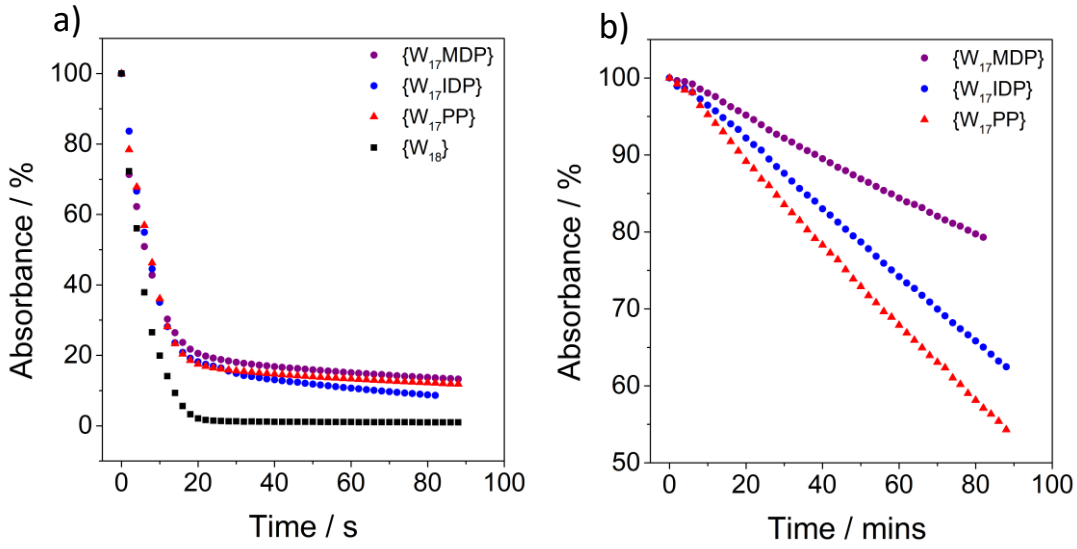

Figure 77 - Absorbance *vs*. time plots for the reoxidation of a) $3e^-$ and b) $1e^-$ {W_{17}DP} reduced species.

Overall, through the development of **{W_{17}DP}** hybrids, we have demonstrated that DP ligands can hybridise to the POM and be used to modulate the photoactivity of POM clusters. Where the DP hybrid-POMs have shown enhanced photoactivity under both UV-Vis and visible light regimes with respect to their parent analogue **{W_{18}}.**

4.3.5 Functionalisation of POMs through Diphosphonate Linkers

Once we had structurally characterised and probed the electronic structure of the developed Wells-Dawson DP hybrid POMs, we set out to exploit these ligands as potential linkers to introduce additional functional groups to this new class of Wells-Dawson hybrid POM. Based on the three ligands studied, **{W_{17}MDP}** and **{W_{17}IDP}** possessed the ability to be employed as linkers to which other organic moieties could be grafted to. For this project, we focused on the functionalisation of methylene -based diphosphonates. Due to the ease of functionality and the commercial availability, we employed tetraisopropylvinilydene diphosphonate (VinDp) as our linker system. VinDP possess a reactive vinyl group which is attached to electron withdrawing phosphonates. This allows nucleophilic addition reactions to occur readily with mild conditions. Our aim was to explore the versatility of this new route and demonstrate the opportunities surrounding this route to synthesise organofunctionalized hybrid POMs (i.e. synthesis of biomolecules or amphiphiles). Michael additions in general are mild which is why they can be used in ligation coupling reactions to peptides.[24] Inspired the work of Klumpp *et al*.,[25] where successful Michael-addition of amnio acid esters to *N*-heterocycles,

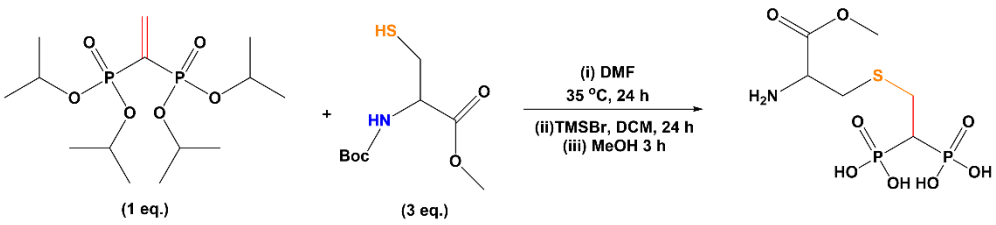

Figure 78 - Reaction scheme for thiol Michael-addition of ester protected cysteine.

we set out to test Michael-addition reaction on VinDP. Initially, we focused on testing the reaction with biological molecules, which would allow us to synthesise materials with biological and amphiphilic properties.

We employed an ester-protected cysteine as our chosen nucleophilic reagent, to perform a thiol-based Michael-addition (Figure 78). We found that at low temperature of 35 °C, the Michael addition was successful with 100 % conversion in 24 h. Further work carried out also demonstrated that amine

Michael-addition reactions are also successful, however, the purification procedure for these compounds needs further development. Now that we had successfully coupled our chosen ligand, phosphonate-isopropyl ester and amine-Boc protecting groups were cleaved with TMSBr overnight at room temperature, and the TMS hydrolysed off the phosphonate with MeOH to generate our cystine-diphosphonic acid ligand. The next stage involved the hybridisation of Cys-DP with **{W_{17}}** POM lacuna site. By employing our previous hybridisation methodology, we found that we could successfully couple Cys-DP to the POM, yielding **{W_{17}CysDP}**.[1] We initially characterised this structure *via* ^{31}P NMR spectroscopy (Figure 79) however, further detailed analysis is needed.

Based on this new approach to synthesise diphosphonate ligands, we have demonstrated that by employing a Michael-addition reaction to commercially available VinDP, it is possible to convert biomolecules to suitable phosphonic acid ligands primed for hybridisation to POMs. Furthermore, the

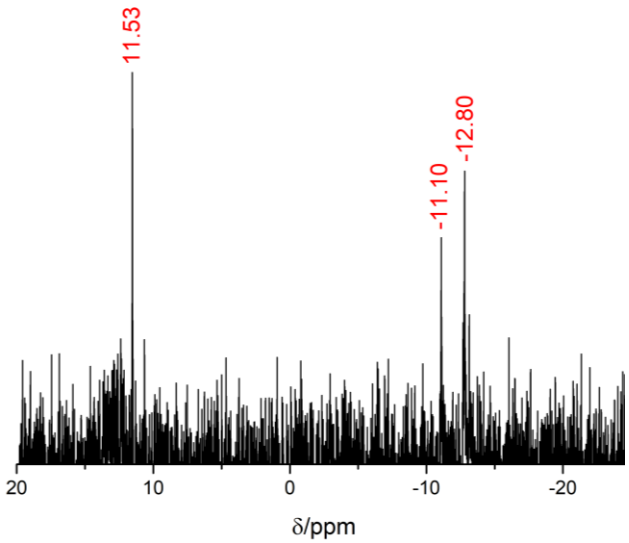

Figure 79 - ^{31}P NMR of {W_{17}Cys} in d_3-MeCN with labels signals.

mild conditions give rise to opportunities to couple more complex protein or peptide structures. Moreover, the possibility of thiol selective coupling of VinDP allows opportunities for site selective addition of POMS to larger peptides or protein structures. Overall, this new approach to generating singly functionalised POMs can be applied to generate a broad range of hybrids. Future work will be

needed to understand the limitations of the reactions and to generate single chain hybrid POM amphiphiles.

4.4 CONCLUSION

In summary, we have synthesised a new class of hybrid polyoxometalates based on the hybridisation of diphosphonate. These clusters were structurally characterised *via* NMR spectroscopy and MS. There electronic properties were also probed by employing UV-Vis spectroscopy and CV. We found that these ligands hybridised to the POM cluster stoichiometrically. Based on the electrochemical results, we found that all hybrids were redox-active and displayed a positive shift in the first redox process with respect to parent anion **{W_{18}}**. Across the three hybrids, **{W_{17}MDP}** possessed the most positive reduction (lowest LUMO) followed by **{W_{17}IDP}** and **{W_{17}PP}**, which indicated that it was more readily reduced compared to **{W_{17}IDP}** and **{W_{17}PP}**. This trend could be correlated to the electron donating behaviour of the ligands, where PP possessing two lone pairs contributed the most electron density to the POM cluster and therefore led to the most negative reduction potential (highest LUMO) of the three clusters.

Based on these results the photoreduction properties were compared under UV-Vis and Vis regimes. All hybrids displayed superior rates of photo reduction compared to **{W_{18}}** under UV-Vis irradiation. We found as expected **{W_{17}MDP}** possessed the highest rate of reduction under UV-Vis and visible light irradiation. **{W_{17}IDP}** and **{W_{17}PP}** exhibited similar photo reduction rates which corroborates will with the experimentally acquired reduction potentials being very similar. Conversely, **{W_{17}MDP}** was the slowest to oxidise which fits well, possessing the most stable LUMO energy of the three. All three hybrids did show recovery to the ground state through oxidation with atmospheric oxygen.

Finally, we demonstrate that these DP molecules can not only be used as ligands but can be employed as linkers. By employing VinDP we could connect molecules through nucleophilic Michael-addition. Here we showed that ester protected bio molecules could be coupled to VinDP under mild conditions,

and further hybridised to the POM to produce an amino acid functionalised hybrid-POM. This simple and mild approach can be used to fabricate hybrid POMs with single organo-functionalisation. Later work will involve the coupling of hydrophobic peptide molecules or hydrophobic alkyl chains using this method to fabricate redox-active bio molecules with supramolecular assembly properties.

Overall, we have demonstrated that DP based molecules can be employed as linkers and ligands for lacunary POMs. Upon hybridisation, they possess the ability to modulate the HOMO-LUMO energies of the POM based on the combined electronic effects of the phosphonate and central heteroatom. DP molecules can, therefore, be employed as a way to enhance the photocatalytic ability of the POM clusters whilst simultaneously grafting ligand moieties such as bio molecules to generate enhanced hybrid molecules with potential applications in medicine, drug delivery and photocatalysis.

4.5 EXPERIMENTAL

Synthesis of Wells-Dawson - α,β-$K_6[P_2W_{18}O_{62}]$ - $\{W_{18}\}$

$Na_2WO_4.2H_2O$ (100 g,0.303 mol) was dissolved in deionised H_2O (117 mL) and stirred for 10 mins. To the colourless solution, 4 M HCl (83 ml, 0.33 mol) was added to the solution dropwise, forming a white precipitate that dissolved with further stirring. 4 M H_3PO_4 (83 mL, 0.33 mol) was then added drop wise to form a pale-yellow solution. The mixture was heated at reflux (100 °C) for 24 h. The bright yellow solution was then cooled to r.t., followed by addition of KCl (50 g, 0.67 mol) to form a chalky-yellow precipitate. The solution was stirred for 10 mins and filtered using a glass porous frit. The crude product was then recrystallized using minimum amount of hot H_2O to yield compound **1** (78 g, 96 %) as yellow crystals. ^{31}P NMR (162 MHz, D_2O) δ -13.02 ppm. IR(ATR) cm^{-1}: 1086.64, 952.23, 930.47, 899.11, 734.82.

Synthesis of Lacunary Wells-Dawson - α- $K_{10}[P_2W_{17}O_{61}]$ – $\{W_{17}\}$

$K_6[P_2W_{18}O_{62}]$ (40 g, 5.75 mmol) was dissolved in deionised water (100 mL). $KHCO_3$ (10 g, 0.1 mol) was then added to the reaction mixture and stirred overnight, forming a milky white precipitate. The precipitate was filtered and washed with deionised H_2O and acetone. The crude was recrystallized from minimum amount of hot H_2O to form $K_{10}[P_2W_{17}O_{61}]$ (32.99 g, 91 %) as white powder crystals.^{31}P NMR (162 MHz, D_2O) δ -7.19, -14.37. IR(ATR)cm^{-1}: 3540, 3442 (O-H, b), 1080.21, 1048.53, 1013.9, 935, 882.45, 796.88, 719.22.

Synthesis of $\{W_{17}MDP\}$

Methylenediphosphonic acid (15 mg, 0.056 mmol) was added to DMF (40 mL) followed by **$K_{10}[P_2W_{17}O_{61}]$** (0.25 g, 0.055 mmol) and 12 M HCl was added (50 μL). The temperature was then raised to 70 °C and left to stir for 16 h. The solution was then cooled to r.t. and centrifuged (8000 rpm, 5 mins) to remove the remaining solid. Et_2O was added (150 mL) to the solution until a white suspension was formed. The white suspension was then centrifuged, and the solvent was decanted off. The centrifuge tube with the remain white solid was when attached to the dried *in vacuo*, before being redissolved in a minimum amount of MeCN (5 mL). The suspension was centrifuged (8000 rpm, 5 mins) and decanted off before adding an excess of Et_2O (40 mL) to the solution. The white suspension was then centrifuged, and the solvent was decanted off. The centrifuge tube with the remain white solid was then dried *in vacuo*, before being redissolved in a minimum amount of acetone (2 mL). The suspension was centrifuged (8000 rpm, 5 mins) and decanted off before adding an excess of Et_2O (40 mL) to the solution and further centrifuged. The solution was decanted off and centrifuge tube with the remaining white solid was then dried under vacuum to yield **$K_6[P_2W_{17}O_{61}(P_2O_2CH_2)]$** as a grey solid (0.148 g, 61 %).^1H NMR (400 MHz, MeCN-d_3) δ 1.99 (s, 2H).^{31}P NMR (162 MHz, MeCN-d_3) δ 14.64, -11.00, -12.32; ATR-IR (cm^{-1}): 3650, 3201,1630, 1445, 1070, 945, 905, 800, 600.

Synthesis of $\{W_{17}IDP\}$

Tetrasodium imidodiphosphate (15 mg, 0.056 mmol) was added to DMF (20 mL) and 12 M HCl (25 μL). The suspension was stirred at 35 °C for 2 mins. The temperature was then raised to 70 °C, **$K_{10}[P_2W_{17}O_{61}]$** (0.25g, 0.055 mmol) was added to DMF (20 mL) and 12 M HCl (25 μL). The suspension

was also stirred at 35 °C for 2 mins. The two suspension mixtures were then added together and stirred for a further 2 mins at 35 °C before raising the temperature to 75 °C and stirring for 16 h. The solution was then cooled to r.t. and centrifuged (8000 rpm, 5 mins) to remove the remaining solid. Et_2O (150 mL) was added to the solution to form a white suspension which was then centrifuged. The solution was decanted and the solid was dried *in vacuo* and redissolved in MeCN (5 mL) where any precipitate was sonicated and centrifuged. Et_2O (40 mL) was added to the solution until a white suspension was formed. The white suspension was then centrifuged, and the solvent was decanted off. The centrifuge tube with the remaining white solid was then dried *in vacuo*, before being redissolved in a minimum amount of acetone (2 mL) and MeOH (1 mL). The suspension was centrifuged (8000 rpm, 5 mins) and decanted off before adding an excess of Et_2O (40 mL) again until a precipitate was formed. The centrifuge tube with the remain white solid was when then dried *in vacuo* to yield **$K_6[P_2W_{17}O_{61}(P_2O_2NH)]$** as a grey solid (0.0371 g, 15%).^{1}H NMR (400 MHz, MeCN-d_3) δ 3.45 (q, 1H); ^{31}P NMR (162 MHz, MeCN-d_3) δ -5.44, -10.96, -12.44; ATR-IR (cm^{-1}): 3650, 3201, 2987, 1731, 1390, 1222, 1070, 945, 905, 800 ,555.

Synthesis of {W_{17}PP}

Tetrasodium pyrophosphate (15 mg, 0.056 mmol) was added to DMF (20 mL) and 12 M HCl (25 μL). The suspension was stirred at 35 °C for 2 mins, **$K_{10}[P_2W_{17}O_{61}]$** (0.25g, 0.055 mmol) was also added to a separate solution of DMF (20 mL) and 12 M HCl (25 μL). The suspension was also stirred at 35 °C for 2 mins. The two suspension mixtures were then added together and stirred for a further 2 mins at 35 °C before raising the temperature to 75 °C and stirring for 16 h. The solution was then cooled to r.t. and centrifuged (8000 rpm, 5 mins) to remove the remaining solid. Et_2O was added (150 mL) to the solution until a white suspension was formed. The white suspension was then centrifuged, and the solvent was decanted off. The centrifuge tube with the remaining white solid was when dried *in vacuo*, before being redissolved in a minimum amount of MeCN (4 mL). The suspension was centrifuged (8000 rpm, 5 mins) and decanted off before adding an excess of Et_2O (40 mL) to the solution. The white suspension was then centrifuged, and the solvent was decanted off. The centrifuge tube with the remain white solid was dried *in vacuo*, before being redissolved in a minimum amount of acetone (4 mL). The suspension was centrifuged (8000 rpm, 5 mins) and decanted off before adding an excess of Et_2O (40 mL) to the solution. The centrifuge tube with the remain white solid was dried *in vacuo* to yield **$K_6[P_2W_{17}O_{61}(P_2O_3)]$** as a grey solid (0.0495 g, 20 %).^{31}P NMR (162 MHz, MeCN-d_3) δ -10.98, -12.47, -18.07ppm; ATR-IR (cm^{-1}): 3650, 3201, 1634, 1404, 1180, 1115, 937, 795, 660, 500, 480.

Synthesis of Cys-DP

N(*tert*-butoxycarbonyl)-L-cysteine methyl ester (428 mg, 2.26 mmol) was dried *in vacuo* for 30 mins before backfilling with argon, to this was added to tetraisopropyl vinylidenediphosphonate (184 mg, 0.516 mmol). To the mixture was added an DMF (1 mL) and stirred vigorously at 35 °C overnight. The mixture was centrifuged (8000 rpm, 5 mins) and concentrated *in vacuo* before sonicating in Et_2O. The protected product (400 mg, 0.676 mmol) was dried *in vacuo* and the flask evacuated before backfilling with argon. Dry CH_2Cl_2 (3 mL) was added followed by TMSBr (1.42 mL, 10.82 mmol). The mixture was stirred at 30 °C for 20 h. Upon completion excess TMSBr and solvent was removed *in vacuo*. The product was dissolved in minimum amount MeOH and precipitated out with an excess of acetone. The product was collected as a white powder and dried under vacuum (0.292 g, 0.904 mmol, 40 % yield). ^{31}P NMR (162 MHz, DMSO-d_6) δ 17.45; ESI-MS (MeCN) *m/z* (calculated, found): $[L\text{-}H]^-$ (323.00, 321.99).

Synthesis of Cys-DP hybrid-POM

$K_{10}[P_2W_{17}O_{61}]$ (0.25g, 0.055 mmol) was added to DMF (40 mL) at 40 °C followed by the **Cys-DP** (**$C_6H_{15}NO_8P_2S$**, 0.03 g, 0.093 mmol). To the suspension was added conc. HCl (50 µL) and stirred for a further 5 mins. The mixture was then heated to 75 °C and stirred overnight. The solution was then cooled to r.t. and centrifuged (8000 rpm, 5 mins) to remove the remaining solid. Et_2O was added (150 mL) to the solution until a white suspension was formed. The white suspension was then centrifuged, and the solvent was decanted off. The centrifuge tube with the remaining white solid was then dried *in vacuo*, before being redissolved in a minimum amount of acetonitrile (4 mL). The suspension was centrifuged (8000 rpm, 5 mins) and decanted off before adding an excess of Et_2O (40 mL) to the solution. The white suspension was then centrifuged, and the solvent was decanted off. The centrifuge tube with the remaining white solid was the dried *in vacuo*, before being redissolved in a minimum amount of acetone. The suspension was centrifuged (8000 rpm, 5 mins) and decanted off before adding an excess of Et_2O (40 mL) to the solution. The centrifuge tube with the remaining white solid was dried *in vacuo* to yield **$K_6[P_2W_{17}O_{61}(C_6H_{11}NO_8P_2S)]$** as a white solid (0.156 g, 0.033 mmol, 70 % yield). ^{31}P NMR (162 MHz, MeCN-d_3) δ 11.53, -11.10, -12.80.

4.6 REFERENCES

1. S. Amin, J. M. Cameron, J. A. Watts, D. A. Walsh, V. Sans and G. N. Newton, *Mol. Syst. Des.*, **2019**, 4, 995-999.
2. K. Kastner, A. J. Kibler, E. Karjalainen, J. A. Fernandes, V. Sans and G. N. Newton, *J. Mater. Chem. A*, **2017**, 5, 11577-11581.
3. A. Klaiber, T. Kollek, S. Cardinal, N. Hug, M. Drechsler and S. Polarz, *Adv. Mater. Interfaces*, **2018**, 5, 1701430.
4. J. M. Cameron, S. Fujimoto, K. Kastner, R. J. Wei, D. Robinson, V. Sans, G. N. Newton and H. H. Oshio, *Chem. Eur. J.,* **2017**, 23, 47-50.
5. J. M. Cameron, S. Fujimoto, R.-J. Wei, G. N. Newton and H. Oshio, *Dalton T.*, **2018**, 47, 10590-10594.
6. A. J. Kibler and G. N. Newton, *Polyhedron*, **2018**, 154, 1-20.
7. S. Fujimoto, J. M. Cameron, R.-J. Wei, K. Kastner, D. Robinson, V. Sans, G. N. Newton and H. Oshio, *Inorg.Chem.* **2017**, 56, 12169-12177.
8. M. Boujtita, J. Boixel, E. Blart, C. R. Mayer and F. Odobel, *Polyhedron*, **2008**, 27, 688-692.
9. S. G. Ziegler, W. A. Gahl and C. R. Ferreira, in *Genetics of Bone Biology and Skeletal Disease (Second Edition)*, eds. R. V. Thakker, M. P. Whyte, J. A. Eisman and T. Igarashi, Academic Press, **2018**, 571-595.
10. Y. Tanaka, M. Iwasaki, K. Murata-Hirai, K. Matsumoto, K. Hayashi, H. Okamura, T. Sugie, N. Minato, C. T. Morita and M. Toi, *Sci. Rep.*, **2017**, 7, 5987.
11. Y. Zhang, M. P. Hudock, K. Krysiak, R. Cao, K. Bergan, F. Yin, A. Leon and E. Oldfield, *J. Med. Chem.,* **2007**, 50, 6067-6079.
12. M. Egorov, S. Aoun, M. Padrines, F. Redini, D. Heymann, J. Lebreton and M. Mathé-Allainmat, *Eur. J. Org. Chem.*, **2011**, 7148-7154.
13. A. Boulmier, X. Feng, O. Oms, P. Mialane, E. Rivière, C. J. Shin, J. Yao, T. Kubo, T. Furuta, E. Oldfield and A. Dolbecq, *Inorg. Chem.*, **2017**, 56, 7558-7565.
14. A. Saad, W. Zhu, G. Rousseau, P. Mialane, J. Marrot, M. Haouas, F. Taulelle, R. Dessapt, H. Serier-Brault, E. Rivière, T. Kubo, E. Oldfield and A. Dolbecq, *Chem. Eur. J.*, **2015**, 21, 10537-10547.
15. A. Banerjee, B. S. Bassil, G.-V. Röschenthaler and U. Kortz, *Chem. Soc. Rev.*, **2012**, 41, 7590-7604.
16. S. G. Sarafianos, U. Kortz, M. T. Pope and M. J. Modak, *Biochem. J.*, **1996**, 319 (Pt 2), 619-626.
17. M. T. Pope, in *Polyoxometalate Molecular Science*, eds. J. J. Borrás-Almenar, E. Coronado, A. Müller and M. Pope, Springer Netherlands, Dordrecht, **2003**, 3-31.
18. C. Streb, *Dalton T.*, **2012**, 41, 1651-1659.
19. D. Ravelli, M. Fagnoni, T. Fukuyama, T. Nishikawa and I. Ryu, *ACS Catal.*, **2018**, 8, 701-713.
20. J. M. Cameron, S. Fujimoto, K. Kastner, R.-J. Wei, D. Robinson, V. Sans, G. N. Newton and H. H. Oshio, *Chem. Eur. J.*, **2017**, 23, 47-50.
21. M. T. Pope and E. Papaconstantinou, *Inorg.Chem.*, **1967**, 6, 1147-1152.
22. G. M. Varga, E. Papaconstantinou and M. T. Pope, *Inorg. Chem.*, **1970**, 9, 662-667.
23. S. Kan, Y. Jin, X. He, J. Chen, H. Wu, P. Ouyang, K. Guo and Z. Li, *Polym. Chem.*, **2013**, 4, 5432-5439.
24. A. M. Freedy, M. J. Matos, O. Boutureira, F. Corzana, A. Guerreiro, P. Akkapeddi, V. J. Somovilla, T. Rodrigues, K. Nicholls, B. Xie, G. Jiménez-Osés, K. M. Brindle, A. A. Neves and G. J. L. Bernardes, *J. Am. Chem.Soc.,* **2017**, 139, 18365-18375.
25. S. H. Kennedy and D. A. Klumpp, *J. Org. Chem.*, **2017**, 82, 10219-10225.

5 SYNTHESIS AND ELECTRONIC CHARACTERISATION OF MIXED-ADDENDA ORGANOPHOSPHONATE HYBRID POMS

5.1 INTRODUCTION

Although we understand the contrasting behaviour between assemblies and their molecular building blocks, the overall complexity of the electronic structure with regards to the supramolecular assembly is difficult to comprehend, due to the tremendous charge and potential electron delocalisation between neighbouring POMs. In conjunction with the work discussed in Chapters 1 and 2, redox activity of hybrid-POM assemblies has been closely studied by Newton and Polarz *et al.*[1-3] Now that we have explored the redox properties of the supramolecular assembly and hierarchical structures with regards to our model compound **{$W_{17}C_{20}$}**, we aimed to develop this system further by probing the effects of manipulating the metal oxide composition on the superstructure assembly and redox behaviour.

Previously, we mentioned that lacunary POMs offer a route to POM modification through addition of new components to the lacuna pocket. This modification usually involves: i) addition of metals or ii) addition of organic ligands; both of which can have profound effects on the intrinsic properties of the POM cluster. Being able to combine the effects of metal substitution and organo-functionlisation could bring about a greater scope for tuning the POM cluster, and synergistic properties brought by both inorganic and organic components. Moreover, organo-functionalisation could be employed to modulate properties of multiple distinct metal atoms within the clusters. However, it is synthetically challenging to form mixed-metal organo-functionalised hybrid systems. Only a handful of mixed-metal Class II hybrid species exist, some examples include tungstovanadate hybrids,[4] "tris"-functionalised hetero-metal centred Anderson hybrids[5] and more recently lanthanide substituted polyphosphotungstate.[6]

Furthermore, two structural families based on class II mixed-metal hybrid-POM amphiphiles exist, but none study the effects of metal doping on the intrinsic redox-activity or assembly of the supramolecular assemblies. These two families of mixed-metal hybrid POM amphiphiles are based on Anderson-based amphiphiles and tungstovanadate "tris"-functionalise dumb-bell molecules.[7, 8]

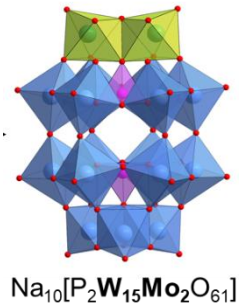

Figure 80 - $\{W_{15}Mo_2\}$ cluster representation. Molecule colour code: green polyhedra = $\{MoO_6\}$, blue polyhedra = $\{WO_6\}$, purple polyhedra = $\{PO_4\}$ and red spheres = oxygen.

Led by this fundamental curiosity and relatively unexplored area, we set out to build a comparative model system that was composed of C_{20} chain and a mixed metal lacunary Wells-Dawson cluster. We discovered a new route to mixed-metal hybrids through an established but relatively unexplored Wells-Dawson lacunary structure $Na_{10}[P_2W_{15}Mo_2O_{61}]$ **$\{W_{15}Mo_2\}$**. This cluster was developed by Contant *et al*. when establishing the number of possible substitutions of Mo into a **$\{W_{18}\}$** cluster.[9] This example of a mixed metal mono-lacunary species is particularly unusual, as one would expect the full substitution when filling the cap of the Wells-Dawson cluster through the adopted bottom-up approach *via* **$\{W_{15}\}$**. This cluster consists of 15 tungstate fragments composing the bottom cap and belt region, and 2 molybdate fragments occupying the lacuna-cap site.

The exploration of similar mixed metal polyoxotungstomolybdates has been well established by the likes of Papaconstantinou, Hill, Keita and Contant *et al.* to develop POMs that incorporate the benefits of both tungstate and molybdate POMs. Both polyoxotungstates and polyoxomolybdates demonstrate rich and reversible multi-electron redox process however, there are some substantial differences between the two. For instance, polyoxotungstates possess shorter M-O bond lengths than

polyoxomolybdates, and are therefore generally more stable.[10, 11] Furthermore, polyoxomolybdates tend to be less hydrolytically stable compared to their pure tungsten conjugates.[12] However, the benefits of polyoxomolybdates over polyoxotungstates, are based around the exhibition of generally more positive redox potentials, therefore polyoxomolybdates are more readily reduced.[13] The electrochemical differences arise from their contrasting electronic structure, where the HOMO-LUMO energy gap for polyoxomolybdates tends to be lower.[14]

The electrochemical behaviour of these mixed metal polynuclear systems are relatively complex. Fundamental studies carry out by Poblet *et al*. shed light on the electronic structure and electron delocalisation in mixed added Wells-Dawson system.[15] Here, four compounds with varying numbers of Mo addenda's were synthesised (α_1- and α_2-$[P_2W_{17}MoO_{62}]^{6-}$, α-$[P_2W_{15}Mo_3O_{62}]^{6-}$, and α-$[P_2W_{12}Mo_6O_{62}]^{6-}$) and characterised. Furthermore, a combination of DFT and experiments concluded that the Mo^{VI} centres in each of the systems were reduced first, regardless of their positions or number; W^{VI} centres were then successively reduced. It was found that by replacing more W atoms with Mo resulted in a higher degree of delocalisation of electrons, this caused a positive shift in all reduction potentials since the electron-accepting orbitals are lower in energy, due to higher participation of Mo orbitals. Therefore the larger number of Mo addenda rendered the POM a better oxidizing agent.[15] However, it is important to note that the number of Mo *vs.* W addenda have to be carefully tuned to maintain optimal redox-activity as well as stability.

To exploit the beneficial properties of both tungstate and molybdates, approaches towards development of tungstomolybdates POMs have previously led towards clusters with enhanced catalytic properties. In particular Contant *et al*. reported the introduction of a single Mo centre in the framework of wells-Dawson cluster $[P_2W_{17}MoO_{62}]^{6-}$ resulted in a positive shift of 0.270 V in the potential at which the catalytic process (reduction of NO to N_2O) is observed compared to the same process with $[P_2W_{18}O_{62}]^{6-}$.[16] Such clusters have been well-explored in a quest to access desirable electrochemical properties for applications in catalysis, sensing and energy storage.[17, 18]

To the best of our knowledge, lacunary mixed-metal Wells-Dawson POMs, specifically **{$W_{15}Mo_2$}**, have not been hybridised with organic moieties. This raises opportunities to explore the synergistic effects of LUMO lowering effects of phosphonate hybridisation, as well as Mo substitution effects.

5.2 AIMS

The aim of this project is to is to explore the effects of coupling organo-functionalisation and metal substitution on the electronic properties of the POM. We will synthesise and characterise a mixed-metal hybrid cluster based on the coupling of phenyl phosphonic acid (PPh) and $Na_{10}[P_2W_{15}Mo_2O_{61}]$ (**{$W_{15}Mo_2$}** and compare the properties of the product **{$W_{15}Mo_2PPh$}** to its pure tungsten hybrid analogue **{$W_{17}PPh$}**. Furthermore, we will then seek to develop a C_{20} mixed-metal hybrid-POM and explore how metal substitution effects the redox-activity and structure of the supramolecular assembly.

5.3 RESULTS AND DISCUSSION

5.3.1 Synthesis and Characterisation

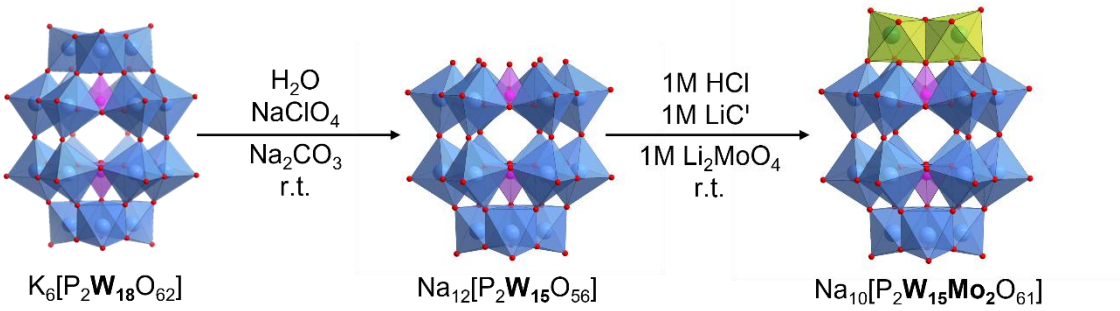

Figure 81 - Schematic illustration depicting the synthesis of {$W_{15}Mo_2$}.

The lacunary cluster was synthesised from an existing methodology published by Contant *et al.*,[9] where tri-lacunary analogue **{W_{15}}** was synthesised from controlled pH hydrolysis of its parent analogue **{W_{18}}** (Figure 81). Li_2MoO_4 was then added in the presence of LiCl and 1 M HCl (solution lowered to pH 4) to aid condensation of the Mo fragments, yielding $Na_{10}[P_2Mo_2W_{15}O_{61}]$(**{$W_{15}Mo_2$}).** Due to the sensitive electronic nature of POMs, change in composition of the addenda environment surrounding the internal phosphate will have a significant effect on the electron density and shielding of the phosphorus. Therefore, we can rely on ^{31}P NMR to track the addition of Mo fragments to the cluster. Figure 82a displays the NMR spectra where we observe a peak shift of the internal phosphates of **{$W_{15}Mo_2$}** *vs*. **{W_{17}}**. Interestingly, we observe an overall downfield shift of P1 (upper phosphate) a negligible downfield shift in P2 (bottom phosphate). This observation is due to the overall lower electron-donating effect of the Mo compared to W, therefore we can expect a lower degree of shielding of the phosphates closest to the Mo addenda in the POM.

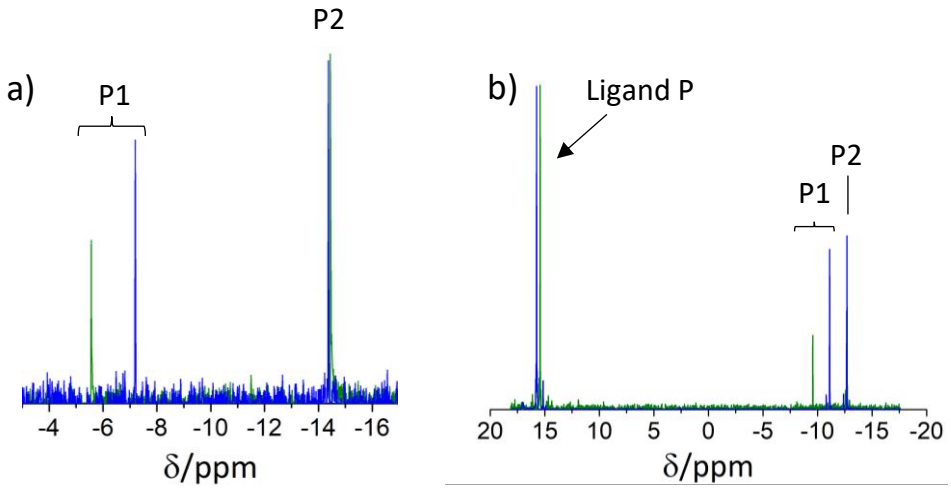

Figure 82 - ^{31}P NMR analysis: (a) of {W_{17}}(blue) and {$W_{15}Mo_2$} (green) d_3-MeCN; (b) {W_{17}PPh} (blue) and {$W_{15}Mo_2$PPh} (green).

With regards to this project, we sought to understand how the redox properties in the molecular and supramolecular domain differ between well-explored pure tungsten **{W_{17}R}** hybrids and mixed metal **{$W_{15}Mo_2$R}** hybrid. To understand the contrasting electronic properties of the molecular hybrid, the electronic structure was studied on phenyl phosphonic (PPh) derivatives of each cluster $K_6[P_2W_{17}O_{61}(POC_6H_5)_2]$ (**{W_{17}PPh}** and $Na_6[P_2Mo_2W_{15}O_{61}(POC_6H_5)_2]$ (**{$W_{15}Mo_2$PPh}**). To couple phenylphosphonic acid ligands to monolacunary **{$W_{15}Mo_2$}** cluster, our previously reported hybridisation method was employed.[1] Figure 82b displays the ^{31}P NMR of **{W_{17}PPh}** and **{$W_{15}Mo_2$PPh}**, where we observe a shift in the P signals post-hybridisation and a shift when comparing **{W_{17}PPh}** and **{$W_{15}Mo_2$PPh}**. Firstly, we observe the characteristic squeeze with the phosphorus environment peaks compared to its unhybridised lacunary species. P1 (upper phosphate) shifts downfield and P2(lower phosphate) shifts upfield which can we attributed to the electron-withdrawing effects exhibited by the phosphonic acid ligands. When comparing **{W_{17}PPh}** and **{$W_{15}Mo_2$PPh}**, the P2 nuclei environment display no observable difference, this indicates they experience the same if not similar ligand effects. Although, P1 for both compounds exhibits an upfield shift post-hybridisation, P1 of **{$W_{15}Mo_2$PPh}** is located +1.6 ppm from **{W_{17}PPh}**, indicating that its nuclei are more deshielded than

its pure tungsten analogue, which is attributed to the weaker electron-donating effects of Mo. The ligand environments display no significant difference in peak shift of the phosphorus nuclei.

Mass spectrometry was also employed to confirm the nature of the **{$W_{15}Mo_2PPh$}** cluster (Figure 83). Table 6 displays the relative m/z with various cation pairings detected in the spectrometer. The most intense peak in the sigmoid for **{$W_{15}Mo_2PPh$}** corresponds to observed m/z = 2130.81 for 2- charged species which is assigned to H_3Na{$W_{15}Mo_2PPh$}$^{2-}$, where 3 protons and a sodium cation are coordinated to the cluster.

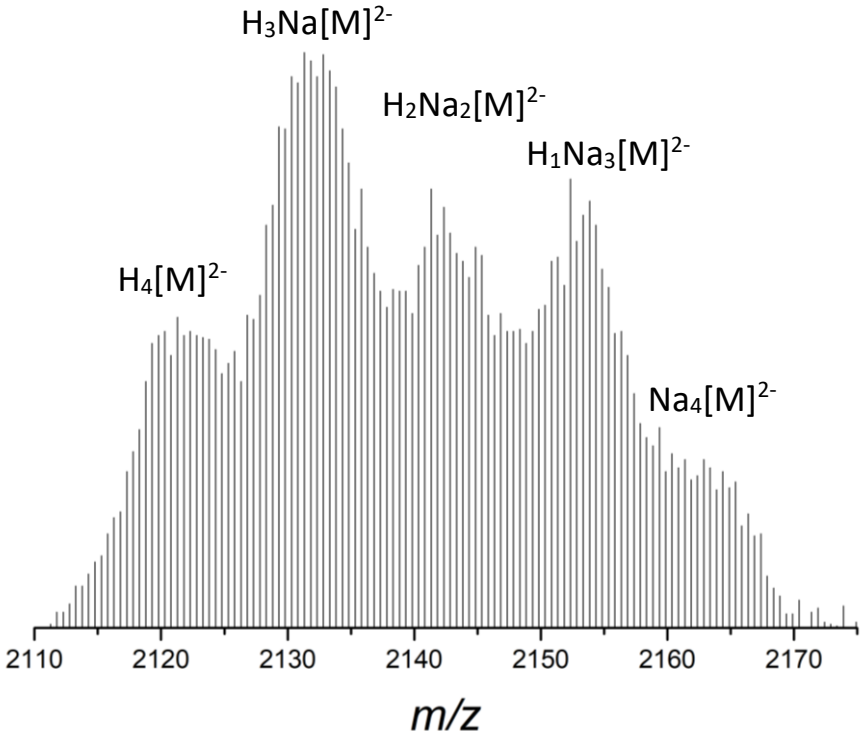

Figure 83 - ESI-MS spectra of {$W_{15}Mo_2PPh$}.

Assignment	z	*m/z (calc.)*	*m/z (obs.)*
{$H_4[W_{15}Mo_2P_2O_{61}(P_2C_{12}H_{10}O_2)_1]$}	2-	2119.849	2119.792
{$H_3Na[W_{15}Mo_2P_2O_{61}(P_2C_{12}H_{10}O_2)_1]$}	2-	2130.84	2130.808
{$H_2Na_2[W_{15}Mo_2P_2O_{61}(P_2C_{12}H_{10}O_2)_1]$}	2-	2141.831	2141.831
{H_1Na_3 $[W_{15}Mo_2P_2O_{61}(P_2C_{12}H_{10}O_2)_1]$}	2-	2152.822	2152.847
{$Na_4[W_{15}Mo_2P_2O_{61}(P_2C_{12}H_{10}O_2)_1]$}	2-	2163.813	2163.873
{$H_3Na_5[W_{15}Mo_2P_2O_{61}]$}	2-	2052.812	2052.671
{$H_3Na_4K_1[W_{15}Mo_2P_2O_{61}]$}	2-	2060.799	2060.7
{$H_3Na_4[W_{15}Mo_2P_2O_{61}]$}	3-	1360.878	1360.91

Table 6 - Assigned MS peaks corresponding to {$W_{15}Mo_2PPh$}$^{n-}$

We were further able to characterise the structure of **{$W_{15}Mo_2PPh$}** by X-ray crystallography. Fortunately, we were able to grow and isolate single crystals through the vapour diffusion of MeOH (antisolvent) into a saturated solution of **{$W_{15}Mo_2PPh$}** in MeCN to yield pale green single crystals. **{$W_{15}Mo_2PPh$}** crystallises in the monoclinic system with space group $P2_1/n$. Further crystallographic can be found in the appendix Table S1. Regarding the structure of the hybrid-POM (Figure 84), we can see that two phenylphosphonic acid moieties are covalently grafted onto the POM in a 2:1 fashion, analogous to previously reported isoelectronic phenylphosphonate hybrid Wells-Dawson POM **{$W_{17}PPh$}**.[19] Furthermore, the presence of the Mo atoms are located in the cap position of the cluster. Direct comparison of the bonding environment around the P centre in the report reveals that the P atom possesses the same tetrahedral geometry. With regards to the P-O-Mo bonding, the P-O bond length is 1.477 Å which is shorter than the same bonding exhibited in **{$W_{17}PPh$}** where P-O bond length is 1.536 Å. Furthermore, the bond length for the O-Mo is 2.095 Å which is longer than the 2.023 Å O-W (P-O-W) bond on the same phosphonate. The longer bonds exhibited by Mo indicate weaker bonds which is why most molybdate compounds exhibited lower stability over tungstate POMs. The P=O bonds for **{$W_{15}Mo_2PPh$}** are found to be 1.580 Å which are shorter than the P=O bonds found on **{$W_{17}PPh$}** (1.525 Å)**.** This suggests that the presence of Mo weakens the P=O bonding.

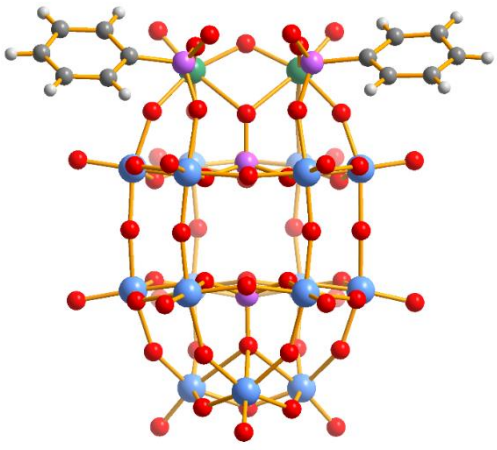

Figure 84 - Crystal structure of {$W_{15}Mo_2PPh$} with solvent molecules removed for clarity. Two Mo addendum are located in the upper cap of the Wells-Dawson cluster with organophosphonates covalently bound to them. Colour scheme of spheres: oxygen (red), tungsten (blue), phosphorus (pink), molybdenum (green), carbon (green) and hydrogen (white).

5.3.2 Electronic Characterisation

Next, we set out to probe the electronic structure of **{$W_{15}Mo_2R$}** based on a simplified non-amphiphilic analogue **{$W_{15}Mo_2PPh$}** and compare it to its pure tungsten conjugate **{$W_{17}PPh$}**. Now that two Mo units have replaced tungsten blocks in the POM framework cap, one would assume the overall electronic structure have been modified significantly. To ascertain relative reduction potentials of **{$W_{15}Mo_2PPh$}** and its comparative analogue **{$W_{17}PPh$}**, CV was conducted in DMF with 0.1 M [TBA][PF_6] supporting electrolyte (Figure 85).

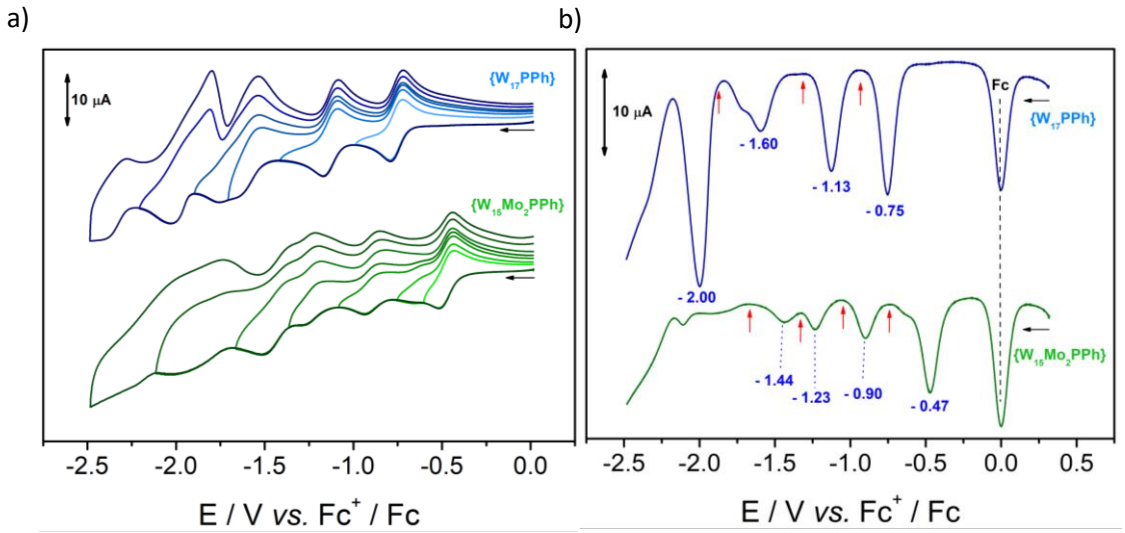

Figure 85 - Displays a) CV and DPV plot of {$W_{17}PPh$} (blue) and {$W_{15}Mo_2PPh$} (green) conducted in DMF and 0.1 M [TBA][PF_6] *vs*. Fc^+/Fc; b) displays a Differential pulse voltamagram (DPV) plot aquired from a) CV solution which highlights the potentials used for spectroelectrochemical analysis.

Figure 5 displays the CV and DPV plot for both molecules under study, this analysis was conducted in DMF at 100 mV/s over a potential range of 0 to - 2.5 V *vs*. Fc^+/Fc. Figure 85a displays 3 and 4 quasi reversible processes situated at for **{$W_{17}PPh$}** and **{$W_{15}Mo_2PPh$}** respectively. DPV analysis (Figure 5b) was conducted on both hybrids to deconvolute the reduction processes, allowing us to confirm appropriate reduction potentials to be applied for spectroelectrochemical analysis. As expected, the first redox process of **{$W_{15}Mo_2PPh$}** is shifted + 280 mV compared to **{$W_{17}PPh$}**. The first reduction of **{$W_{15}Mo_2PPh$}** is associated with a $2e^-$ reduction, corresponding to the $1e^-$ reduction of two Mo centers ($Mo^{VI} \rightarrow Mo^{V}$), which is a result of Mo being more readily reduced compared to W. Based on the electrochemical data, we observe an overall positive shift in the successive redox processes for

{$W_{15}Mo_2PPh$} with respect to **{$W_{17}PPh$}** processes. From this observation we can infer that metal substitution of Mo into the Wells-Dawson polyphosphotungstate cluster leads to an overall lowering of the W centered LUMO energy levels. As previously mentioned, the presence of varying addenda atoms, the electrochemical behaviour of POMs can be significantly changed. Common POM addenda atoms can be ordered by decreasing oxidizing ability in the following way: V(V) > Mo(VI) > W(VI).[20, 21] In the case of one-electron reduced mixed-addenda POMs, the electron is localized on the more reducible atom.[18] In this case, we expect for the single e^- on the reduced POM to be associated with the reduction of Mo centres. To confirm the first reduction process is associated with the reduction of Mo centres, spectroelectrochemistry and electron paramagnetic resonance spectroscopy (EPR) analysis was conducted (Figure 86 and 87).

Typically, the addenda ions in POMs possess d^0 electronic configuration, resulting in one absorption band present in the UV-vis spectrum located between 190 and 400 nm due to the oxygen-to-metal charge transfer transition (LMCT).[22] The spectra associated with reduced POMs, formerly known as "*heteropolyblues"* exhibit intervalence charge transfer bands associated electron "*hopping"* between metal centres.[23, 24] By employing spectroelectrochemical analysis, it is possible to distinguish between the reduction of different addenda when comparing compounds with different compositions (i.e. Mo and W). In Figure 86, we have tracked the growth of the IVCT band with respect to the successive reductions highlighted in Figure 85b. In this experiment the potential was held at sufficiently negative potentials to allow full reduction of POM species in solution with respect to the chosen reduction process. Furthermore, the potential was held until the IVCT absorption band was saturated, indicating that almost all POMs in solution were reduced by x (x = 1, 2, 3, 4 etc.) number of electrons with respect to the reduction processes located at more positive potentials.

The absorbance of the 2e$^-$ reduced species associated with the first reduction process of **{$W_{15}Mo_2$PPh}** gave a broad peak at 800-900 nm. Comparatively, the absorbance associated with the 1st reduction process and 1e$^-$ reduced species of **{W_{17}PPh}** exhibits a broad IVCT band with distinct λ_{max}=837 nm. It is clear that the absorbance profile of **{$W_{15}Mo_2$PPh}** for the first redox process exhibits a clear difference in the IVCT band profile, therefore suggesting that the first reduction process is associated with the reduction of the Mo centres. Furthermore, we observe the IVCT bands associated with further reduction, grow and exhibit a blue shift. This is associated with the increased charge loading onto the POM leading to higher repulsion felt between electrons at the W centers, therefore the magnitude of delocalisation of e$^-$ decreases and a higher energy photon is required for IVCT process to occur.

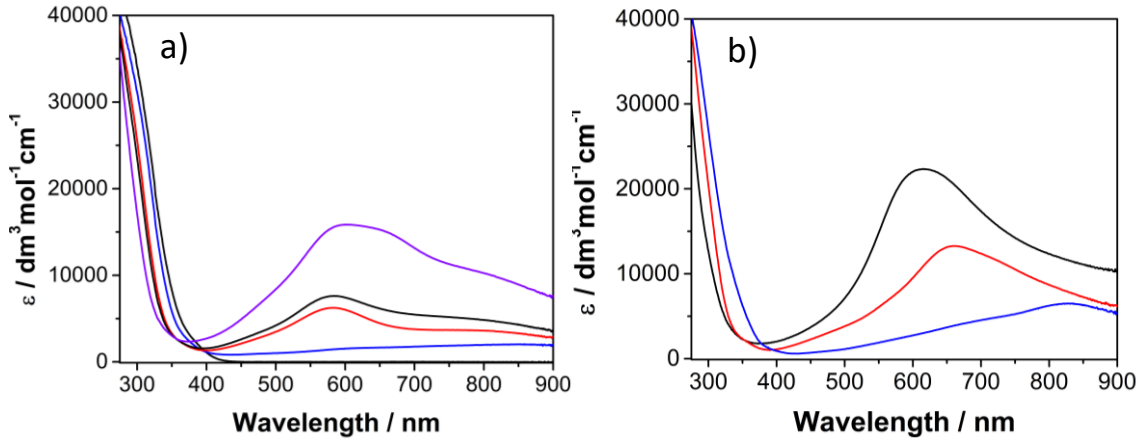

Figure 86 - Display of spectroelectrochemical analysis of a) {$W_{15}Mo_2$PPh} and b) {W_{17}PPh} in DMF with 0.1 M [TBA][PF_6] where plots represent the absorption profile of POM reduced species produced by applying potential past the 1st (blue), 2nd (red), 3rd (black), and 4th (purple) reduction potential (see DPV in Figure 85b).

We observe that the λ_{max} of the comparative IVCT bands are located at higher λ for **{$W_{15}Mo_2$PPh}**. This could be attributed to the lower level of orbital mixing experience in between mixed metal addenda, therefore leading to less delocalisation, and inherently leading to higher energy IVCT transitions. Finally, we employed EPR to compare the localisation of the e$^-$ on a singly reduced **{$W_{15}Mo_2$PPh}** and **{W_{17}PPh}** species (Figure 87). Singly reduced **{$W_{15}Mo_2$PPh}** is EPR active, both as fluid and frozen solution. The 77 K spectrum appears rhombic and displays Mo hyperfine coupling at low field (small bumps) (Figure 87b). The central signal is ascribed to the ions containing ^{98}Mo (I_N =0, 75 % natural abundance) and the sextet to the ^{95}Mo and ^{97}Mo containing ions (I_N = 5/2, 25 % combined natural

abundance).[25] Singly reduced **{W_{17}PPh}** was only EPR active when frozen(Figure 87a), the 77 K spectrum appears axial and might show W hyperfine at low field (small bump) is ascribed to ^{183}W hyperfine coupling (14.31 %, I = 1/2).[26] The two EPR spectra profiles are different and the presence of Mo hyperfine coupling indicates the 1st e- reduction is associated with the reduction of the Mo centre. Furthermore, this EPR spectra profile corroborates well with reported EPR data mixed-metal α_1-$\{HP_2W_{17}MoO_{62}\}^{6-}$ cluster reported by Pope *et al.*[27]

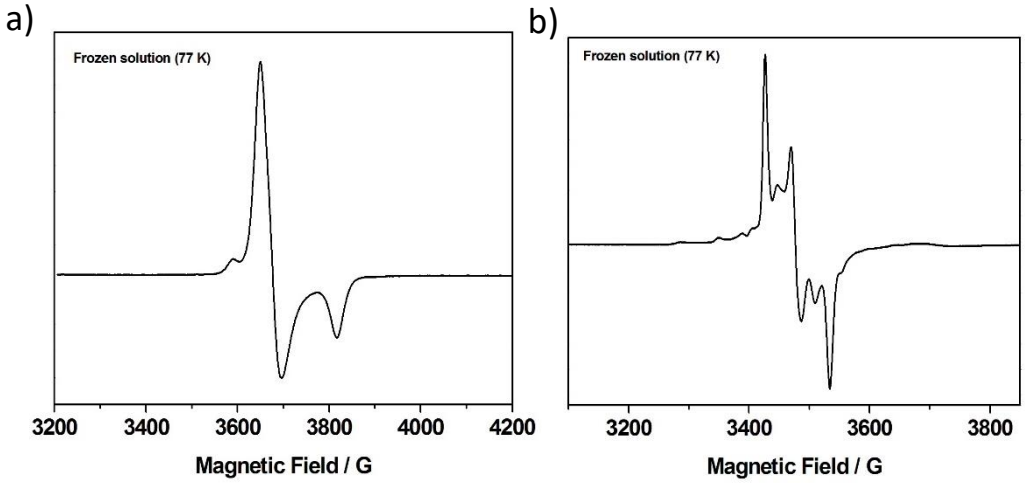

Figure 87 - EPR spectra at 77K of a) {W_{17}PPh} and b) {$W_{15}Mo_2$PPh}.

To calculate the overall frontier molecular HOMO-LUMO energy levels of a molecule, it is possible to combine LUMO energy level from the first reduction process in CV and the absorption data as the Eg. However, based on the broad LMCT associated with POMs arising from the complexity associated with polynuclear clusters, this was not possible. Therefore, DFT modelling was used to acquire calculated energy levels for **{$W_{15}Mo_2PPh$}** and **{$W_{17}PPh$}** (Figure 88).

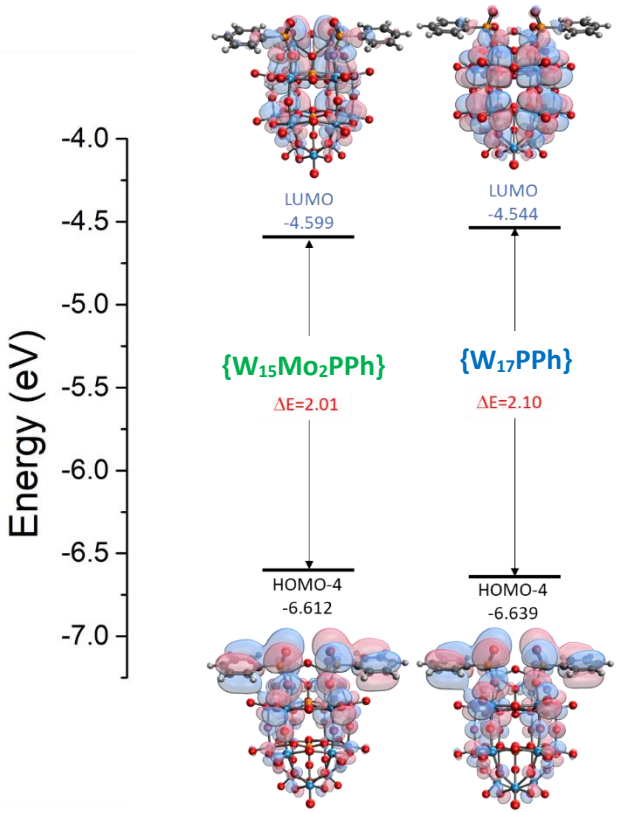

Figure 88 - HOMO-LUMO orbital diagrams of {$W_{15}Mo_2PPh$} (left) and {$W_{17}PPh$} (right) showing the calculated highest POM centred HOMO energies and LUMO energies and calculated HOMO-LUMO energy gaps (E_g).

Here, the geometry of each molecule was optimised in a polarisable continuum based on dielectric constant of DMF. Frontier orbitals consisting of the LUMO and the HOMO with the highest POM based orbital character were chosen. The HOMO-LUMO energy levels are displayed in Figure 88. Based on DFT calculations **{$W_{15}Mo_2PPh$}** possesses a lower LUMO energy than **{$W_{17}PPh$}** which is in agreement with experimental data acquired when comparing the first reduction potentials for the two clusters. Furthermore, based on the LUMO energy density diagram, the LUMO orbital is more evenly distributed across the entire POM for **{$W_{17}PPh$}** whereas the LUMO orbital seemed to be distributed

closer to the Mo centres for **{$W_{15}Mo_2PPh$}**. The distribution of LUMO electron density across the POM corroborates well experimental data as the first reduction of a metal centre usually undergoes rapid IVCT to other like neighbouring addenda, which is most likely why there is a lower degree of LUMO orbital delocalisation across the **{$W_{15}Mo_2PPh$}** cluster. Moreover, the HOMO-LUMO energy gap (E_g) is lower for **{$W_{15}Mo_2PPh$}** which corroborates well with literature values for E_g of Mo based POMs. We have established that the LUMO energies are lower for **{$W_{15}Mo_2PPh$}**, however, **{$W_{15}Mo_2PPh$}** also exhibits a higher HOMO energy which also contributes to the lower E_g (2.01 eV) compared to **{$W_{17}PPh$}** (2.10 eV). The HOMO is raised as a result of lower orbital mixing of LUMO energies due to the different nuclei present. Therefore, **{$W_{17}PPh$}** exhibits larger orbital mixing, a higher degree of electron delocalisation and therefore a more stabilised (i.e. lower) HOMO.[15]

Overall, it is clear that through this new approach to create mixed-metal hybrids *via* organo-functionalising **{$W_{15}Mo_2$}** cluster with phosphonates, we can modulate the energy levels of the cluster towards enhanced photocatalytic and electrocatalytic applications.

5.3.3 Mixed-Addenda Redox-Active Assemblies

Now that we have elucidated the electronic differences between the mixed-metal hybrid **{$W_{15}Mo_2$PPh}** and its pure tungsten analogue **{W_{17}PPh}**, we set out to understand how the mixed-metal cluster would behave as an amphiphile. We were intrigued to explore how the supramolecular assembly of the amphiphile is altered and how the redox properties of the assembly change for the mixed-metal hybrid POM amphiphile. By employing our previously reported method of hybridisation, we synthesised double-chained surfactant **{$W_{15}Mo_2C_{20}$}**.[1]

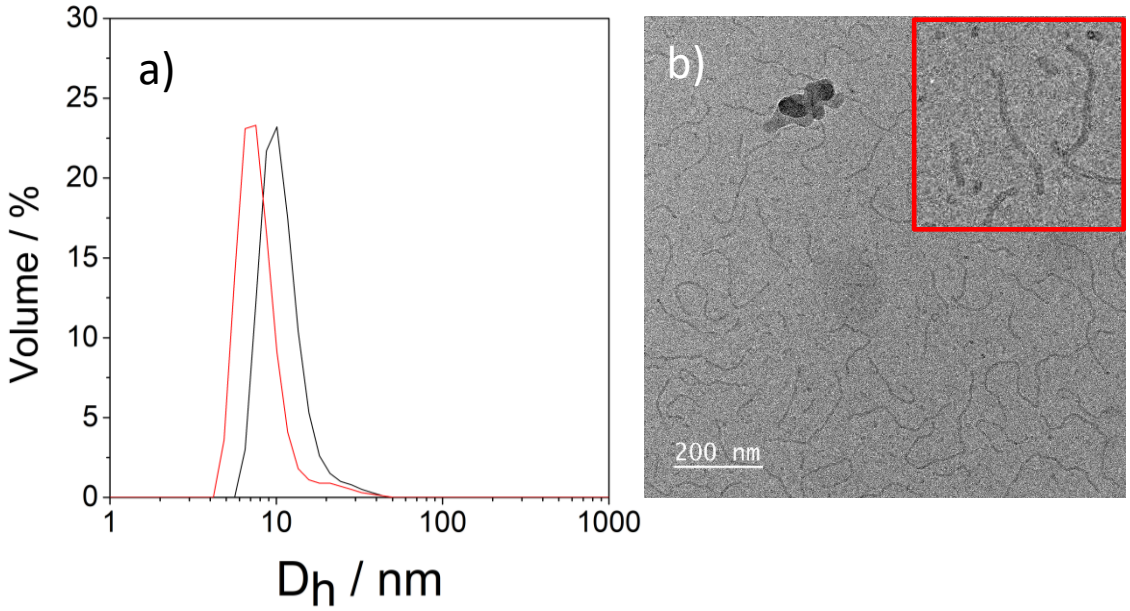

Figure 89 - a) DLS of 1.4 mM in H_2O (black) and 0.1 M H_2SO_4; and b) cryo-TEM analysis of 1.4 mM solution of in H_2O.

Once, our hybrid mixed-metal amphiphile was synthesised, we analysed the supramolecular assembly properties *via* DLS and cryo-TEM (Figure 89). We found that in a 1.4mM aqueous solution of **{$W_{15}Mo_2C_{20}$}**, assemblies with D_h = 10 nm were observed. Based on the size, we are under the assumption that these assemblies are most likely micelles. In the presence of acid, the assemblies shrink to D_h =7 nm, which can be attributed to cation or electrolyte causing an increase in the micelle wall curvature. The observed assemblies are larger than **{$W_{17}C_{20}$}** assemblies by 3 nm. Furthermore, under cryo-TEM conditions "*worm-like*" cylindrical micelles and normal micelles are present with

diameters of 7-11 nm. Interestingly, we observe a large difference compared with the highly ordered network of cylindrical micelles exhibited by **{$W_{17}C_{20}$}** under cryogenic conditions. This disorder may be related to the asymmetry of electron density distributed around **{$W_{15}Mo_2C_{20}$}** affecting the partial charge of the polar head area and therefore lowering the packing parameter. However, it's more likely that the change in cation from K^+ for **{$W_{17}C_{20}$}** to Na^+ for **{$W_{15}Mo_2C_{20}$}** is the cause behind the contrasting assembly, as cations are known to have an effect on the affective head group area of surfactants. Further investigation is needed into this result to determine whether the cation indeed is the cause of a higher degree of disorder observed in the assembly for **{$W_{15}Mo_2C_{20}$}**.

Now that we have established that **{$W_{15}Mo_2C_{20}$}** possesses supramolecular assembly characteristic somewhat similar to **{$W_{17}C_{20}$}**, we set out to examine the redox activity of the observed nanoassemblies.

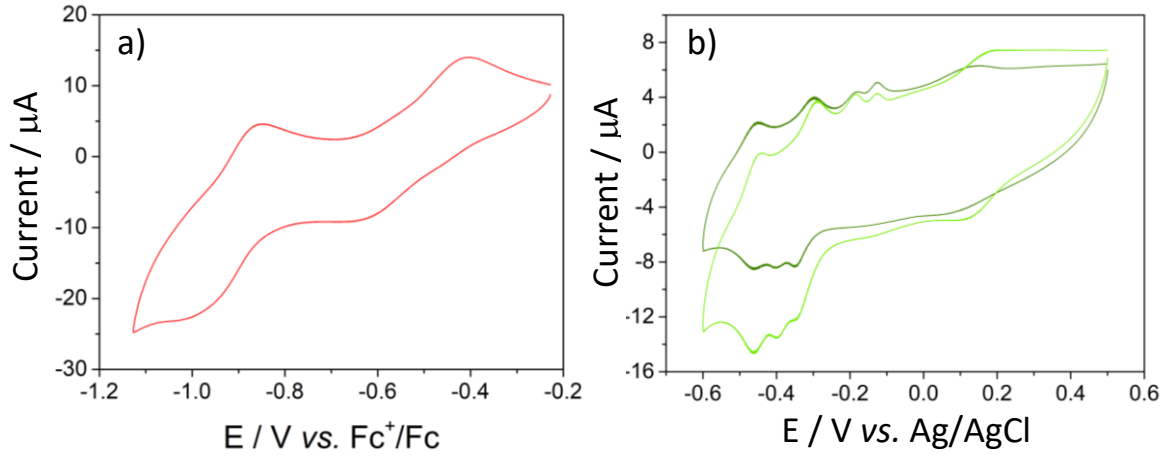

Figure 90 - CVs of 1.4 mM {$W_{15}Mo_2C_{20}$} conducted in: a) 0.1 M [TBA][PF_6] in DMF *vs.* Fc^+/Fc; and b) in 0.1 M H_2SO_4 (light green) and monolayer@ GC electrode (dark green) *vs*. Ag/AgCl.

To confirm the molecular electrochemical profile, cyclic voltammetry was run on **{$W_{15}Mo_2C_{20}$}** in DMF with 0.1 M [TBA][PF_6] supporting electrolyte. Here we can see two redox processes, one quasi-reversible process situated at $E_{1/2}$ = - 0.899 V and an irreversible process at - 0.514 V (Figure 90a). Next, CV was run on the 0.1 M H_2SO_4 solution containing 1.4 mM **{$W_{15}Mo_2C_{20}$}** micelle assemblies (Figure 89a, D_h = 7 nm; and Figure 90b - light green CV). Comparatively, we observe distinctly different CVs between the molecular and supramolecular CV which is what we have previously reported and

discussed in Chapter 2.[1, 2] For the CV in 0.1 M H_2SO_4, we observe 1 broad redox process at $E_{1/2}$ = 0.154 V. Scanning more negative we observe 3 reduction processes situated at E_p = - 0.341 V, - 0.392 V and - 0.466 V, and 4 oxidations situated at E_p = - 0.123 V, - 0.183 V, - 0.289 V and - 0.450 V. To test whether these micelles species also deposit at the electrode surface, the electrode was rinsed, and a CV was run in fresh 0.1 M H_2SO_4. We found that the number of redox process and their relative positions remain, indicating that we have deposited **{$W_{15}Mo_2C_{20}$}** at the surface (Figure 90b - dark green). The most negative reduction processes are particularly unique as the process are small, well-defined, and very close together. Comparing this to the aqueous electrochemical profile of **{$W_{17}C_{20}$}**, it is clear the Mo substitution causes a change in the assembly's redox process. This maybe attributed a number of reasons including, localisation of electrons upon successive reductions as seen in the molecular species, rearrangement of Mo centres around the POM or structural rearrangement of micelles at the surface. However, further analysis is needed to elucidate the surface confined electrochemical behaviour. Moreover, ellipsometry and AFM would be beneficial in identifying the surface structure of the deposited species.

5.4 CONCLUSION

In summary, we established a new approach to a novel class of mixed-addenda hybrid POM molecules based on the coupling of **{$W_{15}Mo_2$}** and phosphonic acid ligands. To study the structural and physio-chemical properties, we synthesised **{$W_{15}Mo_2R$}** and **{$W_{17}R$}** (R = 2 x phenylphosphonic acid). These molecules were structurally characterised by MS, NMR, IR and XRD. Here, XRD confirmed the presence of two Mo addenda located in the cap of the Wells-Dawson cluster. We then employed CV, spectroelectrochemistry and EPR to elucidate the electronic structure differences between **{$W_{15}Mo_2PPh$}** and **{$W_{17}PPh$}**. Based on the CV analysis, we found that the redox process of the **{$W_{15}Mo_2PPh$}** species were shifted positive with respect to its pure tungsten analogue **{$W_{17}PPh$}**, Furthermore the first redox process was attributed to the $2e^-$ reduction of the Mo centers. This was confirmed *via* spectroelectrochemistry and EPR. Spectroelectrochemical analysis of **{$W_{15}Mo_2PPh$}** and **{$W_{17}PPh$}** displayed contrasting absorbance profiles for their reduced species. Based on the first reduction process a $2e^-$ and $1e^-$ of **{$W_{15}Mo_2PPh$}** and **{$W_{17}PPh$}** was produced. Their characteristic absorption profiles of the reduced states differed which indicated potential reduction of the Mo centres for **{$W_{15}Mo_2PPh$}**. EPR spectroscopy was then employed to locate the radical of the single electron reduced species. Here we found that he both species were EPR active however only **{$W_{15}Mo_2PPh$}** was at room temperature. Based on the presence of Mo hyperfine coupling, it was apparent that the electron was indeed located at the Mo centres. Collectively, this data provided a wealth of information, which confirmed the contrasting physio-chemical properties of **{$W_{15}Mo_2PPh$}** compared to **{$W_{17}PPh$}**, were owed to the presence of Mo centres which are more readily reduced than W. These results were in good agreement with the reports into tungstomolybdate POMs. Furthermore, DFT calculations corroborated well with experimental LUMO energies extrapolated from CV data. Thus, demonstrating that through the substitution of Mo into the cluster, the HOMO-LUMO energy levels could be modulated, through lower LUMO contribution of the Mo and destabilisation of the HOMO due to lower orbital mixing, leading to a lower E_g.

Finally, we prepared **{$W_{15}Mo_2C_{20}$}** hybrid POM amphiphile to study the structure and redox properties of its supramolecular assembly. We found structural differences in the morphology of its cylindrical micelles produced under cryo-TEM conditions, compared to **{$W_{17}C_{20}$}**, which were loosely attributed to cation effects, however, further investigation is required to confirm this. The redox properties of the assemblies were also probed in 0.1 M acid where micelles were observed by DLS (D_h = 7 nm). Similar to **{$W_{17}C_{20}$}**, **{$W_{15}Mo_2C_{20}$}** surface deposited species were observed. However, surface-confined electrochemistry displayed obvious differences compared to **{$W_{17}C_{20}$}**, which could be attributed to the presence of Mo centres.

Overall, we have demonstrated a new approach to the synthesis of mixed-metal hybrid POMs, where the combined effects of metal substitution, and electron-withdrawing effects of phosphonate ligands can modulate the LUMO energies of the hybrid-POM. Furthermore, these effects are pronounced within their supramolecular assembly, therefore demonstrating that we can access new and interesting supramolecular redox properties by introduction of mixed metal POM clusters. This new example of hybrid-POM species can lead to a range of materials with interesting electrochemical, photochemical, and supramolecular properties.

5.5 EXPERIMENTAL

Synthesis of {W_{17}PPh}

$K_{10}[P_2W_{17}O_{61}]$ (0.25 g, 0.057 mmol), phenyl phosphonic acid (18 mg, 0.114 mmol), and KCl (126 mg, 1.7 mmol) were suspended in MeCN, and 12 M HCl (100 µL) was then added. The reaction mixture was then heated at 80 °C for 24 h, and after cooling to r.t., the reaction mixture was filtered to give a yellow solution. Subsequent centrifugation with Et_2O, EtOH, and Et_2O gave $K_6[P_2W_{18}O_{61}(POC_6H_5)_2]$ as a yellow powder (0.150 g, 58 %).^{1}H NMR (400 MHz, MeCN-d_3) δ 8.15 (ddt, *J* = 14.2, 6.6, 1.6 Hz, 2H), 7.56 (dtt, *J* = 10.3, 6.3, 1.8 Hz, 3H); ^{31}P NMR (162 MHz, Acetonitrile-d_3) δ 15.58, -11.12, -12.71.

Synthesis of {$W_{15}Mo_2$PPh}

$Na_{10}[P_2W_{15}Mo_2O_{61}]$ (0.25 g, 0.059 mmol), phenyl phosphonic acid (18 mg, 0.114 mmol), and 12 M HCl (50 µL) was then added. The reaction mixture was then heated at 80 °C for 24 h, and after cooling to r.t., the reaction mixture was centrifuged, whereby the solution was filter off to give a green solution. Et_2O was added to the solution and the resulting precipitate was centrifuged to collect the solid. The solid was sonicated in Et_2O to give $K_6[P_2Mo_2W_{15}O_{61}(POC_6H_5)_2]$ green powder (0.164 g, 63.5 %).^{1}H NMR (400 MHz, DMSO-d_6) δ 8.00 – 7.91 (m, 2H), 7.53 – 7.42 (m, 3H); ^{31}P NMR (162 MHz, DMSO-d_6) δ 14.27, -9.79, -12.93.

Synthesis of {$W_{15}Mo_2C_{20}$}

3F (C_{20}) (0.115 mmol) and $Na_{10}[P_2W_{15}Mo_2O_{61}]$ (0.25g, 0.059 mmol) were suspended in MeCN (50 mL) and 12 M HCl (50 µL). The reaction mixture was stirred at 70 °C for 24 h to form a yellow solution. Upon completion, the reaction was cooled to room temperature and centrifuged to remove the precipitate. The solvent was then evaporated *in vacuo,* resulting in an orange solid. The solid was then redissolved in acetone (2 mL), and the resulting precipitate was removed by centrifugation. The solvent was removed *in vacuo* to form a dark red powder. The powder was redissolved in MeCN (2 mL) and Et_2O (40 mL) was added to form a precipitate. The precipitate was separated by centrifugation to form a pale orange solid. The solid was then sonicated in Et_2O (100 mL) and decanted. The remaining solvent was removed *in vacuo*. To yield $Na_6[P_2W_{17}O_{61}(PO_2C_6H_4(C_{20}H_{41})_2]$ as a red powder (0.147g, 50.1%).;^{1}H NMR (400 MHz, MeCN-d_3) δ 8.04 (dd, *J* = 13.7, 8.4 Hz, 4H), 7.07 (dd, *J* = 8.9, 3.2 Hz, 4H), 4.09 (t, *J* = 6.7 Hz, 5H), 3.45 (q, *J* = 7.0 Hz, 10H), 1.30 (s, 54H), 1.15 (t, *J* = 7.0 Hz, 16H), 0.91 (t, *J* = 6.5 Hz, 7H);^{31}P NMR (162 MHz, MeCN-d_3) δ 18.42, -9.57, -12.42, -12.51.

5.6 REFERENCE

1. S. Amin, J. M. Cameron, J. A. Watts, D. A. Walsh, V. Sans and G. N. Newton, *Mol. Syst. Des. Eng.*, **2019**, 4, 995-999.
2. K. Kastner, A. J. Kibler, E. Karjalainen, J. A. Fernandes, V. Sans and G. N. Newton, *J. Mater. Chem. A*, **2017**, 5, 11577-11581.
3. S. Landsmann, C. Lizandara-Pueyo and S. Polarz, *J. Am. Chem. Soc.*, **2010**, 132, 5315-5321.
4. D. Lachkar, D. Vilona, E. Dumont, M. Lelli and E. Lacôte, *Angew. Chem., Int. Ed.*, **2016**, 55, 5961-5965.
5. A. Blazevic, E. Al-Sayed, A. Roller, G. Giester and A. Rompel, *Chem. Eur. J.*, **2015**, 21, 4762-4771.
6. W. Wang, N. V. Izarova, J. van Leusen and P. Kögerler, *ChemCommun.*, **2020**, 56, 14857-14860.
7. M. F. Misdrahi, 2011.
8. C.-G. Lin, W. Chen and Y.-F. Song, *Eur. J. Inorg. Chem.*, **2014**, 3401-3405.
9. M. Abbessi, R. Contant, R. Thouvenot and G. Herve, *Inorg. Chem.*, **1991**, 30, 1695-1702.
10. X. López, J. M. Maestre, C. Bo and J.-M. Poblet, *J. Am. Chem. Soc.*, **2001**, 123, 9571-9576.
11. N. Mizuno and M. Misono, *Chem. Rev.*, **1998**, 98, 199-218.
12. M. T. Pope and E. Papaconstantinou, *Inorg.Chem.*, **1967**, 6, 1147-1152.
13. A. Lewera, M. Chojak, K. Miecznikowski and P. J. Kulesza, *Electroanalysis*, **2005**, 17, 1471-1476.
14. X. Lopez, J. J. Carbo, C. Bo and J. M. Poblet, *Chem. Soc. Rev.*, **2012**, 41, 7537-7571.
15. L. Parent, P. A. Aparicio, P. de Oliveira, A.-L. Teillout, J. M. Poblet, X. López and I. M. Mbomekallé, *Inorg. Chem.*, **2014**, 53, 5941-5949.
16. A. Belhouari, B. Keita, L. Nadjo and R. Contant, *New J. Chem.*, **1998**, 22, 83-86.
17. C. L. Hill and C. M. Prosser-McCartha, *Coord. Chem. Rev.*, **1995**, 143, 407-455.
18. M. Sadakane and E. Steckhan, *Chem. Rev.*, **1998**, 98, 219-238.
19. S. Fujimoto, J. M. Cameron, R.-J. Wei, K. Kastner, D. Robinson, V. Sans, G. N. Newton and H. Oshio, *Inorg. Chem.*, **2017**, 56, 12169-12177.
20. J. J. Altenau, M. T. Pope, R. A. Prados and H. So, *Inorg. Chem.*, **1975**, 14, 417-421.
21. M. Kozik, C. F. Hammer and L. C. W. Baker, *J. Am. Chem. Soc.*, **1986**, 108, 2748-2749.
22. H. So and M. T. Pope, *Inorg. Chem.*, **1972**, 11, 1441-1443.
23. G. M. Varga, E. Papaconstantinou and M. T. Pope, *Inorg. Chem.*, **1970**, 9, 662-667.
24. M. B. Robin and P. Day, in *Advances in Inorganic Chemistry and Radiochemistry*, eds. H. J. Emeléus and A. G. Sharpe, Academic Press, **1968**, 247-422.
25. C. Balagopalakrishna, J. T. Kimbrough and T. D. Westmoreland, *Inorg. Chem.*, **1996**, 35, 7758-7768.
26. R. R. Rakhimov, D. E. Jones, H. L. Rocha, A. I. Prokof'ev and A. I. Aleksandrov, *J. Phys. **Chem.***, **2000**, 104, 10973-10977.
27. J. N. Barrows and M. T. Pope, *Inorganica Chim. Acta*, **1993**, 213, 91-98.

6 HYBRID POMS AS NANOCOMPOSITE FEEDSTOCK MATERIAL FOR METAL OXIDE MICROSHELL SYNTHESIS

6.1 INTRODUCTION

Metal oxides are an extremely important class of materials due their generally low-cost, high abundance, redox-activity, stability and tuneability. Owing to their highly desirable properties, they have been applied in a broad range of applications such as energy storage, sensing and heterogeneous catalysis.[1, 2, 3] The performance of these materials are clearly dominated by the identity of the metal, however it is also highly dependent on their morphology, composition, and crystal phase.[4, 5] The tuning of their surface nanostructure has been shown to lead to the fabrication on potent facets and edges which impart catalytic activity to such materials.[6, 7] Furthermore, developing porous metal oxide nanostructures can expose active surface sites, increase surface area and mass flow through the material.

POMs offer great opportunities as precursors to generate functional metal oxide structures for a number of reasons. Firstly, their advantages lie with their diverse elemental compositions where a broad range of transition metals (e.g. V, Mo, W, Nb, and Ta) and heteroatoms (e.g. P, Si, Ge, Se and Sb) can be incorporated, which offers the potential to dope materials conveniently. Finally, POM precursors can be controllably modulated on an atomic/molecular scale, which enables the construction of designed precursors to fabricate doped metal oxides in a controlled way.[8]

Owing to these advantages, there are many examples of POMs being employed as metal oxide precursors.[8] For example, Lewis *et al.* found that by calcining $[NH_4]_6[H_2W_{12}O_{40}]$ under oxygen rich conditions, a WO_3 phase which exhibited an optical band gap of 1.9 eV was obtained.[9] As a result, this material exhibited photoanodic visible-light water oxidation activity. The unusually low bandgap of the material was concluded to be a result of intercalated N_2 in the WO_3 crystal lattice. Interestingly, the intercalation of N_2 was found to be a by-product of the oxidation of the ammonium cation. This

consequently increased the local symmetry of the crystal lattice which inherently decreased the band gaps of the $xN_2.WO_3$ material. This investigation is a prime example of the opportunities brought about by employing POMs as tuneable feedstock material for fabrication of doped metal oxide materials.

Moreover, POMs have been coupled with organic scaffolds to yield nanostructured metal oxides. As previously mentioned, the work of Deng *et al*. demonstrated the unique ability to couple POM and amphiphilic block copolymer to assemble nanostructured soft templates.[10] Upon calcination they were able to isolate cross-hatched nanowire arrays of monoclinic-WO_3. In this investigation doped-WO_3 was also obtained by exchanging the heteroatom inside the POM which further demonstrated the versatility of the method. Similarly, Breu *et al*. employed $[NH_4]_6[H_2W_{12}O_{40}]$ as the inorganic precursor and core-crosslinked poly(butadiene)-block-poly(2-vinylpyridine) (PB-b-P2VP) nanorods at pH 3, to fabricate metal-oxide soft-templates (Figure 91).[11] Upon calcination, the organic scaffold was removed and left mesostructured nanotubular crystalline WO_3, constructed by polycrystalline assembly of the metastable, orthorhombic polymorph of WO_3 which is stabilized by a crystallite nanosize effect.

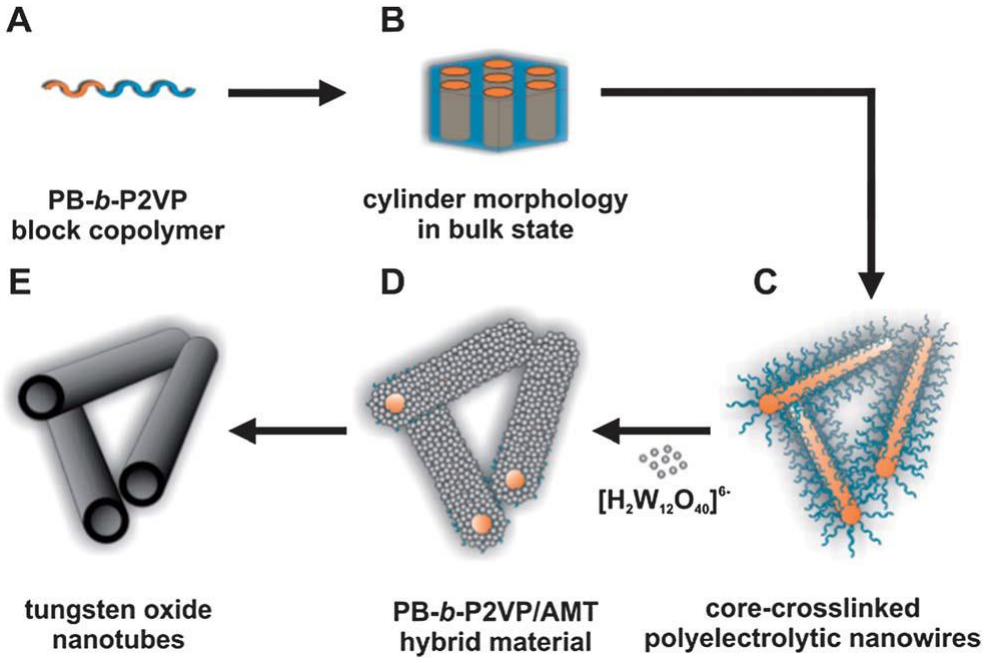

Figure 91 - Schematic illustrating templating route to WO_3 nanotubes: self-assembly of thePB-b-P2VP block copolymer (A) core-crosslinking of cylinders in the bulk state (B), dissolution of the rigid cylindrical template at pH 3 (C), formation of the PB-b-P2VP–AMT hybrid material by addition of POM (D), and calcination in an oxidative atmosphere resulting in tungsten oxide nanotubes (E). Reproduced from ref.11 with permission from the Royal Society of Chemistry.

Although these examples offer routes to nanostructured metal oxide soft-templates and solid-state materials, template assembly can be slow, and up-scaling can be extremely complex. Therefore, to upscale the assembly of POMs into soft-template precursors, an expedient approach is needed.

Spray-drying is a technique that offers a low-cost, rapid and scalable method to synthesise soft-template spherical hollow shells. Spray-drying is a widely used technique that has been employed to dry suspensions or encapsulate active species for various applications in the food and drug industry.[12, 13] This technique has also been useful in the fabrication of nanoMOF materials. Maspoch *et al.* demonstrated that by spray drying a solution of MOF precursors, the MOF components would react under specific conditions to form microshells composed of crystallised MOF material. In this way they demonstrated that MOF materials could be produced on scale (Figure 92).[14, 15]

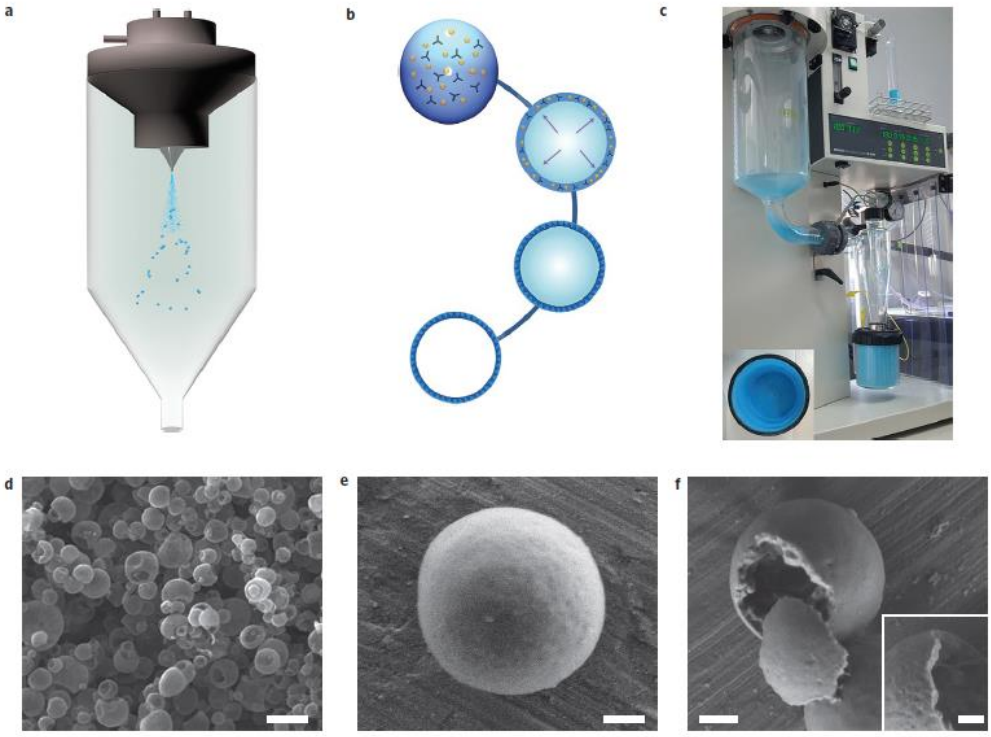

Figure 92 - Spray-drying synthesis of spherical hollow structures: a) Schematic showing the spray-drying process where blue dots represent sprayed material; b) Proposed spherical superstructure formation process where MOF precursors concentrate and crystallize at the surface into spherical superstructures; c) photograph of the spray-dryer after its use in synthesizing large amounts of blue HKUST-1 superstructures; (d–f) SEM images displaying a general view of the spherical HKUST-1 superstructures d), the wall of a single HKUST-1 superstructure showing the assembly of nanoHKUST-1 crystals e), and a mechanically broken hollow superstructure showing the internal cavity and the thickness of its wall (f and inset). Scale bars: 5 mm d), 500 nm (e,f), 200 nm (f, inset). Reproduced from ref.14 with permission from Springer Nature.

This technique works by firstly atomizing a solution of feedstock into a spray of microdroplets using a two-fluid nozzle (Figure 92a). This step involves simultaneously injecting the solution at a specified rate (feed rate) and compressed air or nitrogen gas at another rate (flow rate). In doing so, the feedstock droplet is suspended by a gas stream and heated to a certain temperature (inlet temperature) at the nozzle, causing the solvent to evaporate. This induces the precursors to diffuse to the droplet surface (Figure 92b). As the evaporating droplet shrinks, its receding droplet surface leads to increasing feedstock concentrations at the surface, causing the material to dry or crystalise at the surface. This technique offers a rapid and scalable method to produce microshell particles which can be combined with POM feedstock materials to produce soft metal oxide template precursors at scale and rapidly.

6.2 AIM

The aim of this chapter is to test the ability of hybrid-POMs to act as feedstock materials to produce soft metal oxide templates. Furthermore, we aim to explore the effects of using Hybrid-POMs over plenary POMs and highlight any differences we observe in the soft template and calcined product. We will fabricate nanostructured WO_3 shells from POM based feedstock by employing spray-drying to produces soft-template shells, and then calcine these shells to produce solid-state particles. The feedstock material will be based on: 1) **{W_{18}}**, 2) **{$W_{17}C_{20}$}** and 3) **{$W_{15}Mo_2C_{20}$}**. Furthermore, we will demonstrate the opportunities to dope these WO_3 shells by processing mixed addenda POMs. These clusters will be sprayed, calcined, and examined *via* SEM, IR and PXRD.

6.3 METHODOLOGY

Spray-drying will be employed to convert POMs to soft template microshells. This will be conducted by dissolving the POM in aqueous solutions which will be sprayed at a selected temperature with a flow rate of min^{-1} and a feed rate of mL min^{-1}. The product will then be caught in the trap or in rare cases the vortex (Figure 93). The synthesis of the POM feedstock materials has been discussed in previous chapters, so will not be covered here.

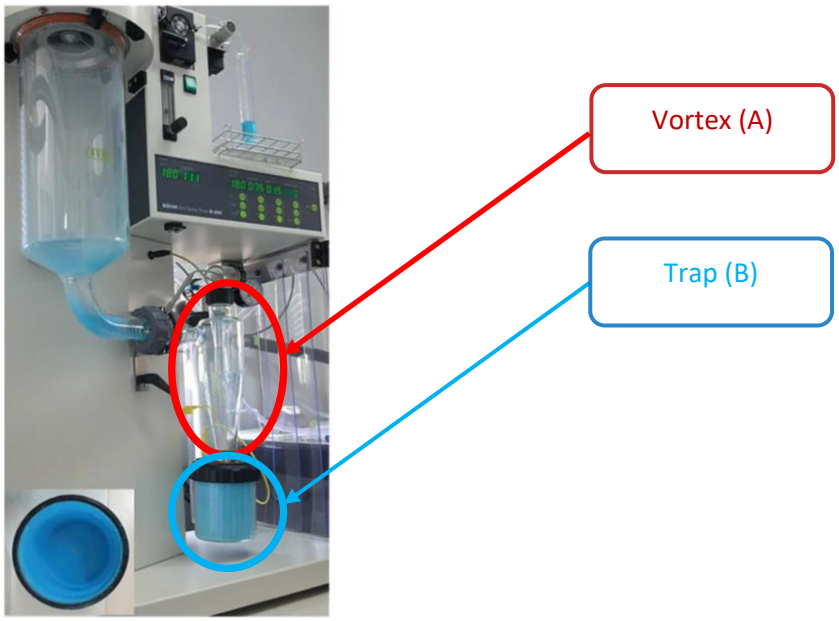

Figure 93 - Photograph of the spray-dryer after its use in synthesizing blue HKUST-structures which highlights the trap and vortex components. Reproduced from ref.14 with permission from Springer Nature.

6.4 RESULTS AND DISCUSSION

6.4.1 Preliminary results

To produce WO_3 metal oxide shells, we employed POMs as a tuneable tungstate feedstock material and spray-drying as the processing methodology. Firstly, we set out to understand how the composition and structure of the calcined WO_3 shells would change when sprayed from a solution of hybrid-POM micelles. To do this, we employed **{$W_{17}C_{20}$}** as our micelle feedstock and **{W_{18}}** as our plenary POM control. Developing this further, we were curious to prove whether it was possible to produce doped WO_3 shells, therefore **{$W_{15}Mo_2C_{20}$}** was employed as our mixed metal oxide feedstock. Furthermore, there are also possibilities of P doping from the hybridised ligand or POM phosphate template.

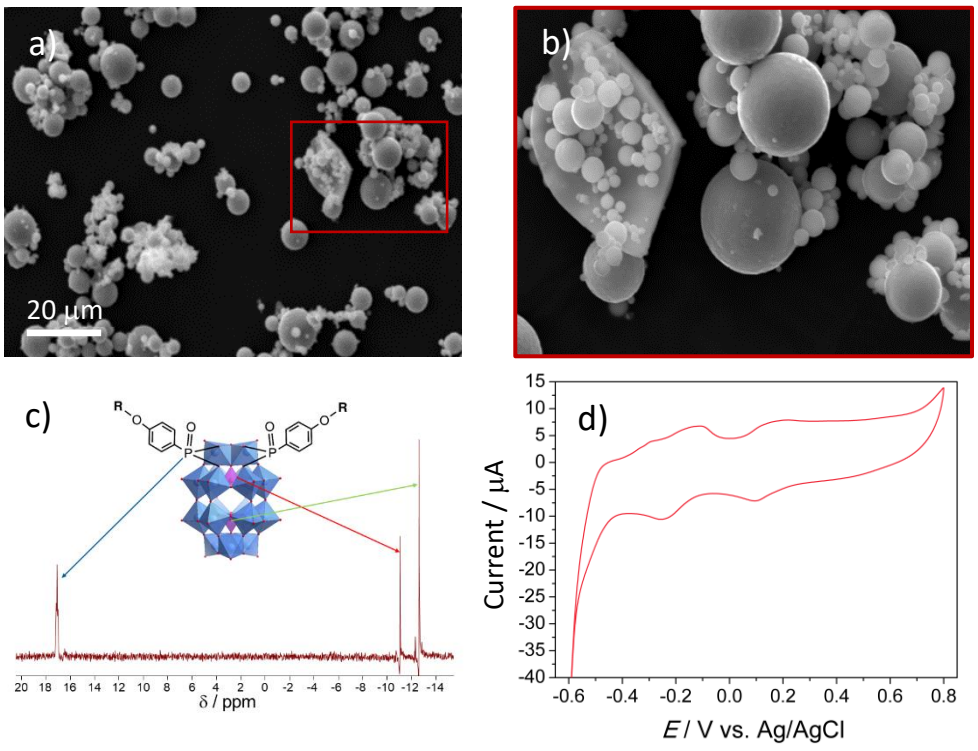

Figure 94 - Characterisation of 2 mM spray-dried {$W_{17}C_{20}$} material: a) SEM characterisation of spherical spray-dried particles with highlighted region shown in b); c) ^{31}P NMR of redissolved spray-dried material in d_3-MeCN where R = C_{20}; and d) a CV of spray-dried material redissolved in 0.1 M H_2SO_4 supporting electrolyte and conducted with a GC working electrode, Pt counter electrode and Ag/AgCl reference electrode.

Our preliminary experiments involved the spray drying of 2 mM **{$W_{17}C_{20}$}** H_2O solution, where **{$W_{17}C_{20}$}** forms a micellar solution. Upon spraying at 100 °C, spherical hollow shells were observed, and these conditions led to a polydisperse sample with the diameters of the shells ranging from 300 nm to 5 μm (Figure 94a and b). To test the whether the POM had degraded, we firstly dispersed the spray-dried material into water. We found that the material redissolved into micelles based on DLS analysis (D_h = 7 nm). Furthermore, ^{31}P NMR of the redissolved spray-dried materials in d_3-MeCN displayed no degradation of **{$W_{17}C_{20}$}** and the overall surface-confined electrochemical behaviour was also retained in acid at the GC electrode (Figure 94d). Thus, based on these conditions we found that the molecular integrity was maintained. We can infer from these results that the materials produced are soft templates constructed from **{$W_{17}C_{20}$}**, which can be recovered back to the molecular form.

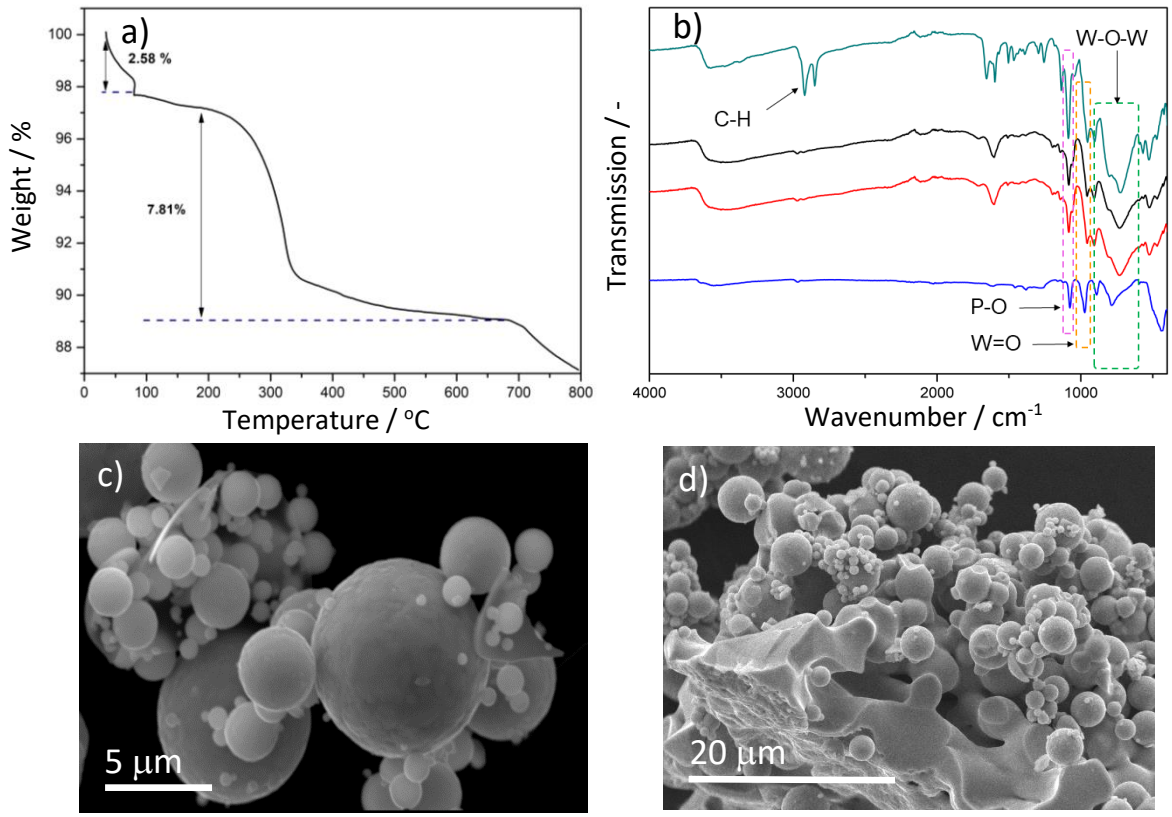

Figure 95 - Characterisation of calcined 2 mM {$W_{17}C_{20}$} spray-dried material: a) TGA of {$W_{17}C_{20}$}; b) FT-IR of spray-dried material (green), and spray-dried material calcined for 1min@600°C (black), 10min@600°C (red) and 1min@900°C (blue) with key signals highlighted; c) SEM of material calcines 1min@600°C; and d) 1min@900°C.

Once recoverability of the clusters was confirmed, the shells were annealed to various temperatures based on the TGA analysis of **{$W_{17}C_{20}$}** (Figure 95a). TGA analysis shows an initial 2.87 % mass loss associated with solvent (H_2O and MeCN) and a 7.81% mass loss associated with the combustion of the ligands. The mass loss associated with the ligand does not calculate to full mass loss of two ligands, indicating there may be potential charring or, carbon and phosphorus residues doped in the metal oxide phase. The spray-dried shells were calcined at two temperatures, 600 ^oC and 900 ^oC. Both materials were insoluble in water, which indicated that the molecule had degraded. Based on IR spectroscopy of the calcined materials (Figure 95b), we observe the of loss of C-H stretches at 2924 cm^{-1} and 2846 cm^{-1}, indicating the combustion of the organic ligand. Characteristic peaks in the spray-dried shells corresponding to the POM core can be observed with the P-O stretches occurring at ~1080 cm^{-1}, the W=O stretches of the terminal oxo groups are seen at ~945 cm^{-1} and the W-O-W bends of the bridging oxygens occurring as a broad band between 600 cm^{-1} and 900 cm^{-1}. When the shells are calcined, there is a change in the W-O-W bending peaks which potentially indicates a transition in the POM structure to WO_3 phase. However, a phase transition is witnessed at 700 ^oC by TGA, which confirms the difference in the IR spectrum observed between calcined product at 600 ^oC and 900 ^oC. The IR spectrum of WO_3 typically displays a broad peak between 500-1000 cm^{-1}. SEM analysis (Figure 95c and d) shows the shells structural integrity remains when calcined at 600 ^oC, however, at 900 ^oC, there are large areas where the shells have sintered. Therefore, a fine balance is needed with the calcination temperature in order to reach phase crystallinity and reduce sintering.

6.4.2 Optimisation of Spray-Drying

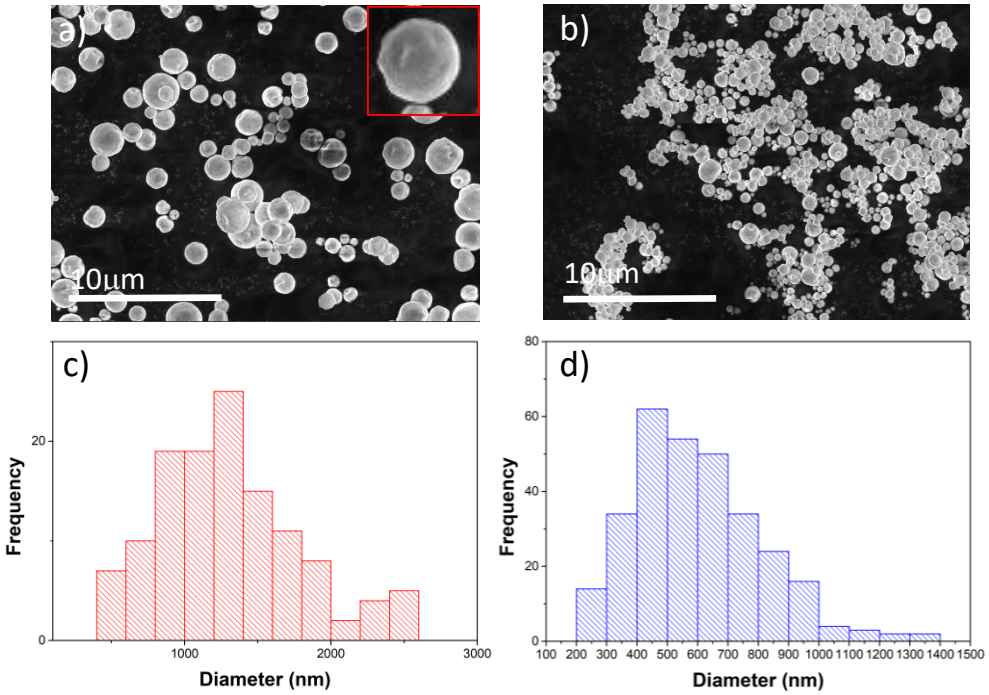

Figure 96 - SEM characterisation of 0.045 mM $\{W_{17}C_{20}\}$ spray-dried material: a) particles caught in vortex with size *vs*. frequency plot c); b) particles caught in trap with size *vs*. frequency plot d).

Following the above analysis, it was clear we were able to fabricate hollow WO_3 microshells from the calcination of soft-template precursors assembled from POMs. Our next aim was to then reduce the size and polydispersity of the shells. To do so, a number of parameters were tested such as temperature, flow rate and concentration. We found that by reducing the concentration to 0.045 mM, the overall size and polydispersity decreased significantly. However, the higher water content in the sample caused the smaller shells to fuse. To mitigate the solvent induced fusion of the shells, the temperature was increase to an optimal temperature of 200 °C, which allowed us to spray discrete shells. With these conditions, we observed a size-based separation, where larger clusters would aggregate in the vortex and smaller shells separated out into the trap. Thus, we have observed an *in-situ* size separation in the instrument for all samples. SEM images in Figure 96 show two size ranges, where an average size (diameter) of 1250 nm and 450 nm were caught in the vortex and trap, respectively for **$\{W_{17}C_{20}\}$**. The shells observed for **$\{W_{17}C_{20}\}$** had unique curvature features, morphologically resembling collapsed shells. Comparatively, this was different to the shell

morphology observed for **{W_{18}}** where the shells were smooth and featureless. Here the shells observed were larger, average size of 1250 nm and 600 nm was found in the vortex and trap respectively (Figure 97a and b). **{$W_{15}Mo_2C_{20}$}** exhibited a similar size and (1300 nm vortex and 750 nm trap) collapsed shell morphology to **{$W_{17}C_{20}$}**, which suggests that the presence of amphiphilic chains or the spraying from micelles plays a dominant role in the packing of the molecules in the shell walls (Figure 97c and d). Perhaps the amphiphilic chains bring about a larger degree of disorder in the packing which is amplified in the larger microstructure. Furthermore, it is worth noting that by applying these spray-drying conditions, **{$W_{17}C_{20}$}** and **{$W_{15}Mo_2C_{20}$}** decomposed. By ^{31}P NMR analysis, free ligand peaks were found, and multiple phosphorus peaks were observed between -10 ppm to -16 ppm, which suggest POM decomposition. An intense peak at -13 ppm suggests upon hydrolytic cleaving of the ligands from the POM, the POM reorganised to **{W_{18}}**. On the other hand, no structural perturbation was found for **{W_{18}}** by ^{31}P NMR under these conditions.

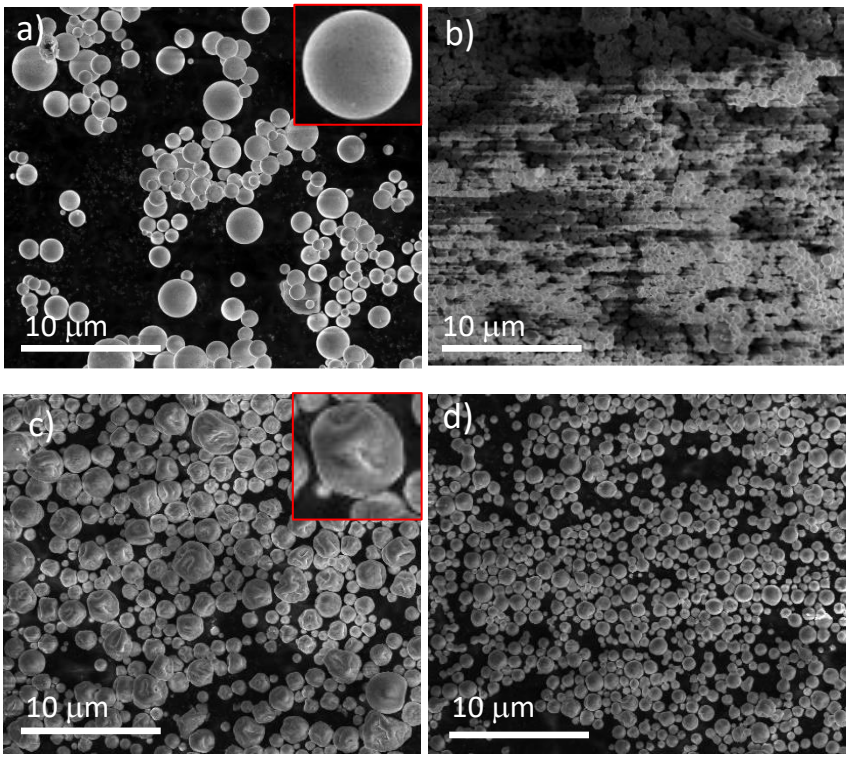

Figure 97 - SEM characterisation of 0.045 mM spray-dried material: {W_{18}} particles caught in vortex (a) and trap (b); {$W_{15}Mo_2C_{20}$} particles caught in vortex (c) and trap (d).

6.4.3 Calcination

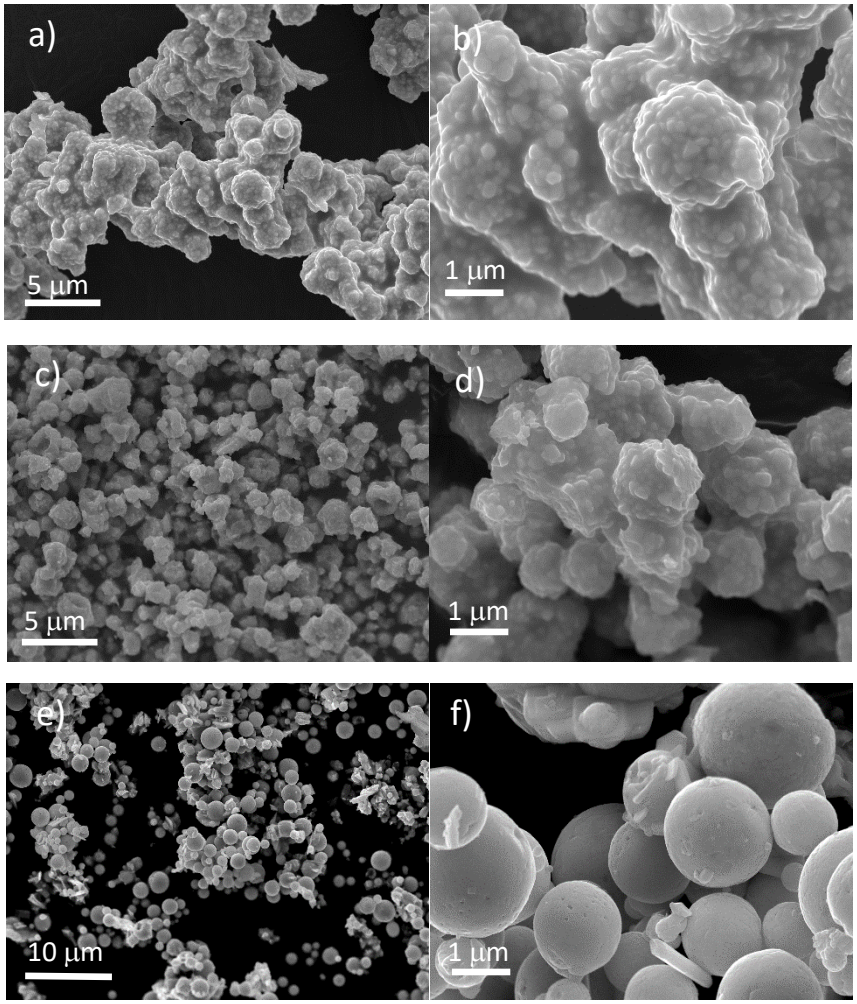

Figure 98 - SEM characterisation of calcined 0.045 mM spray-dried material: {$W_{17}C_{20}$} a) and b); {$W_{15}Mo_2C_{20}$} c) and d); {W_{18}} e) and f).

Following our calcination results, we concluded that 900 °C was too high and led to sintering of the shells. Furthermore, at 600 °C the material may have potentially been in a *pseudo*-WO_3-POM phase, therefore a higher temperature was needed in order to reach a pure WO_3 phase. For the calcination experiments, we moved forward with the larger shells found in the vortex. Successive calcination test was then run in the TGA to determine the optimal temperature and time when considering sintering and crystallinity. For **{$W_{17}C_{20}$}** 10 °C / min ramp to 800 °C and a 15 min isotherm gave us crystalline material (Figure 98a and b). Here we can see that the shells have unfortunately fused, however, there are interesting surface crystallite features which are approximately 100 nm in size. When **{$W_{15}Mo_2C_{20}$}**

was ramped 10 °C / min to 700 °C with a 1 h isotherm, a similar surface structure was observed (Figure 98c and d). The low crystallisation temperature observed for this compound can be attributed to the lower thermal stability associated with Mo addenda, which can reduce the over thermal stability of the cluster.[16] Interestingly, **{W_{18}}** was calcined under the same conditions as **{$W_{15}Mo_2C_{20}$}** and no surface nanostructure features were observed (Figure 98e and f). Only a smooth surface structure was observed. When **{W_{18}}** was exposed to the same calcination conditions as **{$W_{17}C_{20}$}**, no surface nanostructuring was observed, only additional sintering. Comparatively, **{W_{18}}** showed a lower degree of sintering compared to **{$W_{17}C_{20}$}** and **{$W_{15}Mo_2C_{20}$}**. This could be related to the reactivity of the POM degradation products being extruded from the metal oxide phase, specifically any trapped carbon residues being combusted.

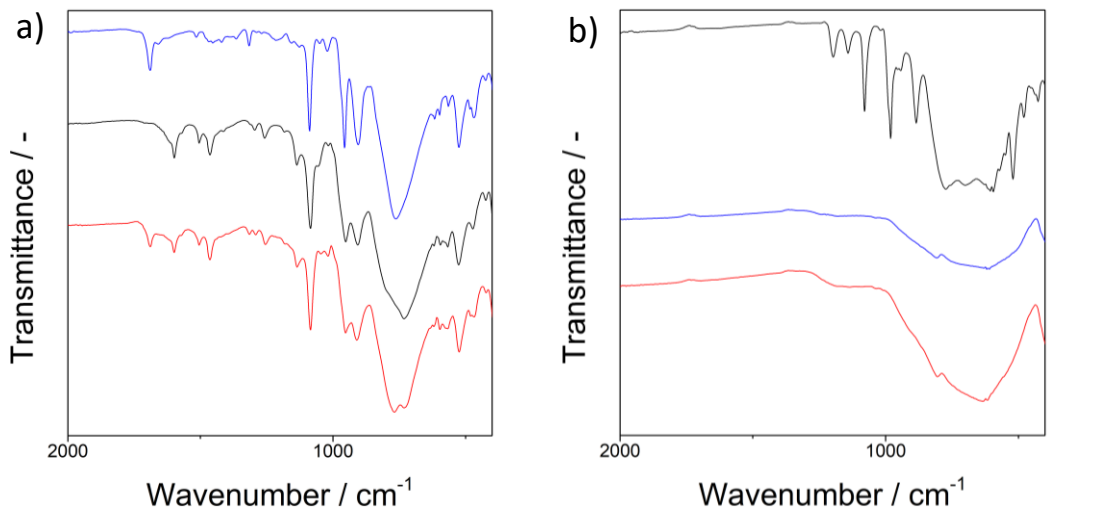

Figure 99 - FT-IR analysis of spray-dried material a) and calcined spray-dried material b) of {W_{18}} (black), {$W_{17}C_{20}$} (blue) and {$W_{15}Mo_2C_{20}$} (red).

Figure 99 displays the FT-IR analysis of the spray dried material pre- and post-calcination. Comparing the two there is a clear broadening of the W-O-W stretch at 1000-500 cm^{-1} for all three compounds. This broadening is more pronounced for **{$W_{17}C_{20}$}** and **{$W_{15}Mo_2C_{20}$}**. Interestingly, the P-O stretch at 1084cm^{-1} is present in the spray-dried soft material, however, this peak is absent post calcination for **{$W_{17}C_{20}$}** and **{$W_{15}Mo_2C_{20}$}**. Under these conditions the phosphate backbone may have been extruded from the structure. Interestingly, **{W_{18}}** calcined material still possesses this stretch. This indicated that the material has not been uniformly calcined or the new WO_3 material is P doped. IR spectrum for WO_3 materials typically displays a broad peak 500-900 cm^{-1} assigned to the W-O-W stretching modes. This also suggests that **{W_{18}}** possesses a higher thermal stability than the hybrid structures. There is a clear difference in the IR spectra of the hybrids and the parent anion which suggests that the either **{W_{18}}** has not been fully calcined to WO_3 or it possesses a different WO_3 phase.

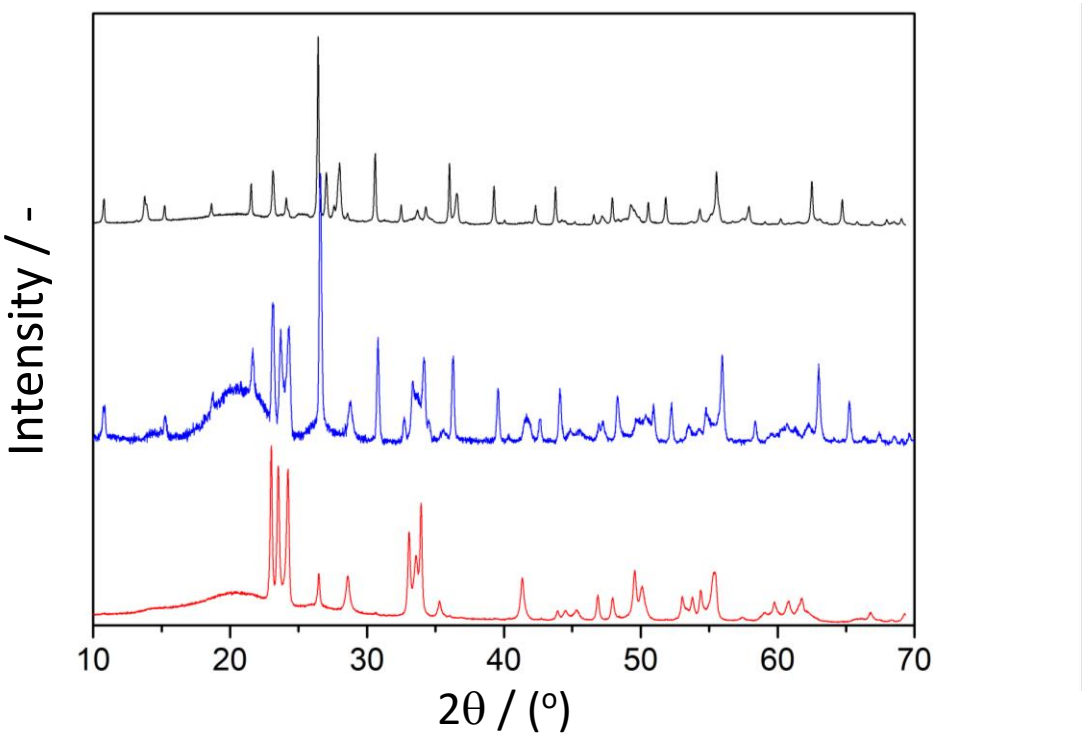

Figure 100 - PXRD analysis of calcined spray-dried material: of {W_{18}} (black), {$W_{17}C_{20}$} (blue) and {$W_{15}Mo_2C_{20}$} (red).

PXRD analysis of the calcined products indicated all compounds are crystalline (Figure 100). In particular, 2θ peaks for **{$W_{17}C_{20}$}** (23.1°, 23.7° and 24.3°) and {$W_{15}Mo_2C_{20}$} (23.0°, 23.5° and 24.2°) indicate the presence of monoclinic-WO_3 phases. Interestingly, these diffraction peaks are not observed for **{W_{18}}**, indicating that it may possess a different phase. Additional peaks suggest a mixed phase material. The diffractions peaks do however differ slightly between **{$W_{17}C_{20}$}** and **{$W_{15}Mo_2C_{20}$}** which may be attributed to the presence of Mo doped WO_3. Further analysis is needed to index the peaks and reference these products to known WO_3 materials.

6.5 CONCLUSION

In summary, we have demonstrated the synthesis of soft template precursors for WO_3 microshell fabrication through spray-drying POM based feedstock. We found that by spraying POM amphiphiles, the overall morphology of the soft-template changes when compared to shells produced from parent anion **{W_{18}}**. Furthermore, we found that by lowering the concentration of the feedstock solution, the size of the shells and dispersity generally decreased. These shells were characterised *via* SEM.

Upon calcination of these shells, we were able to access crystalline WO_3 shells. Based on the surface structure, we observed key differences between parent anion **{W_{18}}** and hybrids, **{$W_{17}C_{20}$}** and **{$W_{15}Mo_2C_{20}$}**. Here we found that the calcination products of the hybrids displayed a higher degree of sintering however also displayed nanostructured crystallite patterns on the surface. Conversely, this was not observed for {W_{18}}, here the shells displayed an overall smooth surface. Furthermore, based on the IR and PXRD, **{$W_{17}C_{20}$}** and **{$W_{15}Mo_2C_{20}$}** displayed similar characteristics which indicated they may possess similar phases of WO_3. Similar characterisation of **{W_{18}}** displayed contrasting results which suggest the product may not have been fully calcined or displays a different phase.

Overall, we observe distinct differences in the morphology of the shells pre- and post-calcination based on whether the material is sprayed from amphiphilic hybrid POM or plenary POM structure. Through this methodology, we demonstrated that POMs can be employed as a tuneable feedstock for WO_3 materials. Additionally, the use of spray-drying promotes opportunities to up-scale the fabrication of bespoke WO_3 nanostructured materials for a number of applications including photocatalysis, electrocatalysis and sensing.[17]

6.6 REFERENCES

1. Y. Zhao, L. P. Wang, M. T. Sougrati, Z. Feng, Y. Leconte, A. Fisher, M. Srinivasan and Z. Xu, *Adv. En.Mater.*, **2017**, 7, 1601424.
2. G. S. Hutchings, Y. Zhang, J. Li, B. T. Yonemoto, X. Zhou, K. Zhu and F. Jiao, *J. Am. Chem. Soc.*, **2015**, 137, 4223-4229.
3. A. Dey, *Mater. Sci. Eng., B*, **2018**, 229, 206-217.
4. J. Fang, L. Zhang, J. Li, L. Lu, C. Ma, S. Cheng, Z. Li, Q. Xiong and H. You, *Nat. Commun.*, **2018**, 9, 521.
5. H. Wang, S. Zhuo, Y. Liang, X. Han and B. Zhang, *Angew. Chem. Int. Ed*, **2016**, 55, 9055-9059.
6. J. Byun, H. A. Patel, D. J. Kim, C. H. Jung, J. Y. Park, J. W. Choi and C. T. Yavuz, *J. Mater. Chem. A*, **2015**, **3**, 15489-15497.
7. Y. Ren, Z. Ma and P. G. Bruce, *Chem. Soc. Rev.*, **2012**, 41, 4909-4927.
8. B. Huang, D.-H. Yang and B.-H. Han, *J. Mater. Chem. A*, **2020**, 8, 4593-4628.
9. Q. Mi, Y. Ping, Y. Li, B. Cao, B. S. Brunschwig, P. G. Khalifah, G. A. Galli, H. B. Gray and N. S. Lewis, *J. Am. Chem. Soc.*, **2012**, 134, 18318-18324.
10. Y. Ren, Y. Zou, Y. Liu, X. Zhou, J. Ma, D. Zhao, G. Wei, Y. Ai, S. Xi and Y. Deng, *Nat. Mater.*, **2020**, 19, 203-211.
11. M. Schieder, T. Lunkenbein, T. Martin, W. Milius, G. Auffermann and J. Breu, *J. Mater. Chem. A*, **2013**, 1, 381-387.
12. R. Vehring, *Pharm. Res.*, **2008**, 25, 999-1022.
13. L. Yu, *Adv. Drug Deliv. Rev.*, **2001**, 48, 27-42.
14. A. Carné-Sánchez, I. Imaz, M. Cano-Sarabia and D. Maspoch, *Nat. Chem.*, 2013, **5**, 203-211.
15. C. Avci-Camur, J. Troyano, J. Pérez-Carvajal, A. Legrand, D. Farrusseng, I. Imaz and D. Maspoch, *Green. Chem.*, **2018**, 20, 873-878.
16. N. Mizuno and M. Misono, *Chem. Rev.*, **1998**, 98, 199-218.
17. C. C. Mardare and A. W. Hassel, *phys. Status Solidi (a)*, **2019**, 216, 1900047.

7 CONCLUSION AND OUTLOOK

Within each chapter, we have discussed the goals we set out to achieve, summarised the results and considered what the future for each research project holds. Therefore, in this section we will discuss the overarching aim of the broader research regarding this thesis project and how the overall research contributes to the theme. The narrative of this thesis was focused on the supramolecular assembly of Class II hybrid-POM amphiphiles, where we set out to develop a novel modifiable amphiphile system with the aim to probe its supramolecular assembly, develop avenues to tune the amphiphiles and study the relatively unexplored properties of the assembled structures. In this way we could better understand the relationship between the hybrid-POM molecule properties in its molecular form compared to its supramolecular form. This has been achieved in various ways through discussion across each chapter.

With regards to modification of the amphiphile molecule, three avenues were explored, which focused on the three components of the overall hybrid-POM structure: 1) hydrophobic chain (ligand), 2) phosphonate linker and 3) addenda composition. Through the modification of the chain-length of the amphiphile, we explored trends in the supramolecular assembly sizes and the inherent redox behaviour of the assemblies. Longer chain-lengths resulted in the assembly of well-defined, monodispersed micellar structures which displayed contrasting redox properties to its molecular form. Comparatively, the shorter chain-lengths assembled into structures with greater disorder and the redox profiles of the assemblies displayed molecular characteristics. This ties into the driving force of the assembly – *hydrophobic effect*. Therefore, through grafting longer chain-lengths it is possible to access unique redox-activity of the hybrid-POM supramolecular assemblies. Furthermore, supramolecular assembly of longer chain-length amphiphiles demonstrated a greater ability to assemble into hierarchical structures, with increasing degrees of order. Overall, it's clear that through employing longer chain-lengths, we can drive the assembly of redox-active POM clusters to larger

complex structures and translate the molecular properties to the superstructure. Furthermore, these molecules can be stimulated by a range of environmental factors to force supramolecular assembly transitions where temperature, concentration and surface hydrophobicity can stimulate morphological transitions of the supramolecular assemblies to higher-order structures. Based on the linker, we explored a DP linker system, which proved to be employable as ligands that can modulate the electronic properties of the POM and can be modified to attach various organic moieties, including amino acids and hydrophobic chains. The prospect of single chain amphiphiles by modifying these molecules offers routes to further probe the assembly properties and modulate the assembly's redox properties. Modification of the metal addenda composition of the POM also demonstrated a new avenue to couple the effects of organo-functionalisation and metal substitution to modulate the POM molecular properties which have shown to translate to the interesting and unique redox-properties of its assembly; further demonstrating opportunities to tune the properties of the supramolecular assembly. Finally, we demonstrated that hybrid-POM molecules can bring about opportunities when employed as feedstock to generate bespoke doped nanostructured metal oxide materials.

Overall, we have gained a better understanding of the factors that affect the supramolecular assembly of hybrid-POM amphiphiles, how modify the amphiphiles electronic properties and further probe the system. Therefore, we have explored a number of avenues which can be exploited to develop tuneable redox-active advanced soft-materials.

8 METHODS, MATERIALS AND INSTRUMENTATION

All commercially available solvents and reagents were purchased from *Thermo Fisher Scientific*, *Sigma Aldrich*, *Alfa Aesar* and used without purification.

Nulcear Magnetic Resonance (NMR) spectroscopy was performed using a Bruker AV400 or Bruker AV(III)500 spectrometer at 298K. Chemical shifts (δ) are recorded in parts per million (ppm), coupling constants (J) are given in Hertz (Hz). Peak multiplicity is denoted by the following abbreviations: singlet (s), doublet (d), triplet (t), quartet (q), multiplet (m) and triplet of triplets (tt).

Electrospray ionisation mass spectrometry (ESI-MS) was performed on a Bruker MicroTOF spectrometer operating in negative mode. Samples were prepared for analysis by dissolving ca. 1 mg of the solid compound in 1 mL of HPLC grade acetonitrile. 50 μL of this stock solution was then introduced to the spectrometer through an auto-sampler by mixing into a stream of 30:70 H_2O:MeOH. All data was subsequently analysed using the Bruker DataAnalysis software suite. Modified instrument parameters were used for the detection of high molecular weight polyoxometalate anions.

Attenuated Total Reflection Fourier-transform Infra-red spectroscopy (ATR-FTIR) was recorded on a Bruker Tensor 27 spectrometer equipped with a Pike GladiATR module with a diamond crystal.

UV-vis spectroscopy (UV-vis) was performed on an Agilent Cary 5000 UV-Vis-NIR Absorption spectrometer. Solution phase measurements were performed using the standard double cuvette holder module in absorption mode. Solid state diffuse reflectance absorption measurements were performed using a DRA-900 InGaAs integrating sphere.

CHN Elemental Microanalysis was performed by the University of Nottingham School of Chemistry elemental microanalysis services using a Exeter analytical CE-440 Elemental Analyzer.

Single crystal X-ray diffraction measurements were performed using the following procedure: a single crystal was selected and mounted using Fomblin® (YR-1800 perfluoropolyether oil) on a polymer-tipped MiTeGen MicroMountTM and cooled rapidly to 120 K in a stream of cold N_2 using an Oxford Cryosystems open flow cryostat. Single crystal X-ray diffraction data were collected on a SuperNovaDuo diffractometer (Atlas CCD area detector, mirror-monochromated Mo-Ka radiation source; λ = 0.71073 Å; ω scans) or an XtaLAB PRO MM007 (PILATUS3 R 200K Hybrid Pixel Array detector, mirrormonochromated Cu-Ka radiation source; λ = 1.54184 Å, ω scans). Cell parameters were refined, and absorption corrections were applied using a Gaussian numerical method with beam profile correction (CrysAlisPro). The structure was solved within Olex2. PLATON SQUEEZE procedure

was employed to solve the electronic contribution of disordered solvent molecules and cations in the structure. Structures were checked with checkCIF.

Powder X-ray Diffraction (PXRD) measurements were performed using a PANalytical X'Pert PRO diffractometer with a Copper line focus X-ray tube (40 kV, 40 mA), with monochromator tuned to Kalphα1 (Kα1 = 1.540598) and a PIXcel detector (length 3^{o}). The diffractometer had Bragg Brentano geometry and was operated in reflection transmission mode with samples mounted on brass powder sample holders on a spinning stage. An incident beam Soller slit of 0.04 rad, 1° fixed anti scatter slit, incident beam mask of 10 mm and programmable automated divergence slit giving a constant illuminated path length of 5.0 mm were used.

Thermogravimetric Analysis (TGA) were performed either using a TA-Q500 (TA Instruments) or a TGA Discovery Instrument using a high temperature platinum pan within a temperature range of 25 °C to 1000 °C under air flow streams.

Electrochemical methods, cyclic voltammetry (CV) and differential pulse voltammetry (DPV), were performed on a CHI600E workstation for solution state measurements. A standard three electrode set-up was employed with a glassy carbon working electrode (d = 3 mm), Pt wire counter electrode and either a Ag wire pseudo reference with the addition of ferrocene as an external reference (solution state) or a AgCl/Ag non-aqueous reference electrode.

Photooxidaiton measurements were carried out by preparing 3 x 10^{-5} M solutions of the analyte in DMF (deoxygenated and anhydrous), 2.5 mL of sample is transferred to a sealable cuvette in the glovebox with an argon atmosphere to avoid any oxygen being sealed in the system. The solution was then irradiated with a Xe 300 W Cermax lamp (operating at 200 W) either with or without a UV cut-off filter with no stirring. The sample was measured at specific time intervals and transferred in a contained to avoid the sample being in contact with light.

Spray-drying experiments were performed using a Mini Spray Dryer B-290 (BÜCHI Labortechnik AG, Flawil, Switzerland).

9 APPENDIX

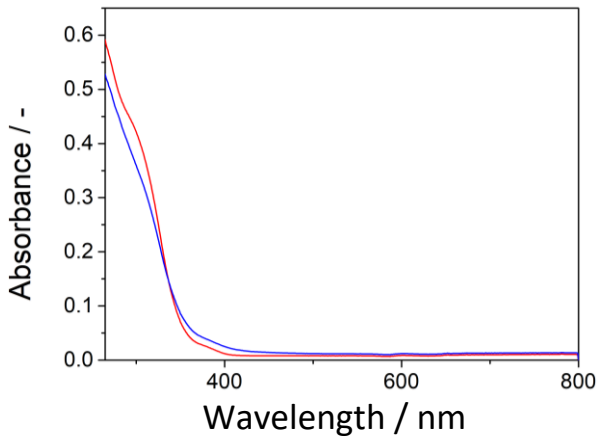

Figure S1 - UV-Vis spectrum of $1x10^{-5}$ M{W_{18}} (red) and {$W_{17}C_{20}$} (blue) in DMF.

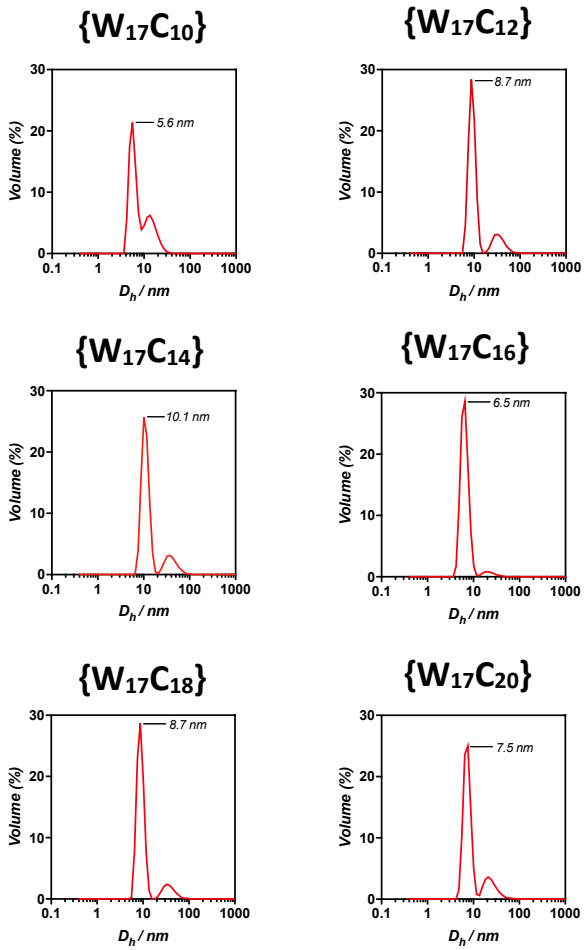

Figure S2 - Particle-size distribution analysis of {$W_{17}C_{10\text{-}20}$} (1.4 mM) in 0.1 M H_2SO_4.

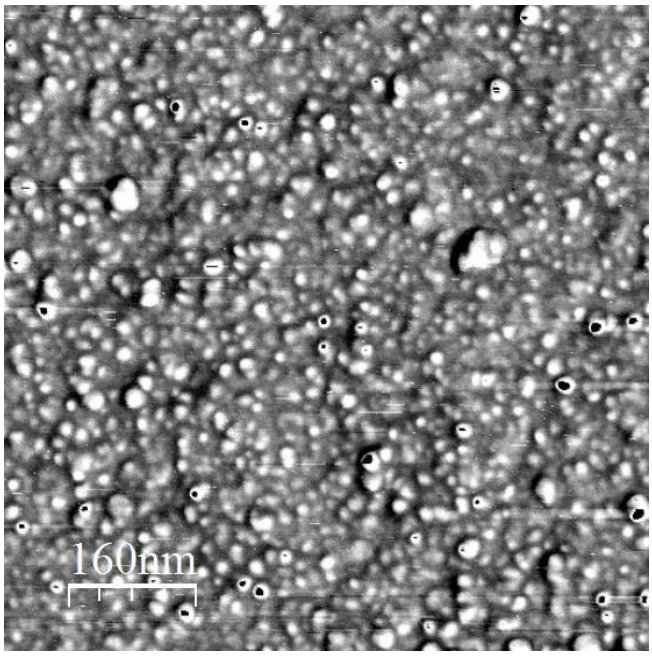

Figure S3 - AFM phase image of {$W_{17}C_{20}$} micelles@GC prepared from 0.1 M H_2SO_4.

Table S1 Crystal data and structure refinement for {$W_{15}Mo_2PPh$}

Identification code	MOSALA_H2
Empirical formula	C12H80K6Mo2O98P4W15
Formula weight	5100.87
Temperature/K	100(2)
Crystal system	monoclinic
Space group	P21/n
a/Å	13.5019(3)
b/Å	34.5202(8)
c/Å	20.1134(5)
α/°	90
β/°	93.385(2)
γ/°	90
Volume/Å3	9358.3(4)
Z	4
ρcalcg/cm3	3.620
μ/mm 1	17.417
F(000)	9216.0
Crystal size/mm3	0.08 × 0.03 × 0.025
Radiation	Synchrotron (λ = 0.6889)
2Θ range for data collection/°	2.274 to 40.294
Index ranges	-13 ≤ h ≤ 13, -34 ≤ k ≤ 34, -20 ≤ l ≤ 20
Reflections collected	59323
Independent reflections	9798 [Rint = 0.0798, Rsigma = 0.0739]
Data/restraints/parameters	9798/1408/865
Goodness-of-fit on F2	1.073
Final R indexes [I>=2σ (I)]	R1 = 0.0603, wR2 = 0.1803
Final R indexes [all data]	R1 = 0.0780, wR2 = 0.1946
Largest diff. peak/hole / e Å-3	2.55/-1.31